The University of Maine
DigitalCommons@UMaine

Summer 8-14-2015

Topographic Signatures of Geodynamics

Samuel G. Roy

Earth and Climate Sciences, samuel.g.roy@umit.maine.edu

Recommended Citation

TOPOGRAPHIC SIGNATURES OF GEODYNAMICS

By

Samuel Geoffrey Roy

B.S. University of Maine, 2008

M.S. University of Maine, 2011

A DISSERTATION

Submitted in Partial Fulfillment of the

Requirements for the Degree of

Doctor of Philosophy

(in Earth and Climate Sciences)

The Graduate School

The University of Maine

August 2015

Advisory Committee:

Peter Koons, Professor of Earth and Climate Sciences, Advisor

Christopher Gerbi, Associate Professor of Earth and Climate Sciences

Sean Smith, Assistant Professor of Earth and Climate Sciences

Phaedra Upton, Geodynamic/Geomorphic Modeler, GNS Science

Gregory Tucker, CIRES Fellow, Department of Geological Sciences, University of

Colorado Boulder

DISSERTATION ACCEPTANCE STATEMENT

On behalf of the Graduate Committee for Samuel Geoffrey Roy, I affirm that this manuscript is the final and accepted dissertation. Signatures of all committee members are on file with the Graduate School at the University of Maine, 42 Stodder Hall, Orono, Maine.

Dr. Peter Ortqvist Koons, Professor of Earth and Climate Sciences   August 14, 2015

LIBRARY RIGHTS STATEMENT

In presenting this dissertation in partial fulfillment of the requirements for an advanced degree at the University of Maine, I agree that the Library shall make it freely available for inspection. I further agree that permission for "fair use" copying of this dissertation for scholarly purposes may be granted to the Librarian. It is understood that any copying of publication of this dissertation for financial gain shall not be allowed without written permission.

Signature:

Date:

TOPOGRAPHIC SIGNATURES OF GEODYNAMICS

By
Samuel Geoffrey Roy

Dissertation Advisor: Dr. Peter Ortqvist Koons

An Abstract of the Dissertation Presented
in Partial Fulfillment of the Requirements for the
Degree of Doctor of Philosophy
(in Earth and Climate Sciences)
August 2015

The surface of the Earth retains an imperfect memory of the diverse geodynamic, climatic, and surface transport processes that cooperatively drive the evolution of Earth. In this thesis I explore the potential of using topographic analysis and landscape evolution models to unlock past and/or present evidence for geodynamic activity. I explore the potential isolated effects of geodynamics on landscape evolution, particularly focusing on two byproducts of tectonic strain: rock displacement and damage. Field evidence supports a strong correlation between rock damage and erodibility, and a numerical sensitivity analysis supports the hypothesis that an order of magnitude weakening in rock, well within naturally occurring weakening levels, can have significant effects on the rates and patterns of landscape evolution. More specifically, weak zones associated with fault damage erode relatively quickly and hence attract a greater proportion of surface runoff, causing many rivers to become confined to the exposed structures of fault zones. In many cases this influence is independent of how evolved a landscape is prior to weak zone introduction. When combined, displacement and damage along a fault cooperatively control the drainage network pattern, hillslopes, and channel gradients. Quantitative methods for measuring topographic anisotropy indicate signature patterns associated with specific scale-dependent

geodynamic and geomorphic processes that could otherwise go unnoticed when attempting to identify features from raw topographic data alone. The sharp relief associated with weak zone erosion leads to a significant perturbation of the near surface stress field that can potentially localize crustal failure under active tectonic conditions. Models used to study interactions between climate, surface processes, and crustal tectonics suggest a strong positive feedback between erosion and strain caused by the mechanical link between rock damage and erodibility. The rapid erosion of shear zones leads to greater topographic stress and hence greater strain localization. The link between erodibility and strain localization scales with greater damage, particularly due to structurally confined drainage patterns focusing a greater degree of fluvial incision in regions that already accommodate the majority of strain, resulting in a greater concentration and greater longevity of strain in narrow shear zones.

DEDICATION

For Teagan, Evangeline, and Baxter

ACKNOWLEDGEMENTS

as a lab assistant. Of course I must also give a great big thank you to all faculty and staff in the School of Earth and Climate Sciences for cultivating such a positive culture of exploration and friendship.

I have many people to thank when it comes to my research. In no particular order this includes Nancy Price, Jeff Marsh, Felice Naus-Thijssen, Ben Frieman, Jamie Howarth, Nicholas Richmond, Won Joon Song, Bora Song, Bipush Osti, Deborah Shulman, Maura Foley, Stephanie Mills, Brett Gerard, Lauren Wheeler, Annie Boucher, Lynn Kaluzienski, Bess Koffman, Jason Monk, Forrest Flagg, Seth Campbell, Alison Duval, Chris Thomas, James O'Neil, Cory Johnson, Adam Rogers, Tim Paylor, and the countless others who met me at poster and oral presentations.

Finally, thanks to my family and friends who have always motivated me to do greater things. In particular I want to thank my wife Teagan for putting up with my monkish work ethic. You and Evie have helped me to understand what life is really all about and how it ought to be lived. I am truly blessed to have been able to pursue my Ph.D. without sacrificing time with my family and friends. I'm sure each and every one of you was wondering when I would finally graduate for the last time. Thank you all for your patience and support.

TABLE OF CONTENTS

LIST OF TABLES

LIST OF FIGURES

LIST OF EQUATIONS

CHAPTER 1

INTRODUCTION

1.1. Memoirs of a Landscape

In this thesis I explore the simple observation that the shape of landscapes tends to reflect the shape of tectonic activity, both past and present. The surface of the Earth retains valuable information about tectonic strain, generated by mantle flow and distributed by the rheological responses of the lithosphere; processes that are otherwise impossible to directly observe. However, the memory of tectonic strain at the surface is often obscured by other interconnected processes (Figure 1.1). For example, in orogenic regions, relief generated by tectonic strain gives a gravitational potential to various surface processes that can erode and transport material downslope. In addition to relief, tectonic strain can mechanically weaken the crust through shear damage along fault slip surfaces. These heavily disaggregated zones of fault gouge tend to erode rapidly relative to surrounding intact rock and as a result often control the drainage network pattern. As a consequence, erosion and transport reduce stresses from the topographic load and promotes further tectonic strain. This effect of stress unloading is amplified locally in fault damage zones due to rapid, localized erosion but also because the damage zones already host large strain rates. Additionally, many of these surface processes rely on climate to deliver precipitation, which is strongly influenced by the topography generated from tectonic strain and reshaped by erosion.

It becomes clear that using topography purely as a proxy for tectonic activity is problematic due to the dynamic links introduced above. However, if there is some

understanding of the sensitivity of these links, particularly between tectonics and surface processes, then one can obtain a greater understanding of topography and what information it contains. Many have explored the links between tectonics, surface processes, and climate over the last several decades and many unanswered questions have been raised as a result. I pursue some of these questions and explore possible answers in the following chapters.
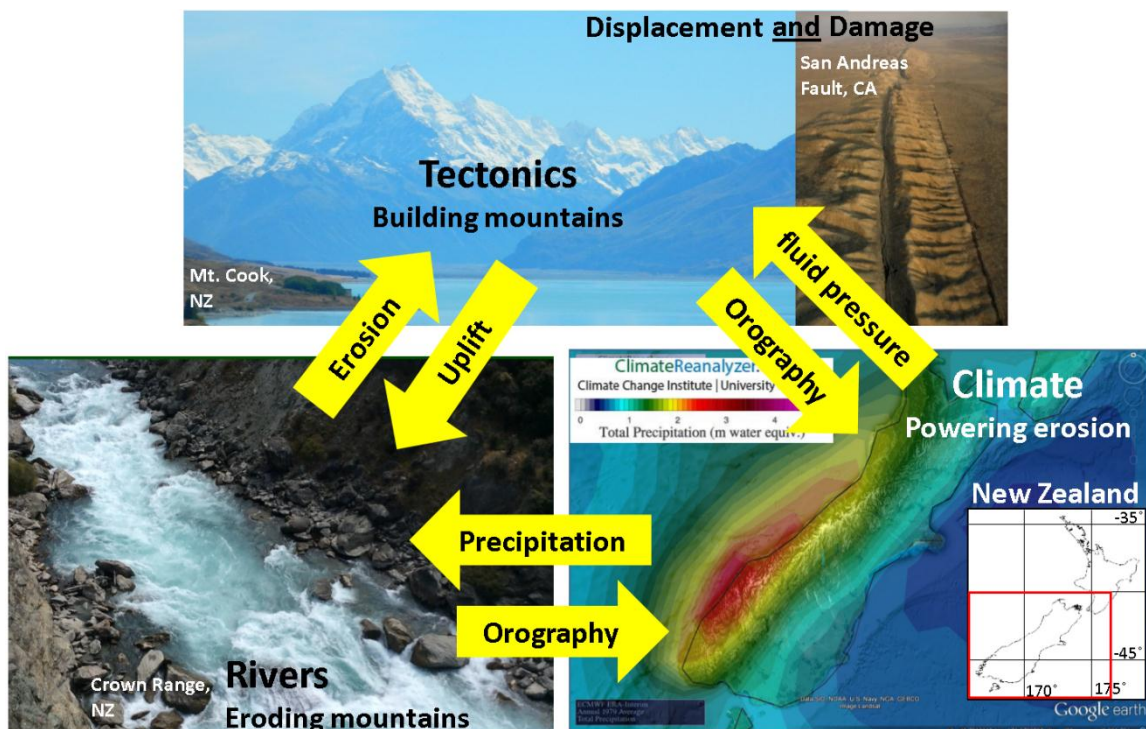
Figure 1.1. Dynamic links between tectonics, surface processes, and climate. In this thesis I explore tectonics as two interconnected components: displacement, and damage.

1.2. Mechanical Properties and Erosion Processes

One major unanswered question is, what is the role of rock strength in erosion? Moore et al. (2009) found a relation between the volume of sediment yield and the angular coincidence of slope to joints and fractures, suggesting that these mechanical defects have a measurable influence on erosion rate. Additionally, Sklar and Dietrich (2001; 2004) found a robust inverse relationship between rock anelastic strength and fluvial erosion rate. Rock disaggregation through tectonic fracture is often perceived as the first step in erosion

(Scheidegger, 1979; Scheidegger, 1998; Scheidegger, 2001; Molnar et al., 2007; Koons et al., 2012) and there are several examples in which the rapid erosion of faults leads to the confinement of rivers to structural features, such as fault damage zones (Thomson, 1993; Koons et al., 2012; Roy et al., 2015).

From these observations it is clear that there is an important link between the mechanical properties of rock and the fluvial and hillslope processes of erosion and transport, but there has been little effort to explore the sensitivity between the two. In Chapters 2 and 3 I study the link between mechanics and erosion in a combined approach that utilizes field measurements of rock strength and damage zone geometry with numerical models that incorporate these data in a landscape evolution framework. Strain-induced disaggregation generates heterogeneous grain size distributions in league with heterogeneous mechanical strength, so I also explore the sensitivity of sediment transport across faulted landscapes using a mixed bedload model in Chapter 4.

1.3. Topographic Anisotropy

Another major question that has been posed is, what kind of information is really contained in topographic shape? To begin to answer this question, I introduce a statistical method for measuring topographic anisotropy, or the directional dependence of landscape features, in Chapter 5. Measuring anisotropy over multiple scales can yield information about the dominant processes that shape topography and the scale at which they typically operate. I use this method on a number of characteristic landforms to determine if they yield signature patterns of anisotropy, to be used diagnostically in other landscapes on Earth and potentially other planets.

1.4. Dynamics

How does strain weakening alter the dynamic responses between tectonics, climate, and surface processes? In Chapter 6 I first explore this question by measuring the stress field underneath a faulted landscape to determine whether fault erosion can perturb the near surface stress field enough to influence the distribution of further tectonic strain. Simple fault motion is then combined with shear damage in a landscape evolution model to determine how different forms of fault slip can generate different landscape patterns in Chapter 7. In Chapter 8, I incorporate the rock damage-erosion link into a dynamically coupled rheological-erosion model of the upper crust. A sensitivity analysis is later performed to determine how rock damage and rapid erosion contribute to evolution of the drainage network pattern, stress field, strain, and strain rate. Chapter 9 is used to share some concluding remarks and explore more complex tectonism in collisional plate corners.

1.5. Education

How can numerical models of coupled tectonic-geomorphic systems serve in a student's education? In Appendix A I describe a graphical user interface in which users can easily access a sophisticated model of landscape evolution with relative ease. A number of theoretical course modules are included with suggestions on how they can be supplemental to other common modules in geology, ecology, economics, and sociology.

1.6. Fundamental Equations

Before I begin a thorough discussion of the questions posed above, it is important to explain the fundamental equations that make this form of coupled numerical modeling possible. These equations are needed to describe the driving forces and differential motion behind tectonic strain, the erosional potential of rivers, the circulation patterns of the atmosphere and implications for climate, and the brittle behavior of the upper crust. Each of these components plays a fundamental role in landscape evolution.

1.6.1. Thermogravitational Instability in the Mantle

Tectonism is often what initiates topography on Earth, and large scale tectonics are driven by a thermogravitational anomaly between the lithosphere and the asthenosphere, the cause of which is a difference in density associated with a temperature gradient. Decay of radionuclides throughout the Earth (plus some heat saved from the violent formation of Earth) produces a vertical thermal gradient, with temperature decreasing with distance from the Earth's center. Transient perturbations to this gradient can be adequately described by the Fourier heat equation

$$\frac{\partial T}{\partial t} = \kappa \frac{\partial^2 T}{\partial z^2} + w \frac{\partial T}{\partial z} + \frac{H}{C_p \rho} \tag{1.1.}$$

where T is temperature, t is time, κ is thermal diffusivity, z is depth, w is velocity parallel to the axis of z, H is heat generation, C_p is specific heat, and ρ is density. The equation is split into heat transfer mechanisms of conduction and advection, the heat source, and heat transience. One crucial phenomenon in the thermogravitational instability is that temperature can continuously alter the density of matter by affecting volume through the expansion or contraction of atomic bonds. An object with mass is acted upon by the force

of gravity, therefore temperature can alter the relative influence of gravity on an object, and hence its buoyancy, by changing its density

$$\Delta\rho = \rho_0\alpha_v\Delta T \qquad (1.2.)$$

where α_v is the coefficient of volumetric thermal expansion that changes the initial density ρ_0 over a change in temperature ΔT. Like most materials in Earth, the density of the mantle will increase with a decrease in temperature. This means that there is an inherent gravitational instability established by the thermal gradient: the mantle is naturally stratified in such a way that places dense mantle lithosphere over a more buoyant asthenosphere, assuming uniform assemblage and increasing pressure with depth. This arrangement can initiate subduction and ultimately drive flow within the mantle. Flow within the mantle drives plate deformation, which is reflected in the surface topography.

1.6.2. Flow Dynamics

The buoyancy instability described above drives flow within the mantle. I use the Navier-Stokes equations to quantitatively describe this flow in a 3D non-rotating reference frame, considering conservation of mass

$$\nabla \cdot V_{x,y,z} = 0 \qquad (1.3.)$$

and momentum

$$\Delta\rho \frac{\partial V_{x,y,z}}{\partial t} = \Delta\rho g - \nabla P + \mu\nabla\dot\gamma \qquad (1.4.)$$

Acceleration = volume force – pressure gradient + viscosity

where $\frac{\partial V_{x,y,z}}{\partial t}$ represents unsteady acceleration in 3D, g is acceleration due to gravity, ∇P is the pressure gradient, μ is viscosity, and $\nabla\dot\gamma$ is the shear strain rate gradient in an incompressible fluid. Viscosity is the resistance to shear strain, representing the diffusion

of momentum, and decreases with increasing temperature, much like density. The mantle is incapable of significant acceleration values because of its large inertia, and flow is driven predominantly by gravitational forcing with insignificant contributions from pressure gradients created by variable mantle thickness, therefore we can simplify mantle flow to the Stokes flow equation

$$\Delta\rho g = \mu\nabla\dot{\gamma} \tag{1.5.}$$

where flow is driven by gravitational forcing, dependent on the thermal gradient, and resisted by viscosity. The mantle may therefore be able to convect if gravitational forcing exceeds viscosity, which is exactly the case at plate subduction boundaries.

The Navier-Stokes equations can also be adapted to model flow dynamics in rivers, a crucial component of coupled modeling because it is flow that can impose the stresses needed to detach and transport rock on the bed of a river. This problem is commonly framed using the shallow water approximation to describe conservation of mass

$$\frac{\partial R}{\partial t} = i - \left(\frac{\partial uR}{\partial x} + \frac{\partial vR}{\partial y}\right) \tag{1.6.}$$

and momentum

$$\frac{\partial uR}{\partial t} + \frac{\partial}{\partial x}(Ru^2) + \frac{\partial}{\partial y}(Ruv) + gR\frac{\partial R}{\partial x} + gR\frac{\partial \eta}{\partial x} + \frac{\tau_{bx}}{\rho} = 0 \tag{1.7.}$$

$$\frac{\partial vR}{\partial t} + \frac{\partial}{\partial y}(Rv^2) + \frac{\partial}{\partial x}(Ruv) + gR\frac{\partial R}{\partial y} + gR\frac{\partial \eta}{\partial y} + \frac{\tau_{by}}{\rho} = 0 \tag{1.8.}$$

(Acceleration + inertia + fluid pressure + gravity + friction = 0)

where R is hydraulic radius or flow area divided by wetted perimeter of the channel, t is time, i is the rate of precipitation minus losses to evapotranspiration and groundwater (contribution to surface runoff only), u is velocity in the x direction, v is velocity in the y direction, η is topographic relief, τ_{bx} is x coordinate bed shear stress, and τ_{by} is y

coordinate bed shear stress. A simplified verbal form of the momentum equations is given under the equations. These equations include all components needed to fully describe shallow fluid flow. However, the downstream components of gravitationally driven flow and bed shear stress are often considered to be the only two of interest when estimating the ability of the river to incise into bedrock and transport the disaggregated material over thousand- to million-year timescales (Whipple and Tucker, 1999). Using only these two components we create an equation for bed shear stress

$$gR\frac{\partial \eta}{\partial y} + \frac{\tau_0}{\rho} = 0,$$

$$\tau_0 = \rho gRS$$

(1.9.)

Where S is slope (change in relief η with channel length y) and R is the hydraulic radius or flow area divided by wetted perimeter (Wobus et al., 2006; Wilcock et al., 2009; Tucker and Hancock, 2010). This equation can then be used to estimate the erosional power of a river reach as a scalar value. The basal shear stress applied to sediments within the bed load is therefore dependent on the density of water, acceleration due to gravity, the hydraulic radius of the channel, and channel slope for the studied channel length, assuming that all flow is driven by gravitational force and resisted by friction at the bed of the channel.

Atmospheric circulation can also be modeled by Navier-Stokes when described in a rotating reference frame

$$\Delta\rho\frac{\partial V_{x,y,z}}{\partial t} = \Delta\rho(g_n - \Omega^2 R) + \mu\nabla\dot{\gamma} - \nabla P - 2\Omega \times V_{x,y,z}$$

$$\text{Acceleration} = \text{effective gravity}$$

$$+ \text{viscosity}(\text{diffusion of momentum})$$

$$- \text{pressure gradient} - \text{coriolis}$$

(1.10.)

where g_n is acceleration due to gravity, Ω is vorticity, and R is the Earth's radius. Flow in the atmosphere is generally driven by pressure gradients, established by thermal gradients, but because airflow occurs over the surface of a rotating sphere, there is a component of angular acceleration that deflects flow orthogonally. This is called geostrophic winds, in which packets of air migrate from high to low pressure on an indirect route that follows generally parallel to isobars. The pattern of geostrophic winds is critical to understanding the general distribution of climate, and consequently the accumulation and routing of precipitated water, across Earth. Components of acceleration, force of gravity, and the diffusion of momentum are assumed to be negligible when considering circulation at the orogenic scale (>100 km) and over geologic time (thousands to millions of years).

1.6.3. Brittle Failure

There is a need to understand how mantle flow imposes stress on the lithosphere and what rheological responses are triggered in the eroding crust in order to make predictions about the geometry and magnitude of rock strength across a landscape. Convection of the underlying mantle leads to deformation in the overlying lithosphere. The lithosphere hosts numerous rheological boundaries separating temperature- and pressure-dependent responses to tectonic stress, but for this thesis I am interested in the plastic, pressure-dependent responses to stress located in the upper 15 km of the Earth's crust (e.g. Brace and Kohlstedt, 1980; Bürgmann and Dresen, 2008). The Plastic rheology is characterized by the rupture of atomic bonds, or slip on a frictional surface, by achieving a yield stress threshold that is met where an elastic rheology is no longer capable of

accommodating increasing amounts of strain (Coulomb, 1773). We can define the critical yield stress of plastic rheology using the Mohr-Coulomb failure criterion

$$\tau_{crit} = \mu(\sigma_n - P_f) + C \tag{1.11.}$$

where σ_n is a stress applied normal to the plane of failure and opposed by pore fluid pressure P_f, μ is the coefficient of friction equal to the ratio of shear to normal stress partitioning for a given friction angle $\tan(\varphi)$ (typically about 0.6), and C is the cohesion, or bond strength, of the material. At depth, where the normal stress is large, the friction coefficient is dominant in controlling strength. However, cohesion becomes singularly important right at the surface of the Earth. Cohesion is therefore a critical gauge for mechanical strength for the purposes of this thesis and it is used in the proceeding chapters as a link to rock erodibility.

Upon failure, the crust tends to form fault planes to accommodate strain. The seismic energy released upon formation of faults leads to fragmentation and cataclasis in rock surrounding the slip plane, generating a fault damage zone (Sammis et al., 1987; Ben-Zion and Sammis, 2003; Faulkner et al., 2010). The particle size distribution resulting from cataclasis is important to predict because it controls the initial grain size distribution freed upon the erosion of bedrock and can have major implications for the transportability of bedload across a landscape. Fragmentation of the neighboring rock is generally fractal in that the size distribution of rock particles follows a power law frequency distribution

$$N_{(>r)} = kr^{-D} \tag{1.12.}$$

where $N_{(>r)}$ is the cumulate frequency of particles with radius greater than or equal to r, D is the power law scaling parameter (also known as the fractal dimension), and k is a coefficient for scaling (Mandelbrot, 1967; Sammis et al., 1986; Jébrak, 1997). The scaling

parameter, and hence the grain size distribution, varies depending on the mechanism, intensity, and frequency of fragmentation. For this reason there can be potentially interesting dynamics associated with different grain size sources detached and transported across a landscape, which is the focus of Chapter 4.

The basic equations of Fourier heat and thermal expansion describe the driving force for mantle flow, Navier-Stokes describes the flow dynamics in the mantle, rivers, and the atmosphere, and the Mohr-Coulomb equation and the power law distribution equations can describe the plastic response of the crust to excess shear stress and the resulting pattern of fragmentation in damage zones. The proceeding chapters of this thesis rely on these equations in order to explore the link between tectonics, climate, and surface processes. But first, I start by measuring rock mass strength and observing some mechanical controls on erosion in various field sites across New Zealand that host heavily eroded fault damage zones.

CHAPTER 2

FIELD MEASUREMENTS OF BULK ROCK STRENGTH

2.1. Chapter Introduction

In this section I discuss methods of measuring rock mass strength and grain size in the field and report rock mass strength data for a number of field sites in New Zealand. Field measurements are an important first step in quantifying rock mass strength at the outcrop scale and this information is necessary for determining rock strength and erodibility gradients across an evolving landscape. All measurements were taken in exposed bedrock regions host to or adjacent to fault damage. These numbers are used to scale the erodibility values needed for landscape evolution modeling in Chapters 3-8.

2.2. Method and Technique of Strength/Grain Size Measurement

The Hoek-Brown (Hoek and Brown, 1980; Hoek and Brown, 1997; Hoek, 2001) Criterion was used to estimate rock mass strength from field measurements of structural competence and base rock competence. The Hoek-Brown criterion is based on the Rock Mass Rating of Bieniawski (1974) but features a greater rating accuracy for rocks with very low cohesive strength (Hoek and Brown, 1997), and is therefore the most suitable rating method for fault damaged rock. The Slope Mass Rating index implemented by Moore (2009) is a similar rating method which puts a greater focus on joint orientation relative to surface slope. However, I do not use this method because I am interested in bulk rock strength, rather than the strength of exposed hillslopes. Structural competence data is also

useful for estimating the grain size distribution of sediments that would be produced upon erosion of the bedrock units.

2.2.1. Structural Competence

Structural competence is estimated by using the Geological Strength Index (GSI), which is a basic measure of outcrop structure and surface quality over a representative outcrop area (see Figure 2.2 for an example worksheet). Rock structure is a function of fracture spacing, fracture orientation, and the degree of interlocking between rock fragments. GSI measurements require an outcrop sample large enough to include a good representation of the local fracture spacing and all dominant fracture orientations. In many cases, fractures and joints play the largest role in the strength of rock and their inclusion will provide a much more accurate GSI measurement. The degree of fracture spacing, combined with the number of fracture orientations, provides quantitative information about rock fabric and the degree of interlocking between larger rock fragments. Fracture spacing and orientation data can also be used to estimate the expected grain size distribution of sediments produced upon the erosion of the rock unit. Surface conditions provide information on the strength of fracture surfaces through observations of surface weathering, roughness, evidence for fluid flow, and indications of slip accommodation. Surface conditions are poor for fracture surfaces that have previously accommodated slip and will probably accommodate slip in the future.

For example, fault gouge is generally so damaged that it generally lies in the DISINTEGRATED or FOLIATED/LAMINATED structural fields, where rock fabric is defined by a disaggregated, thick clayey matrix. Surface conditions are generally rated

POOR to VERY POOR indicating evidence for slip accommodation, weathering, clay coating, and/or presence of fluids. Conversely, cataclasites along the flanks of fault damage zones may fall in the BLOCKY/DISTURBED to DISINTEGRATED fields where there is still some interlocking between coarse rock fragments. Surface conditions along fractures are generally rated as FAIR to POOR, indicating smooth fractures with some weathering, little or no soft clay, and a lesser degree of slip accommodation when compared to gouge. Rocks that are well out of the range of fault damage may be BLOCKY or VERY BLOCKY, having inherited a small amount of fracturing associated with past tectonic activity. Surface conditions may range from VERY GOOD to FAIR indicating less slip accommodation along rough fractures and no clay filling.

2.2.2. Base Rock Competence

Base rock competence is a function of rock type and uniaxial compressive strength (UCS). Obtaining a truly representative estimation of rock type and UCS requires a rock sample size that is larger than the average spacing of fractures that allow the rock pieces to slide and rotate under different stress conditions (Hoek and Brown, 1997). It is possible to obtain a rough estimate of UCS from the field. UCS field estimates are adequate for analysis in fault damage zones because the range of error is miniscule compared to the degree of strength difference between fault gouge and solid rock. Rock mass strength is also dependent on base rock type. The base rock type value can change if rock failure occurs along a plane of weakness, so you can expect a smaller number for a schist that became fault gouge through shear abrasion. However, base rock type plays a minimal role in rock mass strength compared to joints and fractures.

2.3. Field Locations

Field locations were chosen based on accessibility, degree of strain weakening, quality of damage zone exposure, and whether the exposure is expansive enough to see all (or a large portion) of the damage gradient from the center of the fault zone to local intact bedrock. The best damage zone exposures tend to be along saddles or drainage divides, but some can be found stranded up on the flanks of river valleys. In many cases, rivers that follow fault structures often cover up a large portion of the damage zone, making it nearly impossible to measure strength.

2.3.1. Alpine Fault

The Alpine Fault is a dextral oblique reverse fault that divides the Indo-Australian and Pacific Plates on the South Island of New Zealand. The Alpine Fault became a distinct tectonic feature at circa 45 Ma (Sutherland, 1999). 460 km of dextral strike-slip shear has accommodated along the Alpine Fault (Norris et al., 1990), and a total of 850 km of dextral shear is thought to have occurred across the South Island (Sutherland, 1999). The fault is inferred to dip 50-55° SE to a depth of 25-30 km (Norris and Cooper, 1995; Kleffmann et al., 1998). Pacific Plate motion is directed WSW with a relative motion of 35.5 mm a^{-1} parallel to the fault and 10 mm a^{-1} perpendicular (DeMets et al., 1994). Exhumation rates are estimated to be 6-9 mm a^{-1} immediately adjacent to the Alpine Fault in the Central Southern Alps and much lower east of the main divide (Wellman, 1979; Simpson et al., 1994; Norris and Cooper, 2001; Little et al., 2005). Rapid exhumation of the Pacific Plate has exposed mylonites and high grade schist along the Alpine Fault. The Indo-Australian side of the fault is composed of greywacke schists, granites, and Pleistocene glacial

sediments. Almost all rock damage associated with motion along the Alpine Fault is located in the mylonite, and there are a number of locations where the gradient of rock damage is visible on the west coast of the South Island, three of which I discuss below.

2.3.1.1. Gorge Near Waikukupa River, New Zealand

One of the best exposures of the Alpine Fault is located beside the Waikukupa River. The four rock units located within the Waikukupa gorge are mylonite, cataclasite, and fault gouge associated with the Alpine Fault, and Western Province Greywacke (Figure 2.1). Incision in the gorge exposed the damage gradient between gouge and cataclasite, but strength measurements of the two intact rock types were taken from nearby locations (mylonite: Franz Joseph Valley; Western Province Greywacke: outcrop by state highway 6). The Hoek-Brown parameters for each unit are shown in Figure 2.2. Intact mylonite is the strongest unit with a massive to blocky structure hosting widely spaced fractures. Fracture surface conditions are very good to good, with predominantly fresh and unweathered surfaces. The cataclasite and gouge units are associated with localized seismogenic cataclasis along the Alpine Fault. These units are much weaker, having a much higher fracture density that increases with proximity to the primary slip surface. Fracture surface quality decreases with proximity to the primary slip surface, and fractures are largely wet, slickensided, and coated with clay. The greywacke unit has a relatively higher fracture density than the mylonite, producing a very blocky rock mass with rough, slightly weathered fracture surfaces. The gouge unit is approximately 25 to 6500 times less cohesive than the intact mylonite.

Figure 2.1. Gorge near Waikukupa River. (A) Reference map. (B) View of slide debris along Hare Mare gorge, Waikukupa River in foreground. (C) Evidence of mass wasting, fault gouge in background. (D) Fault gouge. (E) Cataclasite. (F) Intact mylonite, Franz Josef Valley.

Alpine Fault: Waikukupa River

Geological Strength Index

From the description of structure and surface conditions of the rock mass, pick an appropriate box in this chart. Estimate the average value of the Geological Strength Index (GSI) from contours. Do not attempt to be too precise. Quoting a range of GSI from 36 to 42 is more realistic than stating that GSI = 38. It is also important to recognize that the Hoek-Brown criterion should only be applied to rock masses where the size of the individual blocks or pieces is small compared to with the size of the excavation under consideration. When individual block sizes are more than approximately one quarter of the excavation dimension, failure will generally be structurally controlled and the Hoek-Brown criterion should not be used.

SURFACE CONDITIONS

STRUCTURE

→ DECREASING SURFACE QUALITY →

Surface conditions
VERY GOOD - very rough, fresh unweathered surfaces
GOOD - rough, slightly weathered, iron stained surfaces
FAIR - smooth, moderately weathered and altered surfaces
POOR - slickensided, highly weathered surfaces with compact coatings or fillings of angular fragments
VERY POOR - slickensided, highly weathered surfaces with soft clay coatings or fillings

DECREASING INTERLOCKING OF ROCK PIECES

INTACT OR MASSIVE - intact rock specimens or massive in situ rock with very few widely spaced dicontinuities — 90, N/A, N/A, N/A

BLOCKY - very well interlocked undisturbed rock mass consisting of cubical blocks formed by three orthogonal discontinuity sets — 80, 70, 60 — MYLONITE

VERY BLOCKY - interlocked, partially disturbed rock mass with multifaceted angular blocks formed by four or more discontinuity sets — 50 — W. PROVINCE GREYWACKE

BLOCKY/DISTURBED - folded and/or faulted with angular blocks formed by many intersecting discontinuity sets — 40, 30 — CATACLASITE

DISINTEGRATED - poorly interlocked, heavily broken rock mass with a mixture of angular and rounded rock pieces — 20, GOUGE

FOLIATED/LAMINATED - folded and tectonically sheared foliated rocks. Schistosity prevails over any other discontinuity set, resulting in complete lack of blockiness — N/A, N/A, 10

PARAMETERS	MYLONITE	CATACLASITE	GOUGE	W.P. GREYWACKE
GSI rating	65-90	22-45	5-30	45-75
UCS estimate	50-100 (strong)	5-25 (weak)	<1 (extremely weak)	50-100 (strong)
rock type parameter	6 (mylonite-schist)	6 (mylonite-schist)	6 (mylonite-schist)	10 (greywacke)
mean cohesion, absolute range (Pa)	1×10^7 $3 \times 10^6 - 1.3 \times 10^7$	7.7×10^5 $8.3 \times 10^4 - 8.6 \times 10^5$	1.5×10^4 $2 \times 10^3 - 1.2 \times 10^5$	5.2×10^6 $2 \times 10^6 - 8.4 \times 10^6$
mean friction angle	$35°$	$22.5°$	$17°$	$33.5°$

Figure 2.2. Hoek-Brown parameters for Waikukupa site.

2.3.1.2. Gaunt Creek, Whataroa, New Zealand

Erosion along Gaunt Creek has exposed cataclasite, ultracataclasite, and gouge units of the Alpine Fault (Figure 2.3), and it is also the location of the first Deep Fault Drilling Project (DFDP-1). In this location, fault gouge is thrust over Pleistocene glacial deposits (Figure 2.3C). Surface conditions indicate that the gouge exposure is rapidly eroding. The Hoek-Brown parameters are shown in Figure 2.4. Cataclasite is the strongest exposed unit with very blocky to blocky/disturbed structure and good to poor surface conditions. Rock quality gradually worsens towards the ultracataclasite unit, with blocky/disturbed to disintegrated structure and fair to very poor surface conditions. The gouge unit is weakest, consisting of a foliated mix of soft and indurated clay with a disintegrated to foliated/laminated structure and poor to very poor surface conditions. From cataclasite to gouge unit there is an estimated 5 to 100 times difference in cohesion.

2.3.1.3. Martyr River, New Zealand

Erosion along the Martyr River has exposed indurated fault gouge from the Alpine Fault (Figure 2.5). Nearby there is an exposure of Western Province Greywacke. I have split the gouge unit into two components: stiff gouge, which appears within 30 cm of the primary slip surface (Figure 2.5C, D), and indurated gouge located outside of the 30 cm range (Figure 2.5B). Stiff gouge shows disintegrated to foliated/laminated structure and surface quality is poor (Figure 2.6). The indurated gouge is well cemented and is exposed as steep cliff faces several meters tall. Structure of the indurated gouge is very blocky to blocky/disturbed, and surface conditions are fair. There is an estimated 1 to 100 times difference in cohesive strength between the two gouge units.

Figure 2.3. Gaunt Creek. (A) Reference map. (B) View of fault gouge from Gaunt Creek, glacial debris in foreground. (C) Fault gouge thrust over glacial debris. (D) Ultracataclasite. (E) Cataclasite close-up. (F) Cataclasite.

Alpine Fault: Gaunt Creek

Geological Strength Index

From the description of structure and surface conditions of the rock mass, pick an appropriate box in this chart. Estimate the average value of the Geological Strength Index (GSI) from contours. Do not attempt to be too precise. Quoting a range of GSI from 36 to 42 is more realistic than stating that GSI = 38. It is also important to recognize that the Hoek-Brown criterion should only be applied to rock masses where the size of the individual blocks or pieces is small compared to with the size of the excavation under consideration. When individual block sizes are more than approximately one quarter of the excavation dimension, failure will generally be structurally controlled and the Hoek-Brown criterion should not be used.

PARAMETERS	CATACLASITE	ULTRACATACLASITE	GOUGE
GSI rating	22-65	10-45	5-30
UCS estimate	5-25 (weak)	1-5 (very weak)	<1 (extremely weak)
rock type parameter	6 (mylonite-schist)	6 (mylonite-schist)	6 (mylonite-schist)
mean cohesion, absolute range (Pa)	5.9×10^5 $8.3 \times 10^4 - 1.5 \times 10^6$	1.7×10^5 $8.8 \times 10^3 - 1.7 \times 10^5$	1.5×10^4 $2 \times 10^3 - 1.3 \times 10^5$
mean friction angle	25°	20°	17.5°

Figure 2.4. Hoek-Brown parameters for Gaunt Creek site.

Figure 2.5. Martyr River. (A) Reference map. (B) View of fault damage zone from Martyr River. (C) Stiff fault gouge thrust over glacial debris. (D) Fault gouge close-up.

Alpine Fault: Martyr River

Geological Strength Index

From the description of structure and surface conditions of the rock mass, pick an appropriate box in this chart. Estimate the average value of the Geological Strength Index (GSI) from contours. Do not attempt to be too precise. Quoting a range of GSI from 36 to 42 is more realistic than stating that GSI = 38. It is also important to recognize that the Hoek-Brown criterion should only be applied to rock masses where the size of the individual blocks or pieces is small compared to with the size of the excavation under consideration. When individual block sizes are more than approximately one quarter of the excavation dimension, failure will generally be structurally controlled and the Hoek-Brown criterion should not be used.

SURFACE CONDITIONS

- VERY GOOD - very rough, fresh unweathered surfaces
- GOOD - rough, slightly weathered, iron stained surfaces
- FAIR - smooth, moderately weathered and altered surfaces
- POOR - slickensided, highly weathered surfaces with compact coatings or fillings of angular fragments
- VERY POOR - slickensided, highly weathered surfaces with soft clay coatings or fillings

STRUCTURE → DECREASING SURFACE QUALITY →

DECREASING INTERLOCKING OF ROCK PIECES

INTACT OR MASSIVE - intact rock specimens or massive in situ rock with very few widely spaced dicontinuities — 90 / 80 / N/A / N/A / N/A

BLOCKY - very well interlocked undisturbed rock mass consisting of cubical blocks formed by three orthogonal discontinuity sets — 70 / 60

VERY BLOCKY - interlocked, partially disturbed rock mass with multifaceted angular blocks formed by four or more discontinuity sets — W. PROVINCE GREYWACKE / 50 / 40

BLOCKY/DISTURBED - folded and/or faulted with angular blocks formed by many intersecting discontinuity sets — INDURATED / 30

DISINTEGRATED - poorly interlocked, heavily broken rock mass with a mixture of angular and rounded rock pieces — STIFF GOUGE / 20

FOLIATED/LAMINATED - folded and tectonically sheared foliated rocks. Schistosity prevails over any other discontinuity set, resulting in complete lack of blockiness — N/A / N/A / 10

PARAMETERS	INDURATED GOUGE	STIFF GOUGE
GSI rating	30-50	12-30
UCS estimate	1-5 (very weak)	<1 (extremely weak)
rock type parameter	6 (mylonite-schist)	6 (mylonite-schist)
mean cohesion, absolute range (Pa)	6×10^4 / $2.5 \times 10^4 - 2 \times 10^5$	1.2×10^4 / $2.7 \times 10^3 - 2.5 \times 10^4$
mean friction angle	$24.5°$	$19°$

Figure 2.6. Hoek-Brown parameters for Martyr River site.

2.3.2. Splay from Fowlers Fault, Exposure North of Henry Saddle, Lewis Pass Region

Lewis pass is host to the Fowlers Fault, an east-northeast striking dextral fault located between the Awatere and Clarence Faults in the Marlborough Fault System (Figure 2.7). The Marlborough Fault System probably formed at around 5 Ma in the early Pliocene due to changes in relative plate motion (Wilson et al., 2004). There is no evidence of recent motion along the Fowlers fault (Richardson, 1982), but estimates of Holocene slip rates on the Clarence and Awatere Faults are 3.5-5 mm yr^{-1} (Browne, 1992; Nicol and Van Dissen, 2002; Mason et al., 2006). Bedrock in the Lewis Pass region consists of Torlesse greywacke (Rattenbury et al., 2006).

The four rock units located within the Henry Saddle region are intact greywacke (Figure 2.7E), greywacke with anastomosing shear zones (Figure 2.7C, D), fault gouge (Figure 2.7B), and cataclasite (Figure 2.7C). We focused our study on damage zone exposures to the north of Henry Saddle, on another saddle that straddles a north trending structural feature potentially related to the Fowlers Fault (Figure 2.7C). Stream incision in the saddle exposed the damage gradient. The strength measurements for the intact greywacke were taken further downstream, approximately 3 km away from the damaged rocks in the saddle. The Hoek-Brown parameters for each unit are listed in Figure 2.8.

The greywacke is the strongest unit with a blocky structure hosting widely spaced fractures. Fracture surface conditions are very good to good, with predominantly fresh and unweathered surfaces. The greywacke unit with anastomosing shear zones hosts a wide range of strength measurements, ranging from very blocky-good to disintegrated-
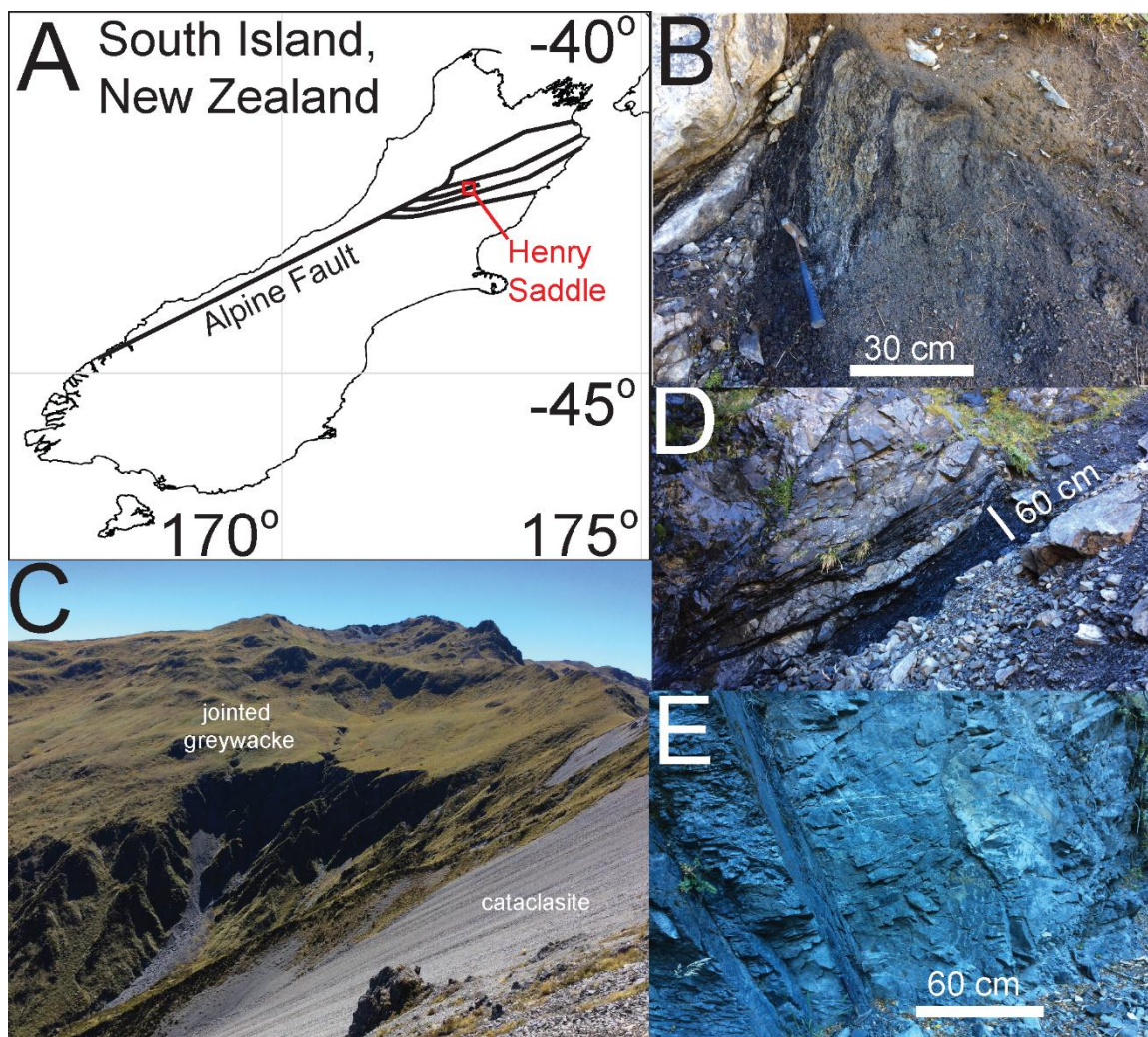
Figure 2.7. Henry Saddle. (A) Reference map. (B) View of fault gouge in the saddle. (C) View of saddle: jointed greywacke to the west (center), cataclasite to the east (right). (D) Greywacke with anastomosing shear zones associated with argillite beds. (E) Strong, jointed greywacke.

Fowlers Fault: Henry Saddle
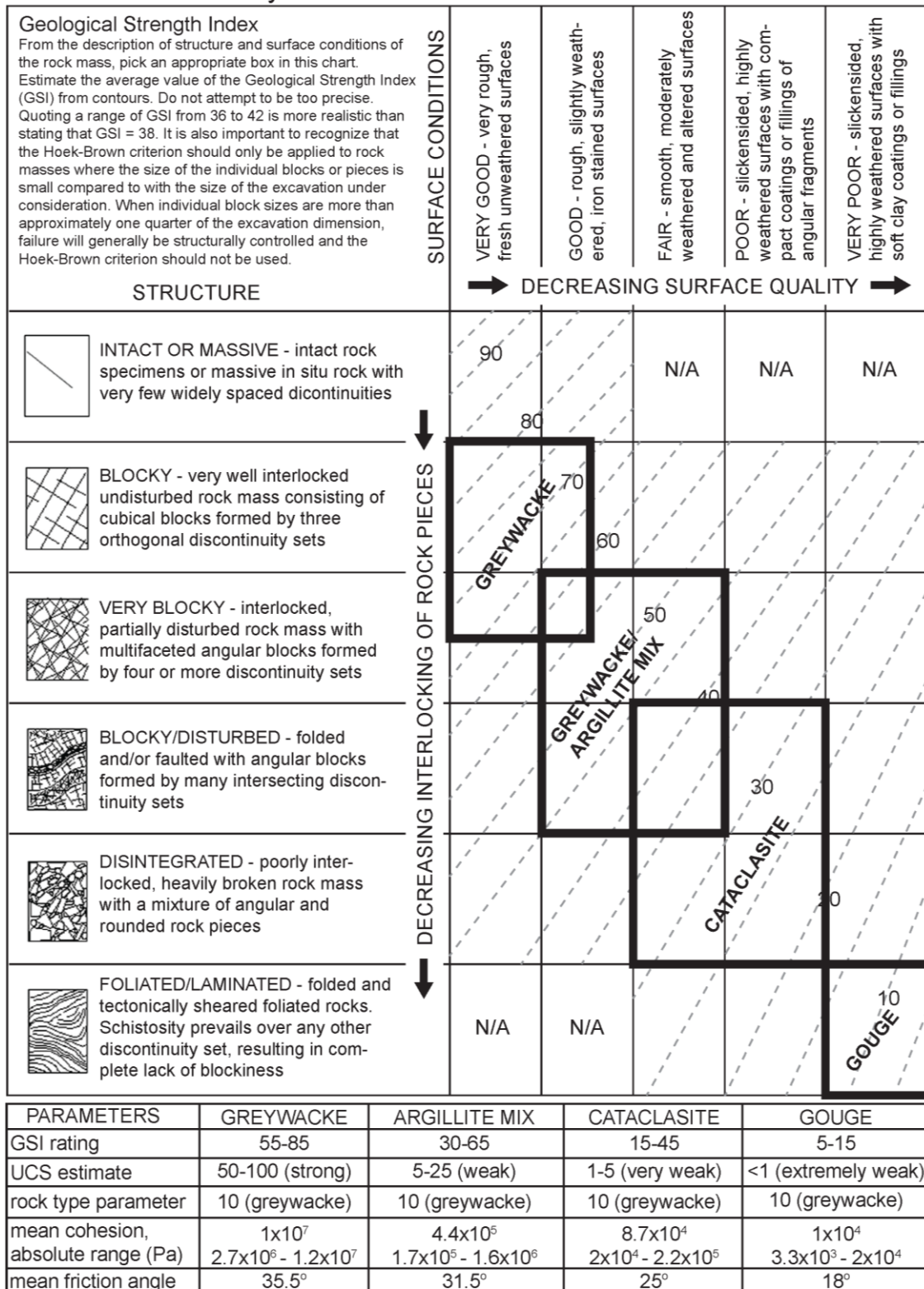
Figure 2.8. Hoek-Brown parameters for Henry Saddle site.

very poor over the meter scale. The sub-meter scale shear zones are heavily incised and host small ravines. The cataclasite and gouge units are associated with localized seismogenic cataclasis along the Alpine Fault. These units are much weaker, having a much higher fracture density that increases with proximity to the primary slip surface. Fracture surface quality decreases with proximity to the primary slip surface, and fractures are largely wet, slickensided, and coated with clay. The greywacke unit has a relatively higher fracture density than the mylonite, producing a very blocky rock mass with rough, slightly weathered fracture surfaces.

2.3.3. Fiddlers Flat: Blue Lake Fault, Central Otago, New Zealand

The Blue Lake Fault Zone defines the lithological boundary between Torlesse Greywacke to the northeast and Otago Schist to the southwest (Figure 2.9A). Mid-Cretaceous normal faulting along this boundary led to shortening of the original metamorphic gradient in the schist formed in the Jurassic (Henne et al., 2011). This lithological boundary represents a significant contrast in rheology with major implications for the pattern of tectonic deformation in the South Island (Upton et al., 2009). The Blue Lake Fault is well exposed in cross-section along the banks of the Manuherikia River (Figure 2.9B). The Fiddlers Flat gouge zone is a particularly well preserved exposure of the Blue Lake Fault within Textural Zone 1 (TZ 1) greywacke (Henne et al., 2011), and it is where the following strength measurements were taken.

Rock mass strength measurements were taken for the gouge zone (Figure 2.9B, C) and the adjacent greywacke (Figure 2.9D, E, F). The gouge zone, approximately 200 m in width, is a mixture of brecciated greywacke and heavily sheared argillite. The texture of
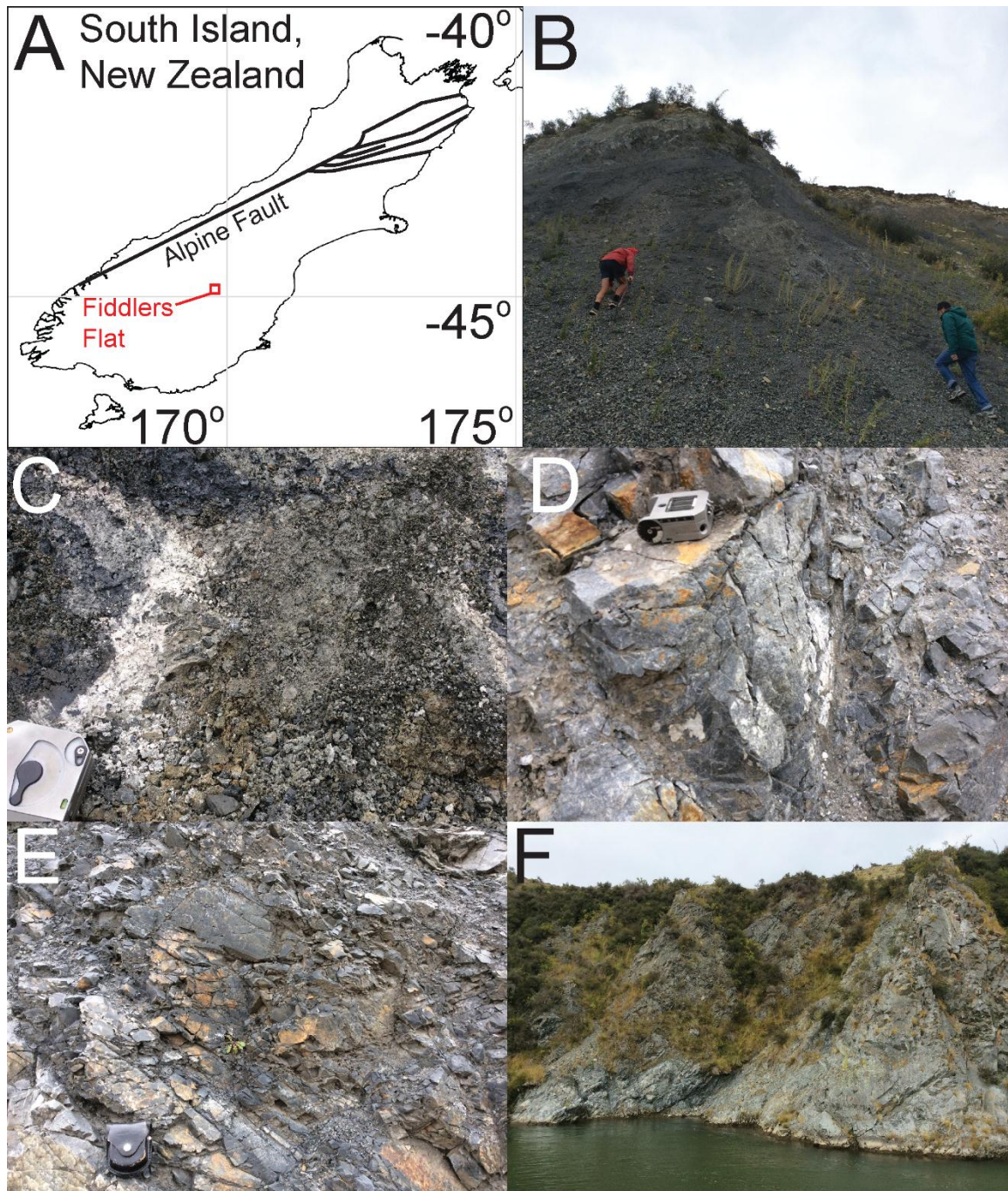
Figure 2.9. Fiddlers Flat. (A) Reference map. (B) View of fault gouge from Manuherikia River. (C) Gouge close-up. (D) Fragmented block. (E) Fractured greywacke adjacent to fault gouge. (F) Cataclasite.

Figure 2.10. Hoek-Brown parameters for Fiddlers Flat site.

the gouge zone ranges from a very fine grained gouge matrix to meter-scale fragmented blocks of greywacke. Hoek-Brown parameters are listed in Figure 2.10. The gouge matrix is in the foliated/laminated structural range and very poor surface quality range, while the fragmented greywacke clasts lie in the disintegrated and fair to very poor structural and surface quality ranges, respectively. A widening of the Manuherikia River coincides with the gouge zone but otherwise there is no influence of rock damage on the local drainage network pattern. Greywacke outside of the shear zone has a noticeably lower fracture density and higher surface quality, with a very blocky to disintegrated structural rating and good to poor surface quality rating.

2.3.4. Ostler Fault, Twin Stream, New Zealand

The Ostler Fault is a north trending reverse fault along the outboard side of the Southern Alps (Figure 2.11). Active slip on the Ostler Fault through the Late Pleistocene has played a major role in sedimentation and landscape evolution in the Mackenzie Basin (Ghisetti et al., 2007) (Figure 2.11F). Rock mass strength measurements were taken in an exposure of the Ostler Fault along a tributary of Twin Stream (Figure 2.11B), located on the flanks of the Ben Ohau Range (Figure 2.11E). The exposed gouge unit is moderately indurated by a calcareous cement, and though the fabric of the gouge unit is suggestive of heavy shear abrasion, cementation has reintegrated the rock structure (Figure 2.11C, D). For this reason I give a structure rating of disintegrated to foliated/laminated and a surface quality rating of poor, despite the pervasiveness of a foliated texture and evidence of very poor surface quality conditions in the past (Figure 2.12).
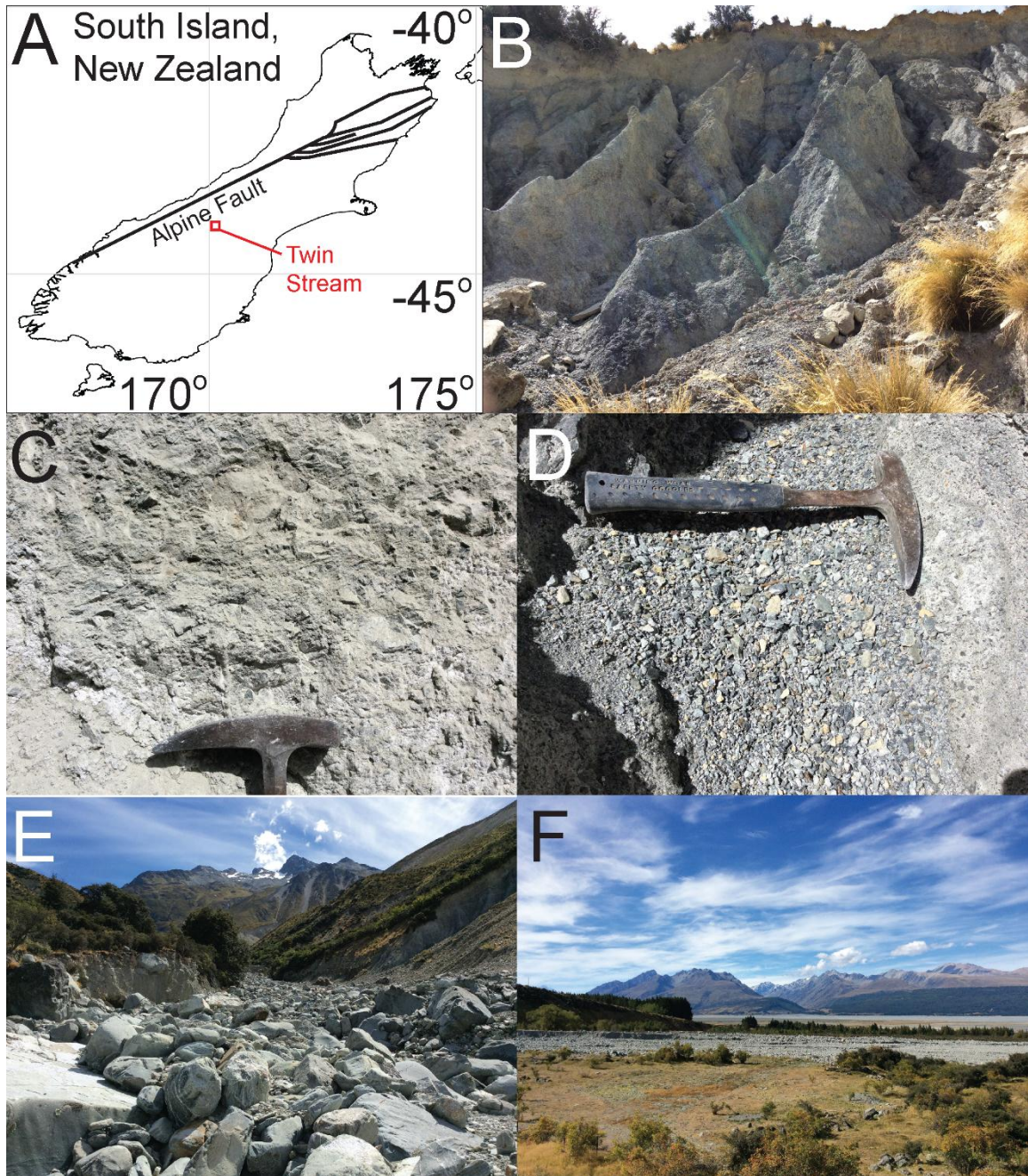
Figure 2.11. Twin Stream. (A) Reference map. (B) Eroded fault gouge. (C) Fault gouge close-up. (D) Sediments from eroded fault gouge. (E) Coarse sediments further down Twin Stream. (F) Lake Pukaki.

Ostler Fault: Twin Stream, Ben Ohau Range
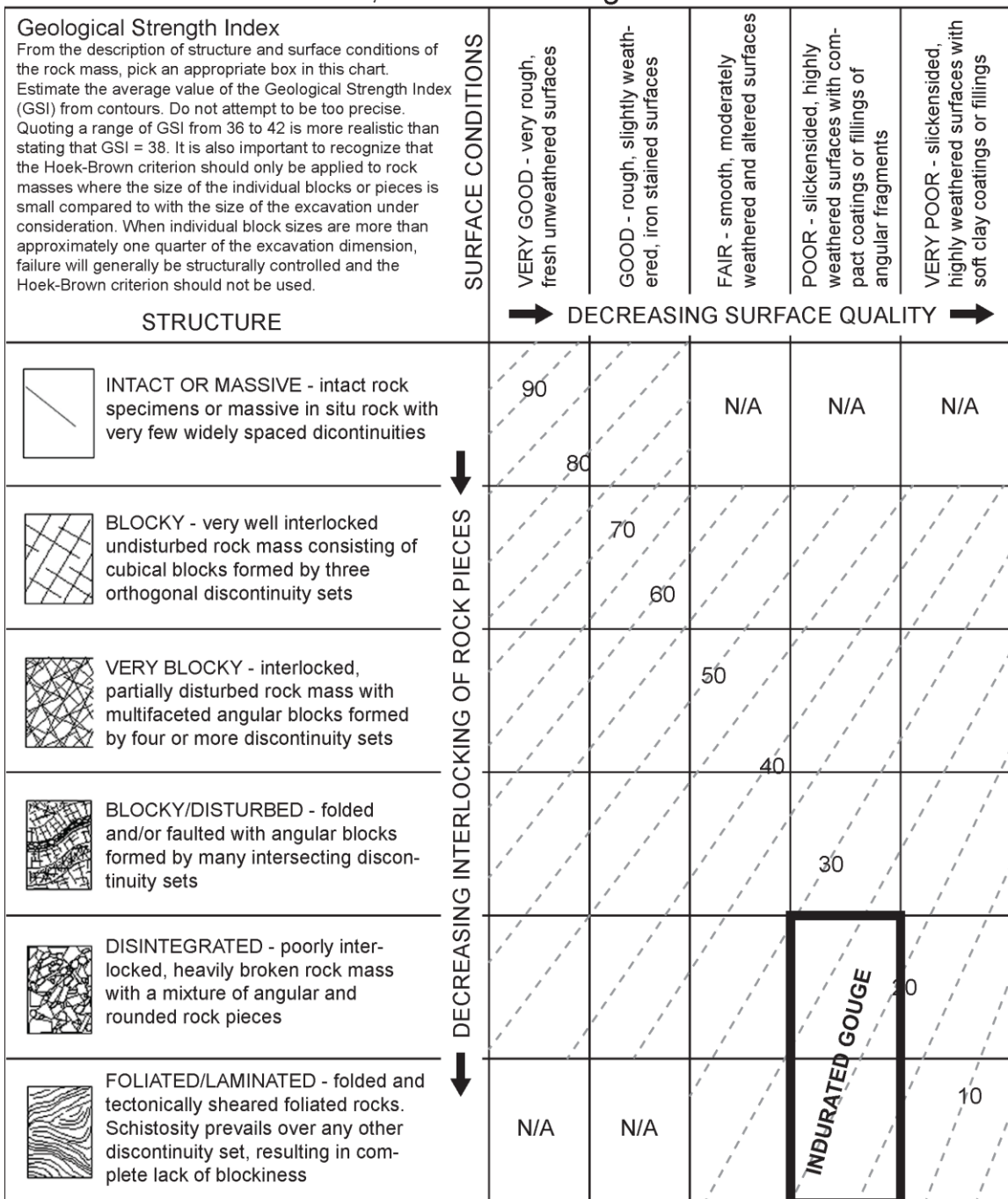
Figure 2.12. Hoek-Brown Parameters for Twin Stream site.

The more interesting observation at the Twin Stream exposure of the Ostler Fault is the downstream change in average grain size with respect to the nearby streambed. Upstream sediments are dominated by the eroded fault gouge material with a much smaller average grain size (Figure 2.11D) than the downstream collection of coarse gravel associated with glacial sediments deposited above the gouge exposure (Figure 2.11E). This is an example of rock mass strength having a significant channel-scale effect on grain size distribution in fluvial systems, a topic I study further in Chapter 4.

2.4. Chapter Conclusions

Fault damage zones host some of the sharpest rock strength gradients on Earth. For example, many intact rock examples exhibit cohesive strength on the order of 10-20 MPa, while fault gouge cohesion is on the order of 10 kPa or less. If there is an influence of rock mass strength on fluvial incision, we would expect to see the greatest effect in fault damage zones. Use of the Hoek and Brown (1980; 1997) criterion provides a relatively easy method for rating rock mass strength while providing reasonable relative estimates of cohesive strength from widely jointed greywacke to loose fault gouge. These values of rock strength can then be used to calibrate landscape evolution models with a heterogeneous distribution of erodibility. In the next chapter, I study the potential influence these fault damage zones have on the rates and patterns of fluvial erosion.

CHAPTER 3

THE INFLUENCE OF CRUSTAL STRENGTH FIELDS ON THE PATTERNS AND RATES OF FLUVIAL INCISION

3.1. Chapter Abstract

Gradients in the bedrock strength field are increasingly recognized as integral to the rates and patterns of landscape evolution. To explore this influence, I incorporate data from fault strength profiles into a landscape evolution model, under the assumption that erodibility of rock is proportional to the inverse square root of cohesion for bedrock rivers incised by bedload abrasion. My model calculations illustrate how patterns in the crustal strength field can play a dominant role in local fluvial erosion rates and consequently the development of fluvial network patterns. Fluvial incision within weak zones can be orders of magnitude faster than for resistant bedrock. The large difference in erosion rate leads to the formation of a straight, high order channel with short, orthogonal tributaries of low order. In comparison, channels incising into homogeneous strength fields produce dendritic drainage patterns with no directional dependence associated with erodibility gradients. Channels that cross the strength gradient experience local variations in knickpoint migration rate and the development of stationary knickpoints. Structurally confined channels can shift laterally if they incise into weak zones with a shallow dip angle, and this effect is strongly dependent on the magnitude of the strength difference, the dip angle, and the symmetry and thickness of the weak zone. The influence of the strength field on drainage network patterns becomes less apparent for erodibility gradients that approach

homogeneity. There are multiple natural examples with drainage network patterns similar to those seen in my numerical experiments.

3.2. Chapter Introduction

The rich and varied topography of the Earth's surface takes shape under the combined influence of three players: tectonics, climate, and lithology. Much research effort has gone into unraveling the first two, with considerable success. Progress in understanding lithology's role, however, has lagged behind. Although lithologic variation gives many landscapes their distinctive character, such as in the fold belts of the Zagros and Appalachian Mountains, much remains to be discerned about the quantitative relations among rock properties, erosion rates, and landscape evolution.

The rock strength field, defined here as the three dimensional (3D) watershed-scale distribution of anelastic crustal strength, is particularly sensitive to pervasive crustal failure in the form of joints, fractures, and fault damage zones. Molnar et al. (2007) suggested that crustal failure is an inherent process of deformation that enhances all forms of erosion. Others have recognized the importance of material strength and joint orientations in measuring slope stability and landsliding (e.g. Densmore et al., 1998; Scheidegger, 1998; Brideau et al., 2006; Brideau et al., 2009; Moore et al., 2009; Clarke and Burbank, 2010; Goode and Wohl, 2010; Ambrosi and Crosta, 2011; Clarke and Burbank, 2011; Egholm et al., 2013). Sklar and Dietrich (2001; 2004) showed that erodibility can be linked to material strength, and suggest that it could play a fundamental role in landscape evolution (e.g. Judson and Andrews, 1955; Moglen and Bras, 1995; Tucker and Slingerland, 1996; Stock and Montgomery, 1999; Koons et al., 2012). Others (e.g. Zernitz, 1932; Lubowe, 1964)

have recognized the strong influence structural features have on the development of common drainage network patterns (Figure 3.1).
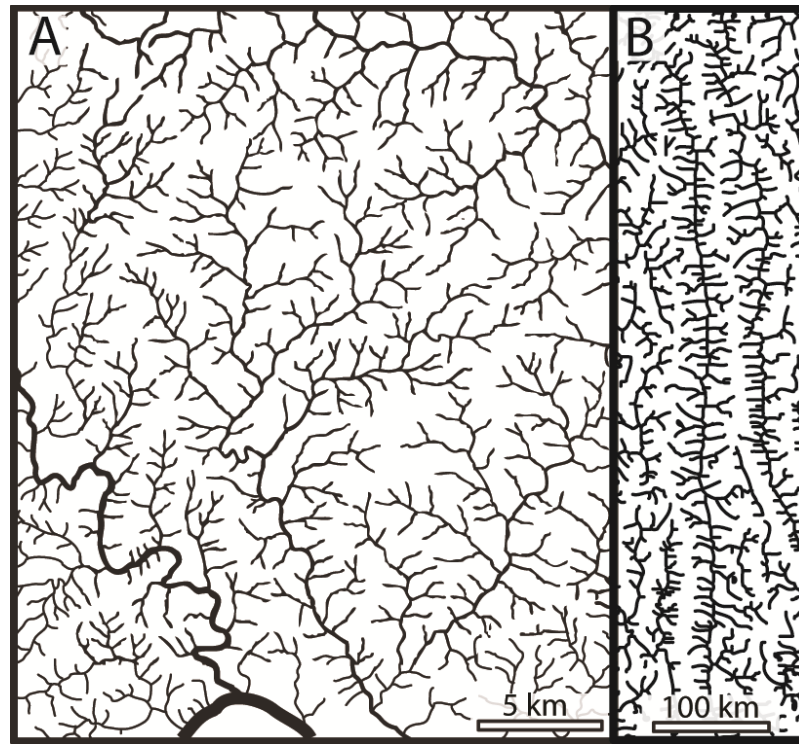
Figure 3.1. Hydrographic map of a dendritic drainage network (A), region east of Palmyra, VA (37.861˚ N, -78.2633˚ W). Channels traced from Palmyra quadrangle, Virginia, 1:24,000, 7.5 minute series, Washington D.C.,USGS, 1897; see also Zernitz (1935). (B) Hydrographic map of the drainage network around part of the Salween River, eastern Himalayan Syntaxis (26.7259˚ N, 98.8973˚ E). Channels in (A) formed in largely homogeneous rock while those in (B) formed amid several steeply dipping tectonic structures striking due north (Liu et al., 2011).

Observations such as these, however, leave several questions unanswered. It is not clear, for example, how large a strength contrast must be in order to have a discernable impact on topography and drainage network patterns. In the specific case of tectonic damage, there is a need for studies that make theoretical predictions about patterns of topographic evolution in rock that contains tabular damage zones created by seismogenic cataclasis along previously active faults. In this paper, I address the latter issue, by using a numerical landscape evolution model to determine how, according to current and relatively

simple geomorphic theory, the strength, width, and dip angle of planar weak zones are predicted to influence topography, drainage patterns, and knickpoint development. The calculations help generate insight into how different lithologically mediated landforms evolve, and they provide a set of testable predictions that can be compared to observed topography.

3.3. Methods

This section is used to describe my numerical approach to landscape evolution, the components and methods I employ in my models, and the important assumptions I make when designing my models to replicate natural conditions on Earth.

3.3.1. Approach and Scope

I generate field-testable theoretical predictions of the ways in which the near surface strength field might influence fluvial incision rates and drainage patterns. Specifically, I aim to identify the logical consequences of the hypothesis that fluvial erosion rate varies inversely with bulk-rock cohesion (Sklar and Dietrich, 2001; Sklar and Dietrich, 2004). This hypothesis has been suggested on the basis of field studies of soil erosion (e.g. Mirtskhoulava, 1966; Mirtskhoulava, 1991; Hanson and Simon, 2001), and to the extent that a similar principle applies to bedrock, its potential consequences are far-reaching. Rock cohesion varies by approximately three orders of magnitude between intact crystalline rock and fault-damaged rock (e.g. Thomson, 1993; Faulkner et al., 2003; Lockner et al., 2009; Faulkner et al., 2010; Mitchell et al., 2011). How would such a contrast be manifest in topography and landscape dynamics? How would the presence of

vertically dipping fault-damage zones be expected to influence drainage network patterns, relief, and transient responses to baselevel perturbations? Does the erosion of obliquely dipping fault-damage zones produce distinctive topographic signatures, and if so, what do they look like?

To begin to answer these questions, I ran a series of experiments with a numerical model of landscape evolution in which three dimensional (3D) planar weak zones were introduced as an initial condition (Figure 3.2A). These weak zones are meant to represent tectonically inactive fault damage zones, but they could also potentially be used to represent other planar geologic features such as lithostratigraphic units, dikes, and sills that introduce a local strength minimum. A suite of values (Figure 3.2B) is used to describe weak zone strength and geometry based on sub-meter scale structural and material strength measurements from naturally occurring weak zones (Thomson, 1993; Ben-Zion and Sammis, 2003; Mooney et al., 2007; Lockner et al., 2009; Mitchell et al., 2011). I describe the strength of the weak zones using cohesion, which I translate into erodibility. The considered geometric variables are weak zone dip, width, and geometric symmetry of the strength gradient.

My numerical experiments are divided into two model sets in order to isolate the individual effects of strength and geometry. The first set of models is used to measure changes in drainage pattern and knickpoint migration rate caused by the presence of fault weak zones with variable strength. The second set addresses drainage patterns associated with weak zones with moderate to shallow dip angle and variable strength, width, and symmetry.
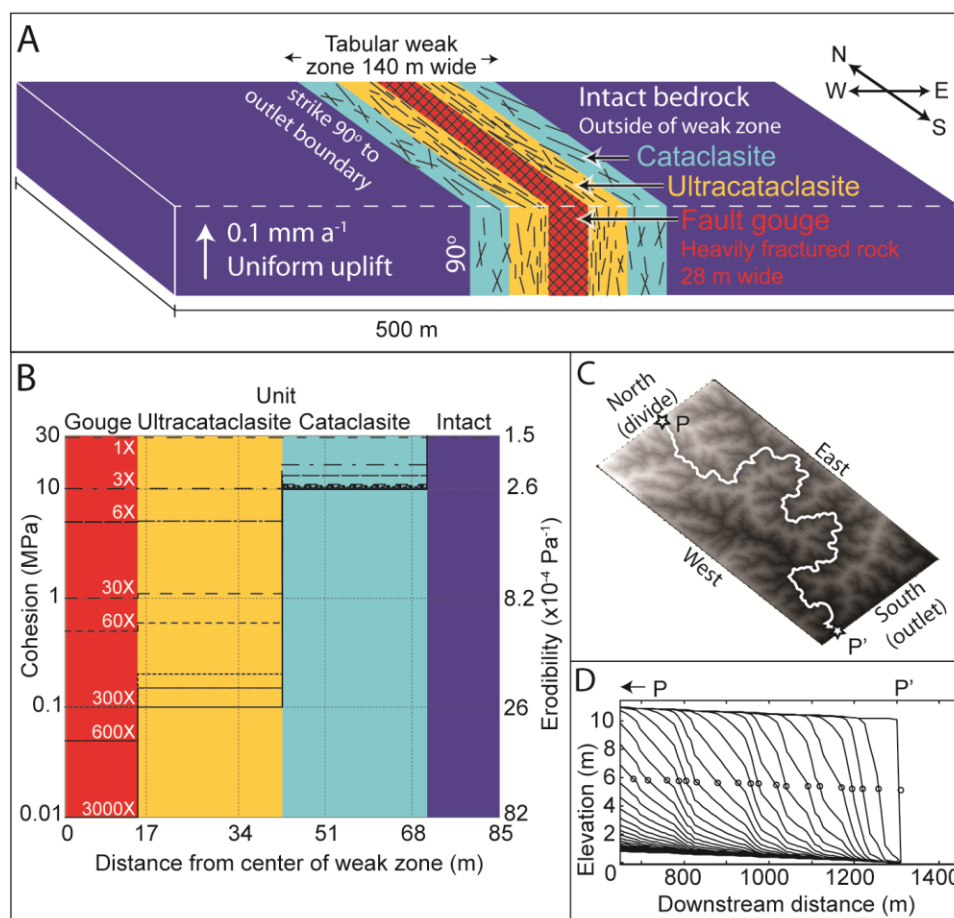
Figure 3.2. Schematic of model set 1 domains (A) with simplified material strength field resembling a symmetric fault damage zone (e.g. Ben-Zion and Sammis, 2003; Mooney et al., 2007; Koons et al., 2012). Weak zone dips vertically, strikes orthogonal to outlet boundary (white dashed line). Strength field is divided into four distinct, symmetric units. From strongest to weakest the units are intact bedrock, cataclasite, ultracataclasite, and gouge. (B) Plot of cohesion vs. width to represent the different modeled strength gradients. Colors represent weak zone units in (A). Erodibility values are displayed on the right-hand axis. Eight different strength gradients are used for model set 1, indicated by the individual dashed line patterns. I refer to the magnitude difference between the intact bedrock and the gouge unit in the weak zone to differentiate each strength gradient, which range from 1X, in which no weak zone exists and all bedrock has a uniform cohesion of 30 MPa, to 3000X, in which the gouge unit has a cohesion reduced by 3000X or from 30 MPa to 10 kPa. The other weak zone units also reduce in cohesion to maintain the common gradient pattern. (C) Example of a channel used to gather longitudinal profile data, white line. All profiles begin at the fixed position (P) on the northern divide boundary. The position of the outlet can change between experiments but is always along the southern outlet boundary (P'). (D) Channel profile time-series of elevation after imposition of an instantaneous 10 m uplift, knickpoint originates at the southern boundary (P' in Figure 3.2A). Position is measured at the knickpoint face, as the location where 50% of knickpoint height remains (circles).

3.3.2. Surface-Dynamics Model

I use a configuration of the Channel-Hillslope Integrated Landscape Developmental (CHILD) model (Tucker et al., 2001) to approximate the physics that control the rate of mechanical wear of the substrate by assuming that fluvial erosion rate scales with unit stream power. This form of model is preferred because there is much published evidence showing that rivers can erode bedrock and transport sediments at a rate roughly proportional to unit stream power (or its near-equivalent, boundary shear stress) (Bagnold, 1966; Howard and Kerby, 1983; Seidl and Dietrich, 1992; Howard et al., 1994; Howard, 1994; Stock and Montgomery, 1999; Whipple and Tucker, 1999; Kirby and Whipple, 2001; Tucker et al., 2001; Hancock and Anderson, 2002; Whipple, 2002; Whipple, 2004; Whittaker et al., 2007b; Yanites et al., 2010; Attal et al., 2011; Kirby and Whipple, 2012). Except for the dependency of erodibility on anelastic rock strength, CHILD has successfully been used to model many surface phenomena including influences of tectonic forcing (Tucker and Slingerland, 1996; Whittaker et al., 2007a; Attal et al., 2008; Attal et al., 2011), sediment transport (Gasparini et al., 2004; Gasparini et al., 2007), and storm events (Tucker and Bras, 2000; Sólyom and Tucker, 2004).

The landscape surface is divided into irregularly discretized elements, each representative of a small equant area (average 81 m^2) and connected to adjacent elements by a Delaunay triangulation. A steepest descent routing algorithm controls the spatial pattern of surface runoff for channels, which are embedded in cells as subgrid-scale features. Surface runoff leaves the model domain through a flow outlet boundary. Closed boundaries represent drainage divides and are assumed to be symmetric. To maintain continuity of crustal mass, the rate of change in surface elevation $\frac{\partial h}{\partial t}$ must be the sum of

bedrock detachment and transport by surface processes and vertical motion relative to baselevel. I assume a supply-limited system wherein all detached material is immediately transported from the domain; this assumption is based on studies that provide evidence for supply-limited behavior (e.g. Howard and Kerby, 1983; Stock et al., 2005; Whittaker et al., 2007a; Attal et al., 2008; Attal et al., 2011; Hobley et al., 2011). I model processes of landscape evolution using the following equation (Tucker et al., 2001; Tucker and Hancock, 2010)

$$\frac{\partial h}{\partial t} = -k_{b(x,y,z)}\omega + k_d\nabla^2 h + V_z + V_h\nabla h \qquad (3.1.)$$

where the rate of elevation change $\frac{\partial h}{\partial t}$ at any point on a surface depends on spatially variable erodibility $k_{b(x,y,z)}$, stream power ω per unit width, hillslope diffusivity k_d, hillslope curvature $\nabla^2 h$, vertical rock motion relative to baselevel V_z, and lateral topographic advection $V_h\nabla h$, which I assume here to be negligible. My description of the heterogeneous 3D erodibility field is in Section 3.3.3 below.

The first term on the right-hand side of Equation 3.1 represents the average rate of channel-bed incision, which I assume is proportional to stream power per unit width ω at every element (Whipple and Tucker, 1999; Whipple, 2004; Tucker and Hancock, 2010)

$$\omega = k_t\left(\frac{Q}{W}\right)S \qquad (3.2.)$$

where k_t is the unit weight of water (9800 kg m^{-2} s^{-2}), Q is fluid discharge, W is channel width, and S is channel slope. Channel width is calculated using the empirical method (Leopold and Maddock, 1953)

$$W = k_w Q^b \qquad (3.3.)$$

where b is the width-discharge exponent, here given a value of 0.5, and k_w is the width-discharge coefficient, here given a value of 10 $s^{0.5}$ $m^{-0.5}$.

Fluid discharge through each element is the sum of runoff (precipitation minus evapotranspiration), at that element and the accumulated downslope routing of water and sediment along a steepest-descent path from all interconnected upstream elements (Tucker et al., 2001; Tucker and Hancock, 2010). Because I assume a spatiotemporally homogeneous runoff distribution, I calculate $Q = RA$, where R is runoff rate and A is drainage area. However, others have explored the importance of storm events (Tucker and Bras, 2000; Sólyom and Tucker, 2004) and the orographic precipitation associated with high relief (Smith, 1979; Smith and Barstad, 2004; Roe, 2005). A steady runoff rate of 1 m y^{-1} is used for all models (Tomlinson and Sansom, 1994; Hicks et al., 2011).

Hillslope mass transport is expressed as a diffusion process. In many cases, a scarcity of regolith makes hillslope diffusion minimal in high relief cohesive bedrock substrates, and there is evidence that the traditional nonlinear hillslope diffusion function breaks down in these regions because steeper slopes may actually represent greater stability (Moore et al., 2009; Koons et al., 2012). Hillslope stability in these regions is therefore a function of cohesion, the spacing and orientation of fractures relative to the face of the hillslope, and fluid flow along joints (Scheidegger, 1998; Scheidegger, 2001; Scheidegger, 2004; Brideau et al., 2006; Brideau et al., 2009; Moore et al., 2009). Notwithstanding these complications, for the sake of simplicity and for my focused interest in the fluvial regime I employ a uniform linear hillslope diffusion equation with a k_d value of 4.4×10^{-4} m^2 y^{-1} (Nash, 1980) and neglect material-dependent variations in diffusivity and landslide erosion in these models. However, if I were to employ nonlinear diffusion with diffusivity values

scaled to cohesion, I would expect greater sensitivity of surface processes to mechanical weaknesses. It is appropriate to consider my numerical results as displaying the minimal possible sensitivity of hillslopes to weak zones.

A steady, uniform rate of rock uplift relative to baselevel, 0.1 mm y^{-1}, is used in order to represent a gently rising and completely exposed crustal basement initially at sea level. Sub-meter random noise is applied to the initial model relief in order to stimulate the development of a dendritic drainage pattern that strongly contrasts with the expected drainage pattern influenced by weak zone erosion. Because the focus here is on erosion of inactive weak zones, none of the modeled weak zones allow for slip or further weakening.

3.3.3. Relationship between Crustal Strength and Erodibility in 3D

Experimental and observational evidence suggests that erosion rate is inversely proportional to rock anelastic strength for bedrock rivers host to a saltating bedload (Sklar and Dietrich, 2001; Sklar and Dietrich, 2004; Stock et al., 2005). However, scaling erodibility to rock strength is still not well understood for the problem of fluvial erosion, particularly for use in shear stress/stream power models. I choose to scale erodibility (k_b) to cohesive strength because 1) it is a fundamental component of the Mohr-Coulomb failure criterion and is frequently used to report the anelastic strength of both rock and soil at the Earth's surface (Bieniawski, 1974; Brace and Kohlstedt, 1980; Hoek and Brown, 1980; Hoek and Brown, 1997; Enlow and Koons, 1998; Schellart, 2000), 2) it is a measure of shear strength (Coulomb, 1773; Sibson, 1977; Koons et al., 2012), which seems appropriate for shear stress/stream power-based fluvial incision models, and 3) a conservative scaling

relation exists for stream power models that is based on empirical study (Hanson and Simon, 2001).

The coefficient k_b is a function of rock strength, water density, gravitational acceleration, and channel geometry and roughness. All else being equal, a large value of k_b represents weak or highly erodible rock, and a small value represents strong, resistant rock (Stock and Montgomery, 1999). Erodibility has units equal to the inverse of stress (units m s^2 kg^{-1}), which is in agreement with the inverse proportionality of anelastic strength and erosion rate (Sklar and Dietrich, 2001; Sklar and Dietrich, 2004). Studies of cohesive soil erodibility exist (Mirtskhoulava, 1966; Mirtskhoulava, 1991; Hanson and Simon, 2001) but few data exist for bedrock erodibility (Stock et al., 2005). I use the empirical relation put forward by Hanson and Simon (2001) for cohesive soils, modified for use in a stream power model framework

$$k_{b(x,y,z)} = k_c C_{(x,y,z)}^{-1/2} \qquad (3.4.)$$

where C is cohesion and k_c is a coefficient equal to 0.2 with units $m^{1/2}$ s $kg^{-1/2}$.

An argument can also be made for scaling erodibility to tensile strength based on an empirically derived proportionality between erosion rate and the inverse square of tensile strength (Sklar and Dietrich, 2001). However, the presence of fractures or joints can reduce tensile strength almost completely or make for difficult and imprecise measurements (Bieniawski, 1974; Hoek and Brown, 1980; Hoek and Brown, 1997). Tensile strength-based scaling may be accurate for intact, unjointed rocks and cements, but materials such as cataclasites and fault gouge have essentially no tensile strength, while cohesion is still consistently measureable over many orders of magnitude (Hoek and Brown, 1980; Hoek and Brown, 1997; Molnar et al., 2007). The occurrence of mechanical

defects increases with scale, making cohesion the more reliable and more conservative (C$^{-1/2}$ versus T^{-2}) scale for erodibility of rock and soil strength at the resolution of my experiments. If the experiments show sensitivity to my conservative scaling method, results for tensile strength scaling would be even more dramatic.

It is necessary to approximate a relative strength factor when sources provided either alternative measurements of rock strength or strictly qualitative information about rock quality. I used the Hoek-Brown failure criterion to estimate rock cohesion based on lithology and the Geological Strength Index (GSI), a measure of fracture density and roughness (Hoek and Brown, 1997). The Hoek-Brown failure criterion is a well-recognized method used in the geotechnical (e.g. Read et al., 2000), mining (e.g. Demirel, 2011; Schumacher and Kim, 2014), and engineering (e.g. Brideau et al., 2006; Brideau et al., 2009) literature.

3.3.4. Analytical Comparison

Equations 3.1 and 3.4 allow us to predict the difference in erosion rates between intact and weakened bedrock. If fault-damaged rock is on the order of 300 times less cohesive than intact bedrock, as suggested by several studies (Thomson, 1993; Ben-Zion and Sammis, 2003; Lockner et al., 2009; Mitchell et al., 2011), then I can expect fault zones to erode approximately 17 times faster than intact rock with all else being equal. Variations in the slope-area trend with rock strength reflect the expected scaling: combining Equations 3.1-3.4, applying the steady state condition $\omega * k_b = V_z$, and solving for slope, the slope-area relationship is

$$s = \left(\frac{k_w V_z}{k_b k_t}\right)(RA)^{-1/2} = \left(\frac{k_w V_z C^{1/2}}{k_c k_t}\right)(RA)^{-1/2} \qquad (3.5.)$$

Assuming the same scaling of cohesion, fluvial slopes in fault damaged rock will be $\sqrt{300}$, or approximately 17 times lower than the intact rock assuming equal drainage area.

These simple approximations suggest that the strong rate and slope contrasts should be reflected in drainage-network development and topographic evolution. However, this analytical method ignores heterogeneous strength-related complexities such as the connectivity of weak elements along weak zone strike and the 2D implications for drainage network patterns, spatial controls on channel gradient and erosion rate associated with different rock strengths, effects on regional relief, lateral shifting of the weak zone exposure with continued erosion, or other effects that a 3D weak zone geometry may impose on a landscape surface. Additionally, it is useful to visualize results using a numerical model, especially when considering 3D strength fields.

3.4. Model Set 1: Fluvial Incision Sensitivity to Variations in Weak Zone Strength

3.4.1. Description of Geometry and Strength

In the first set of experiments, the initial model configuration consists of a vertically dipping damage zone with a cohesion field that increases progressively away from the zone's center, in a manner similar to that of naturally occurring fault weak zones (Thomson, 1993; Ben-Zion and Sammis, 2003; Mitchell et al., 2011) (Figure 3.2). The gradual change in cohesion/erodibility is discretized by dividing the weak zone width into parallel planar layers that strengthen with distance from the weak zone interior (Figure 3.2A,B). This stepwise transition in strength is an approximate representation of the strength gradient from weak fault gouge to ultracataclasite, cataclasite, and finally the

strongest unit, intact bedrock (Figure 3.2B, the stepwise pattern is referred to as a gradient henceforth). The entire weak zone is 140 m wide. The exception to this is a supplemental experiment in which the weak zone width is doubled in order to test width scaling effects on channel tortuosity and regional relief; these model results are displayed as supplemental data.

Eight experiments are run to test the sensitivity of fluvial incision to different crustal strength gradients (Figure 3.2B), representing varying degrees of rock damage due to brittle failure. The first example is homogeneous with cohesion/erodibility equal to the intact bedrock strength value (strength difference factor of 1), while each ensuing value hosts a progressively weaker, centrally located weak zone. The cohesion contrast between undamaged rock and weak zone core is varied from a factor of 3 to 3000. The weak zone strikes normal to the flow outlet boundary for all experiments excepting a supplemental experiment in which vertically dipping weak zones strike parallel to the outlet boundary; these model results are displayed as supplemental data. For the sake of model simplicity I impose a uniform scale for weak zone width and do not incorporate the scale-independent properties of material fragmentation (e.g. Sammis et al., 1986; Sammis et al., 1987; Blenkinsop, 1991; Shimamoto and Nagahama, 1992; Jébrak, 1997; Roy et al., 2012) In this study I model weak zone widths that overlap with the typical range of river channel widths (Finnegan et al., 2005).

3.4.2. Steady State Topography

Each experiment is allowed to approach a steady state topography condition under the conditions described above, in which the erosion rate is approximately spatially

uniform and equal to the applied rate of uplift relative to baselevel and there is no change in drainage network geometry or topography. I use steady state topography to compare topographic relief, drainage network patterns, and longitudinal channel profiles for the differing rock strength configurations. Relief is measured as the maximum and average elevations relative to a base level fixed at sea level. Longitudinal profiles follow the channel-wise distance of the highest order channel from the center of the northern flow divide to the outlet boundary (Figure 3.2C). My method of quantifying drainage network pattern is described in Section 3.4.3 below.

3.4.3. Tortuosity

Rapid erosion of weak zone material will potentially confine a developing drainage network to the structure of the weak zone, limiting the direction of flow. I characterize the drainage network pattern in each experiment by using tortuosity, a measurement of change in channel orientation over a prescribed wavelength

$$T = 1 - \frac{l_s}{l_n} \qquad\qquad (3.6.)$$

where tortuosity T equals the ratio of straight line distance l_s over channel-wise distance l_n between two points along a channel. Tortuosity is related to sinuosity via $S = (1-T)^{-1}$. The step length must be greater than element resolution and the channel-wise distance is calculated at element resolution. Tortuosity is measured with l_s equal to 200 m for the highest order channel from flow divide to outlet. I use river channel tortuosity as a measure of directional dependence because it is a simple spatial representation of orientation preference for a prevalent landscape feature, and I feel that it expands on the use of other

measurements of directional dependence as a landscape characterization tool (e.g. Judson and Andrews, 1955; Moglen and Bras, 1995).

3.4.4. Knickpoints

I test the influence of the strength field on fluvial incision by measuring knickpoint migration rates into preexisting vertically dipping weak zones with varied erodibility values. Knickpoints are localized convex features that migrate up concave channel profiles when in a transient state (Gardner, 1983). Upstream knickpoint migration is often a primary erosional response to internal or external perturbations within a watershed and are often used to define the spatial progression of erosion in an evolving landscape (e.g. Crosby and Whipple, 2006; Berlin and Anderson, 2007).

Model topography is allowed to approach a steady state condition as explained above, then a sudden 10 m step in elevation is uniformly introduced to create a knickpoint at the outlet boundary. The landscape is once again allowed to approach a steady state condition. I measure the response rate by tracking the knickpoint position every 100 to 10,000 years along a longitudinal profile that follows the channel-wise profile explained above. The position of the knickpoint is taken at the location where half of its original height has eroded (Figure 3.2D). I compare the knickpoint's behavior, as it traverses the strength gradient, to the analytical solution for knickpoint propagation in a uniform medium in Section 3.4.2. (e.g. Gardner, 1983; Whipple and Tucker, 1999; Niemann et al., 2001).
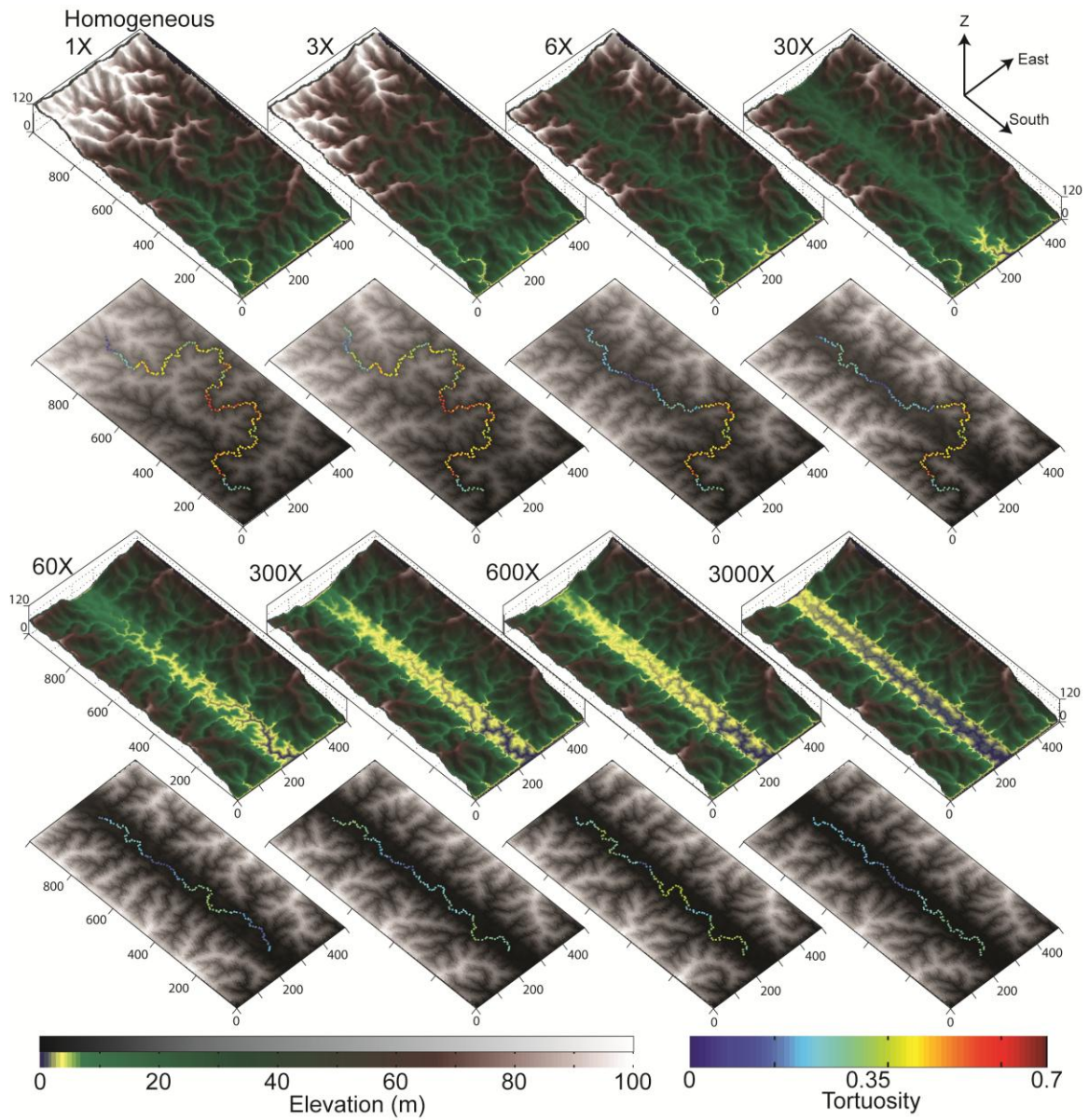
Figure 3.3. Steady state elevation fields for all Model Set 1 experiments. Numbers represent the different strength gradients introduced in Figure 3.2B. Length scale is in meters. The greyscale maps display relief overprinted in color by tortuosity values for the largest fluvial channel in each simulated domain. Color represents degree of tortuosity, measured at the 200 m wavelength. The path of the highest order channel (colored line) is used for measuring knickpoint migration rate (Figure 3.7) and longitudinal profiles (Figure 3.8, 9).
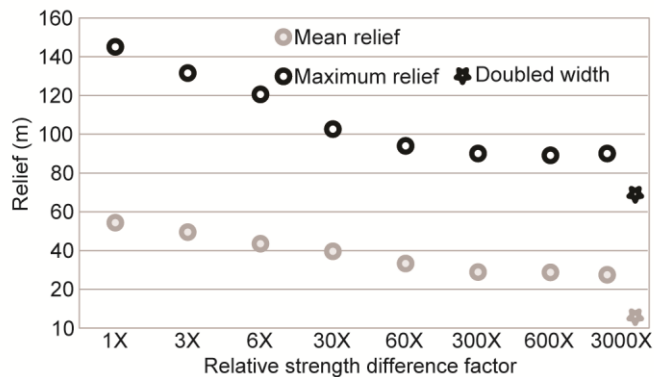
Figure 3.4. Maximum (black dots) and mean (grey dots) topographic relief. Data for doubled weak zone width (stars) and weak zone parallel to outlet (squares) are for the supplemental experiments shown in Figure 3.S1.
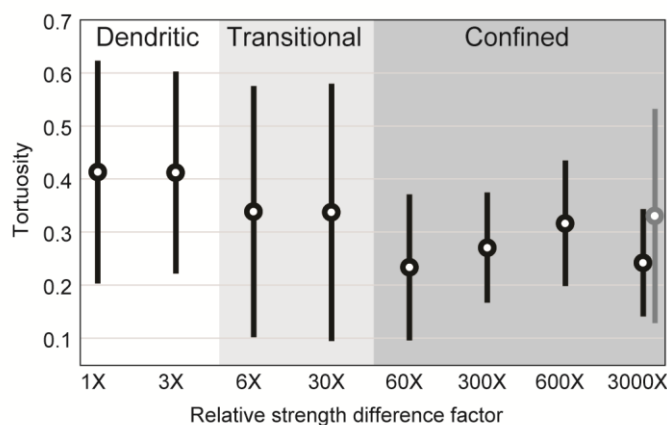
Figure 3.5. Mean tortuosity values for each experiment. Values measured for the highest-order channel. Error bars represent two standard deviations. Experiments are divided into three patterns: 1) dendritic, where mean tortuosity is high and the range of values is relatively narrow, 2) transitional, where mean tortuosity is moderate and the range of values is wider, representing the presence of both dendritic and confined patterns in a single high-order channel, and 3) confined, where mean tortuosity is low and the range of values once again narrows. The grey marker is from a 3000X experiment with doubled width.

3.4.5. Model Set 1 Results

3.4.5.1. Steady State Landscape Patterns

Results of the steady state experiments in Figure 3.3 indicate that the presence of a weak zone leaves a lasting influence on the landscape in the form of a straight, high-order channel with short, orthogonal tributaries of low order. Additionally, the local presence of weak zones reduces total relief in a region (Figure 3.3, 3.4). In comparison, the 1X

experiment is completely homogeneous and produces a drainage pattern with no strong directional dependence caused by strength (Figure 3.3), the highest maximum relief (Figure 3.4), and relatively high average tortuosity (Figure 3.5, dendritic; see also supplemental videos).

A low relative strength difference is included in the 3X experiment, causing topography to locally reflect the weak zone in tributaries, saddles, and local channel slope (Figure 3.3). Figure 3.6A displays the marked step in slope-area relationship between different erodibility values for the 3X experiment. For a given drainage area, slope in the weak zone is up to $\sqrt{3}$ less than for intact bedrock, but this is not great enough to influence the dendritic path of the high-order channel. However, the presence of a weak zone does limit the maximum relief within the model domain (Figure 3.4).

Tortuosity values from the 6X to 30X experiments reflect the transition from unconfined and dendritic to a channel that is confined to the structure of the weak zone, where the northern section of the drainage network has low tortuosity values and a strong directional dependence, but the southern section remains dendritic. This pattern is represented in Figure 3.5 as a transition from a high mean tortuosity with a relatively narrow range of values to a lower average tortuosity with a wider range representing a combination of dendritic and structurally confined drainage patterns. There is a gradual decrease in maximum and mean relief with increasing relative strength difference for these transitional experiments (Figure 3.4).

The 60X to 3000X experiments confine the main drainage network completely within the weak zone. Though these high-order channels are structurally confined and as a consequence have relatively low tortuosity values, they nonetheless traverse the full width

of the damage zone in the 60X to 600X experiments. The ability of the weak zone to reduce maximum relief begins to plateau at 300X. At this magnitude of weakening the slope of the highest order channel begins to approach zero and therefore cannot further reduce the regional relief.
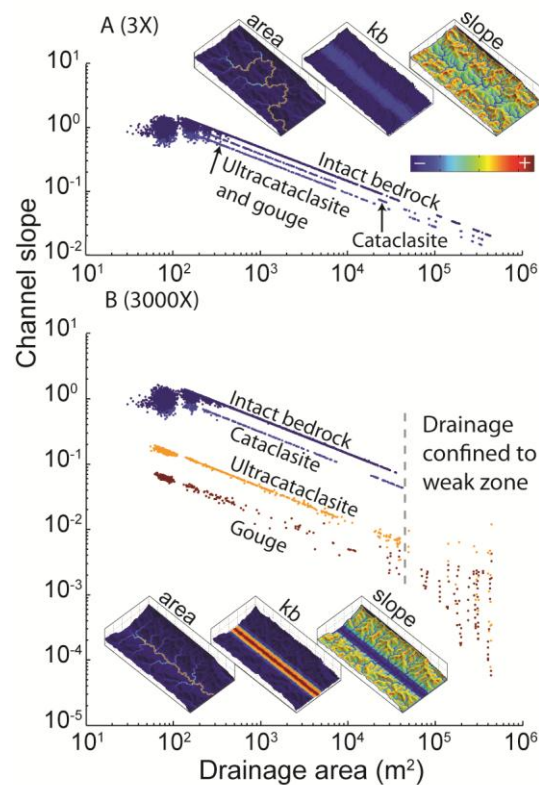
Figure 3.6. Slope versus drainage area plots. (A) 3X and (B) 3000X experiments. Color scale denotes magnitude of erodibility for the slope versus drainage area plots, in addition to drainage area and slope for the inset maps. For equal drainage area, slope differs by erodibility. The weaker units host low slope features such as saddles and tributaries in the 3X experiment, seen in the drainage area, kb, and slope insets. The 3X strength gradient is small enough to have little difference in erodibility between gouge and ultracataclasite units (see also Figure 3.2B). The 3000X experiment has a higher magnitude strength gradient between intact rock and weak zone, leading to greatly reduced slopes in the gouge unit and confinement of the high-order channel to the gouge and ultracataclasite units, seen for drainage area values greater than approximately 4×10^4 m^2. Color bar: blue to red range for slope: 0 to 1.8, erodibility: 3.6×10^{-5} to 2×10^{-3} m s^2 kg^{-1}, and drainage area 81 to 5×10^5 m^2.

For the 3000X experiment, slope in the weak zone is up to $\sqrt{3000}$, or ~55X, less than for intact bedrock (Figure 3.6B, Equation 3.6) and the high-order channel is

completely confined to the gouge and ultracataclasite units. All high order drainage is dominated by the weak zone and the majority of low order drainage is dominated by intact bedrock (Figure 3.6B). In Figure 3.5 the structurally confined pattern is represented by low mean tortuosity with a narrow range. These steady state experiments are used as the initial condition for the knickpoint models discussed below.

3.4.5.2. Knickpoint Migration Rate, Regional Response Rate

The modeled crustal strength fields influence the rate of knickpoint migration into an eroding landscape (Figure 3.7A), however, the rate of knickpoint migration is non-uniform for all simulations. The average rate of knickpoint migration, calculated as the average of all migration rates measured along the channel-wise distance, increases with decreasing strength. The linear stream-power erosion law predicts that convexities in a stream longitudinal profile should travel upstream as knickpoints, with a wave celerity that depends on rock erodibility (e.g. Rosenbloom and Anderson, 1994; Whipple and Tucker, 1999; Loget and Van Den Driessche, 2009), and hence on cohesion,

$$V_k = \frac{k_b k_t}{k_w} (RA)^{1/2} = \frac{k_c k_t}{C^{1/2} k_w} (RA)^{1/2} \qquad (3.7.)$$

Using Equation 3.7, knickpoint migration rate in the 60X experiment should be up to ~7.7X faster than in the homogeneous 1X example, while the 3000X example should show a knickpoint migration speed up to ~55X faster (Figure 3.7A, grey bars). Experimental rates are less, with an approximately 7X faster average knickpoint migration rate for the 60X example and an approximately 35X faster average rate for the 3000X example (Figure 3.7, black bars). In the homogeneous case, reduction in knickpoint speed arises solely from the progressive loss in drainage area as the knickpoint moves upstream (Figure 3.8). In

experiments with weak zones, lower than expected migration rates and local fluctuations in migration rate arise from variations in erodibility along the channel profile (Figure 3.8, Figure 3.9). For the 60X to 3000X simulations, structurally confined channels are mostly constrained to the gouge unit, but the channel winds across the erodibility gradient, intermittently crossing into the stronger and slower to erode ultracataclasite or cataclasite units. Channel occupation of the stronger units is more common in the 3X to 30X simulations, which have a less erodible gouge unit and a smaller relative strength difference (Figure 3.9).
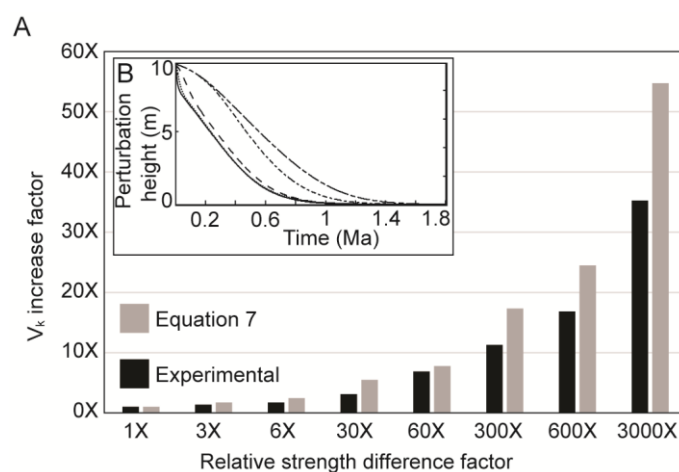
Figure 3.7. Knickpoint migration rate (V_k) increase factor with respect to the strength gradient increase factor. (A) The rate increase factor is the ratio of knickpoint migration rate with respect to the homogeneous 1X experiment, a simplified method to compare relative knickpoint migration rates with respect to crustal weakening. Grey bars: expected values using Equation 3.7. Black bars: measured average migration rate from experimental data. (B) Total response time from the start of the base level perturbation event to the time at which a steady state topography is reestablished. Lines represent 3000X (solid), 300X (dotted), 30X (dashed), 3X (short dash-dot), and 1X (long dash-dot).

In addition to hosting higher knickpoint migration rates, weak zones reduce the total response time of a region to base-level perturbations (Figure 3.7B). The 3000X experiment is characterized by a rapid drop in mean perturbation height associated with total erosion of the weak zone, followed by a protracted period in which steep gradients

traverse the low order tributaries and hillslopes that transect the strong adjacent rock. Steep gradients associated with the base-level perturbation cause local increases in erosion rate, both by fluvial and hillslope processes, until the landscape again approaches steady-state. A similar pattern exists for other examples where the highest order channel is at least partially confined to the weak zone (30X, 300X) but the initial response from the 3X example is identical to the homogeneous 1X experiment, increasing in rate later on. This is due to the weak zone's control on low order, rather than high order channels; the response rate does not increase until the perturbation is felt in the lower order tributaries.

3.4.5.3. Stationary Knickpoints Associated with Erodibility Gradients

Fluvial incision across the erodibility gradient causes local stationary knickpoints which are not associated with the externally introduced transient knickpoint (Figure 3.8, Figure 3.9). The stationary knickpoints are best seen in the 3X, 6X, and 30X experiments when the high-order channel transitions from a steep sloped intact bedrock reach to a gently sloped weak zone reach (Figure 3.8-9B-D red arrows). These knickpoints remain in the channel profile after the landscape has approached a steady state condition. The 600X and 300X experiments also host stationary knickpoints that correlate with a transition from cataclasite to ultracataclasite units (Figure 3.8-9F-G). The 30X experiment hosts stationary knickpoints with the greatest relief, which correlate to a transition from intact bedrock to gouge unit (Figure 3.8-9D, arrows). The profile for the homogeneous 1X experiment does not host any stationary convex features (Figure 3.8A). The positioning of these stationary knickpoints also correlates with local reductions in transient knickpoint migration speeds as discussed above (Figure 3.9).

Figure 3.8. Longitudinal profile data for each Model Set 1 experiment. (A) 1X, (B) 3X, (C) 6X, (D) 30X, (E) 60X, (F) 300X, (G) 600X, (H) 3000X. Channel-wise elevation (solid black) is displayed for a series of time steps just after the base level perturbation is introduced until the channel again approaches a steady-state condition. Drainage area is displayed in dotted grey. Arrows point to stationary knickpoints formed across an erodibility gradient. Snapshots of knickpoint progression in map view are shown for (A) 1X and (I) 3000X experiments. White stars represent the start and finish of the longitudinal profiles.

Figure axes: Elevation (m) [left vertical], Area (1×10⁵ m²) [right vertical], Downstream distance (m) [horizontal].

A (1X) — 100 ky, 300 ky, 1000 ky — 20ky steps

B (3X) — 20ky steps

C (6X) — 20ky steps

D (30X) — 10ky steps

E (60X) — 1ky steps

F (300X) — 1ky steps

G (600X) — 1ky steps

H (3000X) — 1ky steps

I (3000X) — 1 ky, 5 ky, 10 ky
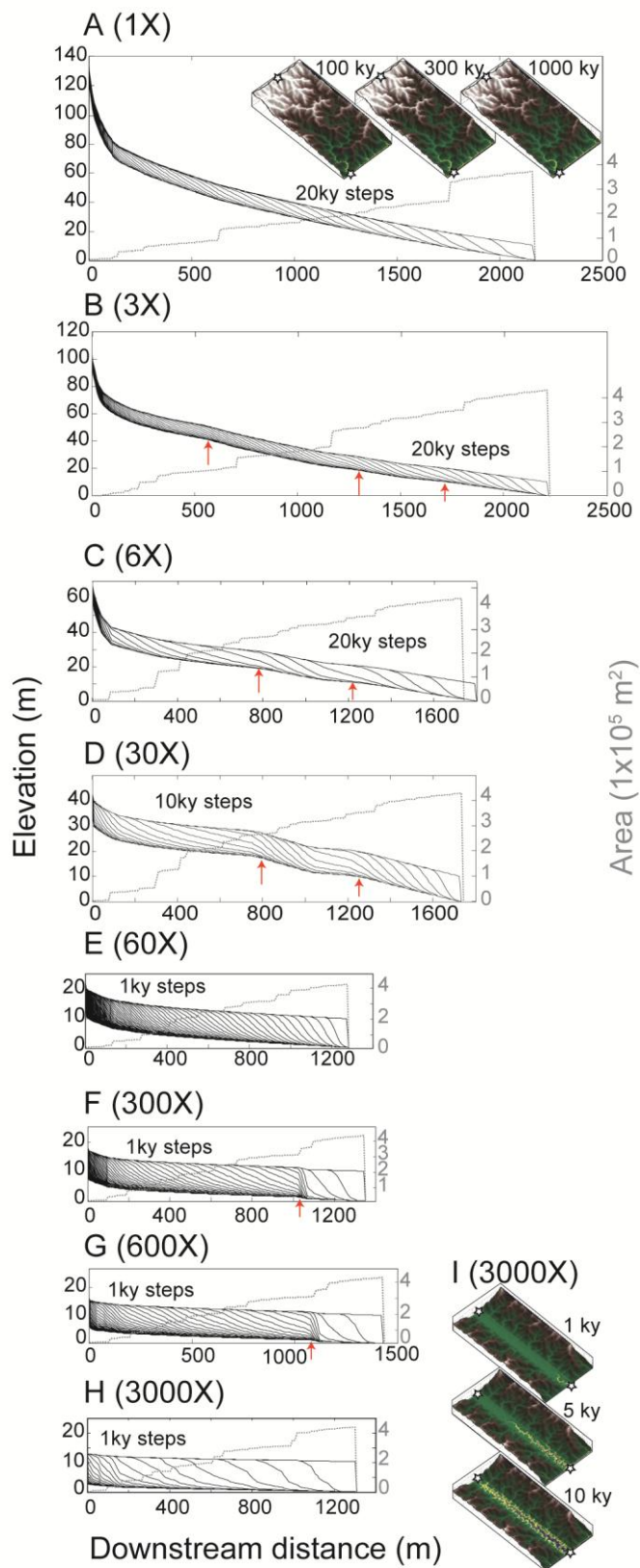
Figure 3.9. Channel-wise knickpoint migration rate (solid black) and erodibility (dashed grey) as a function of downstream distance from point P-P'. Plot organization is identical to Figure 3.8. Arrows point to stationary knickpoints formed across an erodibility gradient, also where knickpoint migration rate decreases. The knickpoint position and migration rate are measured at every time step, and migration rate is plotted with respect to downstream distance.

A (1X)

B (3X)

C (6X)

D (30X)

E (60X)

F (300X)

G (600X)

H (3000X)

Migration rate (m y^{-1})

Kb (1x10^{-5} m s^2 kg^{-1})

Downstream distance (m)
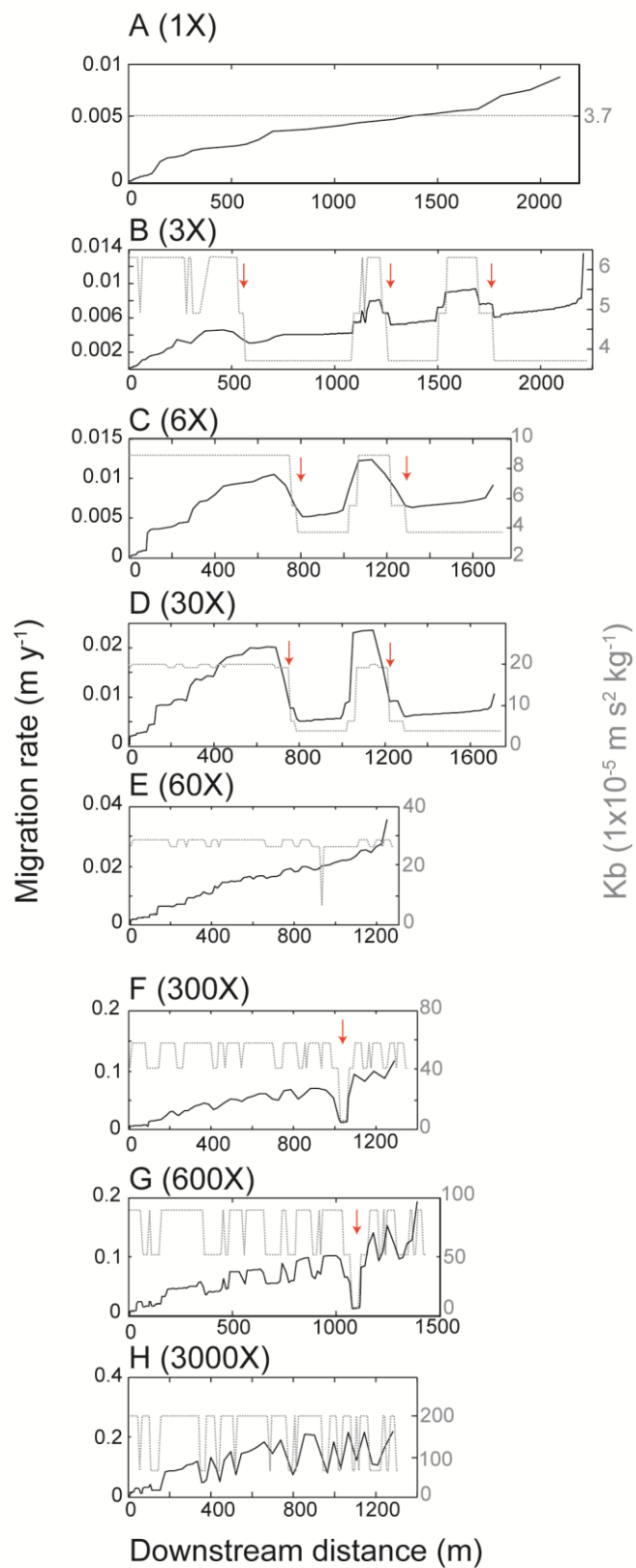
3.5. Model Set 2: Fluvial Incision Sensitivity to Variations in Weak Zone Geometry

I use my second set of numerical experiments to test the sensitivity of fluvial incision to variations in weak zone dip, width, symmetry (Figure 3.10), and erodibility (Figure 3.1B). Model set 2 experiments feature symmetric and asymmetric weak zones, both forms of which are naturally common (Faulkner et al., 2003; Faulkner et al., 2010; Mitchell et al., 2011; Rempe et al., 2013) and could produce different erosional patterns under these geometric conditions.

While the previous models incorporated vertically continuous erodibility fields, erosion into dipping weak zones requires a truly 3D erodibility field. Steady state is not possible with these complex erodibility fields because the exposure will continuously shift down-dip as bedrock is constantly uplifted and eroded. For this reason I elect to study fluvial incision sensitivity beginning from a low-relief surface, as described above.
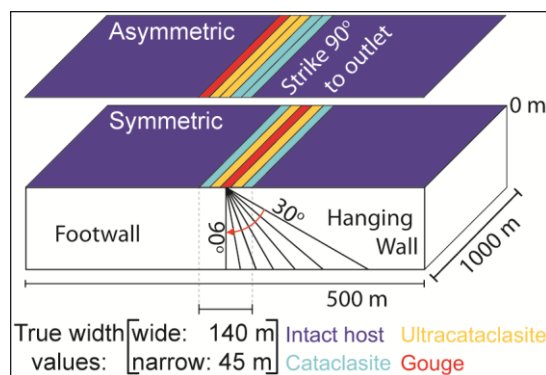
Figure 3.10. Schematic for Model Set 2. Fault dip varies from 30 to 90 degrees. Model set 2 uses symmetric and asymmetric weak zones. The same strength values are used from Figure 3.1. The gouge unit is always on the footwall side of the weak zone. True weak zone width values are displayed below the schematic, two values are used for sensitivity analysis: wide 140 m and narrow 45 m weak zones.

3.5.1. Lateral Shifting

Figure 3.11 displays time series of elevation, fluid discharge Q, and erodibility, respectively for an asymmetric 30° dip example in which cohesion varies by a factor of

3000X. Initially the high-order channel is structurally confined near the western boundary (Figure 3.11, 150 ky). As bedrock is uplifted and the surface erodes, the weak zone exposure shifts laterally to the east at a rate set by the weak zone dip angle. The strong hanging wall must erode to expose the underlying weak zone. The structurally confined high-order channel experiences a series of eastward trending channel-shifting events that correlate with the lateral shift and subsequent erosion of the weak zone exposure Figure 3.11, 750 ky, 1650 ky). This response is similar to fluvial incision into vertically dipping faults in that the channel remains within the confines of the weak zone, but is dissimilar in that the lateral position of the structurally confined channel is transient and does not approach a steady state condition.

3.5.2. Valley Asymmetry

Unlike the symmetric tributaries developed in Model Set 1, Model Set 2 tributaries are steep and tortuous on the headwall side of the valley, while footwall tributaries are straight and gently sloping at an angle that approaches that of the weak zone dip (Figure 3.11). Hanging wall tributaries are more widely spaced and shorten in length as the high-order channel shifts eastward and the footwall tributaries lengthen. Valley profiles for variable dip (Figure 3.12A) display a degree of asymmetry inversely proportional to weak zone dip. Valley asymmetry is a product of lateral shifting by the structurally confined channel and asymmetry increases with decreasing dip angle (Figure 3. 12B). For a given drainage area, channel slope on the footwall side is noticeably more shallow than on the head wall side, despite an identical erodibility value on both sides (Figure 3.12C).
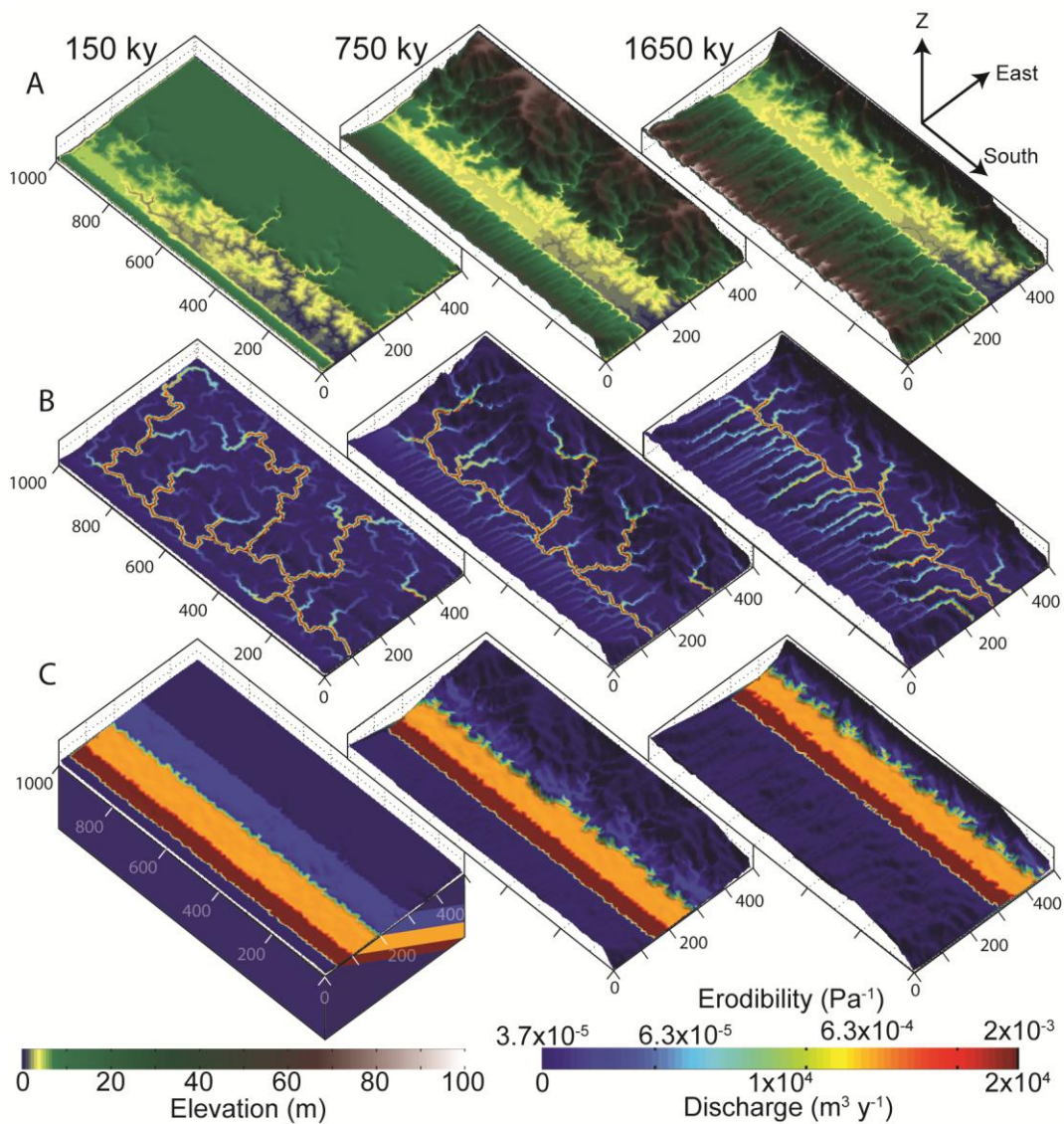
Figure 3.11. Example time series of lateral migration of a river channel confined to an asymmetric weak zone. (A) elevation, (B) fluid discharge, and (C) erodibility. The erodibility color scheme matches the scale in Figure 3.2B, 3000X. Length scale is in meters.
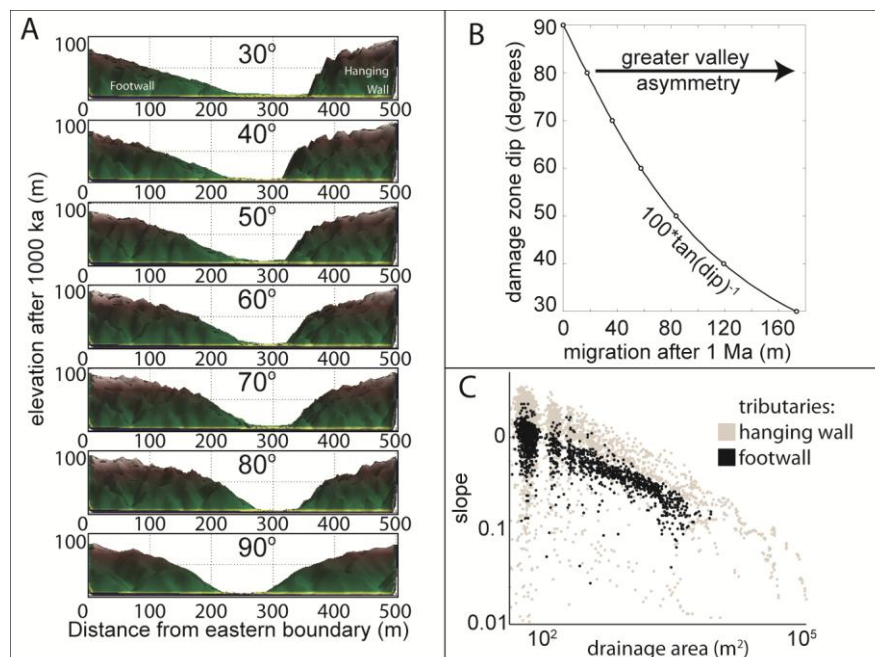
Figure 3.12. Cross-sectional valley profiles for faults with indicated dip. (A) Relief is always greatest downdip, in the hanging wall bedrock, while the updip, footwall bedrock gradually steepens with increasing dip angle. (B) The expected distance of channel lateral shifting as a function of total uplift (100 m) after 1 Ma and the inverse tangent of fault dip. Dots indicate the weak zone dip for the experiments in (A). Valley asymmetry increases with decreasing fault dip. (C) slope-area plot of hanging wall (grey dots) and footwall (black dots) tributaries for the example shown in Figure 3.11, time 750 ky. Though both regions are composed predominantly of the same bedrock unit, slopes along footwall tributaries are noticeably less steep. Channel slope in the footwall is influenced by the dip of the eroded weak zone, though its signal is slowly removed by incising tributaries and steepening gullies. The scatter of shallow slope values in the hanging wall is associated with the weaker bedrock units that the tributaries cross before reaching the main channel. There is no strong slope-area relation associated with erodibility because the weak zone is continuously exposed and eroded, never reaching a stable slope condition.

3.5.3. Strength, Width, Asymmetry Sensitivity

Sensitivity to strength and geometry is displayed using plots of lateral shifting for channels confined to 30° dipping weak zones (Figure 3.13A-D). The plots represent the west-east position of the outlet for the largest drainage as it shifts in time and uplifted height. The plots contain strength sensitivity data for asymmetric 140 m wide (Figure 3.13A), symmetric 140 m wide (Figure 3.13B), asymmetric 45 m wide (Figure 3.13C), and

symmetric 45 m wide weak zone experiments (Figure 3.13D). In summary, lateral channel

shifting is generally hindered by 1) decreasing the strength differential between weak zone

and intact bedrock, 2) decreasing weak zone width, and 3) geometric symmetry in the weak

zones as detailed below (Figure 3.13).
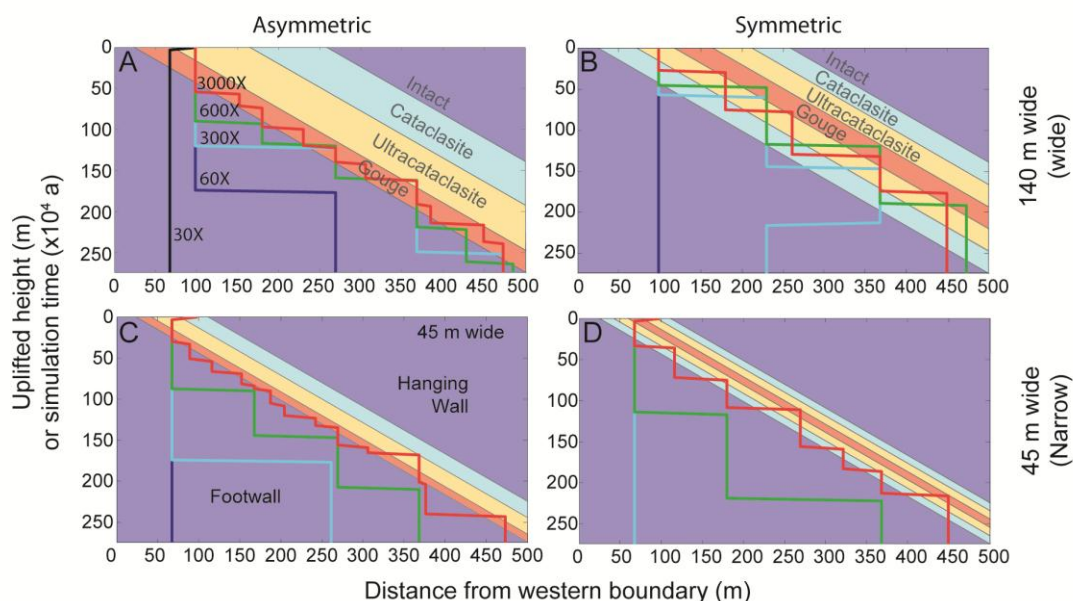
Figure 3.13. Plots of west-east channel outlet position (horizontal axis) as a function of uplifted height or time (x10^4 years, increasing downward). A transparency of the strength field indicating the different units is included to better interpret the correlation between shifting pattern and weak zone position. Each plot contains data on strength sensitivity, results are divided between asymmetric, symmetric, 140 m wide, and 45 m wide weak zones. Strength experiments are indicated by line color and represent the values featured in Figure 3.1C: red: 3000X, green: 600X, cyan: 300X, blue: 60X, black: 30X. (A) Asymmetric, 140 m wide weak zone experiment. (B) Symmetric, 140 m wide weak zone experiment. (C) Asymmetric, 45 m wide weak zone experiment. (D) Symmetric, 45 m wide weak zone experiment.

For the asymmetric 140 m wide experiments (Figure 3.11, 13A), the 3000X

experiment hosts a structurally confined channel that takes short (~25-75 m), frequent

eastward shifts, matching the dip of the gouge unit (Figure 3.13A, red line, gouge unit).

Lateral channel-switching events are longer (~75-100 m) and less frequent with shifting

events less able to keep up with the gouge unit exposure as the strength gradient reduces

in the 600X (green), 300X (cyan), and 60X (blue) experiments. No lateral shifting occurs

for the 30X weakened experiment; the channel continues to incise vertically through the weak zone and into the resistant, underlying footwall.

In the case of a wide, symmetric weak zone (Figure 3.13B), structurally confined channels from the 3000X and 600X experiments migrate laterally and match the shifting exposure of the gouge unit. Lateral channel-switching events are longer (~75-125 m) and less frequent than the asymmetric experiments in Figure 3.13A. The 100X experiment begins to migrate laterally but shifts back to a previous position before 1500 ky. No lateral shifting occurs for the 60X weakened experiment.

The asymmetric 45 m wide experiments (Figure 3.13C) resemble the wide, asymmetric cases (Figure 3.13A) in that the 3000X experiment hosts a structurally confined channel whose position strongly correlates with the gouge unit exposure. Lateral channel-switching events are very short (~10-50 m) and frequent up to about 1500 ky, after which they become longer (~75-100 m) and less frequent. Lateral channel-switching events become much less frequent in the 600X and the 100X experiments and they incise deeply into the strong footwall. The 60X experiment incises vertically with no lateral shifting.

In the symmetric, narrow experiments (Figure 3.13D), the 3000X experiment hosts a structurally confined channel that jumps laterally in concert with the gouge unit exposure, though the channel comes in contact with the strong footwall before every shifting event (red line crossing into dark blue background). Lateral channel-switching events are shorter (~50-75 m) and more frequent than the wide symmetric experiment. Shifting becomes far less frequent for the 600X weakened experiment, in which the main channel shifts eastward even though it almost never touches the weak zone and lags behind in the intact bedrock. This weak influence also occurs to a lesser extent for some of the lower strength gradient

experiments described above. The 300X experiment incises vertically with no lateral shifting.

3.6. Discussion

3.6.1. Drainage Network Pattern and Controls on Relief

The drainage network patterns in Model Set 1 reflect the underlying crustal strength field, but the degree of correlation between the main channel position and the outcrop of the weakest rocks is sensitive to the strength difference between intact bedrock and the weak zone. Structural confinement of high order channels is attributed to comparably minimal channel slopes within the weakest units, subsequently reducing the local relief and accumulating surface runoff, which is then able to pass through the weak zone to the outlet boundary. Fluvial incision into extremely weak zones causes the rock strength field to dominate the drainage network pattern of a landscape (Figure 3.3, 60X to 3000X), while moderately weak zones influence drainage patterns further up channel (Figure 3.3, 6X to 30X) or only influence the position and orientation of tributaries and saddles (Figure 3.3, 3X). The strength gradients associated with naturally occurring crustal failure fall within the limits of simulated fluvial incision sensitivity.

3.6.1.1. Drainage Network Pattern

The unconfined, dendritic pattern represented by greater long-wavelength tortuosity in the 1X to 30X experiments is a consequence of the random noise applied to the initially flat domain, as explained in Section 2.2. This drainage pattern conforms to a dendritic classification (e.g. Zernitz, 1932; Lubowe, 1964), in which channel orientation is

not strongly influenced by any gradient and therefore has no strong directional dependence. The dendritic drainage pattern is replaced by a structurally controlled pattern for large strength gradients (60X to 3000X experiments), while the dendritic pattern persists for smaller strength gradients (1X to 30X experiments). Structurally confined channels are still able to traverse the width of the weak zone, and the tortuosity at this scale is a function of weak zone width and the random height field within the weak zone. For example, doubling the width of the 3000X weak zone will still produce a structurally confined drainage pattern, but the increase in weak zone width allows for less constriction at my scale of observation. As a result there is a greater range of tortuosity values with higher average tortuosity, despite the highest order channel still being confined to the weak zone (Figure 3.5, grey point, Figure 3.S1). Once this drainage pattern is established it will remain unchanged as the landscape approaches a steady state. The drainage network pattern reflects the orientation of weak zones associated with prominent structural features and as such could be an indicator of past or present tectonic strain.

3.6.1.2. Relief of Hillslopes

It is well recognized that rivers have the potential to control orogenic relief (e.g. Whipple and Tucker, 1999; Whipple et al., 2013) but their ability to limit relief is amplified by the presence of weak zones that introduce localized, relatively low channel slope corridors. Tabular weak zones have a regional effect on relief (Figure 3.4) and hillslope gradients (Figure 3.6). The effect on maximum relief is apparent even without a structurally confined high order channel (3X to 30X experiments). For examples when the highest order channel becomes structurally confined, any increase in relative strength difference

will have almost no progressive effect on maximum relief as the channel slope approaches zero and the weak zone essentially becomes an extension of the outlet boundary (Figures 3, 4, 60X to 3000X). Please see Supplemental Figure 3.1 to see the sensitivity of relief to 1) doubling weak zone width and 2) weak zones that do not intersect the outlet boundary.

Though I do not test strength-dependent nonlinear hillslope diffusion, it is instructive to explore a situation in which slope thresholds are set equal to the internal angle of friction of the substrate (Roering et al., 2001). For such a model, strong bedrock generally has an internal angle of friction equal to 35° (slope of 0.7), whereas highly fractured rock can be as low as 5° (slope of 8.75×10^{-2}) in extreme cases (Hoek and Brown, 1980; Hoek and Brown, 1997). The gouge unit in the 3000X experiment never obtains a slope that would exceed 5° under the chosen model conditions, while the intact bedrock unit does exceed 35° in locations where hillslope processes already dominate (Figure 3.6). The regions that would feel the influence of greater diffusivity appear to be limited to hillslopes for intact bedrock and therefore should not produce significantly different results within the scope of this paper.

3.6.2. Response Rate

The rate at which a landscape responds to a base-level perturbation is strongly sensitive to the magnitude and geometry of the crustal strength field. The simple relative comparison of knickpoint migration rate in Figure 3.7A shows that a landscape responds more quickly when crustal strength is reduced (the response time scales inversely with k_b and hence with $k_c C^{-1/2}$; Whipple and Tucker (1999)), but the local rate of knickpoint migration depends strongly on 1) the predictable, steady decrease of drainage area

upstream and 2) local variations in erodibility. The regional response rate to base-level perturbations is also highly sensitive to local weak zones (Figure 3.7B). I focus further discussion on effects caused by the applied strength field: local variations in erodibility.

Fluvial incision in the 60X to 3000X experiments produces channels that are confined to the width of the weak zone, and are flanked on either side by sharp strength gradients. The majority of the main channel is confined to the gouge unit, but the channel frequently crosses into the ultracataclasite unit, and occasionally into cataclasite (Figure 3.8E-H, 9E-H). Tortuosity generally increases, channel-wise erodibility fluctuations become more pervasive, and knickpoint migration rate decreases at the local and catchment scale as the strength gradient between gouge and intact bedrock reduces. The experimental results suggest that structurally confined channels should have comparably fast rates of knickpoint migration overall, but the local rate of knickpoint migration should vary as a function of the erodibility gradient. Because knickpoint migration is slowest in locations where the channel traverses a resistant unit, transient knickpoints are statistically more likely to be found in resistant units when observed in the field.

3.6.3. Stationary Knickpoints

Knickpoints are not necessarily transient, migratory features in natural landscapes and it can be difficult to interpret the possible migratory conditions of a knickpoint based on its morphology (Stock and Montgomery, 1999; Kirby et al., 2003; Crosby and Whipple, 2006; Kirby and Whipple, 2012; Whipple et al., 2013). However, based on my theoretical predictions it is possible to partially predict knickpoint morphology and migration rate if the strength field is well constrained. For my experiments with vertically continuous

strength fields, channel-wise transitions in erodibility create stationary knickpoints that persist as the landscape approaches steady state. The magnitude of the erodibility gradient and the widths of the damage zone units determines the relief of the knickpoint; however the magnitude must be large enough to generate the knickpoint, but not so large as to prevent the channel from incising across the gradient and confine drainage to the weaker unit (Figure 3.6). For example, the highest-order channel in the 3X experiment traverses the relatively small strength gradient and hosts stationary knickpoints, while the highest-order channel in the 3000X experiment is unable to cross the large strength gradient and becomes structurally confined.

The natural presence of these stationary features could cause confusion in the field, where the ability to determine whether a knickpoint is migrating is extremely limited over observational timescales (Crosby and Whipple, 2006; Whipple et al., 2013). However, researchers have been able to recognize transient and stationary knickpoints in the South Fork Eel River, California (Foster and Kelsey, 2012). Tabular weak zones create a situation in which large strength-induced knickpoints are not likely to exist because the interconnectedness of erodible bedrock does not require a structurally confined channel to cross extreme strength thresholds. Further still, weak zones associated with faulting can traverse different lithological units and mitigate the strength difference between them. The geometry of weak units can potentially explain why in the field, knickpoints based on lithology may be uncommon (e.g. Robl et al., 2008; Stüwe et al., 2008; Wagner et al., 2010; Wagner et al., 2011).

3.6.4. Lateral Shifting

Structurally confined channels can migrate laterally in response to the continuously shifting exposure of a weak zone, but the effect is strongly dependent on the dip of the weak zone, magnitude of the strength gradient, weak zone width, and geometric symmetry. My experiments underestimate lateral channel migration because they rely on a shifting exposure of the weak zone to stimulate lateral channel-shifting events rather than solving for lateral erosion in a channel. However, the model results are considered to be robust because lateral shifting occurs even without lateral channel erosion. Lateral shifting occurs as successive events of river capture as the weak zone exposure continues to migrate away from the incising channel at a rate controlled by erosion into the hanging wall (Figure 3.11, see supplemental videos). Channels begin to incise vertically into the strong footwall rather than migrate laterally with the weak zone exposure in cases where the strength gradient is reduced or the weak zone width is reduced.

Lateral shifting persists for asymmetric weak zones at lower strength gradients. This is probably due to the extreme strength gradient between gouge unit and intact bedrock on the footwall, which cannot be traversed as easily as the gradient between gouge and ultracataclasite (Figure 3.12C, Figure 3.13A, C). Unlike footwall tributaries, hanging wall tributaries must completely cross the strength gradient to reach the structurally confined channel. The resulting combination creates asymmetric valleys: the hanging wall valley side hosts tributaries with high tortuosity values and steep slopes, while the footwall tributaries are relatively straight and have slopes that are partially limited to the dip angle of the weak zone (Figure 3.12C).

3.6.5. Natural Examples of Structurally Confined Drainage

My numerical experiments have provided a number of testable predictions for determining strength controls on landscape, including 1) the presence of anomalously straight channels of high order with frequent low order, orthogonal tributaries; 2) the potential presence of small stationary knickpoints, 3) relatively fast transient knickpoint migration rates and response time in regions responding to base level perturbations, 4) reduced relief close to the drainage divide caused by low slope in structurally confined channels, and if the weak zone is dipping at a less than vertical angle, 5) asymmetric valleys with possible lateral channel migration. The only prediction that is mutually exclusive to strength heterogeneity is channel pattern. Effects on relief, knickpoint positioning, or response rate can also be a function of past changes in climate, tectonics, sedimentation, or glaciation, and their interpretation would require a great deal of additional information. For this reason I have chosen field examples where 1) the structural field is well mapped, 2) strength data exist, and 3) rivers appear to be anomalously straight and tend to correlate with weak zone strike. Several natural examples exist for structurally confined drainages. The examples listed in Table 1 and discussed below (Figure 3.14) host strength differences that span several orders of magnitude, varied width, and varied weak zone dip angle. Where necessary, the Hoek and Brown (1997) criterion was used to determine the relative strength difference for a field location.

Figure 3.14. Mean tortuosity values for natural examples. (A) Error bars represent two standard deviations. Natural examples include (B) Rivanna River, VA (37.861˚ N, -78.2633˚ W), (C) Shenandoah River, VA (38.9661˚ N, -78.2425˚ W), including (C1) the north fork, (C2) south fork, (C3) Passage Creek, and (C4) the section below the confluence, (D) Cottonwood Creek on the Eastern Kaibab Monocline, UT (37.3289˚ N, -111.8778˚ W), stars indicate the position of stationary knickpoints, (E) Big Rock Creek on the Punchbowl Fault, CA (34.405˚ N, -117.8212˚ W), (F) Bright Angel Gorge on the Bright Angel Fault, AZ (36.1737˚ N, -112.049˚ W), (G) Lone Pine Canyon on the San Andreas Fault, CA (34.303˚ N, -117.53˚ W), (H) Yoshino River partially following the Median Tectonic Line, Japan (33.9089˚ N, 134.0332˚ E), and the (I1) Salween, (I2) Mekong, and (I3) Yangtze Rivers (27.194˚ N, 99.2848˚ E) following the Bangong-Nujiang suture, Longmu Co-Shuang hu suture, and Jinsha suture, respectively (Hallet and Molnar, 2001a; Sol et al., 2007; Liu et al., 2011). (J) Stationary knickpoint where Passage Creek traverses resistant quartzite unit, and (K) another knickpoint where the Shenandoah River traverses another quartzite unit. (L) Satellite image of the Eastern Kaibab Monocline with Cottonwood Creek following the San Rafael Group (source: 37.3289˚ N, -111.8778˚ W, Google Earth, imagery date 5/30/2013, accessed 10/2/2014). (M-M') Transect taken across the monocline displays an asymmetric gorge.
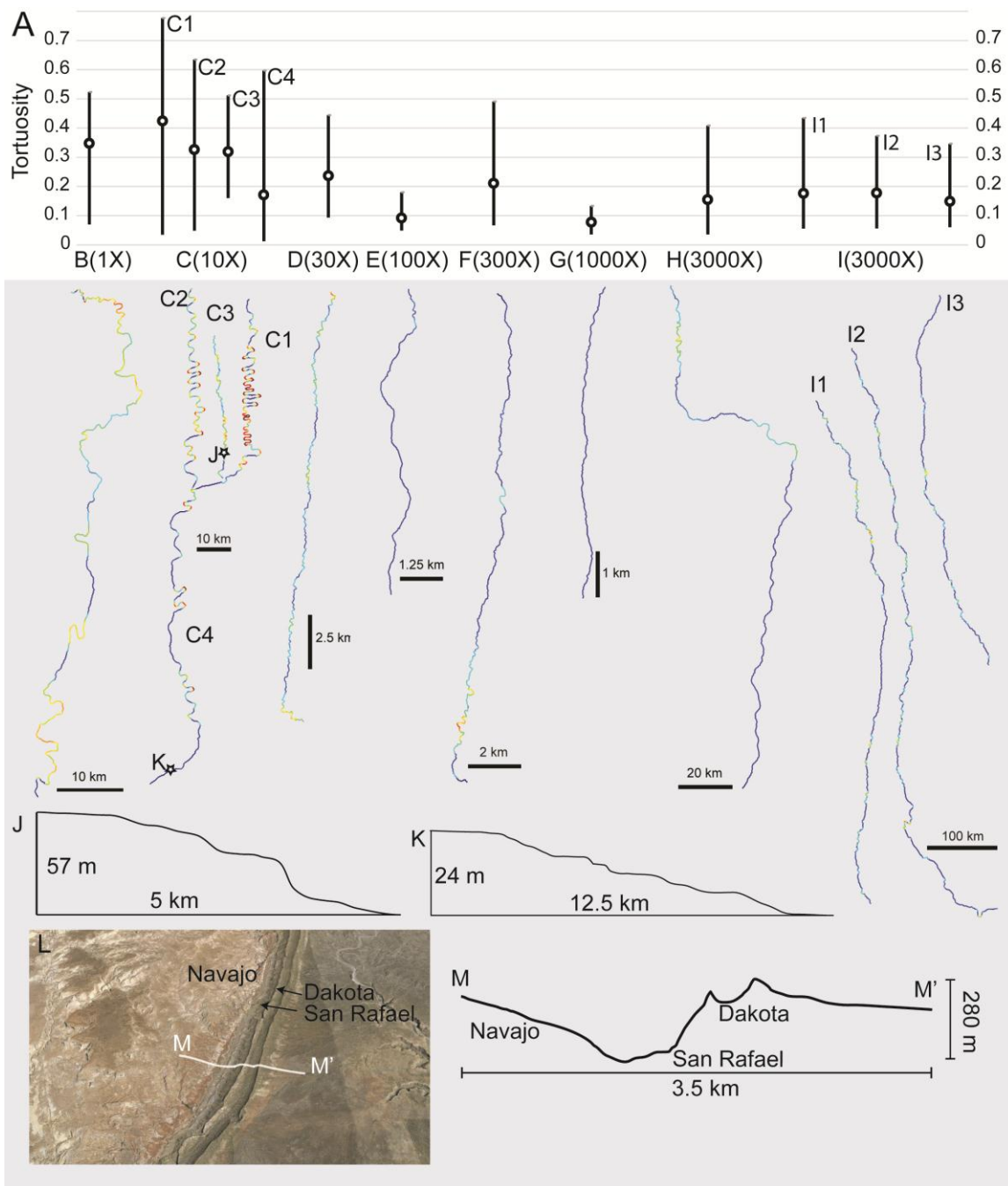
3.6.5.1. Homogeneous Example

The Rivanna River and adjacent tributaries near Palmyra, Virginia (Figure 3.1A) are part of a dendritic drainage network (Zernitz, 1932) in the Piedmont Province of the Eastern United States. This location is horizontally homogeneous in strength and there are no structural features that directly influence the drainage pattern (Figure 3.14A). The chosen section of river has an average tortuosity value of 0.35 with a wide range between 0.07 and 0.52, measured at a wavelength of 10 km. These tortuosity values are comparable to measurements taken for the 1X and 3X experiments (Figure 3.5) in which structural confinement is weak or nonexistent.

3.6.5.2. Low Relative Strength Factor Examples

The north fork of the Shenandoah River (Figure 3.14C1) is largely confined to the erodible shale of the Martinsburg Formation bound on either side by relatively resistant quartzite (Dicken et al., 2005). Large mean tortuosity values in the confined channel are associated with a foliation in the shale that is normal to the orientation of the valley, yet the overall orientation of the channel is valley-parallel (Hack and Young, 1959). A similar pattern can be seen in the south fork, where the Martinsburg Formation is also exposed (Figure 3.14C2). The drainage pattern of both forks of the Shenandoah reflect two different scales of structural confinement: strength variations caused by shale foliations control the spacing of meanders at sub-kilometer scales, while the thickness of the shale unit controls the kilometer scale drainage orientation. Tortuosity diminishes further downriver as the Shenandoah crosses into a weak limestone unit (Figure 3.14C4) (Dicken et al., 2005). Conversely, Passage Creek (Figure 3.14C3) is also confined to a sandstone-shale unit of

similar strength that is approximately the same width, but does not share the foliated structure of the Martinsburg Formation and subsequently hosts a much lower tortuosity value. There are two instances where the Shenandoah, or one of its tributaries, hosts a stationary knickpoint associated with crossing the quartzite units (black lines, Figure 3.14C). In both cases, channel profiles exhibit convexities similar to my experimental results (Figure 3.14J, K).

The Eastern Kaibab Monocline, located in southeastern Utah, is not associated with an exposed fault zone but does host shallowly dipping sedimentary units with varying erodibility, similar to some of the lower strength gradients featured in my numerical experiments. In this region the monocline dips at a maximum of 45° eastward, exposing resistant Navajo Sandstone, the erodible San Rafael Group of sandstones and shales, and resistant Dakota Sandstone (Babenroth and Strahler, 1945). Cottonwood Creek (Figure 3.14D) follows the exposed San Rafael Group for 15 miles as it flows south to the Paria River. The difference in erodibility between weak units in the San Rafael Group and the surrounding sandstone units is comparable to my 30X model example, resulting in 1) structural confinement of Cottonwood Creek in the erodible San Rafael Group, and 2) a highly asymmetric valley as influenced by the eastward dip of the monocline (Figure 3.14L,M). Tortuosity in Cottonwood Creek is relatively moderate but reaches maximum values to the north and south where it departs from the San Rafael Group (Figure 3.14D).

3.6.5.3. Moderate Relative Strength Factor Examples

Channels that follow the strike of the Punchbowl Fault in the San Gabriel Mountains of California, USA, display a low mean tortuosity value with minimal range

(Figure 3.14E). The Punchbowl Fault is an inactive shear zone of the San Andreas system that has become partially indurated at its core (Chester and Logan, 1986; Chester and Logan, 1987). The relative strength factor is low due to the cemented gouge unit, however the weak zone still hosts a confined channel.

The Bright Angel Gorge (Figure 3.14F) follows the strike of the Bright Angel Fault Zone, a collection of steeply dipping and tectonically inactive shear zones that trend northeast across the Grand Canyon in southwestern North America (Hodgson, 1961; Shoemaker et al., 1978). Motion on the fault dates back to Precambrian time, when the feature formed initially as a reverse fault. The Bright Angel Fault Zone was later reactivated as a normal fault in the Cenozoic, vertically displacing Paleozoic strata by as much as 60 m (Huntoon and Sears, 1975). Tortuosity values for the gorge average 0.21 for a 1 km wavelength.

3.6.5.4. High Relative Strength Factor Examples

The San Andreas Fault is a large active strike-slip fault system in California that has accommodated possibly over 300 miles of displacement over the past 20 million years (Crowell, 1962). There are many examples where the San Andreas Fault transects mountain ranges, creating anomalously straight channels with divides that expose loose fault scarps (Crowell, 1962). The active strand of the San Andreas Fault north of the San Gabriel Mountains in California, USA, hosts a ~200 m wide weak zone with an approximate 1000X strength difference between host rock and gouge (Rempe et al., 2013). Relief in the area around the damage zone is limited by the amount of vertical displacement associated with oblique collision along the bend of the San Andreas Fault (Lifton and

Chase, 1992; DiBiase et al., 2010). Tortuosity values from Lone Pine Canyon average 0.078.

A large section of the Yoshino River is structurally confined to the Median Tectonic Line in Southwest Japan. This section of the river hosts very few, long wavelength meanders represented by a minimal tortuosity. However, the river diverges from the Median Tectonic Line for a time, then eventually intersects a minor structural feature further up river. The relative strength difference between weak and resistant rock often exceeds 3000X in this region (Wibberley and Shimamoto, 2003; Faulkner et al., 2010). Similar to my example shown in Figure 3.14B, D, the river crosses resistant bedrock and connects with other structural features that parallel the Median Tectonic Line.

The Salween, Mekong, and Yangtze Rivers located in the Himalayan Eastern Syntaxis (Figure 3.14I, 1B) are three examples of structurally confined rivers in which active deformation plays a significant role in drainage morphology. Each river follows a north trending suture zone (Liu et al., 2011) associated with active tectonic deformation between India and South China, with approximately 2000 km of shortening north of India and an equivalent amount of right lateral shear displacement along the east (Hallet and Molnar, 2001b; Sol et al., 2007). The Salween, Mekong, and Yangtze River channels come within 70 km of one another and follow nearly parallel courses for almost 300 km. The mean tortuosity value from all three rivers is 0.168 and values range from 0.07 to 0.43 within two standard deviations, measured at a wavelength of 10 km. The topography in this region is not simply a product of differential strength but also of differential displacement. However, if it were simply a question of the latter, river patterns would be

deformed but not necessarily aligned with the weak zones, as can be clearly seen in this region.

3.6.5.5. Summary of Natural Examples

The examples of muted tortuosity from the Salween, Mekong, and Yangtze Rivers, Bright Angel Gorge, the Punchbowl Fault, and the San Andreas Fault are all comparable to the measurements taken for the structurally confined examples (Figure 3.5, 60X to 3000X experiments), in which mean tortuosity values are low and the range of values is narrow. Valley asymmetry on the Eastern Kaibab Monocline is comparable to my numerical predictions for a similar dip angle. High mean tortuosity in the north fork of the Shenandoah River opposes my hypothesis that structurally confined drainages tend to be straighter, however the increase in tortuosity is explained by shorter scale strength patterns with an orientation that opposes the larger scale orientation of the confining unit. Further still, the divergence of the Yoshino River and subsequent increase in tortuosity is associated with the orientation of inland structures relative to the flow outlet.

These examples have large implications for the scale-dependent controls that rock strength may have on topographic development and the significance of geometry and orientation of weak zones. My results suggest that drainage network patterns are strong indicators of the crustal strength field, and although the theory explored here grossly simplifies the physics associated with the development of these natural rivers, it nonetheless can help to explain the development of naturally occurring drainage network patterns.

Table 3.1. Natural examples of structurally confined drainages

Figure 3.14 letter, weak zone Name/location		Estimated strength difference	Weak zone width	Type of contact, condition	Tortuosity, length scale (km)	Weak zone dip, valley asymmetry
B	Rivanna R., VA	1X	N/A	Homogeneous	0.347, 10	N/A
C	Shenandoah R., VA					
C 1	North Fork	10X	4 km	Unconformity, fold belt, inactive	0.424, 4	N/A
C 2	South Fork	10X	4 km	Unconformity, fold belt, inactive	0.326, 4	
C 3	Passage Ck.	10X	3.5 km	Unconformity, fold belt, inactive	0.319, 4	N/A
C 4	Below confluence	10X	4 km	Unconformity, fold belt, inactive	0.171, 4	
D	Eastern Kaibab Monocline, UT	30X	300 m	Unconformity, some shear damage, inactive	0.237, 1	45˚
E	Punchbowl Fault, San Bernardino Mtns., CA	100X	100 m	Strike-Slip, partly indurated, inactive	0.092, 1	60-70˚
F	Bright Angel Gorge, AZ	300X	100 m	Normal, inactive	0.211, 1	70˚
G	San Andreas, San Gabriel Mtns., CA	1000X	200 m	Strike-Slip, active trace	0.078, 1	Steeply dipping
H	Median Tectonic Line, Japan	3000X	0.8 to >1 km	Oblique thrust, active	0.155, 10	Steeply dipping
I	Himalayan Eastern Syntaxis					
I 1	Salween R.	3000X	0.1 to >1 km	Oblique Strike-Slip, active	0.177, 10	Steeply dipping
I 2	Mekong R.	3000X	0.1 to >1 km	Oblique Strike-Slip, active	0.178, 10	Steeply dipping
I 3	Yangtze R.	3000X	0.1 to >1 km	Oblique Strike-Slip, active	0.149, 10	Steeply dipping

3.7. Chapter Conclusions

I use numerical experiments with a landscape evolution model to demonstrate the strong sensitivity of fluvial incision to the potentially extreme erodibility gradient between fault weak zones and the surrounding intact bedrock. The model calculations illustrate how patterns in the crustal strength field can play a dominant role in local fluvial erosion rates and consequently the development of fluvial network patterns. Fluvial incision can potentially be orders of magnitude faster within weak zones, as compared with incision rates for intact bedrock. The large incision rate difference leads to the formation of a valley along the strike of the weak zone, and confinement of the main channel to the weak zone structure. Structurally confined drainage takes the form of a straight, low tortuosity, high order channel with short, orthogonal tributaries of low order. In comparison, channels incising into homogeneous strength fields produce a dendritic, unconfined drainage pattern with high tortuosity values. Structurally confined channels occasionally cross the strength gradient represented by the weak zone units, leading to local variations in knickpoint migration rate and the development of stationary knickpoints. Structurally confined channels can migrate laterally if they incise into dipping weak zones with less than vertical dip. The influence of the strength field on drainage network patterns lessens as the erodibility gradient reduces between weak zone and intact bedrock, until the signal is completely removed in a homogeneous strength field.

CHAPTER 4

MODELING THE GENESIS AND TRANSPORT OF HETEROGENEOUS

GRAIN SIZE DISTRIBUTIONS IN A FAULT-DAMAGED LANDSCAPE

4.1. Chapter Abstract

I explore two ways in which the mechanical properties of rock potentially influence fluvial incision of rock and transport of sediments within a watershed: 1) rock erodibility is inversely proportional to rock strength, and 2) fracture density influences the initial grain sizes produced upon erosion. Fault weak zones show these effects particularly well because of the sharp strength and texture gradients associated with localized shear abrasion. A natural example of fault erosion is used to guide my calibration and use of a landscape evolution model. A suite of numerical experiments are used to study the sensitivity of river erosion and transport processes to variable degrees of rock weakening. In my numerical experiments, surface runoff is steered by the rapid erosion and transport of fault gouge, causing high order channels to become confined within the structure of fault weak zones. Erosion of adjacent, intact bedrock produces relatively coarser grained gravels that accumulate in the low relief of the eroded weak zone. The thickness and residence time of sediments stored in the weak zone depends on the degree of rock weakening, which determines the rock erodibility gradient and the sand and gravel texture gradient transported by runoff. As a consequence the frequency at which the weak zone is armored by bedload increases with greater weakening, causing the bedload to control local channel slope rather than the intermittently exposed bedrock. Conversely, small tributaries feeding into the weak zone are predominantly detachment-limited. The amplitude and frequency

of storm events also influence sediment storage by modulating the competence and capacity of accumulated runoff. The prevalence of features that impose strength and texture heterogeneity on the Earth's surface exert significant controls on the rates and patterns of erosion, and it will be important to recognize the role of heterogeneity in future quantitative studies of landscape evolution.

4.2. Introduction

Mechanical defects such as faults, joints, and fractures are commonplace in the brittle crust, and there is clear evidence that their existence and distribution influence rates and patterns of erosion. Some have argued that brittle failure is the first step in erosion and is therefore fundamental to all landscape evolution processes (e.g. Gilbert, 1877; Davis, 1899; Scheidegger, 1979; Scheidegger, 2001; Scheidegger, 2004; Molnar et al., 2007; Koons et al., 2012). Despite the scientific advances made by these arguments, there is still much left to be learned about the quantitative influence of rock mechanics on erosion rates and landscape evolution in general.

Mechanical defects influence surface processes in at least two ways. First, the presence of defects such as fractures and joints facilitates rock disaggregation and particle removal; greater defect frequency leads to smaller blocks that are more easily dislodged by various geomorphological processes (e.g. Molnar et al., 2007). Second, rock bodies with more closely spaced defects yield finer grains when disaggregated (e.g. Sammis et al., 1986); finer grains are more frequently transported by fluid- and gravity-driven processes (e.g. Gilbert, 1877; Davis, 1899). Defect spacing can vary dramatically in space. Often it reflects the inherited tectonic fabric of the landscape in question, and may ultimately lead

to the formation of structurally controlled drainage and topography (e.g. Koons et al., 2012). Roy et al. (2015) studied the first of these effects—that of varying rock resistance to disaggregation—and found theoretical support for the hypothesis that naturally occurring strength gradients have a strong influence on the development of drainage network patterns. More specifically, drainage network patterns tend to reflect the geometry of underlying active or inactive tectonic structures due to the more efficient erosion of pre-existing fault-weak zones, causing channels to become structurally confined. However, still little is known about the influence of mechanical failure on the texture of sediments, and hence whether variations in the size of sediment released by erosion of faulted rock are likely to have a significant influence on patterns of landscape evolution. It is not clear, for example, how the need to transport sediments with varying texture will influence the evolution of drainage network patterns.

Here I build on the results of Roy et al. (2015) and address the combined effects of rock strength and sediment texture by assuming that mechanical defects in bedrock take the form of fault weak zones, establishing a fracture density gradient that controls the heterogeneous distribution of both bedrock strength and initial sediment texture. Here I define texture as the ratio of median sand and gravel grain sizes. I integrate four previously published hypotheses into my models. These are: 1) fluvial erosion rate scales inversely with bulk-rock plastic strength (Sklar and Dietrich, 2001; Sklar and Dietrich, 2004), 2) the spacing of fractures and joints often exhibit power law scaling with implications for initial sediment texture upon erosion (Jébrak, 1997), 3) sediment transport rate scales inversely with grain diameter (Wilcock, 2001; Wilcock, 2005; Wilcock et al., 2009; Julien, 2010), and 4) the presence of sand enhances mobility of gravel, while the presence of gravel

hinders the mobility of sand (Wilcock, 2005). As part of the study, I explore how inclusion of mechanical heterogeneities influences the spatial distribution, texture, and residence times of alluvial sediments. My numerical results are meant to build field-testable theoretical predictions by studying the combined influence of mechanical defects using a combination of long-term detachment theory for bedrock incision and transport theory for sediment movement.

I begin to explore the problem of mechanical heterogeneity in landscape evolution first by studying a natural example of an eroding fault weak zone. I then incorporate field measurements of rock strength and fracture spacing into numerical landscape evolution models with 3D planar fault weak zones introduced as an initial condition. My first set of numerical experiments test the sensitivity of fluvial incision and transport to changes in relative strength difference between weak zone and intact rock, while my second set explores the sensitivity of incision and transport to variations in storm frequency and intensity. The planar weak zones in my models are meant to represent tectonically inactive structural features, but they could also potentially be used to represent other planar geologic features such as lithostratigraphic units, dikes, and sills that introduce local strength and texture gradients. However, it is advantageous to study the effects of fault weak zones over other lithological features because their presence introduces extremely sharp strength and texture gradients over a scale shared by channel width, their planar geometry is largely predictable or measurable in the field, and they are an extremely common and well documented structural feature (Sibson, 1977; Sammis and Biegel, 1989; Ben-Zion and Sammis, 2003a; Mooney et al., 2007).

4.3. A Natural Example of Fault Erosion: Lewis Pass Region, New Zealand

4.3.1. Geological Background

I have observed the processes I am modeling in the Lewis Pass region of the South Island of New Zealand, along a strand of the Fowlers Fault (Figure 4.1A) (Rattenbury et al., 2006). The Fowlers Fault is one of a series of strike-slip faults that make up the Marlborough Fault System, a component of the Australian/Pacific Plate boundary that runs through the South Island of New Zealand (Wilson et al., 2004). The Fowlers and associated faults cut through Torlesse greywacke (Rattenbury et al., 2006). I chose to study the fault weak zone adjacent to the Fowlers Fault (Figure 4.1C) because it is a relatively minor structure and thus preserves the features I am interested in. These features have been eroded or covered by sediments along the more developed fault zones. The weak zone is oriented to the northeast and dips steeply to the northwest, and it is best exposed near the saddle indicated in Figure 4.1B. The fault gouge unit (Figure 4.2A) is ~150 m wide and is flanked by a cataclasite unit to the southeast (Figure 4.2B, C) and a stronger unit of jointed greywacke with widely spaced anastomosing shear zones to the west (Figure 4.2C, D, E). The drainage network pattern in this region tends to follow the strike of the weak zone (Figure 4.1C, 4.2F).

4.3.2. Strength and Sediment Texture Summary

I estimated rock strength, using cohesion, and texture, using grain size, in the field. Cohesion was used as a proxy for rock resistance to detachment because cohesion is an easily measureable form of plastic yield strength and because of its important role in
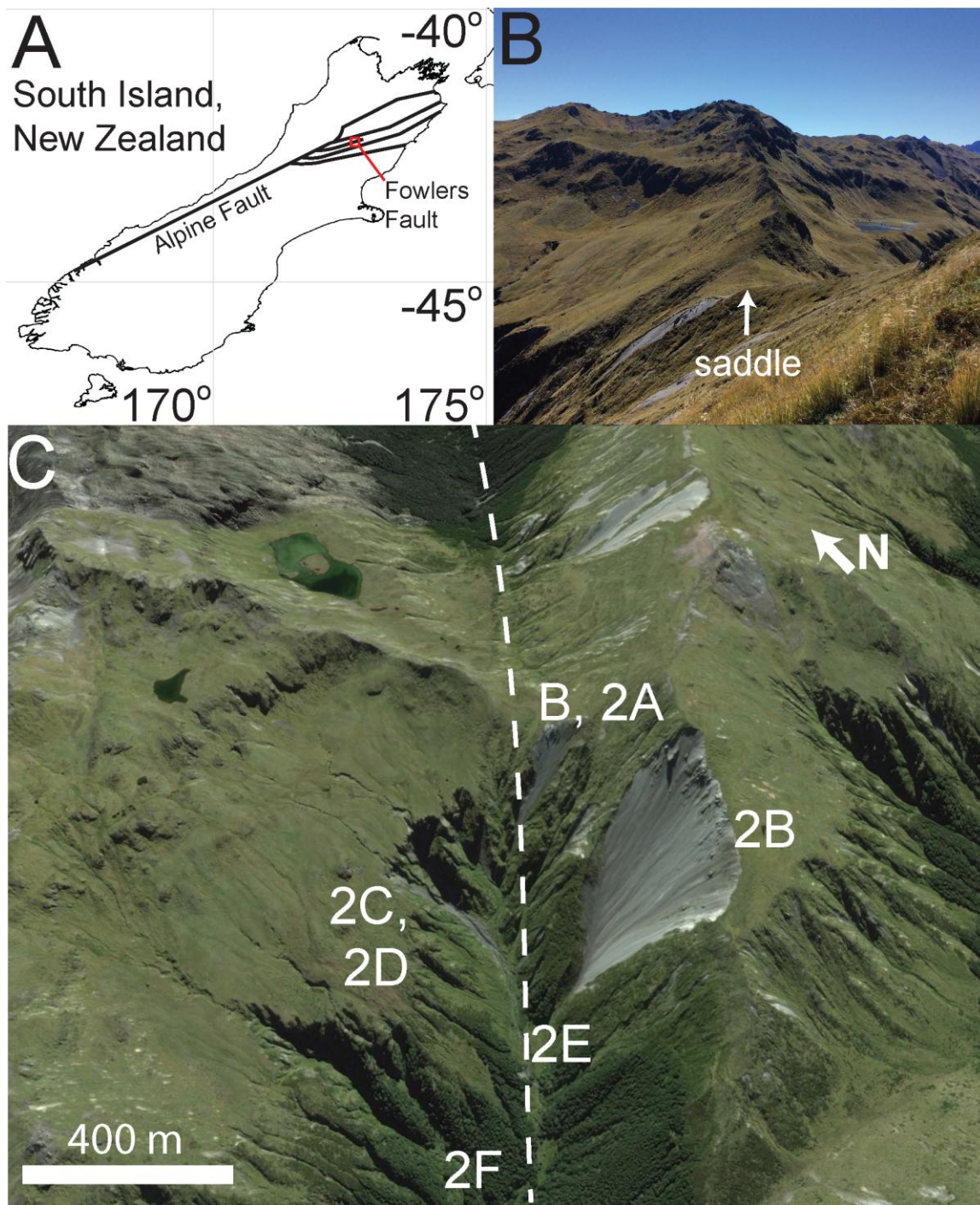
Figure 4.1. Henry Saddle field site. (A) Reference map. Square indicates Lewis pass region, South Island New Zealand. Lines indicate trend of major tectonic structures. (B) Weak zone is exposed along a saddle. (C) Local channel follows strike of weak zone.
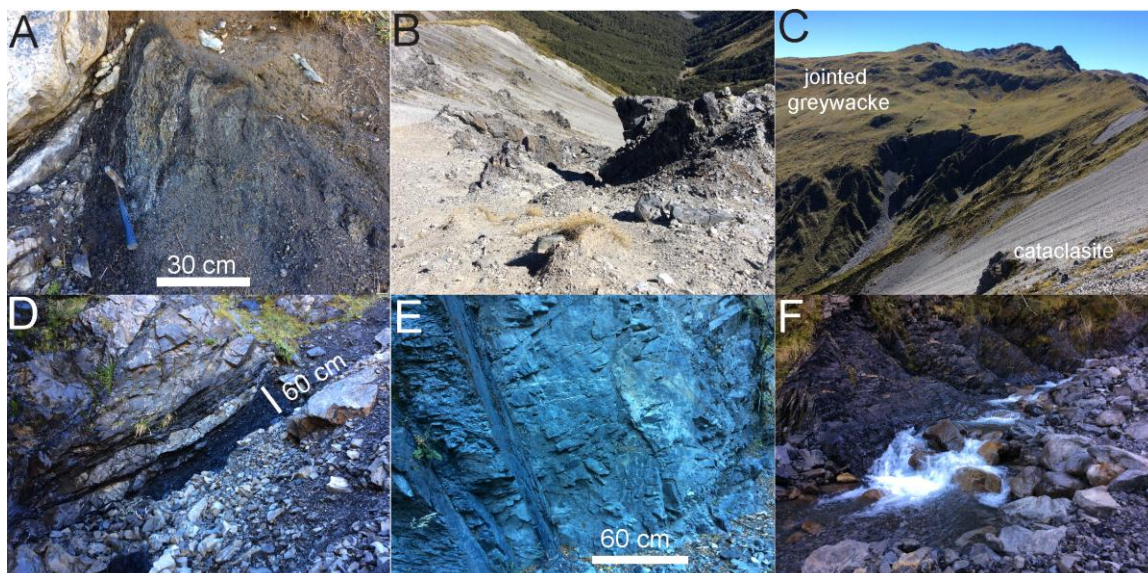
Figure 4.2. Field photos. (A) Gouge unit. The valley walls are composed of cataclasite (B, C), a relatively weak bedrock unit, and jointed greywacke (C, D, E), a relatively strong bedrock unit that produces coarse gravel and boulders upon erosion. Further downchannel the structure is partially buried in coarse alluvium (F), with an average grain size much larger than that of eroded fault gouge.

the Mohr-Coulomb failure criterion (Bieniawski, 1974; Brace and Kohlstedt, 1980; Hoek and Brown, 1980; Hoek and Brown, 1997; Enlow and Koons, 1998; Schellart, 2000). Cohesion was estimated using the Hoek-Brown criterion (Hoek and Brown, 1980; Hoek and Brown, 1997), based on measurements of the Geological Strength Index (GSI), rock type, and an estimate of uniaxial compressive strength (UCS). GSI is a 0-100 scale measure of fracture density and quality with a versatile range that has proven useful as a field estimate of rock strength (Hoek, 1999; Read et al., 2000; Brideau et al., 2006). Obtaining a truly representative estimation of rock type and UCS requires a rock sample size that is larger than the average spacing of fractures that allow the rock pieces to slide and rotate under different stress conditions (Hoek and Brown, 1997). The rock type parameter was taken from Read et al. (2000).

Results are displayed in Table 4.1. Fault gouge is by far the weakest bedrock unit, with a GSI range of 5-15. Gouge is so thoroughly disintegrated and chemically altered that

it often has the consistency of clayey soil. Fracture surfaces are coated in soft, wet clay.

The surrounding cataclasite is also relatively weak, with a GSI range of 20-40. However

fractures in the cataclasite tend to be dry, relatively rough, and uncoated, with little

evidence for shearing or alteration except from landsliding (Figure 4.2B, C). The jointed

greywacke to the northwest (Figure 4.2C) has a bulk GSI range of 55-80 (Figure 4.2E),

punctuated by highly localized, sub-meter scale shear zones with GSI range of 15-25

(Figure 4.2D). This rock unit provides the steepest relief in the region (Figure 4.2C).

Table 4.1. Field characterization of the four rock types including the Hoek-Brown parameters used to estimate cohesion and median grain size.

Sample	GSI	UCS estimate	Rock type parameter	Cohesion (Pa)	Average joint spacing range (mm)	Median grain size (mm)[*]
Jointed greywacke	55-80	100-250	12	2.5×10^7-8.5×10^6	100-500	189 (60,318) Skew: 3.3
Cataclasite	20-40	5-25	12	1.0×10^5-9.2×10^5	5-100	8.8 (1.9,18.9) Skew: 2.6
Gouge	5-15	0.25-1	12	2.8×10^3-1.7×10^4	<1	5.1 (0.3,8) Skew: 8.2
Downstream alluvium	-	-	-	-	-	19 (3.7,35) Skew: 3.8

[*]Values in parentheses represent one standard deviation below and above the mean value, respectively. The grain size skewness calculated here is the moment coefficient of skewness (Bulmer, 2012).

I used field GSI measurements to create a map of rock strength in the Henry Saddle

region (Figure 4.3A) in order to explore the potential controls of rock strength on slope

(Figure 4.3B) and drainage area (Figure 4.3C). The relationship between slope and

drainage area differs significantly between jointed greywacke and the fault weak zone

(Figure 4.3D). Slope histogram plots (Figure 4.3E) display a significant division in median

slope between the two rock units. These cursory results suggest that natural levels of rock

damage can exert a sufficiently strong influence on landscape evolution to be reflected in the slope-area relationship.
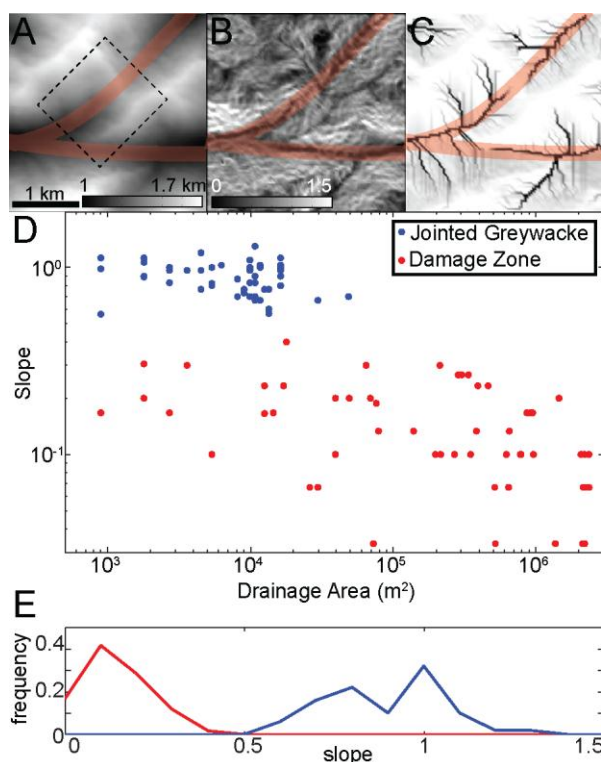
Figure 4.3. Data from Henry Saddle. (A) Digital elevation map (DEM), red areas indicate approximate extent of fault-damaged rock based on field GSI measurements. Black dashed line indicates region of satellite imagery in Figure 4.1C. (B) Slope and (C) drainage area data from the DEM. (D) Slope versus area plot. Points represent locations in jointed greywacke (blue) and weak zone (red). (E) Slope histogram for weak zone (red) and jointed greywacke (blue). Vertical axis is the slope frequency normalized by total sample size.

Grain sizes were measured from loose material that showed evidence for imminent separation from the fresh rock surface. I estimated the median grain size by measuring the intermediate length axis of randomly chosen grains (Wolman, 1954), and use it only for relative comparison between rock units, and between the average joint spacing range for each rock unit. This method of grain size measurement is subject to uncertainty, but I attempted to keep methods consistent between rock types. Fault gouge produces predominantly fine grained sediments upon erosion, whereas the average grain size for the

cataclasite is greater, and the average size for the jointed greywacke is much greater (Table 4.1).

4.3.3. Distribution of Alluvium along Channel Reach

The gouge unit is predominantly covered by alluvium in all locations except at the drainage divide and intermittent locations along the reach of the channel. The texture of the downstream alluvium is on average much coarser than the sediment produced from eroding the underlying fault gouge, but less coarse than boulders and cobbles that come from the jointed bedrock. The valley formed along the weak fault zone acts as storage for nearby sources of sediment. These field observations suggest that rock strength and fracture spacing can influence the drainage network pattern and the distribution of sediment. To gain a better understanding of this relation I require methods for scaling the mechanical properties of rock to fluvial processes of erosion and transport, as well as a robust sensitivity analysis to determine the significance of rock damage. The methods I use are described below.

4.4. Methods

4.4.1. Surface Dynamics Model

I use the Channel-Hillslope Integrated Landscape Development (CHILD) model (Tucker et al., 2001) to compute the erosion of bedrock and transport of sediment by fluvial and hillslope processes in a hypothetical terrain underlain by fault-damaged rocks. The landscape surface is divided into irregularly discretized elements, each representative of a small equant area and connected to adjacent elements by a Delaunay triangulation (Lee and

Schachter, 1980). A steepest descent routing algorithm is used to calculate the spatial pattern of surface runoff accumulation over the discretized landscape surface. I use a general theory for mass continuity

$$\frac{\partial h}{\partial t} = F + H + U \qquad (4.1.)$$

where $\frac{\partial h}{\partial t}$ is time rate of change of land surface elevation (L T^{-1}), F is the fluvial component of erosion or aggradation, H is the hillslope processes component of erosion or aggradation, and U represents all factors contributing to uplift or depression of the surface relative to baselevel. I use a combined rule set for the fluvial component to account for the occurrence of both bedrock detachment and sediment transport conditions in channels. Specifically, F is limited by either the detachment competence and capacity of the flow to detach material, D_c, or by the spatial gradient in sediment transport capacity:

$$F = max(-D_c, \nabla q_c) \qquad (4.2.)$$

where D_c is the detachment capacity (dimensions of L T^{-1}), q_c is the total volumetric sediment-transport capacity per unit width for the available surface grain size mix (dimensions of L^2 T^{-1}), and max is the maximum function. Equation 4.2 expresses the assumption that bedrock detachment occurs where a channel's capacity to mobilize and transport sediments exceeds the local sediment supply; otherwise, the rate of erosion or deposition is set by spatial gradients in sediment transport capacity, which itself depends on the particular grain size mixture on the bed (Gasparini et al., 2004). This approach means that a particular location within the model may be either detachment-limited or transport-limited, and may change behavior over time in response to changes in topography, water discharge, sediment supply, and surface grain size.

4.4.1.1. Bedrock River Incision

Bedrock channels frequently occur in high relief topography (Howard and Kerby, 1983; Sklar and Dietrich, 1994; Tucker and Slingerland, 1996; Stock et al., 2005; Attal et al., 2008; Attal et al., 2011). I approximate the physics that control the rate of mechanical wear of bedrock by assuming that fluvial detachment capacity scales with unit stream power (Seidl and Dietrich, 1992; Howard et al., 1994; Stock and Montgomery, 1999; Whipple and Tucker, 1999; Tucker et al., 2001; Hancock and Anderson, 2002; Whipple, 2002; Whipple, 2004; Whittaker et al., 2007; Yanites et al., 2010; Attal et al., 2011)

$$D_c = -k_{b(x,y,z)}\omega \tag{4.3.}$$

where the fluvial contribution to erosion rate D_c any point on a bedrock surface depends on spatially variable erodibility $k_{b(x,y,z)}$, stream power per unit width ω, and rock uplift rate. Note that the detachability of alluvium is assumed to be effectively infinite, while that of bedrock varies in space as described below. I assume that the average rate of channel-bed incision is proportional to stream power per unit width ω at every element

$$\omega = \gamma \left(\frac{Q}{W}\right) S \tag{4.4.}$$

where γ is the unit weight of water (9800 kg m^{-2} s^{-2}), Q is water discharge, W is channel width, and S is channel slope. Channel width W is calculated using the empirical method (Leopold and Maddock, 1953)

$$W = k_w Q^b \tag{4.5.}$$

where b is the width-discharge exponent, here given a value of 0.5, and k_w is the width-discharge coefficient, here given a value of 10 s$^{0.5}$ m$^{-0.5}$.

4.4.1.2. Fluvial Sediment Transport

Bedrock incision produces sediments. The texture of the newly produced sediments can depend on the bedrock unit that has been eroded, as discussed previously. When sediment supply exceeds the capacity or competence of flow, bedrock becomes covered by accumulating sediments (Wilcock et al., 2009). Alluvial channels frequently occur within sedimentary basins and in regions with low relief topography (Tucker and Slingerland, 1996). I use a pair of sediment carrying capacity equations developed by Gasparini et al. (1999; 2004) for transport-limited alluvial channels. The transport model is based on the work of Wilcock (2001), who developed sediment transport laws for sand and gravel mixtures from field and flume data (Wilcock, 1998). The median sand and gravel grain sizes are used to represent transport for the full distribution of grain sizes. The transport capacities for each of these two size components are given by:

$$Q_{sg} = k f_g A^{0.95} S^{1.05} \left[1 - \frac{\tau_{cg}}{\rho g} n^{-0.6} P A^{-0.3} S^{-0.7} \right]^{4.5} \tag{4.6.}$$

$$Q_{ss} = k f_s A^{0.95} S^{1.05} \left[1 - \frac{\tau_{cs}^{0.5}}{(\rho g)^{0.5}} n^{-0.3} P A^{-0.15} S^{-0.35} \right]^{4.5} \tag{4.7.}$$

$$k = \frac{11.2 k_w^{0.1} P^{0.95} g^{0.5} n^{0.9}}{(s-1)g} \tag{4.8.}$$

where Q_{sg} and Q_{ss} are sediment carrying capacity for gravel and sand, respectively (dimensions of L^3 T^{-1}), f_g and f_s are the fraction of gravel and sand, respectively, P is runoff rate, A is drainage area, n is Manning's roughness coefficient (here given a value of 0.03), ρ is water density, g is gravitational acceleration, s is the specific gravity of the sediment, and τ_{cg} and τ_{cs} are critical shear stresses for gravel and sand, respectively.

The critical shear stresses for sand and gravel depend on grain size and the fraction of sand present in the bed sediment. The critical shear stress τ_c is calculated using a nondimensional reference shear stress τ_r^*

$$\tau_c = \tau_r^*(\rho_a - \rho_w)gD\sin(\alpha) \qquad (4.9.)$$

Where ρ_a is the density of sediment grains, ρ_w is the density of water, D is the grain diameter, and α is the bed friction angle. The value of τ_r^* depends on f_s, the fraction of sand present (Figure 4.4). Generally speaking, the presence of sand enhances the mobility of gravel, while the presence of gravel hinders the mobility of sand (Wilcock, 1998; Gasparini et al., 1999; Gasparini et al., 2004). If sand makes up less than one-tenth of the alluvium, gravel creates an interlocking framework and hinders the transport of both grain sizes. Sand mobility therefore becomes a function of gravel mobility. The gravel framework becomes less influential for the range $0.1 < f_s < 0.4$, where a greater abundance of sand supports a matrix-dominated alluvium. For $f_s > 0.4$, the alluvium is largely sand-matrix dominated and there is a significant decrease in critical shear stress for both sand and gravel (Wilcock, 1998; Wilcock, 2001).

The mass conservation equation (Equation 4.1) is solved on a Voronoi/Delaunay grid using a finite-volume method (Tucker et al., 2001; Tucker and Hancock, 2010). For model cells in which the detachment capacity is greater than the local excess transport capacity, rate of change of local height depends on the difference between incoming sediment and the capacity to transport sediments

$$\nabla q_c = \frac{\sum_{i=1}^2 Q_{si}^{in} - \sum_{i=1}^2 Q_{si}^{out}}{a} \qquad (4.10.)$$

where $\sum_{i=1}^2 Q_{si}^{in}$ (L^3 T^{-1}) is the sum of all gravel and sand discharge rates coming into the element, $\sum_{i=1}^2 Q_{si}^{out}$ (L^3 T^{-1}) is the sum of all gravel and sand discharge rates leaving the

element, i varies from 1 to 2 representing the two grain sizes, and a is the element area. Erosion and deposition are calculated for each individual grain size, and sediment-transport divergence is calculated using Equation 4.10 and the proportions of the two size classes in the active layer. I employ the same active layer configuration as Gasparini et al. (2004) to measure bedload texture.
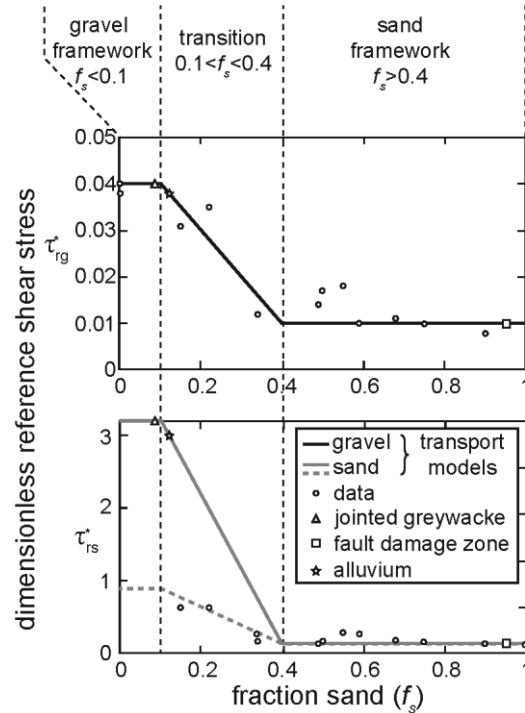
Figure 4.4. Dimensionless reference shear stress for gravel (top) and sand (bottom) (modified from Gasparini et al., 2004). Circles represent data from Wilcock (1998). Lines represent the transport model designed by Wilcock (2001) and adapted for stream power models by Gasparini et al. (1999). Dashed black lines separate zones dominated by gravel framework, sand-matrix, and the transition between the two. When $f_s < 0.1$, the dimensionless reference shear stress for sand $\tau_{rs}^* = \left(0.8\,D_g/D_s\right)\tau_{rg}^*$, where D_g is gravel diameter, D_s is sand diameter, and τ_{rg}^* is the dimensionless reference shear stress for gravel. This means that τ_{rs}^* in the range $f_s < 0.1$ will vary as a function of grain size ratio. All other dimensionless reference shear stress values are independent of grain size. The solid grey line shows the sand transport model used in this paper; it is based on my choice of grain sizes. The dashed grey line is from Gasparini et al. (1999) and follows the experimental data of Wilcock (1998), who used a smaller grain size ratio. Triangle, square, and star represent jointed greywacke, fault weak zone, and alluvium units, respectively, described previously and explored analytically later in this chapter.

4.4.1.3. Additional Parameters

For the sake of simplicity and because of my focused interest in the fluvial regime I approximate natural hillslope processes by a linear diffusion equation

$$H = k_d \nabla^2 h \qquad (4.11.)$$

where k_d is a creep coefficient for alluvium (regolith) with a value of 10^{-3} m^2 a^{-1} and $\nabla^2 h$ is hillslope curvature. There is no soil-creep transport of bedrock, and creep occurs only in locations where alluvium thickness is greater than zero.

The tectonic component of Equation 4.1

$$U = V_z + V_h \nabla h \qquad (4.12.)$$

is the sum of vertical rock motion relative to baselevel, V_z, and lateral topographic advection, $V_h \nabla h$, which I assume here to be negligible. A steady, uniform rate of rock uplift relative to baselevel, 0.1 mm a^{-1}, is used in order to represent a gently rising and completely exposed crustal basement. Sub-meter random noise is applied to the initial model relief in order to stimulate the development of a dendritic drainage pattern that strongly contrasts with the expected drainage pattern influenced by weak-zone erosion. Because the focus here is on erosion of inactive weak zones, none of the modeled weak zones allow for slip or further weakening.

4.4.2. Erodibility and Climatic Parameters

4.4.2.1. Erodibility

I require erodibility and texture values for my landscape evolution models. The parameters I use are based on measurements from naturally occurring fault weak zones such as the one described previously and from the efforts of others (Thomson, 1993;

Faulkner et al., 2003; Lockner et al., 2009; Faulkner et al., 2010; Mitchell et al., 2011) (Figure 4.5A, B). I assume that bedrock anelastic strength is inversely proportional to erodibility (Sklar and Dietrich, 2001; Sklar and Dietrich, 2004) and use the cohesive strength-erodibility relation applied by Roy et al. (2015) and adapted from Hanson and Simon (2001)

$$k_{b(x,y,z)} = k_c C_{(x,y,z)}^{-1/2}$$ (4.13.)

where C is cohesion and k_c is a coefficient equal to 0.2 with units $m^{1/2}$ s $kg^{-1/2}$. Similar assumptions have been made for the erosion of cohesive soils (Mirtskhoulava, 1966; Mirtskhoulava, 1991; Hanson and Simon, 2001) in attempts to link the mechanical properties of the soils to erosion rates.

4.4.2.2. Texture

Brittle failure governs the initial sediment texture that is introduced by the erosion of bedrock (Molnar et al., 2007). Shear abrasion and tectonically inherited fractures are both potentially capable of generating PSDs that can be fit to a power law curve with an inverse proportionality between grain size and the cumulative abundance of grains (Sammis et al., 1986; Sammis and Biegel, 1989; Blenkinsop, 1991; Jébrak, 1997; Bonnet et al., 2001; Roy et al., 2012)

$$N_{\geq r} = kr^{-D}$$ (4.14.)

where $N_{\geq r}$ is the number of grains with median radius $\geq r$, k is equal to $N_{\geq 1}$, and D is an exponent that determines the scaling of PSDs. A strong argument for power law scaling of PSDs produced by the intersection of fractures is the lack of scale dependency in fracture growth processes above the molecular level (Sornette and Davy, 1991; Bonnet et al., 2001; Saether and Ta'asan, 2004). The exponent D can vary substantially between mechanisms
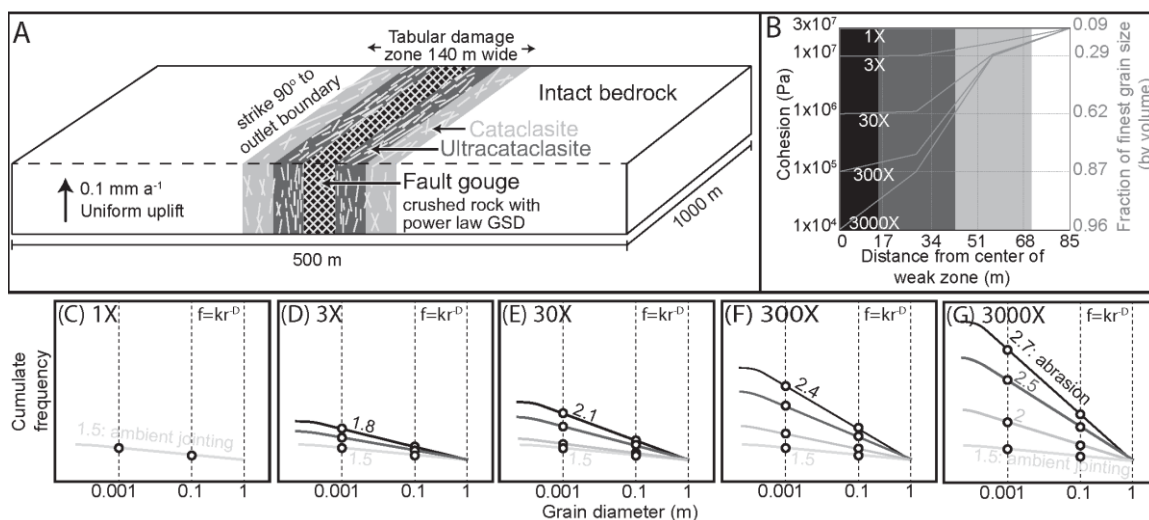
Figure 4.5. Schematic of the model geometry used for strength and texture sensitivity analysis. (A) The weak zone dips vertically and strikes orthogonal to the outlet boundary (dashed boundary). The strength field is divided into four distinct units to create a symmetric strength gradient. From strongest to weakest the units are intact bedrock, cataclasite, ultracataclasite, and gouge. (B) Plot of cohesion versus fault width to represent the different modeled strength gradients. Colors represent the different weak zone units in (A). Erodibility values based on Equation 4.13 are displayed on the right-hand axis for reference, and sediment texture data are shown on the right hand axis. Five different strength gradients are used for model set 1. I refer to the magnitude difference between the intact bedrock and the gouge unit in the weak zone to differentiate each strength gradient. Cases range from control, in which no weak zone exists and all bedrock has a uniform cohesion of 30 MPa, to 3000X, in which the gouge unit has a cohesion reduced by 3000X, from 30 MPa to 10 kPa. The other weak zone units also reduce in cohesion to maintain the common gradient pattern. Also included are PSDs for the (C) control, (D) 3X, (E) 30X, (F) 300X, and (G) 3000X experiments. Ambient tectonic jointing is the primary fragmentation mechanism in intact rock, which produces a relatively low D value and relatively high proportion of coarse grains by volume. From 3X to 3000X the degree of fragmentation is increased and the separation of D values between intact bedrock and gouge becomes more significant. Shear abrasion is the dominant fragmentation mechanism in gouge and the increase in D value represents an increase in the number of shear abrasion events that previously damaged the bedrock. The two circles represent the two grain sizes used to represent the PSDs in the sand-gravel transport model.

and the number of fragmentation events (Sammis et al., 1986; Blenkinsop, 1991; Jébrak, 1997), and can be used to diagnose the fragmentation mechanism (Jébrak, 1997; Barnett, 2004; Roy et al., 2012).

For example, almost all rocks with no deformation history exhibit a low ambient fracture density associated with a possible combination of tectonically inherited fractures, exfoliation jointing, and bedding planes (Molnar et al., 2007). Infrequent fracture intersections are characterized by a relatively small scaling exponent D, reflecting a slight preference for small grains at the expense of fractured larger grains. Conversely, frequent shear abrasion events in fault weak zones drive grain size reduction and increase the cumulate frequency of finer grains at the expense of disintegrating coarse grains. The degree of grain size reduction increases significantly within meters from the ambient fracture density to the core of a fault weak zone (Ben-Zion and Sammis, 2003b). Localized shear abrasion increases fracture density and the scaling exponent D with closer proximity to the primary slip surface, until the ambient fracture density signal is no longer discernable from the more pervasive shear abrasion mechanism (Figure 4.5C-G).

The sediment transport model requires these power law PSDs to be represented by one population of sand and gravel sized grains each. The two grain sizes should both properly represent the transportability of the entire distribution and therefore should have significantly different diameters while still representing two abundant grain sizes. The cumulate frequency of both grain sizes are calculated using Equation 4.14, and then the raw number of grains of each size is calculated by subtracting the number of grains larger than the chosen grain size. Sand and gravel volumetric fractions are then calculated, assuming all grains are spherical

$$V = \frac{4}{3}\pi r^3 (N_{\geq r} - N_{\geq r+b}) \tag{4.15.}$$

$$f_s = \frac{V_s}{V_s + V_g} \tag{4.16.}$$

where b is the binning interval for r and V_s and V_g are the volumes of sand and gravel,

respectively. These data are used to determine the volumetric ratio of sand to gravel sized

grains for use in the sand-gravel sediment transport model. For the purposes of my

experiments, sand and gravel diameters are 1 mm and 100 mm, respectively, and the

binning interval is 0.1 mm. The binning interval is necessary to make sure that my volume

calculation for the sand grain size does not include the cumulate volume of grain sizes

represented by gravel.

4.4.2.3. Storms

Discharge is calculated from the product of runoff rate and local contributing

drainage area. Drainage area in turn is determined using a single-direction downslope

routing algorithm (Tucker et al., 2001; Tucker and Hancock, 2010). Discharge rates are fed

by a temporally stochastic distribution of storm events associated with a rainfall intensity,

a storm duration, and an inter-storm duration chosen at random from exponential

probability distributions (Tucker and Bras, 2000; Sólyom and Tucker, 2004). Due to the

large gap between climatic and geomorphic time scales, storm and interstorm durations are

magnified such that average event spacing is 1000 years; this approach preserves the

frequency distribution of discharge while improving computational efficiency (Tucker et

al., 2001). I set mean annual precipitation for my main experiments to 1 m a^{-1} and assume

that storm events occur 10% of the time on average in order to replicate the typical climate

around Henry Saddle (Tomlinson and Sansom, 1994). The experiments must approach a

steady state elevation condition before I conduct my sensitivity analysis. The use of storm

events causes the steady state mean elevation to fluctuate within a narrow range (Figure

4.6). Due to these frequent storm-induced fluctuations, figures representing sediment texture, thickness, and cover are mean values taken after the model has stabilized within that narrow range of mean elevation. Sediment transport rates are highly sensitive to the frequency and magnitude of storm events (Tucker and Bras, 2000; Sólyom and Tucker, 2004; Tucker, 2004; Lague et al., 2005), however I choose to include my storm sensitivity analysis as Supplementary Material to better focus my discussion on the main objectives of this paper.
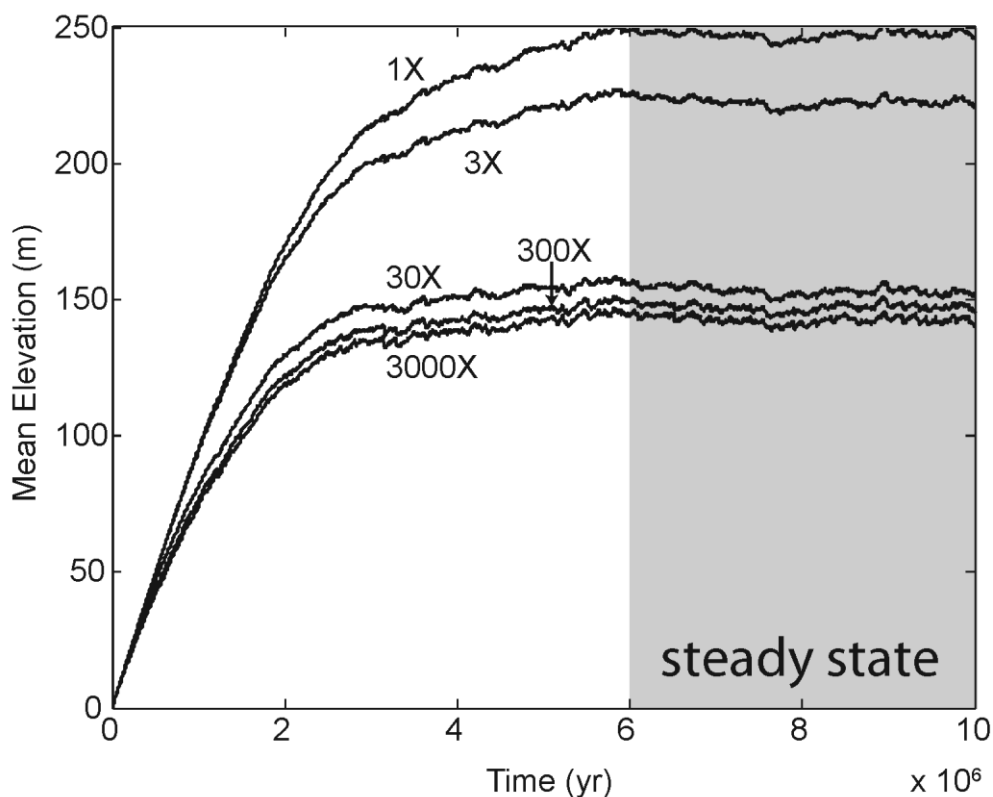
Figure 4.6. Plot of mean elevation over time for the five experiments. All experiments approach a condition in which mean height varies only slightly over time, which I interpret as a steady state condition (grey region). The model data displayed in Figure 4.7 (except elevation) are averaged over the steady state time interval.

4.4.3. Predicting Landscape Response

4.4.3.1. Alluvium Experiments

In this section I use the fluvial incision and transport equations described above to predict drainage network geometry and the spatial patterns of sediment thickness and texture as a channel traverses heterogeneous distributions of rock strength and texture. First, consider a simpler comparison between two uniformly textured alluvial substrates with no underlying bedrock: one with a texture resembling the coarse grained material produced upon the erosion of jointed greywacke in Section 4.2 (9% 1 mm sand, 91% 100 mm gravel), and the other with a texture resembling the eroded fault gouge (95% 1 mm sand, 5% 100 mm gravel). I use Equations 4.6, 4.7, and 4.10 in a 1D version of CHILD to determine channel slope and surface texture under the steady state condition of uniform and constant erosion rate into alluvium with infinite depth exposed by constant uplift rate. The 1D model represents a river longitudinal profile along which the erosion rate is steady and uniform, and the discharge increases linearly downstream.

With a uniform alluvial bed, the model predicts an approximately 16 times contrast in channel gradient between profiles developed on coarse (Figure 4.7a, red line) and fine sediments (Figure 4.7a, green line). Next, consider a channel that crosses a divide between upstream coarse alluvium and downstream fine alluvium (Figure 4.7a, blue line). Under these conditions, the texture difference causes a transition in slope, but it occurs further downstream. The channel profile above this slope transition reflects the profile of the coarse alluvium model, while the downstream slope is similar to the fine grained alluvium model. Much of the fine textured substrate is buried by transport of upstream coarse alluvium. This reflects adjustment of size fractions in the active layer to allow transport of

both fractions at the rate at which they are supplied (Gasparini et al., 1999; Gasparini et al., 2004).
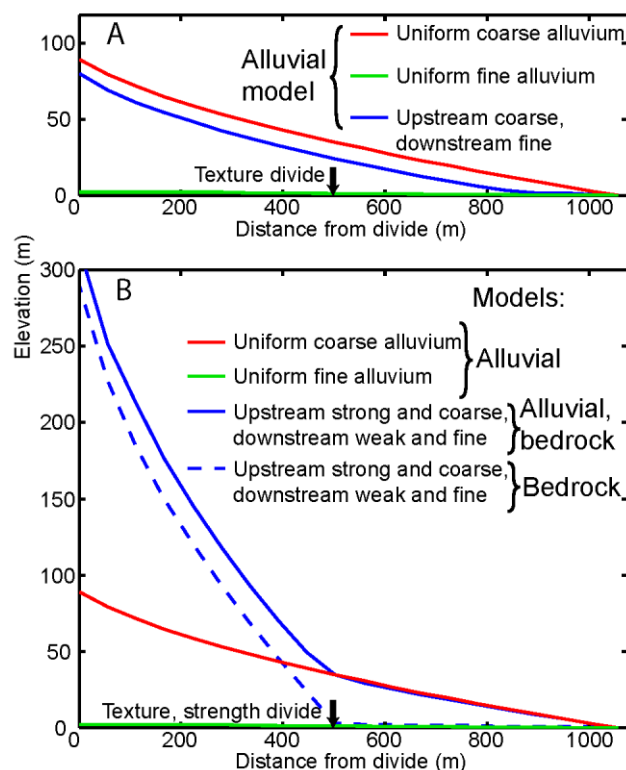
Figure 4.7. Channel profiles. (A) 1D alluvial models. Red and green lines: uniform coarse and fine alluvium substrates, respectively. Blue line: channel crosses coarse alluvium upstream and fine alluvium downstream. Location of the texture transition is indicated by the black arrow. (B) Channel profiles for 1D alluvial, bedrock, and combined fluvial erosion models. Dashed blue line: detachment-limited model in which channel traverses strong upstream bedrock and weak downstream bedrock. Solid blue line: mixed bedrock-alluvial fluvial incision and transport rules; channel traverses strong, coarse-textured bedrock upstream and weak, fine-textured bedrock downstream.

4.4.3.2. Bedrock and Mixed Bedrock-Alluvium Experiments

Now consider an experiment in which I assume the entire channel profile forms by fluvial incision into bedrock, and erosion is described exclusively by Equations 4.3 and 4.13. The channel is divided into strong jointed greywacke (1.7×10^7 Pa) upstream and weak fault gouge (9.9×10^3 Pa) downstream. Under these conditions, there is an approximately 42 times difference in slope between the two rock units, occurring at the strength divide

(Figure 4.7b, dashed blue line). Finally, I consider both alluvial transport and bedrock incision in my experiment, with a combined texture and strength divide halfway down the channel profile. Under these conditions (Figure 4.7b, solid blue line), carrying capacity across the jointed greywacke exceeds the supply produced by incision, and the upstream channel profile is similar to that of the previous experiment (Figure 4.7b, blue dashed line). Conversely, the downstream channel section resembles my uniform coarse alluvium model, rather than the low relief profile that would be produced if bedrock detachment were the rate-limiting process (Figure 4.7b, red line). The downstream channel profile is therefore largely shaped by the upstream source of coarse alluvium, not by the underlying weak bedrock, leading to a channel that is approximately 16 times steeper than it would be if erosion were limited only by the need to detach weak cataclasite material. The texture of this alluvium is 10% sand, 90% gravel, which is very similar to the source texture from the jointed greywacke.

These simple 1D experiments provide basic information about channel profile shape across different lithological and alluvial conditions, but they do not take into account the 2D distribution of drainage network patterns across a surface, or the 3D distribution of heterogeneous mechanical properties of rock. In order to more adequately predict the influence of weak zones on the drainage network pattern and the spatial distribution of sediments, I turn next to planform (2D) models.

4.4.4. Landscape evolution models: Geometry, Initial and Boundary Conditions

Figure 4.5A illustrates the 3D spatial pattern of lithology in the landscape evolution model runs. The model domain initially consists entirely of bedrock, with sediments being

produced as the rock erodes. The topography is initially flat with a sub-meter scale noise applied to the surface; a uniform uplift rate of 0.1 mm a^{-1} relative to baselevel is applied throughout each run. A single, vertically dipping zone of greater erodibility is located in the center of the model and strikes orthogonal to the flow outlet boundary on the southern terminus of the domain. The cohesion and texture gradients are discretized by dividing the weak zone width into parallel planar layers representing the transition from intact, crystalline bedrock to cataclasite, ultracataclasite, and fault gouge located at the center of the weak zone. Five experiments are run to test the sensitivity of surface processes to different bedrock strength and texture gradients; each represents a different increment of brittle failure, including a control case with homogeneous cohesion and texture. Cohesion in the gouge unit is 1X to 3000X lower than that of the intact bedrock (Figure 4.5B). The entire weak zone is 140 m wide. Texture gradients are based on power law PSDs for the dominant mechanisms of fragmentation (Figure 4.5C-G), as explained previously.

4.5. Model Results

4.5.1. Topographic Pattern and Sediments

Results of the steady state experiments in Figure 4.8A-E indicate that topography, and hence the drainage network pattern, reflects the presence of a weak zone, agreeing with the detachment-limited models of Roy et al. (2015). Despite this basic similarity, it is clear that in the experiments presented here, particularly those with large strength and texture gradients, the conditions within the weak zone can lead to a dominantly alluvial regime. In contrast, the control (Figure 4.8A) is completely homogeneous and therefore shows no morphologic variations influenced by a strength gradient. In addition, channel conditions
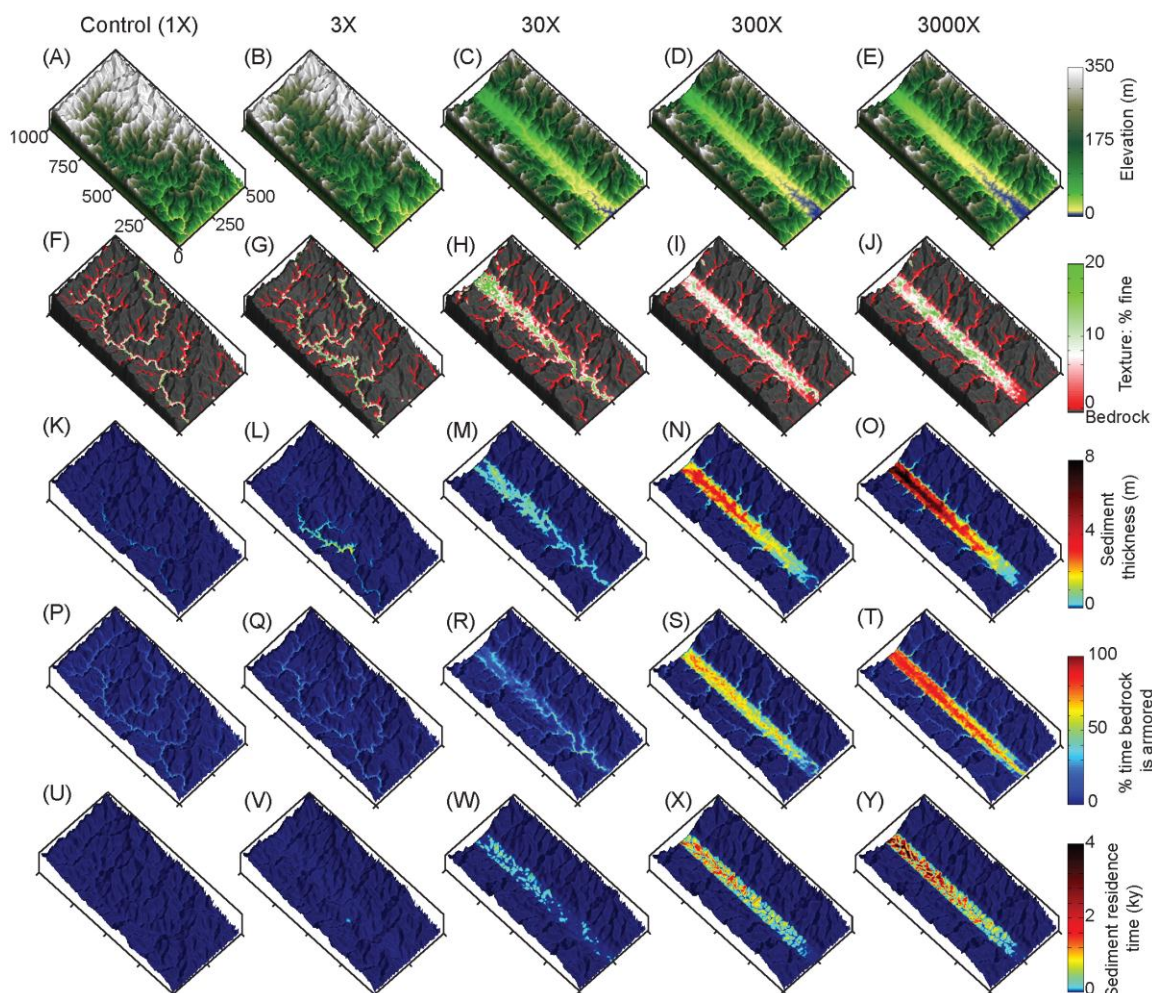
Figure 4.8. Experimental results. From left to right are control to 3000X experiments: (A-E) elevation maps, (F-J) average texture, (K-O) average alluvium thickness, (P-T) the percentage of time bedrock is covered by any alluvium thickness, (U-Y) average residence time of alluvium.

in the control experiment lead to detachment-limited behavior. The drainage pattern within the control is dendritic with no strong directional dependence. Bedrock is only rarely covered by relatively thin alluvium (Figure 4.8K, P). Sediment texture becomes increasingly fine downstream, as a result of the active-layer enrichment mechanism that Gasparini et al. (Gasparini et al., 1999; Gasparini et al., 2004) described, but the fine fraction never exceeds 9%, which is the texture contributed by erosion of the intact bedrock

(Figure 4.8F). Sediment residence times, calculated as the volume of sediment divided by the average sediment flux for every element, approach zero (Figure 4.8U).

The 3X experiment hosts a small strength gradient, causing tributaries and saddles to form in the location of the weak zone. However, the main channel crosses the strength gradient and is not strongly influenced by it. Much as in the control, sediments only occasionally cover bedrock. Sediment thicknesses do not exceed 1.5 m. The texture field is similar to that of the control, except that there is a greater abundance of fine sediments, particularly where sediment thickness is greatest. A slope versus area plot for the 3X experiment (Figure 4.9B, E) shows that much of the bedrock remains exposed and the relationship between channel slope and drainage area matches the expected trend for detachment-limited conditions. However, when drainage area exceeds $\sim 3 \times 10^4$ m^2, sediments begin to influence this relationship. Sediment residence times are similar to the control (Figure 4.8V).
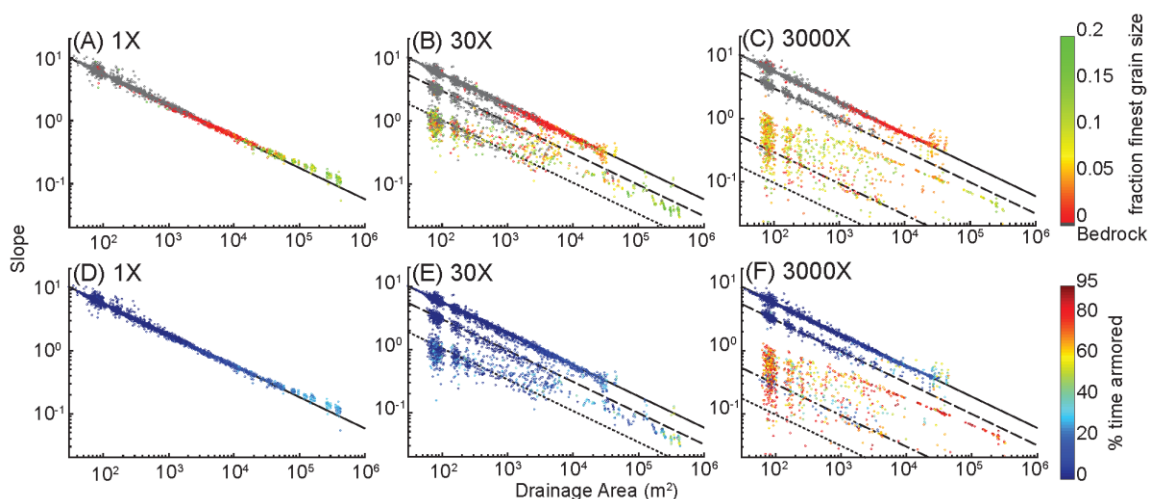
Figure 4.9. Slope versus drainage area plots for Experiments control (1X) to 3000X. (A-E) Colors represent average alluvium texture, grey color represents bedrock channels. (F-J) Colors represent the percentage of time bedrock is covered by alluvium. Lines represent slope-area trends using the stream power equation for intact bedrock (solid), cataclasite (dashed), ultracataclasite (dot-dashed), and fault gouge (dotted).

Topography produced from the 30X to 3000X strength gradient experiments indicates that the weak zones are reflected by straight, high-order channels while the surrounding intact bedrock hosts short, orthogonal tributaries of low order (Roy et al., 2015). These experiments also show an increased prevalence of an alluvial regime overlying the weak zone. For the 30X to 3000X experiments, the weak zone is more easily eroded and its local sediments are more readily transported by the high order channel confined to the structure of the weak zone, leading to relatively low relief. However, erosion of the adjacent, more resistant bedrock produces an abundance of coarse-grained sediments that are transported down steep tributaries into the weak zone. Sediment thickness in the 3000X example can exceed 8 m above the weak zone (Figure 4.8O). From tributaries, the weak zone accumulates sediments that are much coarser than the textures that would be produced by erosion of the weak zone itself (Figure 4.8H-J). The abundant coarse sediments continue to armor the weak zone (Figure 4.8M-O) for the majority of steady state time (Figure 4.8R-T). Armoring in the tributaries is minimal by comparison, and many of the coarse sediments produced by erosion are quickly deposited as small fans in the large valley, as can be seen by the red patches located at the bottom of the tributaries in Figure 4.8H-J. The weak zone is less frequently exposed and sediment thicknesses are greater for larger strength gradient examples. The relationship between slope and drainage area for the 3000X experiment (Figure 4.8E, J) shows that only low order tributaries are bedrock dominant. Sediment residence times for the 30X experiment are noticeably larger than results from those in the control and 3X experiments (Figure 4.8W), and residence time continues to increase for the 300X and 3000X experiments (Figure 4.8X, Y).

4.6. Discussion

4.6.1. Drainage Network Pattern

The regional drainage network patterns in my sensitivity analysis reflect the local underlying strength and texture gradients when the gouge unit is $\geq$30X weaker than surrounding intact bedrock (Figure 4.8A-E). For my experiments, weak bedrock takes the form of a straight corridor that steers surface runoff, leading to the formation of a straight, high order trellis channel with orthogonal tributaries of low order. Greater strength gradients lead to a greater attraction of surface runoff, but for strength gradients less than 30X the influence is only local and the main channel is largely dendritic. The control is not affected by a strength gradient and therefore produces a dendritic drainage pattern.

4.6.2. Aggradation in Structurally Confined Channels

4.6.2.1. Weak Zones and Sediment Storage

The relatively low bedrock relief in the model's fault weak zones leads to intermittent aggradation of coarse sediments. The alluvium thickness, percentage of time bedrock is armored, and the residence time of sediments, are all proportional to the magnitude of strength difference between intact rock and weak zone. Channel slopes in the model's weak zone exceed the equilibrium slope expected for detachment-limited channels, implying that sediment transport is the rate-limiting factor (Figure 4.9E). The tributaries that connect orthogonally to the structurally confined channel cross the strength and texture gradients, bringing gravel-dominant alluvium downslope from steep bedrock channels into the low relief weak zone.

Much as in my 1D experiments in the previous section, the sharp decrease in slope expected between intact bedrock and the gouge unit, up to ~55 times for the 3000X experiment, causes a sharp decrease in carrying capacity in the structurally confined channel. The structurally confined channel attracts drainage from a relatively large area with multiple sources of coarse sediment (Figure 4.8A-E). Coarse sediments aggrade above the weak zone in the 30X-3000X experiments, establishing an equilibrium slope dependent predominantly on the texture of incoming gravel-dominant alluvium, rather than on the erodibility of underlying bedrock (Figure 4.8F-J). Armoring by gravel-dominant alluvium reduces the frequency of bedrock exposure, and frequency decreases with greater erodibility.

The relationship between channel slope and drainage area depends on the percentage of time that bedrock is covered by alluvium, and if it is often covered, the texture of the overlying sediment. For the weak zone, coarse sediments increase the steepness of the main channel to the point at which channel slope is set by the flux and texture of alluvium rather than by the erodibility of the underlying bedrock.

4.6.2.2. Downstream Fining

The modeled alluvial active layer fines downstream, particularly at the major slope transition for tributaries that pass from intact bedrock to weak zone. Fans of coarse alluvium deposit at the confluence of the tributaries and the structurally confined channel (Figure 4.8F-J) and cause a local increase in frequency of bedrock armoring (Figure 4.8P-T). Texture fining from tributary to main channel also correlates with an increase in the percentage of time bedrock is covered, and both are due to the sharp transition in slope and

the distance from the gravel sediment source. The path of the structurally confined channel is occasionally deflected by the coarse alluvial fans (Figure 4.10). Along the structurally confined channel the average alluvial texture is finer than in these coarse fans. In nature it is common for rivers to bend around growing alluvial fans formed by tributaries with high sediment yield. For example, the Salween River, located in the Eastern Syntaxis of the Himalayas, is a large river that follows the Bangong-Nujiang tectonic suture (Hallet and Molnar, 2001; Liu et al., 2011). Short, steep tributaries along the Salween deposit large amounts of coarse sediments in fluvial fans, such as the Fugong fan shown in Figure 4.10B, causing the path of the high order river to deflect around the fan. Similar fluvial responses to large sediment pulses exist in the Navarro River (Sutherland et al., 2002; Cui, 2003) and Lava Falls on the Colorado River (Webb et al., 1999).
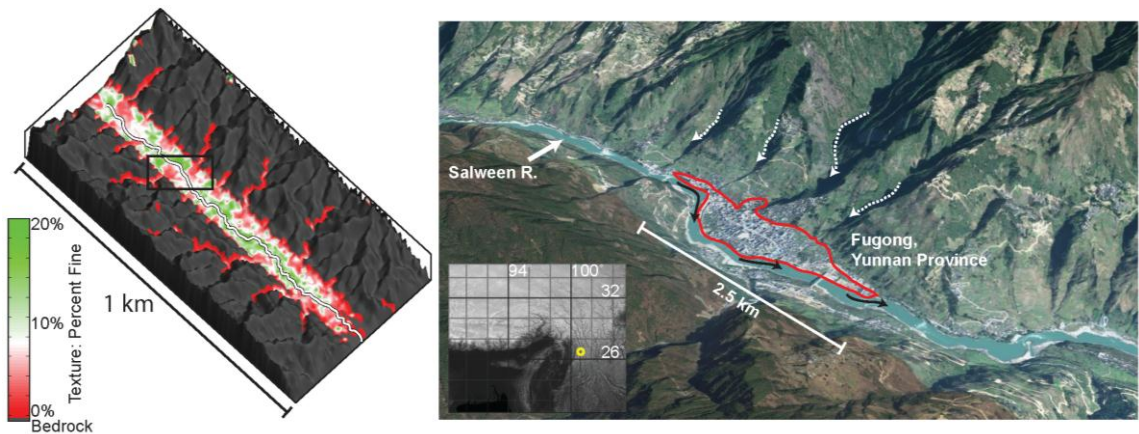
Figure 4.10: Revisiting texture map of 3000X experiment. (A) Black box indicates section of high order, structurally confined channel deflected by coarse alluvial fans deposited by steep tributaries. (B) Along the Salween River, located at yellow dot on reference map of Eastern Himalayan Syntaxis, similar coarse alluvial fans form. Fugong alluvial fan, highlighted in red, is fed by steep bedrock tributaries indicated by dotted white lines. Black lines indicate flow direction of Salween River.

The model equations that I use to approximate landscape evolution create a simplified balance between uplift and erosion averaged over geologic time scales, yet by incorporating stochastic variations in discharge, the model accounts for the formation of

the short-term, transient alluvial fans. This pattern suggests that, for my purposes, storm events are adequately approximated with a stochastic distribution and that the model equations provide sufficient theory to account for transitions between the rate-limiting fluvial processes of erosion and transport.

4.6.2.3. Occasional Bedrock Exposure in the Weak Zone

Under steady-state conditions, bedrock in the weak zone must occasionally become exposed and erode, in order for bedrock erosion to keep pace (on average) with the rate of baselevel fall. Figure 4.11 displays longitudinal profiles of the structurally confined channel in the 3000X experiment at three time steps. Based on my numerical experiments, the weak zone can act as a sediment storage location but bedrock is expected to become exposed intermittently. Intermittent bedrock exposure can lead to intermittent knickpoint migration (Figure 4.11C) because upon exposure the channel slope exceeds the equilibrium slope of weak zone bedrock without alluvial armoring (Figure 4.9C-E, H-J). The armored bedrock will increase in slope in concert with the alluvium until sediments mobilize and the alluvium layer thins, exposing the weak bedrock for a relatively short duration. The irregular bedrock topography underlying the alluvium implies that the channel periodically avulses and then re-incises whenever the bedrock becomes exposed, presumably creating epigenetic gorges that eventually become filled with alluvium from tributaries (e.g. Ouimet et al., 2007). The frequency of bedrock exposure decreases upchannel in the weak zone and increases upchannel in the tributaries (Figure 4.8 P-T). However, based on my numerical experiments I suggest that in a natural setting, the intermittent exposure and

incision of bedrock only plays a short-term role in the local evolution of channel slope in the weak zone, which is dominated by the upstream gravel source.

These experimental results agree well with observations from the Peikang River in Taiwan. Yanites at al. (2011) noted that incision rates in the Peikang River are proportional to 1) the frequency of bedrock exposure and 2) stream power. This field analysis occurred after the 1999 Chi Chi earthquake, in which an excess of sediments was introduced from hillslopes into the river, increasing the average thickness of alluvium, decreasing the frequency of bedrock exposure, and subsequently decreasing incision rates (Hsu et al., 2010; Yanites et al., 2010; Yanites et al., 2011).
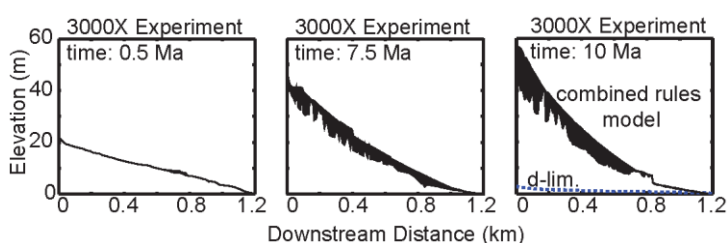
Figure 4.11. Longitudinal channel profiles for 3000X experiment. (A) time 0.5 Ma, (B) time 7.5 Ma, (C) time 10 Ma. Black area represents alluvium covering bedrock. Before approaching a steady state, few gravel-dominant sediments are transported from outside of the weak zone. Bedrock in the weak zone is largely exposed, and the sand-dominant sediments produced by weak zone erosion have a short residence time. Tributaries begin to mobilize gravels by eroding the intact bedrock, causing them to armor the weak, low relief weak zone. Bedrock must occasionally become exposed due to the steady and uniform uplift pattern. Dashed blue line is the profile of a detachment-limited experiment with an identical strength gradient.

4.6.2.4. Sediment Residence Time

The occasional exposure of bedrock in the weak zone limits the residence time of the armoring sediments (Figure 4.8U-Y). Sediment residence time correlates with the relative strength difference between weak zone and intact rock. A greater relative strength difference reduces relief above the weak zone and allows for greater sediment volumes to

accumulate during aggradation. Conversely, average sediment residence times in the control are negligible and agree with the extremely low percentage of time bedrock is covered by alluvium. Residence times are greatest near where the weak zone intersects the northern boundary for the 30X to 3000X experiments, which reflects the tendency for bedrock exposure to initiate near the flow outlet boundary and intermittently migrate upchannel. In these numerical experiments, sediments are stored along the edges of the channel (small colored packets, Figure 4.8W-Y) and remain in place until the channel changes course.

4.7. Conclusions

My model-based analysis of lithologic controls on grain size and rock erodibility implies that drainage network patterns should be highly sensitive to the mechanical weakness, fine texture, and persistent low relief associated with fault weak zones. Field observations of fault weak zone erosion in the South Island of New Zealand also suggest a strong sensitivity between rock damage, grain size distribution, and erosion susceptibility. The sharp transition in erodibility and sediment texture between intact and damaged rock can cause rivers to become structurally confined. Coarse gravel generated from erosion of steep bedrock channels leads to pervasive armoring of the low relief weak zone. The alluvium that armors the weak zone is coarser than the sediments produced by its erosion, causing the relief within the structurally confined channel to increase as a function of alluvium texture, rather than the erodibility of the underlying rock. Occasionally the damaged rock becomes exposed for short periods of time. This periodic exposure allows for continued incision of bedrock, but has a negligible long-term influence on channel

slope. Sediment residence times increase with greater strength difference between intact and damaged rock as a function of relief. Storms that are more frequent but less intense are less able to transport the coarse gravel that deposits in structurally confined channels. Structurally confined channels can store sediment between storms and act as pathways for sediment transport during storms, and their influence can be pervasive through a landscape due to the extreme difference in strength and texture.

CHAPTER 5

MULTI-SCALE CHARACTERIZATION OF TOPOGRAPHIC ANISOTROPY

5.1. Chapter Abstract

I present a method for quantifying orientation and scale dependence of topographic anisotropy to aid in differentiation of the fluvial and tectonic contributions to surface evolution. Using multi-directional variogram statistics to track the spatial persistence of elevation values across a landscape, I calculate anisotropy as a multiscale, direction-sensitive variance in elevation between two points on a surface. Tectonically derived topographic anisotropy is associated with the three-dimensional kinematic field, which contributes 1) differential surface displacement and 2) crustal weakening along shear zones, both of which amplify processes of surface erosion. Based on my analysis, tectonic displacements dominate the topographic field at the scale of mountain ranges, while a combination of the local displacement and strength fields are well represented at the ridge and valley scale. Drainage network patterns tend to reflect the geometry of underlying active or inactive tectonic structures due to the rapid erosion of faults and differential displacement across the fault. The persistence and complexity of correlated anisotropic signals depends on how the strain field evolves with time: new tectonic regimes can overprint the original topographic signal, or the signal can slowly recede as tectonism halts. Regions that have been largely devoid of strain, such as passive coastal margins, have predominantly isotropic topography with typically dendritic drainage network patterns. These methods can be used successfully to infer the settings of past or present tectonic

regimes, and can be particularly useful in predicting the location and orientation of structural features that would otherwise be impossible to interpret in the field.

5.2. Chapter Introduction

Landforms are shaped by the coupled tectonic and climatic processes that drive advection and erosion of rock and transport of sediments. This allows us to make robust interpretations about the geological history of a landscape purely by study of its topography. It is well recognized (e.g. Bercovici and Ricard, 2014; Koons, 1995; Koons et al., 2012; Montési and Zuber, 2002; Montési, 2004; Upton and Craw, 2014; Upton et al., 2009) that the rheological responses of rock to tectonic and topographic stresses determine how strain and associated weakening are partitioned at and below the Earth's surface. The typical rheological response in the upper crust is to localize strain along fault damage zones, which introduces discontinuities in rock strength and uplift relative to baselevel (e.g. Ben-Zion and Sammis, 2003; Faulkner et al., 2010; Mooney et al., 2007; Sammis et al., 1986; Sibson, 1977). Further still, the planar geometry and orientation of fault damage zones are grossly predictable based on the tectonic stress field (Coulomb, 1773; Terzaghi, 1944; Enlow and Koons, 1998). Tectonic strain therefore introduces directionally dependent characteristics of rock displacement and damage, both of which influence the pace of geomorphic responses (Molnar et al., 2007; Roy et al., in press). As a result, drainage network patterns often reflect the underlying anisotropy of fault damage zones, whereas in the absence of strain, drainage network patterns are largely isotropic (Roy et al., 2015).

By measuring topographic anisotropy, or the directional dependence of landforms from the scale of valleys and ridges to entire basins and orogens, I can make an assessment of the magnitude and orientation of past or present tectonic strain fields across multiple length scales. My approach is to create and utilize an every-direction variogram analysis (EVA) technique to quantify topographic anisotropy at multiple scales for any point on a surface. My goal is to make useful first-order interpretations of how topography contains multiscale, spatially dependent information about past and present tectonic strain conditions using simple parallel CUDA code. Specifically, I use EVA on landforms with distinct patterns of anisotropy associated with tectonic strain, river incision, and/or sediment deposition, in order to establish a generalized model for linking the topographic fabric to its formative process. Several synthetic landscapes and natural landscapes from New Zealand are featured in order to test the versatility of my method. I then compare EVA to the self-affine power law scaling method, a popular method for examining the directional dependent and fractal properties of landscapes (Xu et al., 1993; Dodds and Rothman, 2000; Sung and Chen, 2004), in order to understand how these two methods differ in sensitivity to directional dependent landscape fabrics. I conclude with a short discussion on possible future uses and improvements to EVA.

5.3. Every-Direction Variogram Analysis (EVA)

5.3.1. Statistical Method

There is no single method of classification that will adequately characterize and compare the spatial distribution of directional dependence. Some have characterized directional dependence by drawing correlations between the orientations of streams and

bedrock joints (e.g. Ericson et al., 2005; Judson and Andrews, 1955), while others have made useful qualitative descriptions of drainage patterns with respect to strength and uplift gradients and thresholds (e.g. Lubowe, 1964; Zernitz, 1932). Watershed hypsometry (e.g. Lifton and Chase, 1992; Walcott and Summerfield, 2008) and directional dependent fractal analysis (Sung and Chen, 2004) have recently become useful tools for interpreting the influence of spatially variable conditions. Still others have used tortuosity to determine the directional dependence of individual rivers and their correlation to structural features (Roy et al., in press). However, these methods provide limited information about the spatial distribution or directional dependence of anisotropy, are often limited to a single spatial scale, or they do not fully represent all components of the landscape. For this reason I explore the directional and scale dependencies of topography using the variance of elevation along a surface (Kitanidis, 1997; Trevisani et al., 2009; Koons et al., 2012). EVA is an improvement on previous variogram methods because elevation variance is calculated between multiple points at multiple scales and multiple directions, leading to a rich quantitative determination of anisotropy magnitude and orientation at multiple scales for every point on a landscape. I measure variance v^2 using the statistical method

$$v^2 = [z(x, y) - z(x + \Delta x, y + \Delta y)]^2 \qquad (5.1.)$$

where $z(x, y)$ is the elevation at a point with coordinates x, y, and $z(x + \Delta x, y + \Delta y)$ is the elevation at a point with a separation distance, or wavelength, equal to $\Delta x, \Delta y$ using a 2D Cartesian coordinate system (Figure 5.1A). In order to measure directional dependence I must calculate variance over multiple separation distances and directions within a large population of elevation data. Separation distance s is a length scale equal to or greater than the spatial resolution of topographic data. Divided into Cartesian components:

$$\Delta x = s \cos \varphi ,$$

$$\Delta y = s \sin \varphi \tag{5.2.}$$

where φ is the angle between the two points, taken at 5° intervals for my analysis. For simplicity I average variance in opposing directions, assuming that directional dependence is symmetric (Figure 5.1A). Variance is also averaged over separation distance in order to reduce the signal of small scale features over long separation distances

$$v^2(s, \varphi) = \frac{1}{2s} \sum_{i=1}^{s} [v^2(i, \varphi) + v^2(i, \varphi + 180)] \tag{5.3.}$$

where $v^2(s, \varphi)$ is the variance, averaged along all separation distances $i = 1$ to s for angles φ and $\varphi + 180$ (Figure 5.1B). In other words, $v^2(s, \varphi)$ represents the average variance over all separation distances up to and including s for one orientation. The minimum variance for every separation distance and its respective angle are recorded in addition to the variance values orthogonal to the minimum values (Figure 5.1C, D). Anisotropy is the ratio between these two variance values

$$\alpha_s = \frac{v_c^2 + v^2(s, \varphi_{min} + 90)}{v_c^2 + v^2(s, \varphi_{min})} \tag{5.4.}$$

where α_s is anisotropy measured at multiple separation distances, and v_c^2 is equal to the variance of the relative vertical error estimate of the dataset ($v_c^2 = 36$ m² for SRTM3 data, $v_c^2 = 100$ m² for SRTM30 data) used to diminish extreme variance sensitivity at the smallest scales that could be attributed to error (Rabus et al., 2003). The anisotropy can then be used to quantitatively interpret the directional dependence of elevation at a single point (Figure 5.1E, F), or multiple points on a surface, which I discuss in Section 5.4. This method can be used to quantify the anisotropy of any spatially variable parameter, but I limit the scope of this paper to elevation.
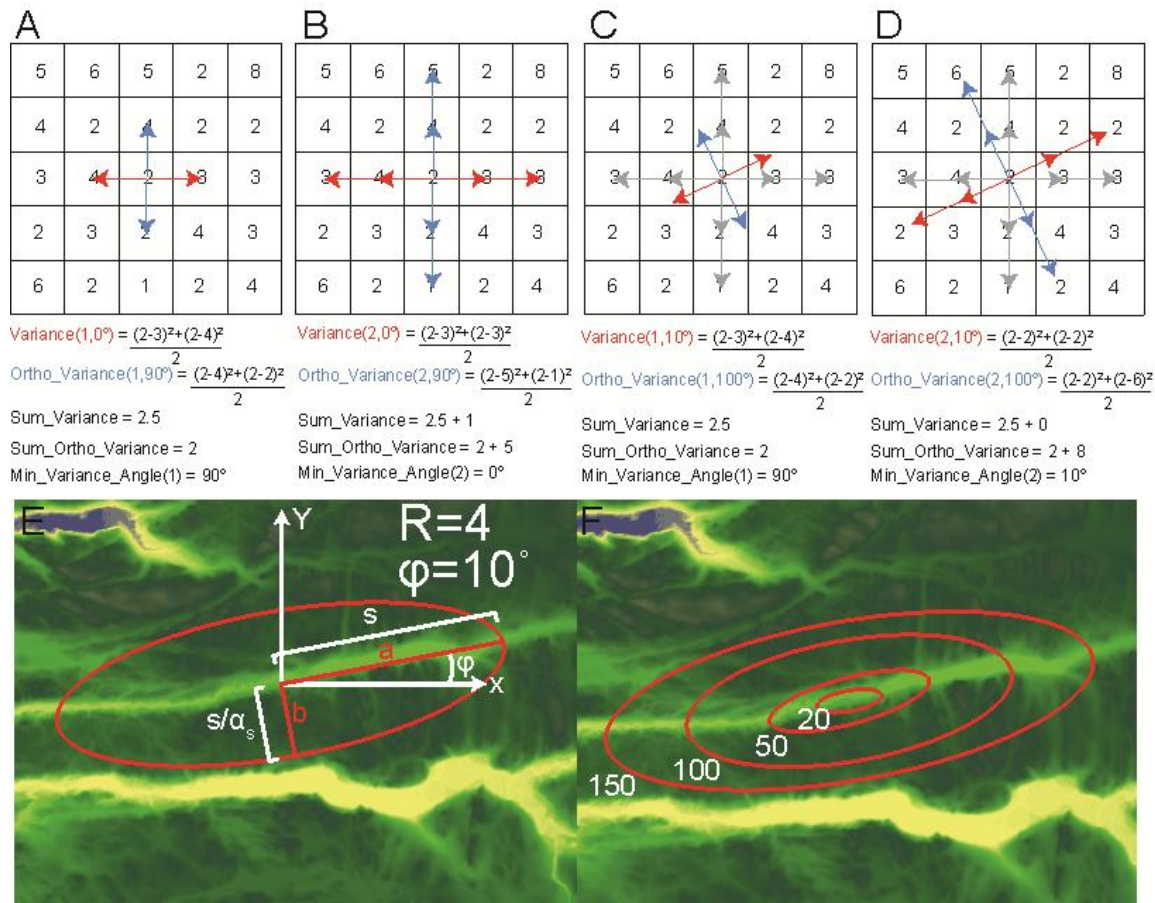
Figure 5.1. An example grid in which I apply my variance algorithm. (A) Starting at $\varphi = 0°$ with separation distance equal to the grid resolution, calculate variance between center point and points $0°$ and $180°$ and separation distance 1 away from center (red arrows). Also calculate variance for points orthogonal to $0°$ and $180°$ (blue arrows). (B) Separation distance is doubled and variance values are calculated for the new scale. The variance for this scale is the average of the new variance and the variance calculated at the previous separation distance. (C) Variance is now measured for $\varphi = 10°, 190°$ and $s = 1$. The new variance value does not exceed the previously calculated value at the given scale and is therefore not used to measure anisotropy. (D) The calculation is repeated at the second scale, variance is less than the previous calculation and so is now used to measure anisotropy for s = 2. (E) Anisotropy is taken by dividing the minimum variance from the variance value measured at a perpendicular angle. The anisotropy value is the magnitude difference in variance for the two perpendicular directions, represented by an ellipse in the figure. (F) The azimuth and magnitude of anisotropy is measured over multiple scales. Red ellipses represent topographic anisotropy magnitude (ellipticity), orientation (direction of semimajor axis), and wavelength (length of semimajor axis).

5.3.2. Computational Method for Generating Anisotropy Maps with EVA

The statistical method mentioned above is deployed in parallel for CUDA, a C-based programming model developed by NVIDIA to accelerate the execution time of numerous parallel statistical calculations by taking advantage of a Graphical Processing Unit (GPU) (Wilt, 2013). The elevation files read by EVA contain elevation integer data in meters for coordinates in degree decimal units at an isotropic resolution of 30 arc seconds for Section 5.4.1.6. and 3 arc seconds for all other examples. All of the elevation data are used for the calculation, but anisotropy is only calculated for points that are at least separation distance s away from the boundaries of the elevation data due to the lack of data beyond the spatial limits. For every point, anisotropy is measured over a scale interval covering three orders of magnitude. Data processing follows the flow chart in Figure 5.2. First, the integer values of elevation are extracted from the elevation data file and stored in a C matrix. Then the matrices and variables required in the CPU and the GPU are initialized. A CUDA kernel is then launched such that each point in the matrix containing the elevation data is a thread. The data passed to the kernel are the elevation matrix and the angle array that contains angles in five degree intervals from 0 to 175. For each of the threads in the GPU the code loops through the scales to calculate variance for all angles in the angle array and determines the azimuth and anisotropy for that particular scale. At the end of the kernel for each (x,y) point in the elevation data matrix, azimuth and anisotropy values are produced for all scales and these values are transferred to the CPU where they can be saved to disk.
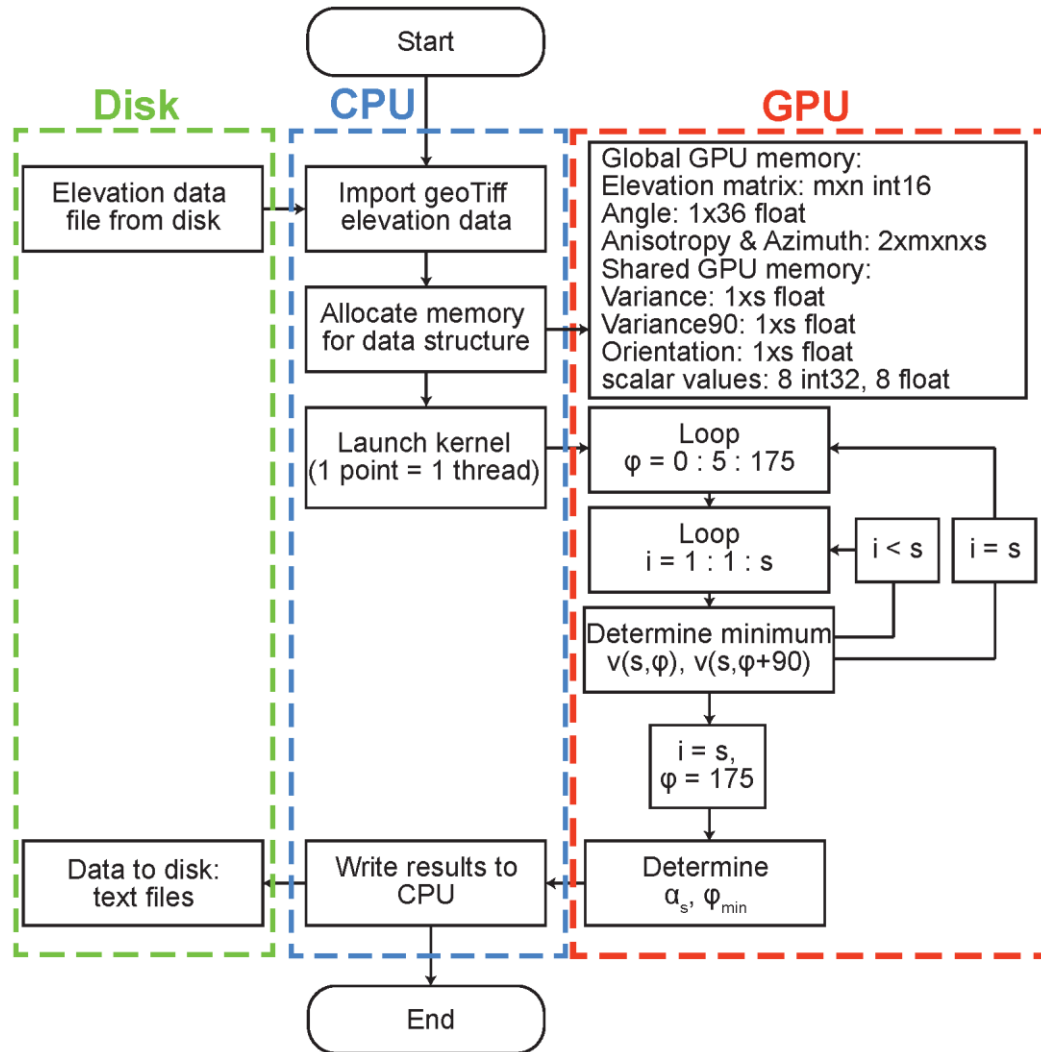
Figure 5.2. Flow chart for the EVA algorithm.

5.3.3. Methods for Delivering Anisotropy Data

Using the equations above it is possible to quantify anisotropy magnitude and direction at any wavelength and any point on a landscape. Information about anisotropy magnitude, orientation, and wavelength for every point on a surface can become difficult to visualize in a meaningful way, so I choose to pursue a three-stage method for delivering anisotropy data from EVA.

I.   First, I create surfaces that resemble very simplified versions of my natural landscape examples, and measure anisotropy at a single point on each surface. I do this in order to understand the basic shape of anisotropy produced by the process that builds that characteristic shape.

II.   Second, after I have determined the basic pattern of anisotropy from the simple surfaces, I perform the same analysis on the natural landscape example. The position of the point used for this analysis should be similar to the point measured in stage one to validate a comparison. In both cases I use ellipses to represent anisotropy (see Figure 5.3F).

III.   Third, I use EVA to calculate anisotropy data for all points on the landscape in order to fully represent the regional topographic fabric and the spatial variations found within. The analysis of multiple points enhances my ability to see local changes in anisotropy that could otherwise become lost in the average topographic fabric or misrepresented by a single point analysis. The use of thousands of ellipses is prohibitive for this multipoint analysis, so I plot two different colors representing the magnitude and orientation of anisotropy for a single scale at every point. The use of color to represent the orientation and magnitude of anisotropy is not unlike electron backscatter diffraction maps produced for interpretation of crystallographic preferred orientations (Dingley, 2004; Schwartz et al., 2009).

5.4. Topographic Fabric in New Zealand

I use field locations in New Zealand for my statistical analysis of topographic anisotropy. The Southern Alps of New Zealand (Figure 5.3A) are an orogenic mountain range wrought from the oblique collision of the Australian and Pacific tectonic plates. Uplift of crust relative to the regional baselevel has produced a mountain range with a directional dependence dictated by the orientation of the Alpine Fault (Koons, 1990; Koons, 1994; Little et al., 2005) and rheological variations along strike (Upton et al., 2009; Upton and Craw, 2014) (Figure 5.3C). Within the Southern Alps, typically at length scales of 20 km or less (Koons, 1994; Koons, 1995; Koons et al., 2012), rock damage in fault structures influences the position and erosive power of streams and rivers as they incise into the uplifting orogen. The largest rivers in the Marlborough district are influenced by damage and deformation along major active tectonic structures (Wilson et al., 2004; Craw et al., 2008) (Figure 5.3D). Conversely, in the Wairoa region fluvial incision produces dendritic drainage patterns as it incises into a largely homogeneous and uniformly uplifted siltstone (Crosby and Whipple, 2006) (Figure 5.3B). Sediments course through drainage networks in the Southern Alps and some deposit in the large, planar delta of the Canterbury Plains region (Figure 5.3E) (Leckie, 1994). On the North Island, volcanism has led to the creation of monolithic stratovolcanoes, such as Mt. Taranaki (Figure 5.3F) (Grant-Taylor, 1964; Harrison and White, 2004).

5.4.1. EVA Results: Anisotropy Maps

I apply EVA to the dendritic (Wairoa, Figure 5.4), deformational (Central Otago, Figure 5.5), fault damage and deformation (Marlborough, Figure 5.6), planar (Canterbury

128

Figure 5.3. Topographic maps. (A) New Zealand and the regions of (B) Wairoa, (C) Central Otago, (D) Marlborough, (E) Canterbury Plains, and (F) Taranaki. These locations are used for further analysis. Map A uses topographic data from the SRTM30 mission (~1 km resolution) and bathymetric data from the ETOPO1 mission (~2 km resolution). Maps B-F use topographic data from the SRTM3 mission (~90 m resolution) (Rabus et al., 2003). Please note scale change between maps and the difference in scale between bathymetric and terrestrial elevation data in map A.
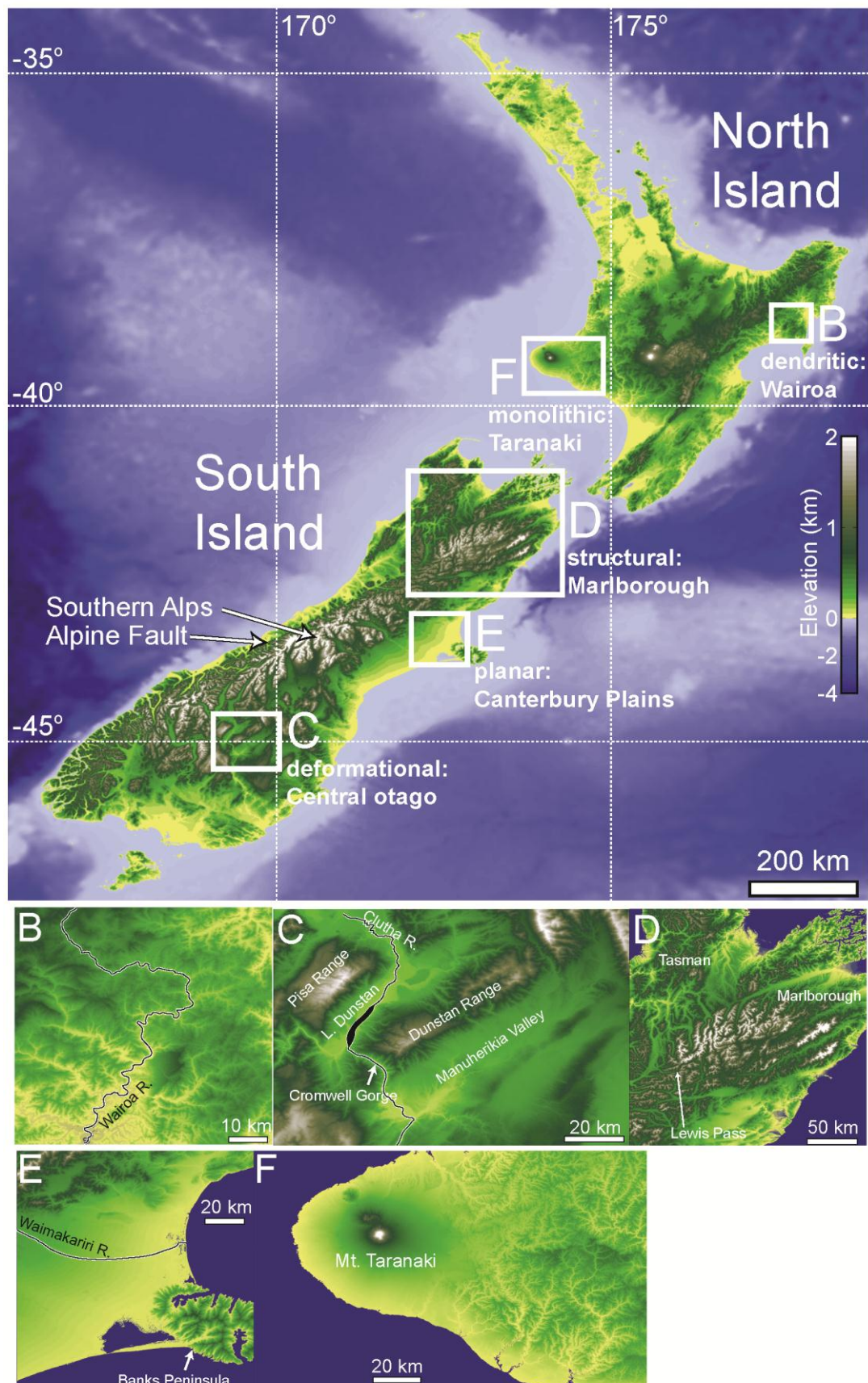
Plains, Figure 5.7), and monolithic (Mt. Taranaki, Figure 5.8) topographic patterns of New Zealand, as well as a larger scale analysis of the entire South Island (Figure 5.9). Topographic anisotropy was measured from 0.1-10 km for the local examples and 1-200 km for the South Island example.

5.4.1.1. Dendritic: Natural Example - Wairoa

Dendritic fluvial networks can display significant relief, but directional dependence may vary significantly with the variable scale of river meanders. I replicate the dendritic shape of a fluvial landscape by using the landscape evolution model CHILD (Figure 5.4A) (Tucker et al., 2001). This model surface is the product of stream power under uniform environmental and geomorphic conditions.

Changes in orientation are common over multiple wavelengths of measurement in the synthetic experiment (Figure 5.4A). Anisotropy measurements are taken at a point located on a low order channel just before confluence with a higher order channel. At a wavelength up to 0.4 km, anisotropy is dominated by the low order channel, but at the 1 km wavelength the high order channel begins to influence anisotropy, and it eventually dominates at longer wavelengths. Meandering rivers and streams in the Wairoa District of New Zealand display a similar spectrum of anisotropy magnitude and orientation from the reference of a single point (Figure 5.4B). In this natural case there are four wavelengths that display a significant shift in orientation. Anisotropy magnitude is greatest at short wavelengths, before the first large shift in orientation (below 6.25 km), but wanes at longer wavelengths as the orientation of dendritic channels become less consistent.
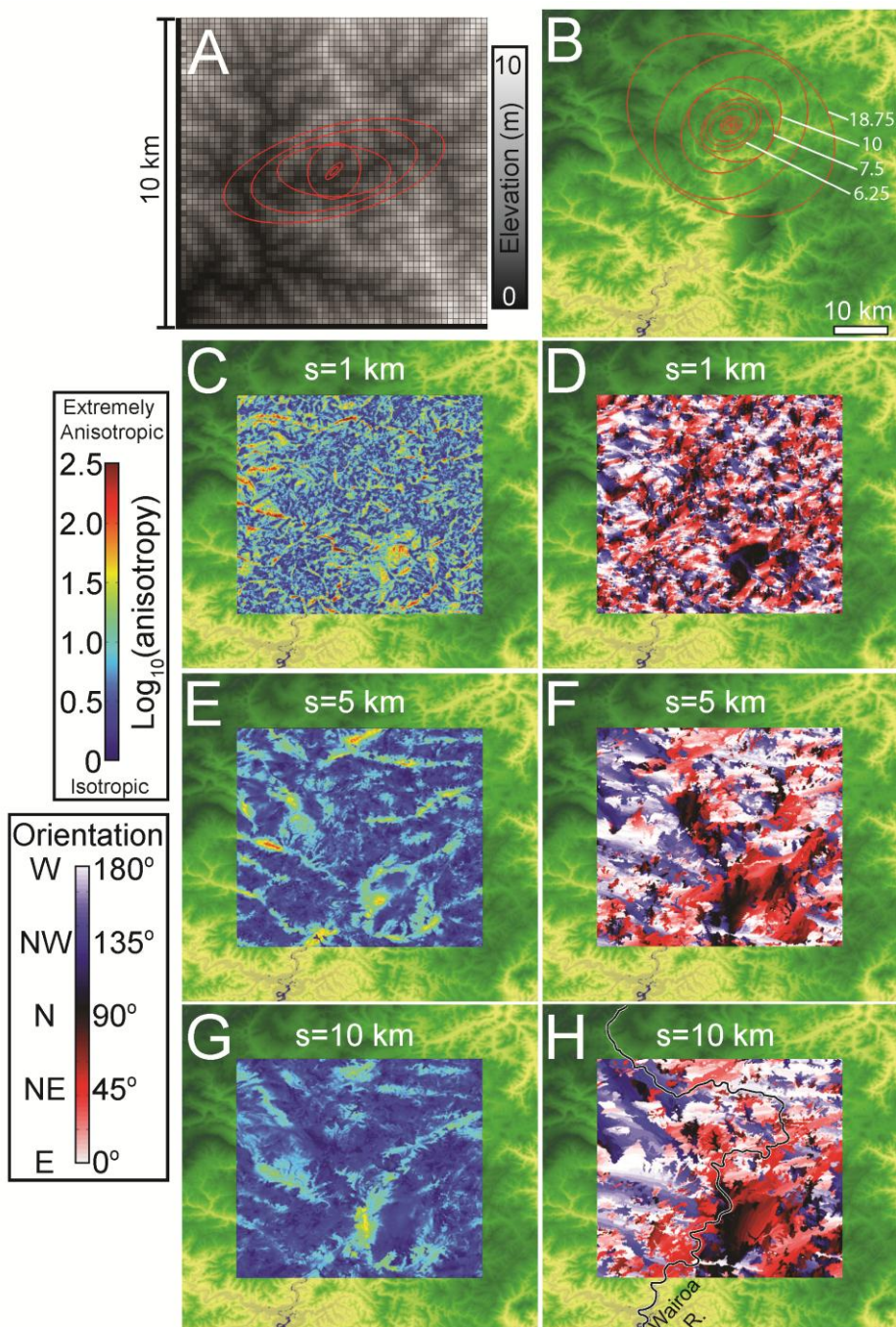
Figure 5.4. Anisotropy of dendritic landform. Dendritic surface (A) created from a stream power-based landscape evolution model created on a uniform substrate. Greyscale: black is low, white is high elevation for this and all proceeding synthetic examples. Anisotropy of single point represented by red ellipses for this and all following figures (see Figure 5.2E,F). (B) Anisotropy measured at single point in Wairoa region. Numbers represent the wavelength in kilometers for the indicated ellipses. Anisotropy measured up to maximum wavelength of 18.75 km. See Figure 5.1A for elevation color scale for this and all proceeding natural examples. (C) Anisotropy magnitude (Equation 5.4) and (D) orientation map at 1 km, (E) (F) 5 km, and (G) (H) 10 km wavelength. Color scales for both map types on left are used for this and all following figures.

The Wairoa region hosts a mélange of anisotropy at a short wavelength, in agreement with the single point analyses above. Anisotropy magnitude (Figure 5.4C) and orientation (Figure 5.4D) are highly variable across sub-kilometer distances. Anisotropy is greatest at 1 km wavelength (Figure 5.4C-G). There are some cases where anisotropy persists at 10 km wavelength along the large ridges separating higher order channels, otherwise the topography becomes generally isotropic (Figure 5.4G). At 5-10 km wavelength, there is generally a divide between an average west-northwest orientation on the west side of the Wairoa River and an east-northeast trend on the eastern side (Figure 5.4F, H). To the south, the Wairoa River valley generally trends to the north-northeast.

5.4.1.2. Deformational: Natural Example - Central Otago

The deformational signal in topography is associated with tectonic strain from differential plate motion. I replicate a fold pattern formed in convergent margins with a simple sinewave function (Figure 5.5A). This deformation pattern is similar to the fold-thrust belts of the Appalachian and Zagros Orogens (Chapple, 1978; Williams and Hatcher, 1982; Tucker and Slingerland, 1996). A point chosen at the trough of the synthetic waveform notices a gradual increase in anisotropy with increasing wavelength and orientation remains parallel to the fold axis (Figure 5.5A).

Central Otago is characterized by widely distributed deformation caused by tectonic strain in a weak lower crust (Upton et al., 2009). Limited rainfall in this region (~200 mm a^{-1} (Tomlinson and Sansom, 1994)) has preserved the antiform-synform pairs associated with this type of deformation (Figure 5.3C). I measure anisotropy at two points: one in the Manuherikia River valley (Figure 5.3C; red ellipses, Figure 5.5B), and one in
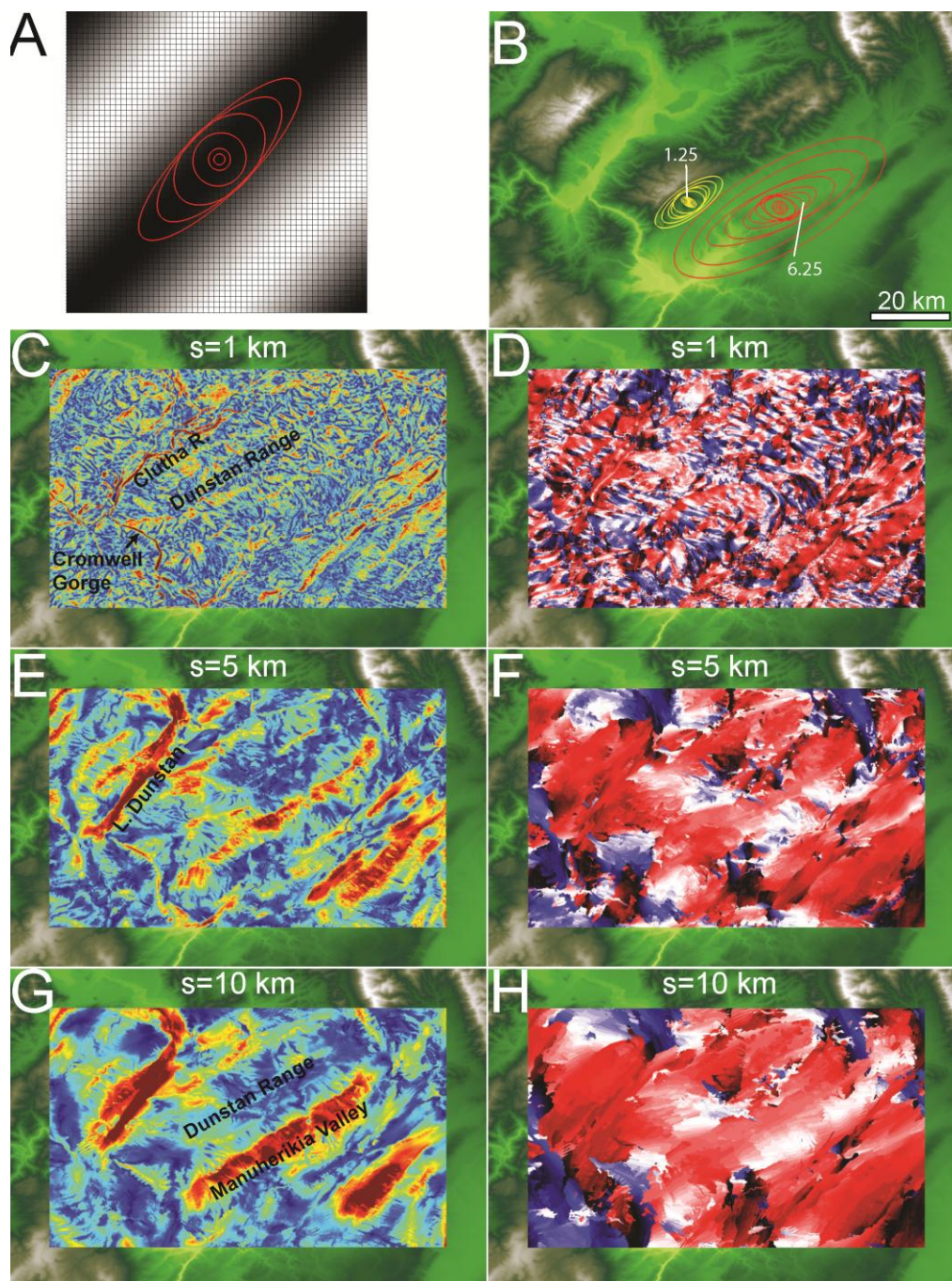
Figure 5.5. Anisotropy of deformational landform. Sine wave surface (A) used as a simplified replication of synform-antiform pairs found in Central Otago. (B) Anisotropy measured at two points in Manuherikia River Valley (red) and the secondary gorge (yellow). Numbers represent the wavelength in kilometers for the indicated ellipses. Anisotropy measured up to maximum wavelength of 25 km in the valley, 7.5 km in the gorge. (C) Anisotropy magnitude and (D) orientation map at 1 km, (E) (F) 5 km, and (G) (H) 10 km wavelength.

a secondary gorge on the Dunstan Range (Figure 5.3C; yellow ellipses, Figure 5.5B). As expected from the synthetic example, the fold axis-parallel trend in anisotropy exists at both locations, but only beyond a wavelength of 6.25 km at Manuherikia River Valley and 1.25 km in the secondary gorge. Below these wavelengths, both locations exhibit a northwest trend that matches the trend of small gorges, ravines, and streams, but opposes the general northeast orientation of the synform-antiform pairs and the larger rivers. Anisotropy magnitude increases with wavelength for both cases.

At a wavelength of 1 km, anisotropy is strongest along the reach of the Clutha River and the anisotropy signal is dominated by rivers, streams, and ravines (Figure 5.5C). The Clutha River follows the axis of a synform valley to the north but crosses the Dunstan Range through Cromwell Gorge (Figure 5.3C), which follows the active River Channel Fault (Thomson, 1993). Orientation is spatially variable at the 1 km wavelength (Figure 5.5D), dominated by streams that incise into the antiform ridges and generally trend orthogonal to the fold axis. At greater length scales (Figure 5.5E-G), anisotropy orientations begin to follow the fold axes of the antiform-synform pairs and the anisotropy signal begins to increase along the fold axes of the synforms. The Clutha River anisotropy signal is mostly diminished at this longer wavelength except for where it follows the synform axis at Lake Dunstan. Anisotropy along the antiform ridges has a somewhat uniform orientation at the 10 km wavelength but a much lower anisotropy compared to the synform valleys.

5.4.1.3. Fault Damage and Deformation: Natural Example - Marlborough

Topographic patterns associated with fault damage features suggest that surface processes are sensitive to the rapid erosion of faults, fractures, and other mechanical defects in the crust (e.g. Becker et al., 2014; Ericson et al., 2005; Koons, 1994; Koons et al., 2012; Molnar et al., 2007; Scheidegger, 1979). I replicate the shape of fault erosion and uplift in my synthetic landscape by applying a narrow trough of low elevation in a flat plateau of high elevation (Figure 5.6A). The ridge and valley fabric associated with drainages confined or influenced by fault damage leads to extreme local anisotropy in the form of long, anomalously straight river reaches (Figure 5.6A). Ridges that separate the eroded fault zones are wider and exhibit the same directional dependence but with lower magnitude anisotropy.

The region of Marlborough, New Zealand hosts a series of nearly vertically dipping NE trending strike-slip faults associated with pervasive distributed strain in the lower crust (Wilson et al., 2004; Craw et al., 2008). However, there is also a component of shortening perpendicular to fault strike that has led to orogenesis (Van Dissen and Yeats, 1991). For this reason the topographic shape of Marlborough cannot be attributed completely to fault damage, but the drainage network pattern in this region does appear to reflect the Marlborough Fault System. In this natural example, anisotropy is greatest in the large river valleys that coincide with large fault zones (Figure 5.6B). This strong signal of anisotropy persists at longer wavelengths.

Anisotropy along the anomalously straight valleys is extremely high and orientation is persistent at all wavelengths (Figure 5.6C-H). The small tributaries that incise into the valley walls and ridges influence the topographic fabric at the 1 km wavelength, producing
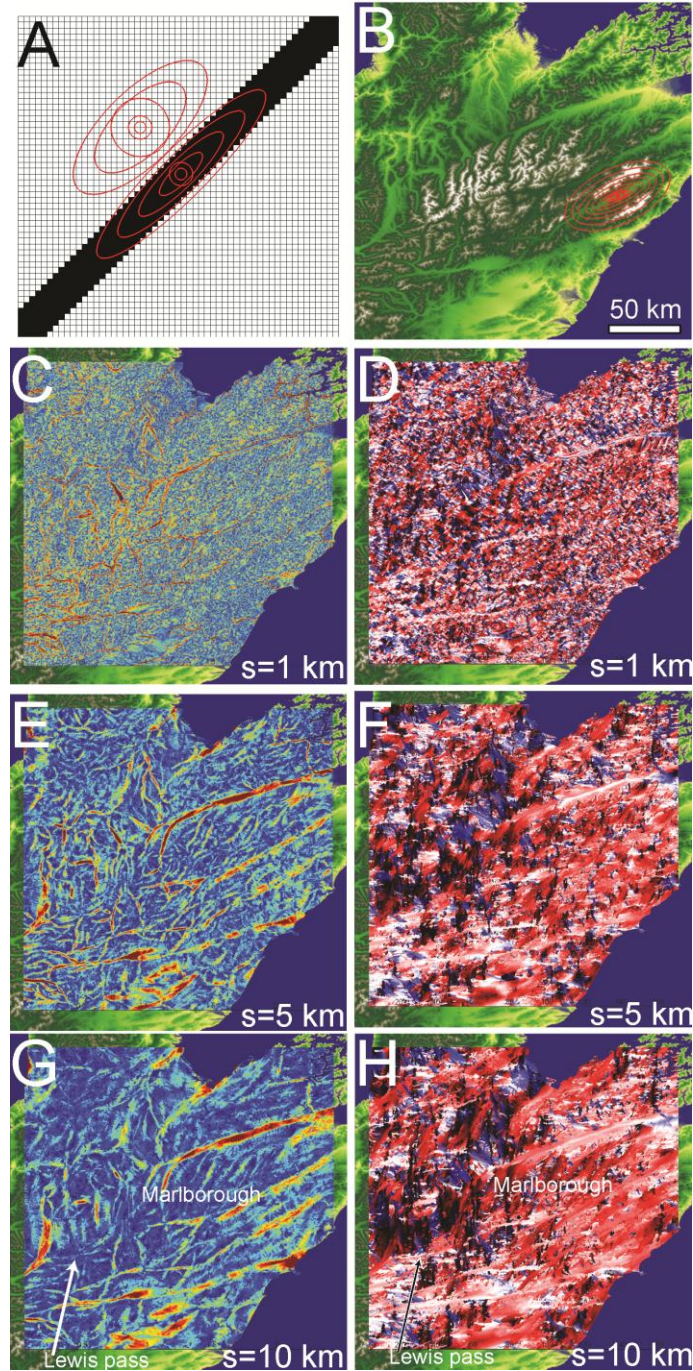
Figure 5.6. Anisotropy of structural landform. Low relief trough bisecting high relief plateau (A); a simplified replication of fault damage influenced topography. (B) Anisotropy measured at single point in Marlborough. Anisotropy measured up to maximum wavelength of 37.5 km. (C) Anisotropy magnitude and (D) orientation map at 1 km, (E) (F) 5 km, and (G) (H) 10 km wavelength.

a high local signal of anisotropy with an orientation roughly orthogonal to the large rivers draining northeastward (Figure 5.6D). From 1 km to 5 km wavelength, topographic orientation in ridges and valley walls tends to align with the large rivers, shifting in an east-northeast direction, particularly in eastern and southern Marlborough (Figure 5.6F). In Western Marlborough and around Lewis Pass, the dominant orientation becomes north-northwest following other valleys that correlate with other fault structures (Craw et al., 2013). There is a significant decrease in anisotropy magnitude in ridges and valley walls at greater wavelength, coinciding with the change in orientation (Figure 5.6G, H). In the western part of the Marlborough region, erosion along intersecting faults causes segmentation of ridges, further reducing ridge anisotropy.

5.4.1.4. Planar: Natural Example - Canterbury Plains

Planar topographic patterns offer minimal topographic relief over kilometer length scales. I replicate the flat, gently dipping form of large deltas in my synthetic landscape by applying a flat plane with low dip angle (Figure 5.7A). Variance tends to be relatively low in all directions due to the lack of relief, represented by circular, generally equant ellipses at short length scales (Figure 5.7A). Anisotropy does increase with greater separation distance along the contour of the plane because variance persistently approaches zero perpendicular to the slope. If the planar feature had no slope, the signal would be isotropic. The degree of anisotropy is proportional to the surface gradient. In Canterbury Plains, New Zealand, large amonts of alluvium have deposited to form a planar delta gently dipping to the southeast (Leckie, 1994). The natural example follows a similar trend but shows slight
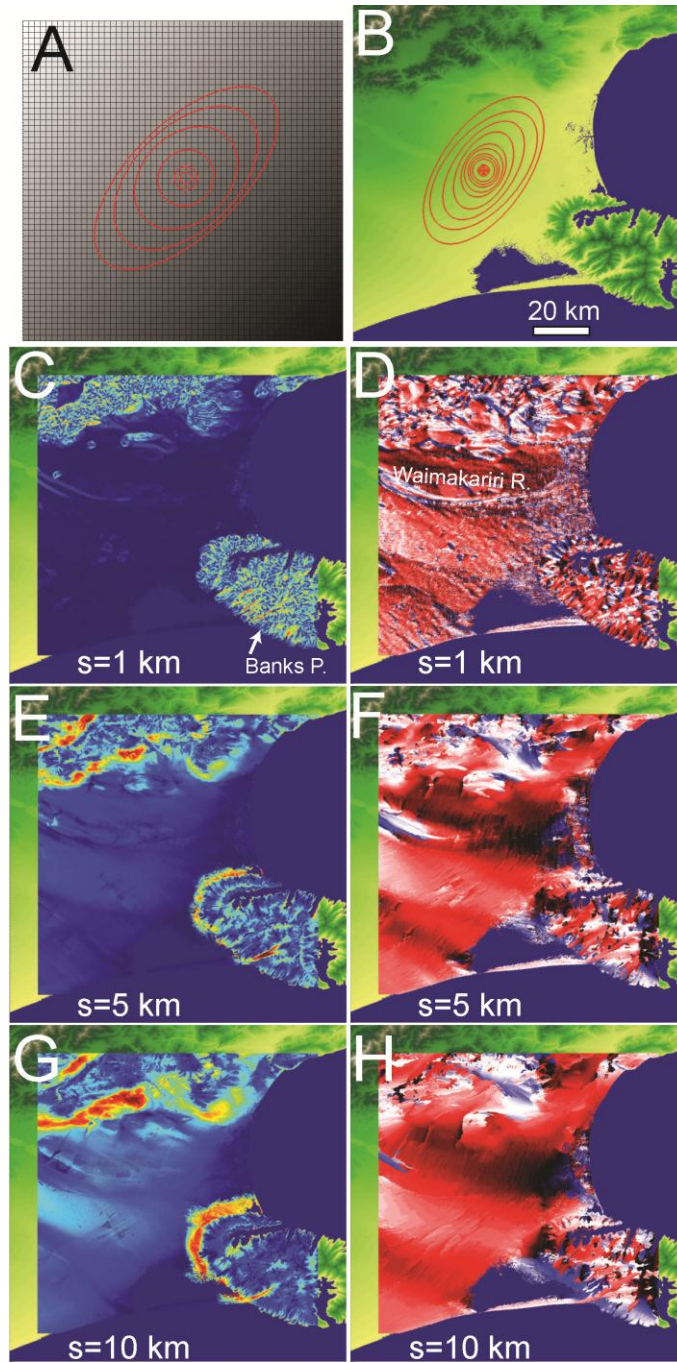
Figure 5.7. Anisotropy of planar landform. Plane gently dipping southeast (A); a simplified replication of low relief planar topography found in Canterbury Plains. (B) Anisotropy measured at single point in center of Canterbury Plains delta. Anisotropy measured up to maximum wavelength of 25 km. (C) Anisotropy magnitude and (D) orientation map at 1 km, (E) (F) 5 km, and (G) (H) 10 km wavelength.

changes in orientation associated with small, kilometer scale lateral changes in surface slope (Figure 5.7B).

The 1 km wavelength pattern displays homogeneous isotropy across the Canterbury Plains delta, in agreement with the single point analysis (Figure 5.7C). The delta is dominantly isotropic but there is a small degree of anisotropy and orientation change associated with the Waimakariri River and small local hills and ridges. Orientation on the delta is more variable but there is a small majority of northeast trending data points south of the Waimakariri River (Figure 5.7D). Outside of the delta the pattern of anisotropy reflects a ridge and valley topography associated with fluvial incision, particularly visible on Banks Peninsula. Anisotropy in the delta is slightly greater at 5-10 km wavelengths, and orientation is parallel to the general northeast strike of the tilted delta surface (Figure 5.7E-H). The steep topography along the Southern Alps to the northwest and the Banks Peninsula to the southeast create a spike in anisotropy along the perimeters in the delta (Figure 5.7G).

5.4.1.5. Monolithic: Natural Example - Taranaki

Monoliths tend to be largely isotropic at their peaks, due to their isolation from other high relief features. I replicate the shape of an isolated stratovolcano in my synthetic landscape by applying a cone shape with maximum elvation centered on the surface (Figure 5.8A). Unlike previously discussed topographic patterns, monolith peaks are persistently isotropic at all scales because variance is extremely high in all directions from the peak, as can be seen in the the concentric equant ellipses of Figure 5.8A. Mt. Taranaki dominates
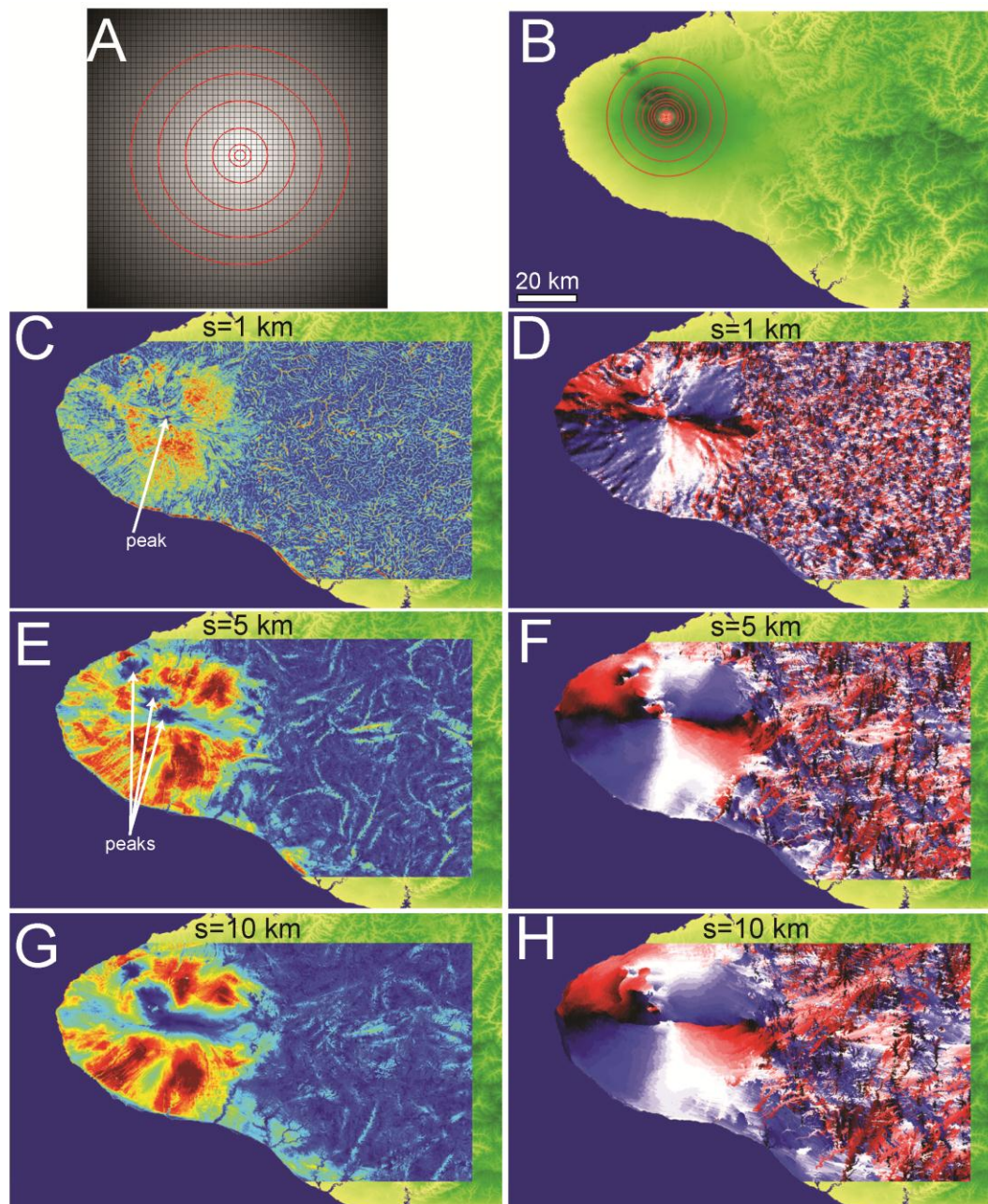
Figure 5.8. Anisotropy of monolithic landform. Idealized cone shape (A); a simplified replication of monolithic stratovolcano Mt. Taranaki. (B) Anisotropy measured at single point at peak of Mt. Taranaki. Anisotropy measured up to maximum wavelength of 25 km. (C) Anisotropy magnitude and (D) orientation map at 1 km, (E) (F) 5 km, and (G) (H) 10 km wavelength.

its regional topographic field as an isolated feature of high relief and is represented by the same pattern of radial isotropy (Figure 5.8B).

Anisotropy maps display a strong signal of isotropy about the peak, closely surrounded by a radially oriented distribution of extremely high magnitude anisotropy at all wavelengths (Figure 5.8C-H). The slopes of the stratovolcano increase in anisotropy magnitude at greater wavelength, but their orientation remains relatively unchanged. Changes in anisotropy magnitude along the slopes reveal the imperfect symmetry of the stratovolcano and the presence of two other extinct and largely incised stratovolcanoes trending northwest (Grant-Taylor, 1964). Anisotropy is particularly low at the peaks of the extinct volcanoes and along the eastern flank of Mt. Taranaki. To the east of Mt. Taranaki relief is largely influenced by fluvial processes and anisotropy in that region is greatest at the 1 km wavelength. Anisotropy on Mt. Taranaki is greatest at 10 km wavelength and could become greater at wavelengths I do not measure here.

5.4.1.6. South Island, New Zealand

Figure 5.9A is an example of EVA used to measure the directional depedence of a single point on the Southern Alps at separation distances up to 450 km. There is an obvious topographic anisotropy in the South Island associated with the trend of the Southern Alps that initially increases, then persists with greater wavelength. This single point analysis is apparently insensitive to more diverse landforms, some of which were explored above, that appear at shorter wavelengths and in other locations (Figure 5.1).

The characteristic patterns of these shorter wavelength landforms are revealed with anisotropy maps covering all of South Island (Figure 5.9B-G). Bathymetric data were used
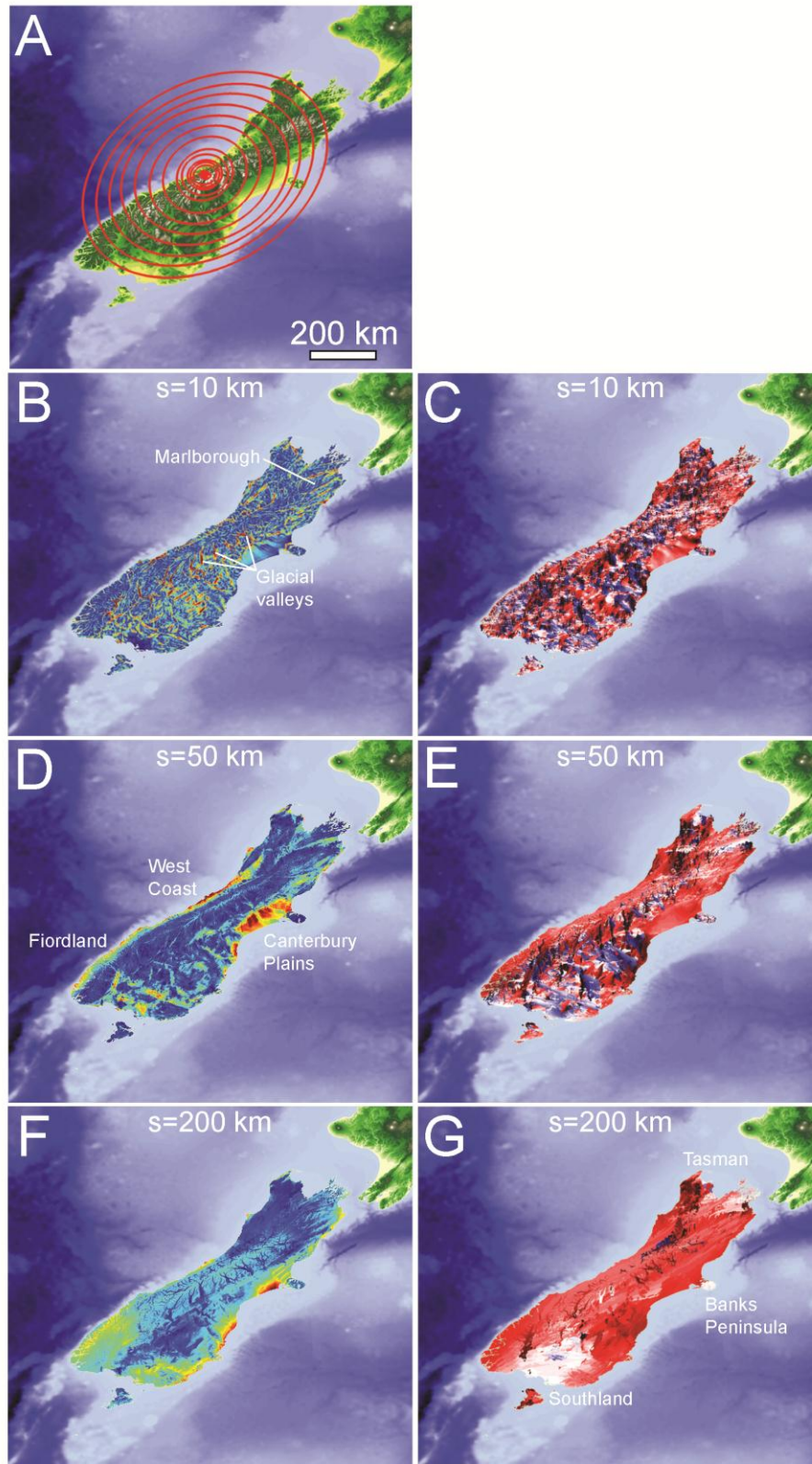
Figure 5.9. Anisotropy of South Island, New Zealand. (A) Anisotropy measured at point near Southern Alps divide. Maximum wavelength: 450 km. (B) Anisotropy magnitude and (C) orientation map at 10 km, (D) (E) 50 km, and (F) (G) 200 km wavelength.

to calculate anisotropy for terrestrial points, but anisotropy was not measured for any bathymetric points. Topographic anisotropy magnitude and orientation were measured from 1 km to 200 km for all points on South Island. At 10 km wavelength, anisotropy is greatest in the eastern glacial valleys of the Southern Alps and along the river valleys in the Marlborough region (Figure 5.9B, C). Orientations are diverse but follow the local directions of ridges and valleys. At 50 km wavelength, the edges of the Southern Alps, particularly the west coast, Fiordland, and Canterbury Plains, exhibit high magnitude anisotropy while anisotropy in the glacial valleys is diminished (Figure 5.9D, E). The orientation data in these regions generally follow the northeast trend of the Southern Alps. At 200 km wavelength, anisotropy increases along the Southern Alps divide, and the orientation data are dominated by the trend of the orogen except in Central Southland, Banks Peninsula, and Tasman regions (Figure 5.9F, G).

5.5. Discussion

5.5.1. Generalized Landform Fabrics

The five types of landforms that I explore (dendritic, deformational, fault damage, planar, and monolithic) host unique patterns of anisotropy associated with the processes that shaped them. In general, tectonic activity can introduce and amplify anisotropy at any wavelength. At the orogenic scale (>100 km wavelength), tectonism dominates the topographic fabric by controlling the gross shape of the Southern Alps (Figure 5.9A). The orogen is the product of oblique collision and so is a deformational landform under my characterization. Below the orogenic scale, the shape of topography, and hence anisotropy,

is dependent on fluvial processes reflecting the presence or absence of tectonic deformation and/or damage gradients.

Regions that lack past or present tectonism or consist of a uniform lithology are generally isotropic. Homogeneous landscapes do not provide a directionally dependent advantage for rivers and a dendritic drainage pattern is the common result. River meanders can occur at a multitude of wavelengths and as a result, topographic anisotropy gradually decreases and orientation frequently changes with increasing wavelength. For this reason dendritic landforms commonly exhibit high anisotropy magnitude with sporadic orientation at short wavelengths and low anisotropy magnitude with sporadic orientation at large wavelengths. This is the case for the Wairoa region, in which a largely homogeneous siltstone unit uplifted uniformly is incised by a series of dendritic rivers. A similar case is made for the region east of Mt. Taranaki.

The influence of glacial/fluvial incision is apparent at wavelengths less than 50 km according to my South Island-scale analysis (Figure 5.9), and 30 km according to other analyses of New Zealand topography (Koons, 1994; Koons, 1995; Koons et al., 2012). The tectonic signature of large anisotropy persists at shorter wavelengths through the introduction of damage and differential uplift along fault structures and the strong sensitivity of fluvial processes to these heterogeneous changes. This is the case for Central Otago, in which distributed deformation is reflected by the topography, and in Marlborough, in which a combination of localized deformation and fault damage is also reflected by the topography. In both cases, rivers conform to the heterogeneous damage and displacement fields, causing high order rivers to follow synforms or fault damage zones while short, low order tributaries convene at an orthogonal angle and incise into the

ridges. The presence of these tributaries causes a shift in anisotropy orientation at a wavelength equal to half of the ridge width. The synthetic landscape in Figure 5.6A fails to replicate this scale-dependent shift in the ridge because it lacks fluvial contributions to topography. In the case of Marlborough, ridge width is a function of the fault spacing width. In the case of Central Otago, ridge width is a function of crustal rheology and the thickness of the deforming layer (Chapple, 1978; Upton et al., 2009). As a consequence, ridge anisotropy contains important quantitative information about scale-dependent interactions between crustal rheology and the drainage network pattern. Deformational landforms do not require fluvial incision to produce their characteristic long wavelength anisotropy. Fault damage landforms depend on fault erosion to produce their characteristically extreme multiscale anisotropy. However, topography in the Marlborough region is more likely attributed to a combination of deformation and river incision along fault structures.

Coastal depositional processes tend to create a wide distribution of low relief and consequently exhibit low anisotropy on their own, but this pattern is commonly punctuated by the edges of the basin in which they are located. This is the case for Canterbury Plains, in which a large delta maintains a consistent shallow dip angle towards the sea. Large rivers may have a small local effect on anisotropy, but in general the weak contour-parallel anisotropy pattern is pervasive. This pattern quickly dissipates when the wavelength is long enough to reach the edge of the basin, at which point there is a significant increase in anisotropy at an orientation parallel to the edge of the basin.

Monoliths are characterized by an isotropic signal at their peak surrounded by concentric high anisotropy along the slopes and a radial pattern of orientation. The pattern of anisotropy remains unchanged over all measured wavelengths because the stratovolcano

is radially symmetric, and the topography surrounding it is relatively consistent. This is the case for Mt. Taranaki, a symmetric stratovolcano. This generalization breaks down slightly in this region due to asymmetric fluvial incision along the flanks of the volcano and the presence of two nearby smaller cones that diminish the symmetry along the flanks of the stratovolcano.

5.5.2. Comparison of EVA to Self-Affine Power Law Scaling

Over the past ~45 years a large body of work has demonstrated that many systems can be described as self-similar, meaning that specific patterns become statistically invariant across multiple scales (e.g. Barnsley et al., 1988; Jébrak, 1997; Klinkenberg and Goodchild, 1992; Mandelbrot, 1967; Roy et al., 2012), or self-affine, meaning the scale-invariant behavior is apparent but limited by directional dependence (Xu et al., 1993; Dodds and Rothman, 2000; Sung and Chen, 2004). I have already recognized directional dependence in my examples, therefore I test for self-affinity.

Measurements of variance in elevation may tend to increase as a power law function with increasing length scale

$$v^2(s) = ks^\alpha \qquad\qquad (5.5.)$$

where $v^2(s)$ is the variance at separation distance, or wavelength s, α is the scaling parameter, and k is equal to $v^2(1)$. For a truly self-affine system the scaling parameter remains constant and contains information about the complexity or roughness of a topographic surface (Chase, 1992; Klinkenberg and Goodchild, 1992; Lifton and Chase, 1992; Shepard et al., 1995). A larger scaling parameter symbolizes a larger increase in surface complexity with scale, requiring a power law increase in variance with increasing

wavelength. A fractal dimension can be calculated from the scaling parameter (Klinkenberg and Goodchild, 1992; Lifton and Chase, 1992; Shepard et al., 1995; Wilson and Dominic, 1998; Sung and Chen, 2004), but I choose to use the scaling parameter on its own as a diagnostic tool for landscape complexity.

I first test the self-affine method on a single, randomly chosen point in Central Otago (Figure 5.3C, Figure 5.5) and measure variance for separation distances up to 9 km in 360 directions in 1° intervals (Figure 5.10A). There is an obvious spread in data owing to the directionally dependent roughness of the landscape. As more points are included in the averaging for each orientation (Figure 5.10B), an apparent power law distribution emerges for all orientations within my range of separation distances. The scaling parameter and the coefficient both vary as a function of orientation. The lowest scaling parameter of 0.52 occurs along 36°, east-northeast, which happens to be virtually parallel to the fold axes in Central Otago (Figure 5.10C). The largest scaling parameter of 0.74 occurs along 124°, north-northwest, virtually orthogonal to the dominant ridge orientation.

These results are suggestive of a distinct fabric that is pervasive throughout the sampled region, with a more complex fabric that exists orthogonal to the main ridge-valley orientation, and less complexity parallel to it. In this way the basic fabric of the landscape is recognized by this analysis and is in agreement with EVA. Despite this result, it is clear that this method is not sensitive to the spatial dependence of topographic fabric. The need to average variance values over 960,000 points spanning a 9600 km^2 area in order to generate the expected power-law distribution diminishes the information about local changes in fabric. Additionally, the need to average variance across large areas to produce the expected power-law trend is not necessarily a self-affine characteristic and it may be

inappropriate to analyze the landscape by such a statistical method (Clauset and Shalizi, 2007).
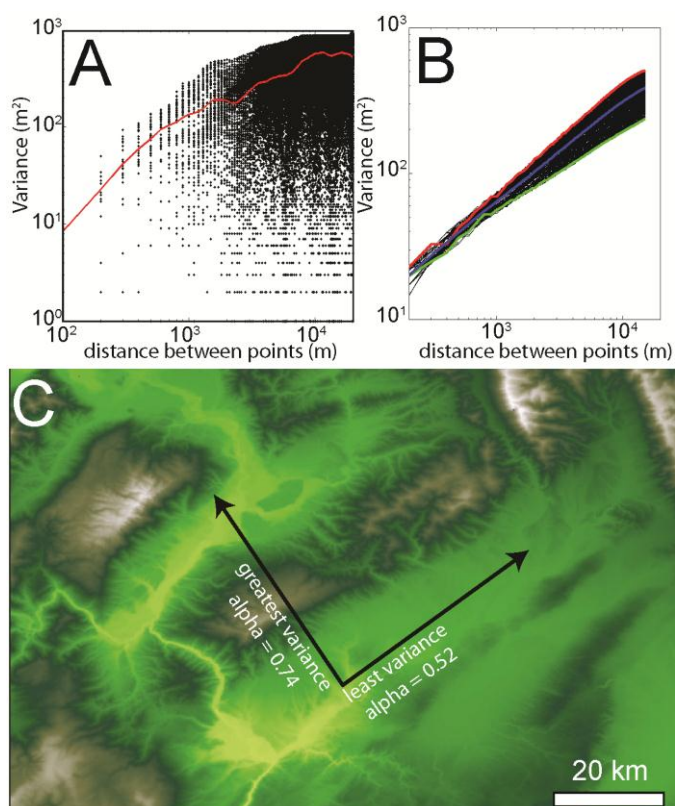
Figure 5.10. Example of self-affine method. Variance measured at single, randomly chosen point (A) along 1 degree intervals for 360 degrees up to 20 km separation distance at ~100 m intervals. Black dots indicate the variance, red line indicates trend of the averaged data. (B) Plot similar to A but for all points in the domain, variance values are averaged by direction to compare scaling by orientation. Maximum scaling parameter indicated in red (0.74), minimum indicated in green (0.52), mean indicated in blue. (C) Central Otago with the maximum and minimum scaling parameter orientations indicated.

EVA is a useful tool for quantifying landscape anisotropy because it gives orientation and magnitude data captured by the analysis at locally representative points. Giving spatial relevance to orientation data provides a better understanding of the topographic fabric in general by being sensitive to local, scale-dependent changes in topographic anisotropy. It is not possible to obtain this resolution by confining the results to regional-scale analysis using the self-affine scaling parameter, which is limited by either lack of directional data or lack of spatial relevance, depending on how data are averaged.

For example, the shift in anisotropy orientations associated with fluvial terrains and fault damage terrains, as seen in the Marlborough region, would preclude these types of terrains from analysis by self-affine statistics because this transition suggests scale-dependent changes in the scaling parameter, which cannot be appropriately defined as self-affine. By rejecting the assumption for self-affinity I are able to more completely determine and characterize the scale dependencies that arise when multiple mechanisms contribute to the landscape at differing wavelengths.

5.5.3. Future Work

My method and analysis provide a small example of the strength of topographic anisotropy in determining and disseminating the scale-dependent contributions of tectonic and fluvial processes. My code allows for the rapid calculation of variograms for every direction and each point on a surface for multiple scales. The next step would be to use EVA to interpret the topographic record of past and present changes in climate and tectonics. I have only explored generalized landscape patterns associated with specific processes, which can be expanded upon by studying a larger sampling of less generalizable landforms, and pursuing more situations in which several processes, occurring at different times or simultaneously, have created an integrated landform that does not reflect a single generalizable shape. Another possibility is to use EVA to explore topographic anisotropy that is not associated with tectonic activity. For example, it would be possible to use EVA to find the edges of paleoshorelines, or to quantify lithological controls on topographic shape that are not specifically related to tectonism. EVA can be used for any spatially variable characteristic, so there are applications beyond elevation variance. The potential

for unearthing the geological history of an area purely from topographic form is an old concept, and the utilization of multiscale EVA can drastically increase the capabilities of these first-order interpretations of landforms.

5.6. Chapter Conclusions

I apply multiscale every-direction variograms analysis (EVA) to quantify the fabric of multiple landforms. Topographic anisotropy, defined as the ratio of minimum variance to the orthogonal variance, is found to be a useful metric for linking generalized topographic landforms to their influential tectonic and fluvial processes. I apply this method in a multiscale approach to help interpret scale-dependent changes in topographic fabric. Generally speaking, fluvial processes tend to reduce anisotropy while tectonic processes tend to increase anisotropy. Depositional environments, such as deltas and basins, are largely isotropic but increase in anisotropy at longer wavelengths. Monolithic landforms, such as stratovolcanoes, are generally isotropic at their peaks with strong radial anisotropy along the surrounding flanks. Other methods for determining topographic fabric such as self-affine power law statistics provide useful information but may lack the sensitivity to spatial and directional fabrics that reveal the relative contributions of tectonics and climate. Further work on this topic should focus on a greater extent of testing upon more landforms with ambiguous or variable tectonic, climatic, and geomorphological histories.

5.7. Chapter Acknowledgements

CHAPTER 6

ROCK STRENGTH HETEROGENEITY AND ITS EFFECTS ON FLUVIAL

INCISION AT THE REGIONAL (100 KM) SCALE AND IMPACTS

ON THE NEAR SURFACE STRESS FIELD

6.1. Chapter Abstract

I explore regional scale implications for fault erosion, the sensitivity of surface processes to the timing of fault zone exposure/introduction, erosion of exhumed plutons, and overall effects of localized fault erosion on the near surface stress field. Results suggest that damage zones influence topographic shape to a greater degree by the erosion of multiple intersections. Whether damage zones are eventually exposed by exhumation or if they are imposed on the landscape at a later time, there is still a strong influence on the drainage network pattern. However, this influence diminishes with greater rate of uplift relative to baselevel. Exposure of damage zones and subsequent localized incision can significantly perturb the near surface stress field to the advantage of continued failure within the damage zone. This stress pattern is expected to play a significant role in the link between tectonics and surface processes.

6.2. Chapter Introduction

A simple scaling rule was applied in Chapter 3 to relate the cohesive strength of damaged and undamaged rock to an erodibility coefficient for use in a stream power model. This scaling rule provided a means to test the effects of localized crustal weakening on the patterns and rates of surface processes. From my results I suggested that the presence of

planar weak zones can strongly influence the evolution of drainage network patterns, limit maximum relief in a region, increase knickpoint migration rates along high order channels, and reduce the overall response time of topography to baselevel perturbations. These experiments were limited in spatial scope: single weak zone sections were isolated at the sub-kilometer scale from the broader scale distribution of weak zones associated with specific tectonic regimes. I use this chapter to explore some of the unanswered questions brought up in Chapter 3, namely 1) the significance of damage zone spacing and orientation in limiting relief and controlling the drainage network pattern, 2) the significance of weak zones as corridors for sediment flux, and 3) the significance of timing between topographic evolution and the emplacement or exhumation of weak zones.

To begin to answer these questions, I produced five experiments in which planar 3D conjugate weak zone pairs were imposed on a numerical model of landscape evolution. The geometry of conjugate weak zone sets was determined analytically by using the Mohr-Coulomb yield criterion (Coulomb, 1773). The weak zones impose a predictable pattern of heterogeneous erodibility within the landscape evolution model with my intent to influence the rates and patterns of fluvial incision. Next, I tested the sensitivity of surface processes to weak zones that are exposed at a later time, both by exhumation and by direct emplacement to represent the uncovering of damaged rock caused by an instantaneous tectonic event, respectively. Finally, I tested sediment transport within the weak zones using a model that combines rock erosion and sediment transport.

6.3. Methods

I use the same unit stream power-based fluvial incision model, assuming detachment-limited conditions, and the same cohesion-erodibility scaling rule as discussed in Chapter 3. Please refer to that chapter for more information.

I model five different groups of weak zones representative of five different currently inactive fault sets, described in Table 1 (Figure 6.1A-E). For a Mohr-Coulomb crustal rheology, damage zone spacing and orientation are a function of 1) the stress regime that caused brittle failure in the crust, 2) the possibility of symmetric, conjugate faults to form upon brittle failure, and 3) the vertical distance from the surface to the decollement. The orientation of these fault zones is broadly predictable for any deformation regime if the principal stress orientations are known (Coulomb, 1773). The internal angle of friction is used to determine fault set orientations but it is not incorporated into the erodibility calculation. The fault orientations, cohesion values, and Equation 3.4 define the 3D erodibility field used in the landscape evolution model.

For my models, the first principal stress axis is fixed normal to the single open boundary along the horizontal plane, and the second and third principal stress axes rotate 90˚ counter-clockwise from convergent to transverse regimes (Figure 6.1). The weak zones convene at the decollement assumed to lie on the Frictional-Viscous Transition at 15 km depth (Price et al., 2012). I change the reference frame for my strike-slip model so that the fault zone strikes orthogonal to the single outlet boundary. I determine fault strike and dip by the intersection between fault plane and the horizontal model surface (Table 1). A uniform uplift rate of 1 mm a^{-1} is applied to perturb an initially flat model domain. Models were run to reach a steady topography at 1 Ma.
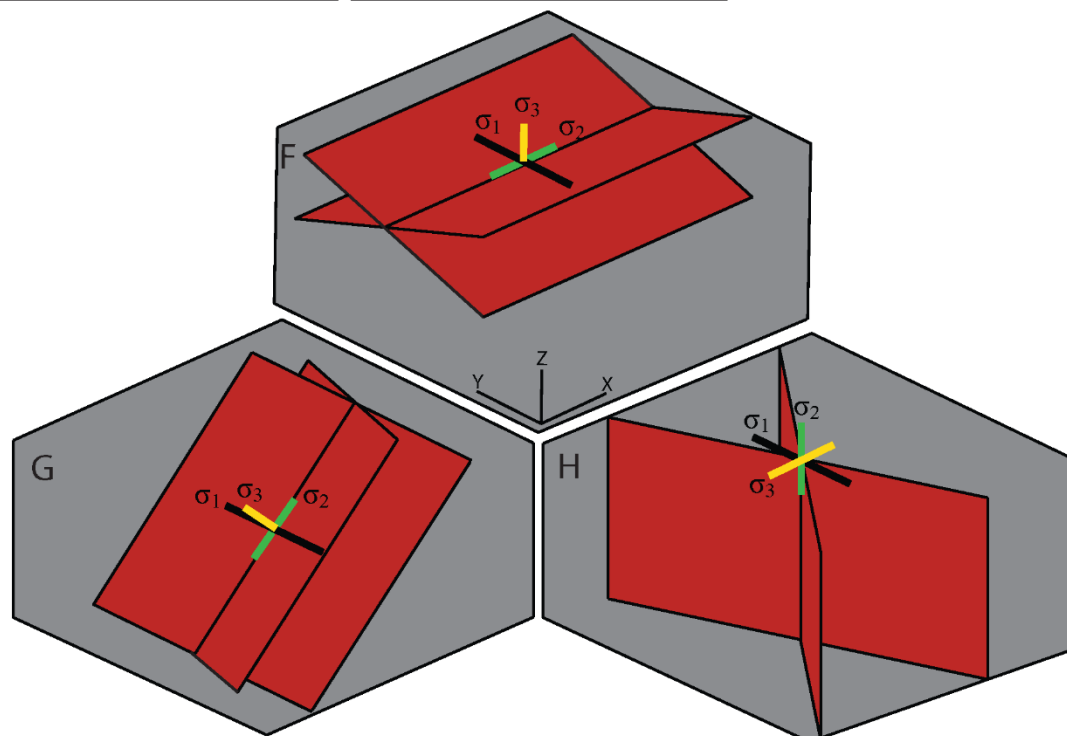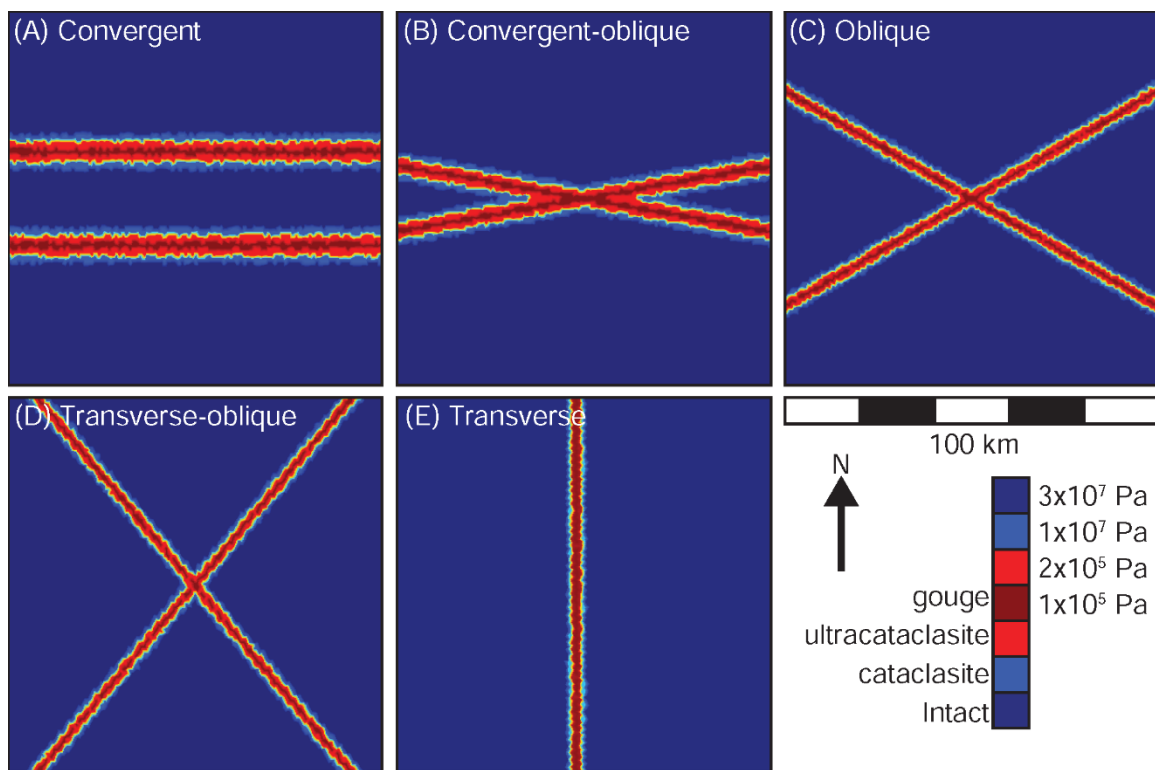
Figure 6.1. Surface exposure of conjugate pairs in map view. (A) Convergent, (B) convergent-oblique, (C) oblique, (D) transverse-oblique, and (E) transverse tectonic regimes. (F-H) the general pattern for failure planes for convergent, oblique, and transverse, respectively.

Table 6.1. Conjugate fault zone pair orientation data

Tectonic regime	Fault set dips	Fault set strikes
None – homogeneous	N/A	N/A
Convergent	30 N and 30 S	Due E-W
Oblique convergent	40 NW and 40 SW	10 SW and 10 NW
Oblique	60 NW and 60 SW	30 SW and 30 NW
Oblique strike-slip	80 NW and 80 SW	50 SW and 50 NW
Strike-slip	Vertical	Due N-S

6.4. Model Set 1: Landscape Sensitivity to 3D Fault Orientations

Results of Model Set 1 (Figure 6.2) indicate a strong influence of weak zone pairs on the drainage network pattern and topography in a landscape, taking the form of long, anomalously straight valleys containing high order channels. The only experiment that does not display this characteristic is the uniform strength example. The difference between these two channel patterns is evident from tortuosity measurements (Chapter 3) and topographic anisotropy measurements taken with EVA (Chapter 5). Where present, fault zones control the spatial distribution of ridge and valley topography and in doing so control the spatial distribution of runoff and erosion for the entire duration of the model run.

6.4.1. Homogeneous

The homogeneous experiment (Figure 6.2A) produces a drainage pattern with no strong directional dependence caused by heterogeneous strength. Low and high order channels form a dendritic drainage pattern (Figure 6.2G). Topographic anisotropy is widely dispersed at the 3 km wavelength and generally does not exceed $10^{1.5}$ at the 10 km wavelength (Figure 6.2M), indicating that there are few topographic features that have a consistent orientation at 10 km length. Anisotropy orientation is also widely distributed for both wavelengths.

6.4.2. Convergent

For convergent deformation regimes (Figure 6.2B) fault zones exposed at the surface are parallel and do not intersect one another or the outlet boundary. High order channels are confined to the weak zones and they are connected to the outlet boundary by a dendritic channel that is generally oriented transverse to the strength gradient. For this reason, erosion of intact rock along the transverse channel limits erosion in the weak zone pair. Most tributaries tend to branch orthogonal to fault zone strike. Tortuosity is generally lower where channels follow weak zones and higher along the transverse channel section, but the highest tortuosity values exist where the channel leaves, crosses, or enters the weak zones (Figure 6.2H). Topographic anisotropy exceeds $10^{2.5}$ in the valleys confined to the weak zones at both studied wavelengths and anisotropy orientation strongly reflects the E-W strike of the weak zones (Figure 6.2N).

6.4.3. Oblique

For oblique slip deformation regimes (Figure 6.2C, D) fault zones intersect and the drainage network relies less on erosion into the strong host rock as displayed by an overall decrease in tortuosity but with a local increase where faults intersect. The conjugate weak zone pair crossing in the convergent-oblique experiment (Figure 6.2I) leads to a significant change in topographic form relative to the convergent experiment. However, the valleys confined to both weak zones are still connected to the outlet boundary by a transverse channel. Extreme tortuosity values in the oblique-convergent (Figure 6.2I) and oblique (Figure 6.2J) are associated with a high order channel crossing between weak zones near their intersection. This is also the case for the oblique-transverse experiment (Figure 6.2K),
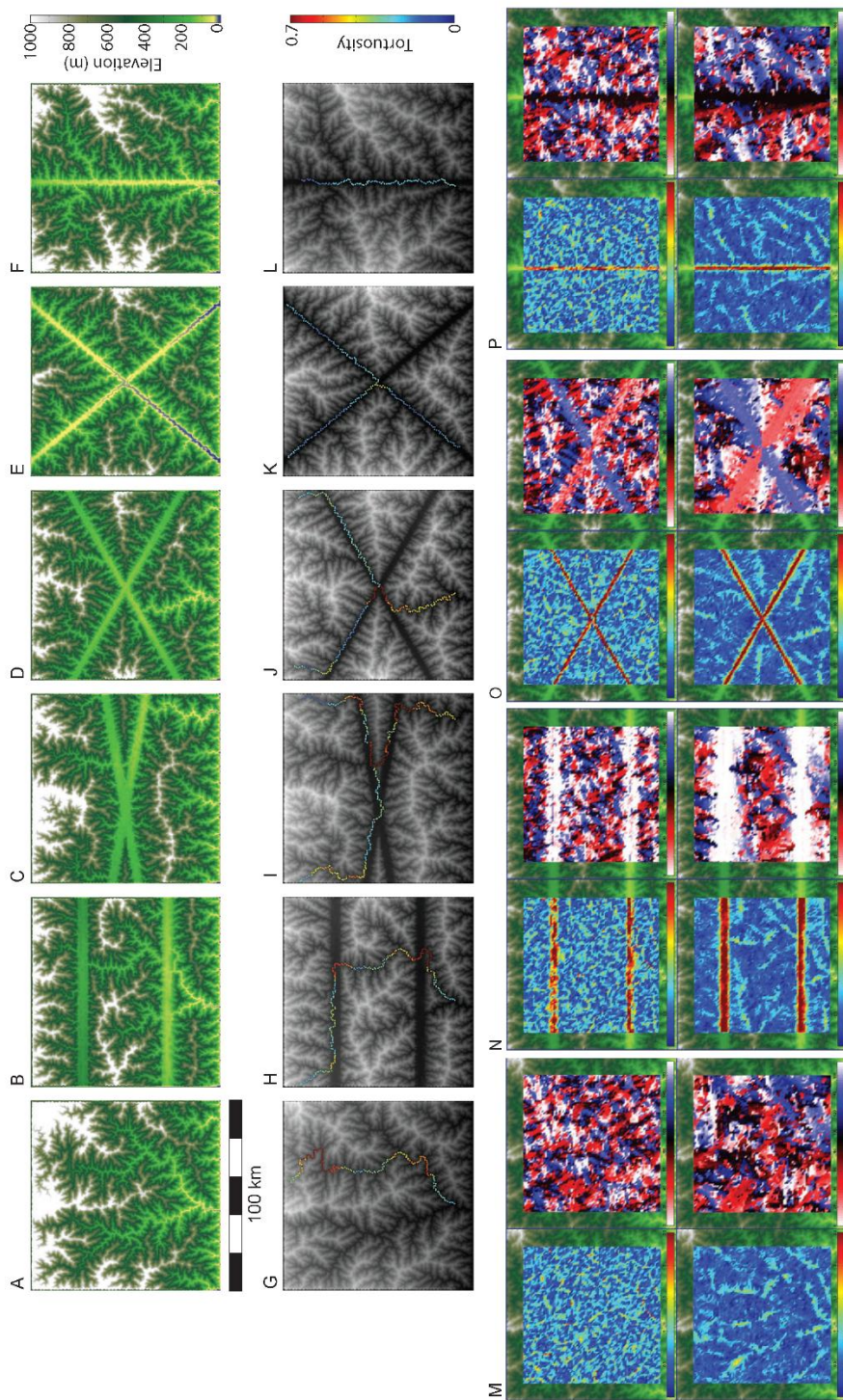
Figure 6.2. Topography, after 2 Ma of erosion and uplift. (A) homogeneous no weakening, (B) convergent, (C) convergent-oblique, (D) oblique, (E) oblique-transverse, and (F) transverse. Tortuosity values, measured at 10 km wavelength, for one or two channels (color lines) over topography (greyscale map) for (G) homogeneous, (H) convergent, (I) convergent-oblique, (J) oblique, (K) oblique-transverse, (L) transverse regimes. EVA results for (M) homogeneous, (N) convergent, (O) oblique, (P) transverse; clockwise from upper left, maps are 3 km anisotropy magnitude and orientation, respectively, and 10 km anisotropy magnitude and orientation, respectively.

but the decrease in maximum tortuosity reflects the wider angle at which the weak zones cross one another. For the oblique experiment, anisotropy magnitude exceeds $10^{2.5}$ along the weak zone controlled valleys and orientations show consistent ENE and WNW across both tested wavelengths (Figure 6.2O).

6.4.4. Transverse

Topography strongly reflects the transverse weak zone by producing a single high order channel fed by multiple short, low order tributaries (Figure 6.2F). Erosion on this vertically dipping weak zone creates an anomalously straight valley oriented normal to the outlet boundary. Tortuosity values are minimal along the high order channel (Figure 6.2L). Anisotropy magnitude exceeds $10^{2.5}$ along the weak zone controlled valley at both wavelengths, and orientations display a strong N direction in the valley and more scattered orientations along the tributaries (Figure 6.2P).

6.5. Model Set 2: Later Introduction of Weak Zone by Exhumation or Emplacement

I now explore the possibility of weak zones that are introduced to a domain after topography has approached a steady state condition in homogeneous crust. There are two methods by which I introduce the weak zone: 1) the weak zone is exhumed to the surface by progressive fluvial erosion, and 2) the weak zone is emplaced on the surface instantaneously. In the first case I explore the plausible situation that weak zones may exist at depth but due to some unconformity they are not immediately exposed at the surface and therefore will not immediately affect the drainage network pattern. For this method the unconformity is always completely horizontal. In the second case I am roughly estimating

damage sustained by the crust during an instantaneous seismogenic tectonic event. For this method I do not include deformation of the surface that would be associated with this tectonic event.

Experimental results in Figure 6.3A-I display an incremental change in topography associated with incremental exhumation of the weak zones. The basic topographic shape of the exhumed convergent, oblique, and transverse experiments resemble results from Model Set 1. Similarly, weak zones that are instantaneously emplaced on the landscape lead to production of the same topographic form. Similar patterns exist for weak zones that are instantaneously emplaced (Figure 6.3J-L).

Despite the similar topographic forms between Model Set 1 and 2, I see that the drainage network patterns associated with weak zone exhumation differ from patterns associated with initially exposed weak zones (Figure 6.4A, B). In the convergent example, weak zones are strongly reflected by topography but only by erosion along tributaries that feed into the higher order channels, which are not significantly influenced by appearance of the weak zones. The oblique experiment does display a greater influence on the drainage network pattern, and the vertically dipping transverse experiment strongly influences the weak zone geometry after exhumation.

The rate at which crust is exhumed has major implications for the ability of weak zones to influence topography (Figure 6.5) and the drainage network pattern (Figure 6.4C), but only for weak zones with shallow dip angle. Figure 6.5 displays results identical to Model Set 2.1 in all respects except uplift rate is increased by an order of magnitude. At this rate, weak zones become exposed more quickly after steady state topography is achieved. The result is a diminished influence of the weak zones on the drainage network
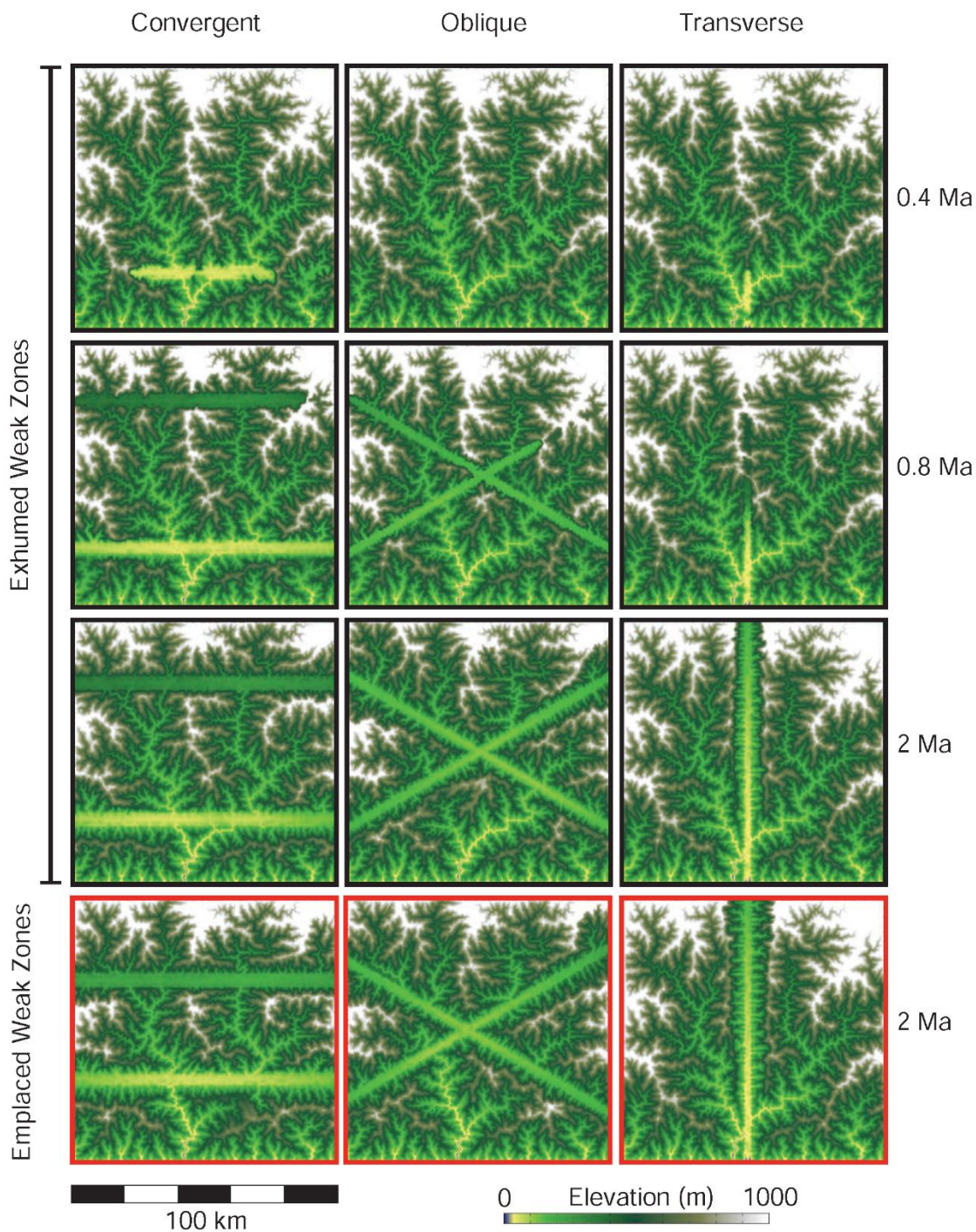
Figure 6.3. Incremental exposure and subsequent rapid erosion of weak zones. Convergent (A, D, G), oblique (B, E, H), and transverse (C, F, I) regimes. Instantaneously emplaced weak zones (J-L) display a similar topographic pattern.
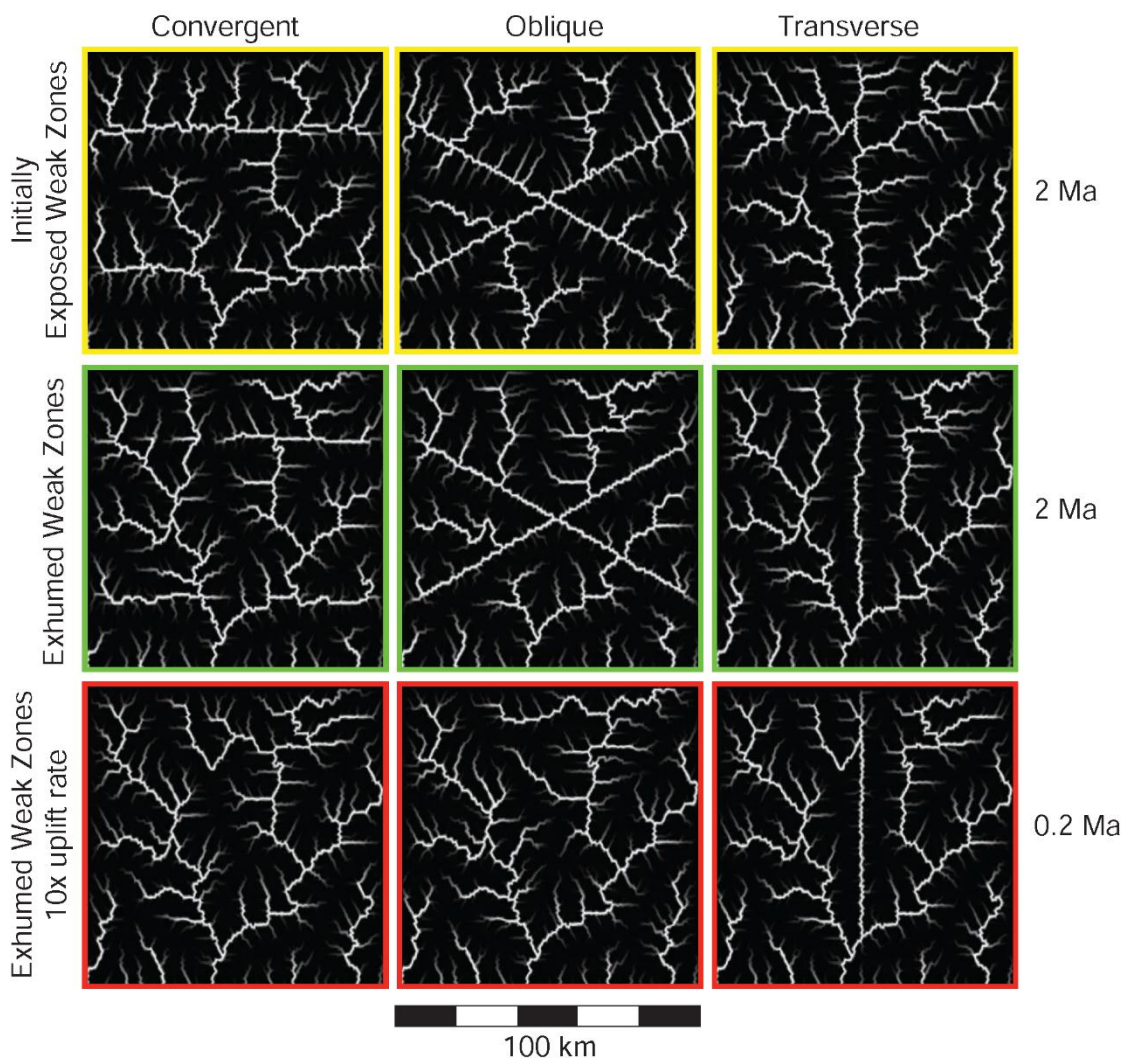
Figure 6.4. Hydrography maps for Model Sets 1 and 2.

pattern and an associated lack of influence on topography. However, the influence of weak zones still increases with weak zone dip angle. This influence is associated with the weak zone's exhumation being less dependent or independent of topography (Figure 6.5, kb maps).

Modeled topographic anisotropy remains relatively unchanged once it becomes established, but perturbations in the strength field may alter the preferred orientation of prominent valleys over time. For example, any shift in the deformation regime will overprint the strength field with new fault zone orientations and a combination of new and

old topographic features (Figure 6.6). This leads to new structurally confined features in the drainage network patterns, potentially causing flow reversals and stream capture among preexisting channels.
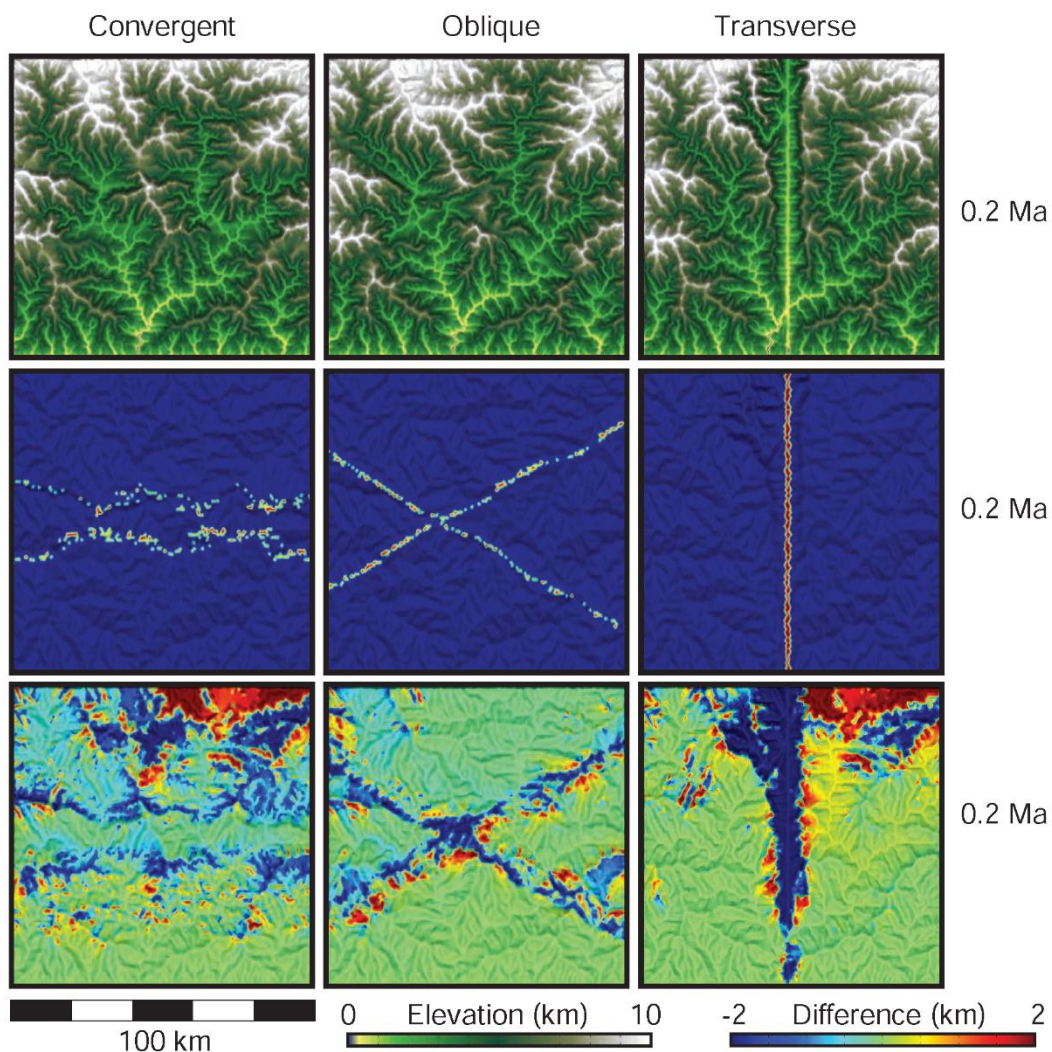
Figure 6.5. Comparison of different tectonic regimes. From top to bottom row, maps of elevation, erodibility, and difference in elevation between homogeneous and heterogeneous strength experiments, respectively. From left to right column, maps are of convergent, oblique, and transverse regimes, respectively.
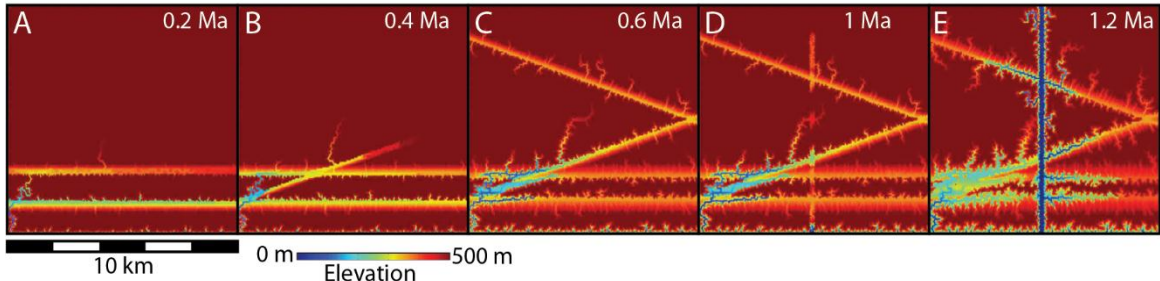
Figure 6.6. Time sequence of progressive damage zone emplacement. (A) Initially convergent regime superimposed by (B) oblique regime, both of which continue to steer topography (C). Later on a transverse regime is superimposed over both (D) and this causes rapid and significant changes to the drainage network pattern (E).

6.6. Model Set 3: Sediment Routing Through Structurally Confined Channels

I now explore the residence and transport of sediments across the drainage network patterns explored above. The grain size distributions and equations for sediment transport and bedrock incision used here are identical to the 3000X example used in Chapter 4.

Much like in Chapter 4, the majority of sediments reside in fault damage zones in part because they tend to attract surface runoff through rapid erosion, and also because they maintain comparably very low relief due to a high erodibility value (Figure 6.7). Conversely, tributaries that traverse the intact bedrock contain very little sediments. In the case of convergent and convergent-oblique regimes, sediments can reside in large transverse channels that connect the damage zones and lateral channel migration creates a wider distribution of sediments (Figure 6.7A, B). For oblique and transverse regimes (Figure 6.7C-E), faults intersect the flow outlet boundary and there are no transverse channels, in which case the majority of sediments reside in the damage zones.
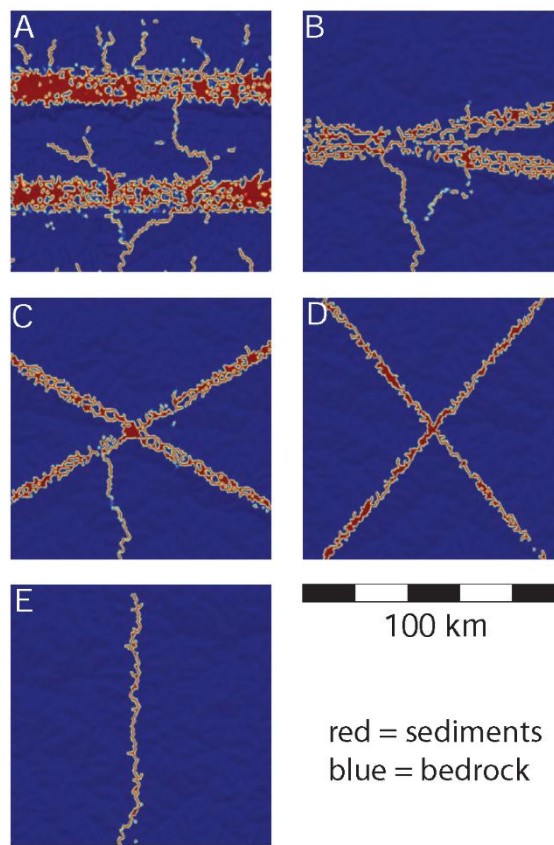
Figure 6.7. Sediment maps. (A) Convergent, (B) convergent-oblique, (C) oblique, (D) oblique-transverse, and (E) transverse regimes. Red indicates presence of bedload, blue indicates exposed bedrock.

6.7. Model Set 4: High Frequency Fault Damage

A higher frequency of fault damage within the crust is possible for more complex tectonic regimes, particularly where more than one decollement may exist. In these cases there is no limit to the minimum spacing between damage zones. For this reason structurally confined channels may become more prominent and there may be a greater limit on total landscape relief. Figure 6.8 displays results from experiments in which a number of damage zones are distributed randomly in a 625 km^2 domain. High frequency damage zones have a similar effect as the damage zones in Experiment 1, using the same rules for erosion. However, there are a greater number of instances in which the intersection
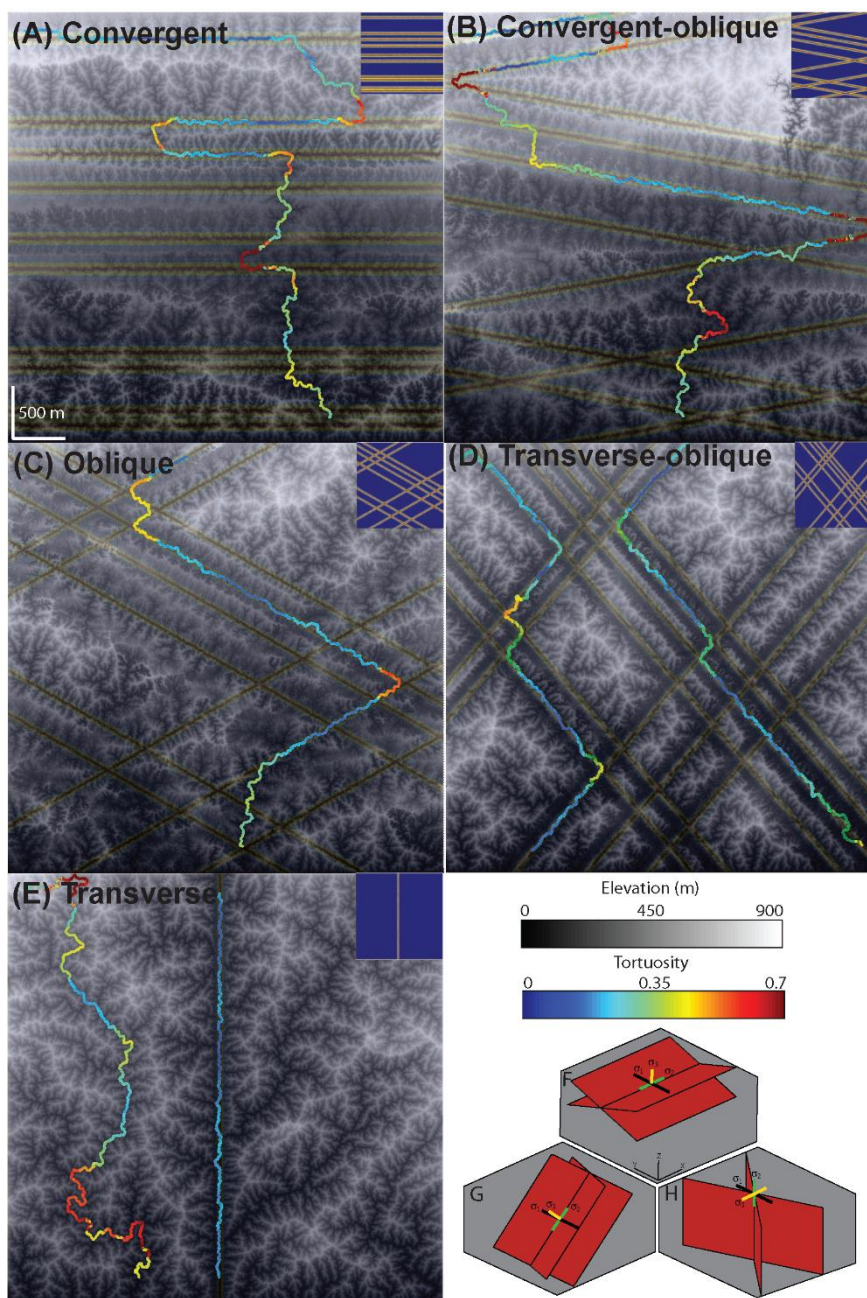
Figure 6.8. Model topography (greyscale images) with maps of rock strength and channel tortuosity superimposed. (A) Convergent, (B) convergent-oblique, (C) oblique, (D) transverse-oblique, and (E) transverse tectonic regimes. (F-H) the general pattern for failure planes for convergent, oblique, and transverse, respectively.

of damage zones can cause a distinct shift in channel orientation as shown by extreme tortuosity values around these intersections. There is also a greater distribution of topographic anisotropy attributed to a greater number of channels and tributaries incising into a greater number of damage zones.

6.8. Model Set 5: Exhumation of a Granitic Pluton

Plutons that are gradually exposed by exhumation often form steep relief relative to their surroundings. For example, the Cairngorm Mountains of Scotland are a low relief plateau consisting of a granitic pluton. The Cairngorms lie 900-1200 m above sea level and peaks are separated by deep troughs eroded into structural weaknesses (Goodfellow et al., 2014). In this section, I explore the influence of lithology and structural weaknesses on landscape evolution by modeling a region with eventual exposure of a resistant granitic pluton. I provide two experiments: one in which the pluton is uniformly more resistant than the surrounding host rock, and another in which the pluton hosts fractures that are less resistant than all other units.

6.8.1. Model Setup

A cube-shaped pluton with a cohesive strength of 30 MPa lies 5 km beneath the surface, surrounded by 3 MPa schist. The pluton takes up $1/9^{th}$ of the model domain and is centrally located upon exposure. There is no strength gradient associated with contact metamorphism. Fractures hosted by the pluton, applied only to the second experiment, strike in a N-S direction and have 3 MPa cohesive strength to match the schist. The model domain is uplifted relative to baselevel at a rate of 1 mm yr^{-1}. All other conditions are equal

to values used in the previous experiments. The combination of pluton depth, domain size, uplift rate, and climate parameters ensure that topography achieves a steady-state condition before the pluton becomes exposed. An initial steady-state condition is important to ensure that the strength differential associated with pluton exhumation does not have an inherited influence on topography, but rather a late stage effect that may perturb the inherited drainage network pattern.

6.8.2. Uniform Strength Pluton

Before pluton exposure, the landscape is dominated by dendritic drainage patterns and low relief topography (Figure 6.9A, D, G). The pluton is exposed after 5 My of uplift and immediately perturbs the steady-state topography, particularly in low order tributaries and hillslopes in the center of the model domain (Figure 6.9B). Channel slopes in the pluton region steepen (Figure 6.9H) and there is small reorganization of the drainage network pattern along the perimeter of the pluton (Figure 6.9E). Reorganization here is associated with stream piracy when channels that previously traversed the pluton lose tributaries across the erodibility gradient.

6.8.3. Pluton with Joints

The topographic response during pluton exposure with embedded fractures is identical to the previous experiment except the fractures influence the drainage network pattern (Figure 6.9C). Channels reorganize to align with the weak fractures as the pluton is exposed, leading to a strong N-S trend in drainage (Figure 6.9F). Low relief along fractures produces a sawtooth topographic profile along the E-W direction (Figure 6.9I).

Erosion along these fractures reduces the local elevation and produces a greater amount of windgaps deep within the pluton.
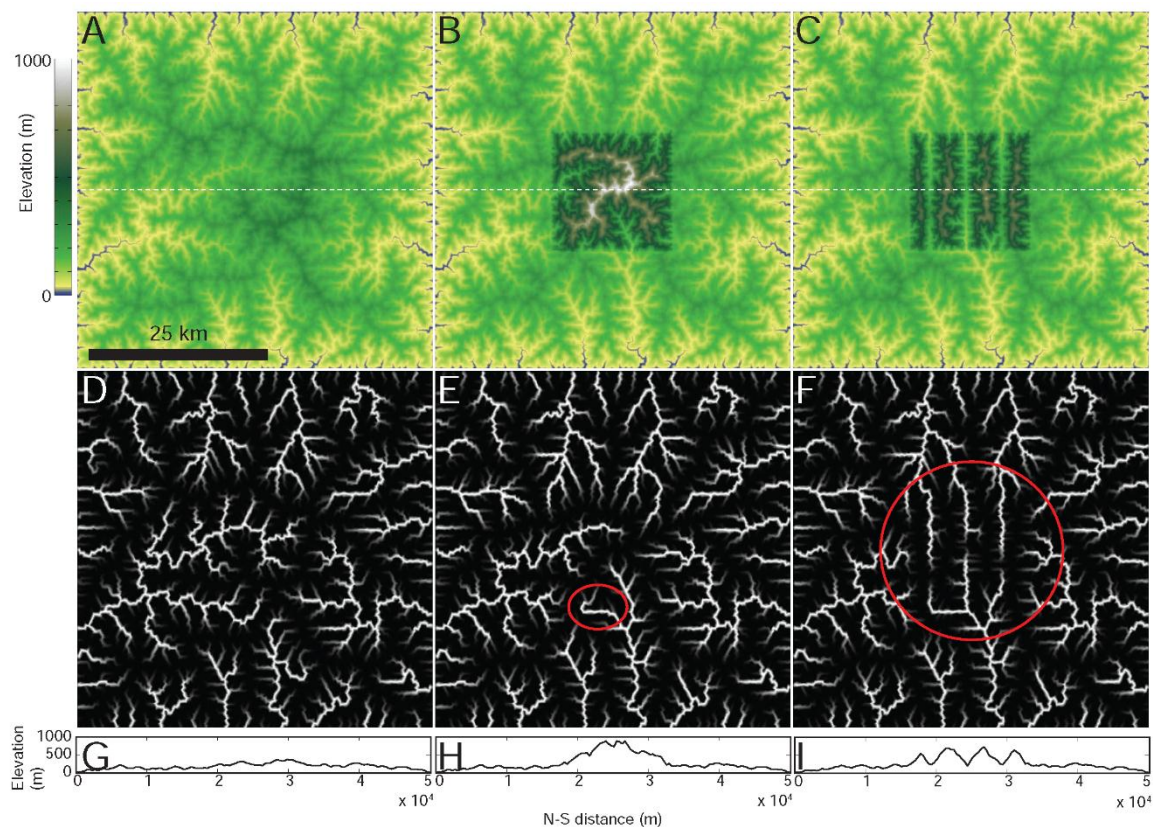
Figure 6.9. Pluton elevation maps. (A) before pluton exposure, (B) after exposure with uniform erodibility, (C) after exposure with N-S trending weak fractures. White dashed line indicates position of topographic profiles in (G-I). Hydrography maps for (D) before exposure, (E) after exposure with uniform strength, and (F) after exposure with N-S trending weak fractures.

6.9. Implications for Topographic Stress and Tectonic Strain

6.9.1. Overview of Topographic Stress

Drainage network patterns, and subsequently topography, may reflect the pattern of strain weakening in the crust. As a consequence, the near surface stress field can be influenced by the topography that results in the rapid erosion of faults and other features with heterogeneous erodibility. Topographic stresses are the result of the force of gravity

on a nonhorizontal surface. They are an internally buffered component of stress dependent on the surface topography. Shear stresses result from when principal stress eigenvectors diverge from Cartesian coordinate axes, and the slope deflects the vertical normal stress to produce a component of vertical coordinate shear. For any topographic load, each tends to deflect deformation from the load to the region at the base of the confining slopes (England and Searle, 1986). If I assume that the slope is at constant failure (i.e. the shear stress imposed on it is always critical) and the crust behaves as a Mohr-Coulomb material then I can determine the critical shear stress required to produce failure by use of the equation

$$\tau_{iz} = \sigma_{zz} \tan \varphi + C,$$

$$\sigma_{zz} = \rho g z$$

(6.1.)

Where τ_{iz} is the topographic stress with respect to a horizontal cartesian axis (x or y), σ_{zz} is the normal vertical stress, φ is the material's internal angle of friction, and C is cohesion. A cohesionless material that slopes greater than its internal angle of friction is beyond critical and will fail. It is also useful to use the shear yield function

$$f^s = \sigma_1 - N\sigma_3 + 2C\sqrt{N}$$

(6.2.)

Using principal stresses and N, which is equal to

$$N = \tan^2 \left[\frac{\pi}{4} + \frac{\varphi}{2} \right]$$

(6.3.)

$$N \equiv \frac{1 + \sin \varphi}{1 - \sin \varphi}$$

(6.4.)

$$N_o \cong \frac{\sigma_1}{\sigma_3}$$

(6.5.)

These equations only hold true if the topographic slope is at failure, which is often not the case for a location without any tectonic forcing. Equation 1 can be used to determine the amount of topographic stress exists for a slope which will be exacerbated by any external

tectonic forcing. The ratio of the stress determinant, approximately N, to N_o, the stress determinant at failure, can be used to determine how close topography lies to failure for cohesionless materials, known as topographic stress index (TSI, 1 is failure).

6.9.2. Results and Discussion

I study the stress state of the crust underneath the homogeneous and transverse regimes of Experiment 1 (Figure 6.10A). The stress state is generated by applying the force of gravity on a 3D elastic-plastic model (2700 kg m^{-3}, 10^{10} Pa bulk modulus, 3×10^9 Pa shear modulus, 3×10^7 Pa cohesion, 30° friction angle) of the crust with lateral dimensions of 100 km, vertical dimension of 15 km, and an elevation raster used to shape the surface topography. Surface elevation is five times greater than in the experiments of Model Set 1 in order to produce a level of topographic stress that would be expected in a tectonically active region.

The image of topographic stress in Figure 6.10B, taken as the difference of normal stress between the surface with topography and a flat surface with elevation equal to mean elevation (approximately 2 km for both experiments), indicates that at 5 km depth the stress field reflects the pattern of surface topography for both regimes. The topographic stress index (Figure 6.10C), measured at 1 km below sea level, indicates a near-failure condition at the base of the structurally confined channel. Dendritic channels do not approach failure under these conditions. On the surface, differential stress (Figure 6.10D), calculated as the difference of first and third principal stresses, is maximal in the structurally confined channel and along major tributaries. At depth, the structurally confined valley influences
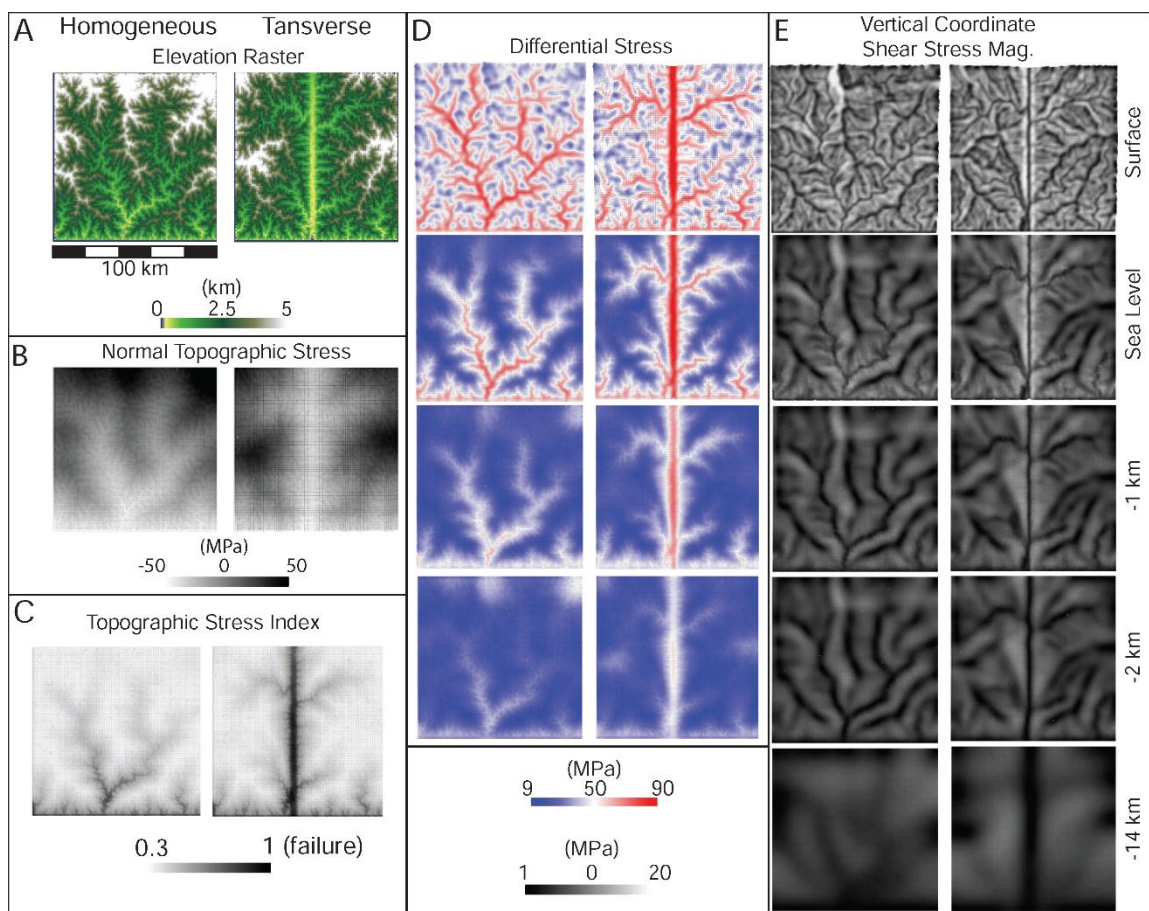
Figure 6.10. Topographic stress maps. (A) Elevation rasters imposed on 3D elastic-plastic crustal model. (B) Normal topographic stress, defined as the difference in vertical coordinate normal stress for this model subtracted by vertical coordinate normal stress for a flat surface model with ~2 km elevation. (C) TSI measured at 1 km depth below sea level. (D) Differential stress and (E) vertical coordinate shear stress magnitude at (top to bottom) surface, sea level, 1 km depth, and 2 km depth.

the differential stress field to a depth of at least 2 km while the stresses imposed by large tributaries start to diminish at that same depth. Likewise, large channels in the homogeneous regime have less impact on differential stress at depth than the structurally confined channel. Plots of vertical coordinate shear stress magnitude (Figure 6.10E), reflecting the vertical shear stresses attributed to topographic slope, impose a strong signal up to 14 km below sea level.

The models of topographic stress suggest that erosion of fault damage zones can nucleate further crustal failure through the accumulation of differential stresses that exceed

the local crustal strength at depths exceeding 2 km, given the chosen amplitude of topography. Dendritic channels may produce high differential stress near the surface but they come in an irregular form not conducive to influencing the deeper stress field (Figure 6.10C), nor does their shape create conditions that encourage localized plane strain. Below the surface, vertical coordinate shear stress magnitude is greatest along the valley walls of the structurally confined channel (Figure 6.10E). The TSI (Figure 6.10C) indicates a state of near failure within the damage zone attributed to this steep relief. The effect of this amplitude topography perturbs the near surface stress field to a depth of at least 14 km, indicating that it can have a potentially significant influence on the positioning of tectonic strain in the upper crust. I further explore the impact of topographic stress on tectonic strain in Chapter 8.

6.9.3. Natural Example: Cromwell Gorge

Cromwell Gorge (Figure 6.11A) in the Dunstan Range of South Island, New Zealand, is one example of a structurally influenced channel. The Cromwell Gorge section of the Clutha River sits above the seismically active River Channel Fault with a damage zone that is ~1000 times weaker than the surrounding intact quartzofeldspathic rock (Thomson, 1993). Incision into the damage zone has produced a steep walled gorge in weakened bedrock host to frequent hillslope failure events (Thomson, 1993). Differential stress (Figure 6.11B) reaches a local maximum of 10 MPa in the gorge, and as a result TSI values (Figure 6.11C) indicate near failure in the gorge and along the surrounding valley walls, purely as a product of topographic slope. Continued shear and mechanical failure is expected in Cromwell Gorge.
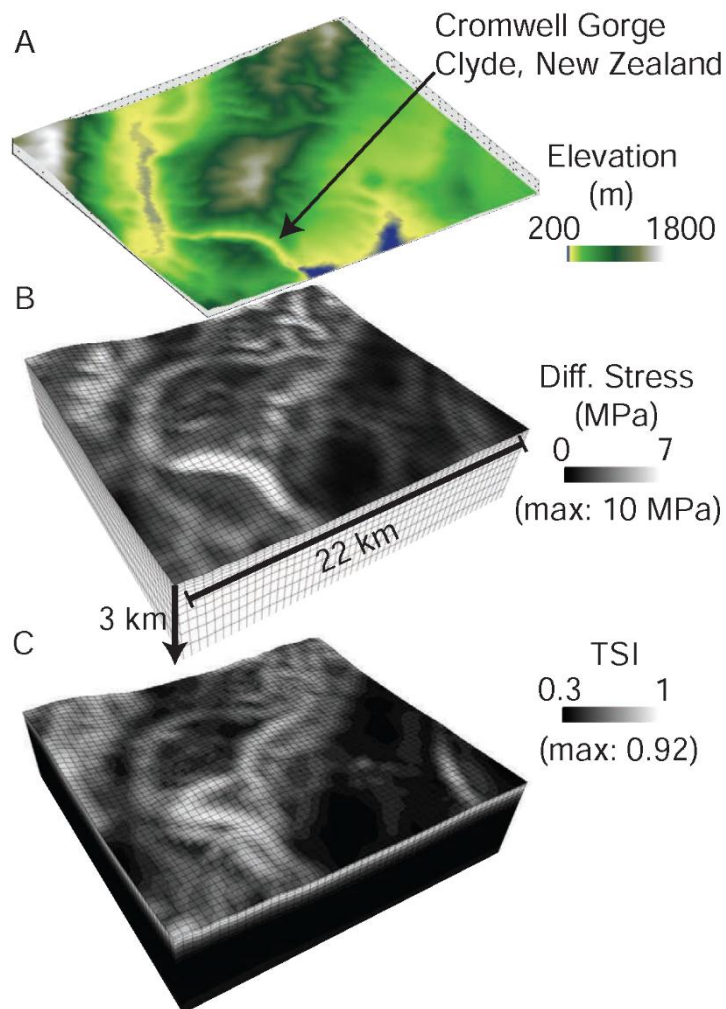
Figure 6.11. Cromwell Gorge. (A) Elevation map of Cromwell Gorge, Dunstan Range area. (B) Surface differential stress. (C) Surface TSI. Maxima occur in Cromwell Gorge.

6.10. Chapter Conclusions and Future Work

Heterogeneity in the material strength field contributes much to the development and rate of landscape form and response. One critical and predictable source of spatially variable strength is seismogenic cataclasis accompanying tectonic deformation (Molnar et al., 2007; Koons et al., 2012). As I demonstrate in my landscape models which incorporate material strength anisotropy, the form and response rate of mountain ranges are strongly sensitive to: 1) the major contrast in erodibility between the damaged fault zones and the

surrounding intact rock and 2) the fault zone orientations as a function of the present deformation regime.

The rate of landscape response to a tectonic or climatic perturbation is linked to the orientation of faults derived from the prevailing tectonic regime. Modeled knickpoint migration rates are approximately an order of magnitude faster in fault zones when compared to intact rock, and the migration rate increases with greater fault dip (Figure 6.3). The modeled topographic anisotropy (Figure 6.4) resulting from heterogeneous strength fields reflects multiple overlapping erosion rates also apparent in natural orogens (Figures 6.1, 6.5). Weakened fault zones allow for a rapid orogenic response to tectonic and climatic perturbations, while the intact rock responds relatively slowly (e.g. Scheidegger, 1979; Molnar et al., 2007).

The contrast in relative erosion rate confines much of the early stage fluvial erosion and establishes a major drainage network that reflects the orientations of exposed fault zones. Erosion into the surrounding intact rock occurs more slowly and typically leads to small tributaries that link orthogonally to the larger, structurally confined channels. The large divide in fluvial erosion rate preserves the tectonic signal in the landscape and partly contributes to landscape response rates. In time the structurally confined drainage network pattern can persist, but the abundance of exposed, highly erodible fault zones will diminish with continued erosion, leaving behind a larger areal proportion of strong, intact rock. The very large differences in material strength resulting from cataclasis imposes a preliminary heterogeneity and anisotropy that strongly influence landscape fabric and response rates. Future exploration of natural material behavior and evolving formulations of surface processes will permit further quantification of the relationships discussed above including

exploration of the dependence of landslides, sediment transport, and other surface processes on heterogeneous and anisotropic material strength.

Fault damage zone incision leads also to significant perturbations of the stress field in the upper 14 km of crust. Topographic stresses alone can increase the likelihood of mechanical failure in the base and slopes of valleys. Damage zones can potentially attract tectonic strain by rapid erosion and greater concentration of differential stress. This effect compounds with the already reduced mechanical strength of the damage zone. I study the implications of amplified tectonic-geomorphic feedbacks in Chapter 8.

CHAPTER 7

EROSION OF ACTIVE FAULTS AND INFLUENCES ON TOPOGRAPHIC SLOPE AND DRAINAGE NETWORK PATTERN

7.1. Chapter Abstract

The combined role of fault displacement and fault damage is explored in this chapter. I initiate the model with rock strength-erodibility scaling rules described in Chapter 3 and a new regrid method implemented to maintain a high mesh quality. Results suggest that the lateral motion attributed to slip along a fault plane can drastically increase channel slope in reverse thrust regimes and decrease slope in normal rift regimes. Greater rock damage associated with fault slip leads to a greater mechanical control on the drainage network pattern, causing a greater potential for fault-parallel flow. Further, greater rates of strike-slip generate greater fault-parallel flow. Dip-slip motion can also induce fault-parallel flow by shifting sections of river channel toward the slip plane.

7.2. Chapter Introduction

Orogenesis is commonly framed as the interaction of tectonically driven material advection and dominantly gravity-driven erosion (Penck and Penck, 1924). Two tectonic processes that play a significant role in this interaction are strain-induced surface displacement and rock damage. It is well recognized that tectonic strain drives surface displacement and produces the relief that initiates gravitationally driven erosive geomorphic mechanisms (Beaumont, 2004; Koons, 1990, 1989; Koons et al., 2013). It is also recognized that strain weakening causes permanent mechanical damage to rock (Ben-

Zion and Sammis, 2003; Hoek and Brown, 1980; Mooney et al., 2007; Sibson, 1977) and evidence is clear that rock damage has a significant influence on the local rates and patterns of erosion (Koons et al., 2012; Molnar et al., 2007; Moore et al., 2009; Roy et al., 2015; Scheidegger, 1979). Some have argued that rock damage associated with strain weakening is the first stage in erosion and is therefore influential for all erosional processes (Gilbert, 1877; Molnar et al., 2007; Scheidegger, 1979).

Despite the recognized influences of surface displacement and rock damage on landscape evolution, there has so far been little exploration of their combined influence. My objective is to build upon previous theory by applying different combinations of these tectonic processes to explore their importance in shaping topography. More specifically, my focus in this chapter is to study the combined influence of rock damage, the focus of Chapter 3, and surface displacement on the patterns and rates of fluvial incision by combining a landscape evolution model with simple models of surface displacement and rock damage. I intend to build on previous work that explored the geomorphic implications of heterogeneous rock strength (e.g. Moglen and Bras, 1995; Roy et al., 2015) and differential uplift (e.g. Attal et al., 2011; Whittaker et al., 2007a, 2007b) by combining the two in a simple kinematic and stream power-based framework.

My analysis is divided into three model sets. In Model Set 1, I explore the contributions of lateral and vertical surface displacement to changes in surface slope in convergent and divergent tectonic settings. In Model Set 2 I study the combined influence of surface displacement and rock damage on topographic shape and drainage network pattern within reverse dip slip, left lateral strike slip, reverse oblique slip, and normal dip

slip tectonic regimes. In Model Set 3 I explore additional questions regarding the potential for lateral channel migration imposed by fault dip (Roy et al., 2015).

7.3. Methods

7.3.1. Landscape Evolution Model

The Channel-Hillslope Integrated Landscape Developmental (CHILD) model (Tucker et al., 2001) is again used in this chapter to approximate the physics behind fluvial incision into bedrock by assuming that fluvial erosion rate scales with unit stream power. Erosion rate is calculated at every node on an irregularly discretized surface (Figure 7.1a) using a variation of Equation 3.1

$$\frac{\partial h}{\partial t} = -k_b \omega + w + u\frac{\partial h}{\partial x} + v\frac{\partial h}{\partial y} \tag{7.1.}$$

where the rate of elevation change $\frac{\partial h}{\partial t}$ at any point on a surface depends on spatially variable erodibility k_b, stream power ω per unit width, vertical tectonic displacement relative to baselevel w, and lateral topographic advection $u\frac{\partial h}{\partial x}$ and $v\frac{\partial h}{\partial y}$. Contributions to surface displacement relative to baselevel and erodibility are explained further below. For the sake of simplicity and my interest in the fluvial regime, I do not include hillslope processes in my model. Eroded material is assumed to be immediately removed from the model domain through a single flow outlet boundary (Figure 7.1a). Steady state topography is achieved when $k_b\omega = w + u\frac{\partial h}{\partial x} + v\frac{\partial h}{\partial y}$ and there is no change in mean surface elevation. I use the same stream power per unit width equation shown in Chapter 3. I use a uniform runoff rate of 1 m yr^{-1} and the domain area is 100 km^2.
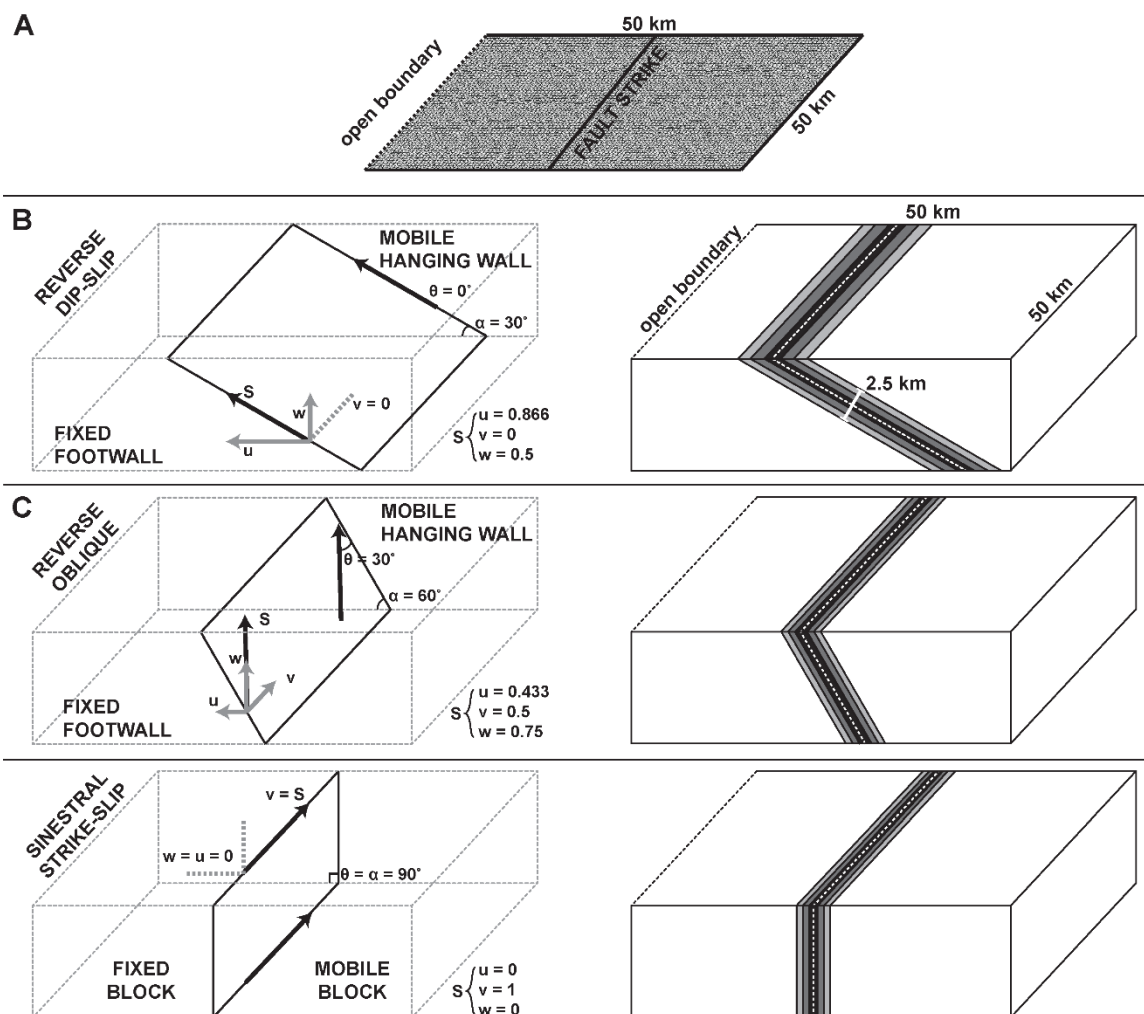
Figure 7.1. Model geometry and kinematic fields. (A) irregularly discretized mesh used for landscape evolution model surface. Single flow outlet boundary is on west side, parallel to fault strike. Model domain is 50x50 km. Kinematic solution (left) and the associated damage zone (right) for (B) reverse dip slip, (C) reverse oblique slip, (D) left lateral strike slip tectonic regimes.

7.3.2. Surface Displacement Model

7.3.2.1. Tectonic Regimes

Fault slip and the subsequent pattern of surface displacement require localized brittle failure in the upper crust. Failure in the upper crust occurs when there is sufficient differential stress to exceed rock mass strength (Bieniawski, 1974; Hoek and Brown, 1980). The pattern of failure in the elastic-plastic upper crust often takes the form of planar faults

whose orientation depends on the local stress tensor and the internal angle of friction at the moment of failure (Coulomb, 1773), assuming that there are no inherited mechanical defects that would complicate the distribution of stress (Koons et al., 2012).

For my experiments I use the Andersonian model (Twiss and Moores, 1992) to determine the fault orientation for reverse dip slip, left lateral strike slip, reverse oblique slip, and normal dip slip regimes. In every experiment, all tectonic strain is accommodated on a single fault slip plane. Reverse dip slip motion is exhibited along convergent tectonic boundaries. Strike slip motion is associated with transform boundaries, and reverse oblique slip motion is associated with a combination of the two. Normal fault slip occurs in regions of local extension, such as in rift margins (e.g. Huismans and Beaumont, 2011, 2014) and backarc basins (e.g. Billen, 2008). Fault geometries are all described in Figure 7.1.

7.3.2.2. Slip Rate

The model domain is divided into two blocks: one moves along a fault slip surface relative to a second block with no motion associated with fault slip. The fault is centrally located in the model domain and strikes north. Dip direction is east for reverse slip tectonic regimes, west for normal slip regimes and the strike slip regime dips vertically. As the mobile block rides along the slip surface, surface nodes are shifted accordingly in three dimensions at each model time step

$$S = \sqrt{u^2 + v^2 + w^2},$$
$$u = S\,cos(\theta)\,cos(\alpha),$$
$$v = S\,sin(\theta),$$
$$w = S\,cos(\theta)\,sin(\alpha)$$

(7.2.)

where S is the total slip rate, u is the horizontal slip rate parallel to dip, v is the horizontal slip rate parallel to strike, w is the vertical slip rate, θ is the slip obliquity, or the difference in angle between slip direction and the direction normal to fault strike, and α is the dip angle, the values of which change between my three kinematic solutions outlined above. There is no variation in dip angle along strike and so v is simply a function of total slip rate and slip obliquity. Values for u and w are functions of total slip rate, the dip of the slip surface, and slip obliquity. Under these kinematic conditions I expect u and w to dominate in the dip-slip experiments and v to dominate in the strike-slip experiment. In order to generate some topography in experiments without dip-slip motion, I apply a small ambient uplift rate relative to baselevel over the entire domain, given a value of 0.1 mm yr^{-1} unless otherwise noted. Please see Appendix C for an overview of grid maintenance techniques.

7.3.3. Rock Damage and the Link to Erodibility

I test the sensitivity of fluvial incision to rock damage by varying the maximum degree of damage surrounding the slip plane, within natural limits (e.g. Carpenter et al., 2011; Faulkner et al., 2010; Lockner et al., 2009; Mitchell et al., 2011; Rempe et al., 2013; Thomson, 1993). The initial cohesive strength of rock is set to 10 MPa, and I use one series of experiments with no damage (1X, 10 MPa), one series in which the damage zone is 10 times weaker than its host (10X, 1 MPa), and one series in which the damage zone is 1000X weaker than its host (1000X, 10 kPa). Rock damage is introduced as a stepwise gradient that decreases in cohesive strength with proximity to the slip surface, contained in a planar fault damage zone (Figure 7.1). I assume that bedrock anelastic strength is inversely

proportional to erodibility (Sklar and Dietrich, 2004, 2001) and use the cohesive strength-erodibility relation used by Roy et al. (2015) and adapted from Hanson and Simon (2001)

$$k_{b(x,y,z)} = k_c C_{(x,y,z)}^{-1/2} \tag{7.3.}$$

where C is cohesion and k_c is a coefficient equal to 0.2 with units $m^{1/2}$ s $kg^{-1/2}$. Similar assumptions have been made for the erosion of cohesive soils (Hanson and Simon, 2001; Mirtskhoulava, 1991, 1966) in attempts to link the mechanical properties of the soils to stream power rules. It is possible to use alternative measures of anelastic rock strength, such as tensile strength, to define erodibility, but I choose to use cohesion based on previous arguments (Roy et al., 2015).

7.4. Results

7.4.1. Model Set 1: Lateral Topographic Advection and Channel Slope

The lateral component of reverse fault slip steepens channel slopes within the mobile block. I show this by comparing a reverse dip-slip experiment with vertical and lateral components of slip to a block uplift experiment with an equal vertical, but no lateral, slip rate (Figure 7.2a,b). During the same amount of simulation time, slopes within the dip-slip experiment meet or exceed the steady state slope-area relationship of the block uplift experiment (Figure 7.2e). Slopes in the reverse dip slip experiment tend to be greatest along the edge of the fault, but the increase in slope is felt throughout the mobile block (Figure 7.2d). Slopes in the block uplift experiment have a more evenly distributed pattern and follow a power law scaling to drainage area (Figure 7.2e). An opposite effect occurs under normal slip conditions, assuming the same dip-slip angle of 30˚ (Figure 7.2c). Under these

conditions channel slopes are equal to or less than the slope-area relationship from the

block uplift experiment (Figure 7.2e). None of these experiments incorporate rock damage.
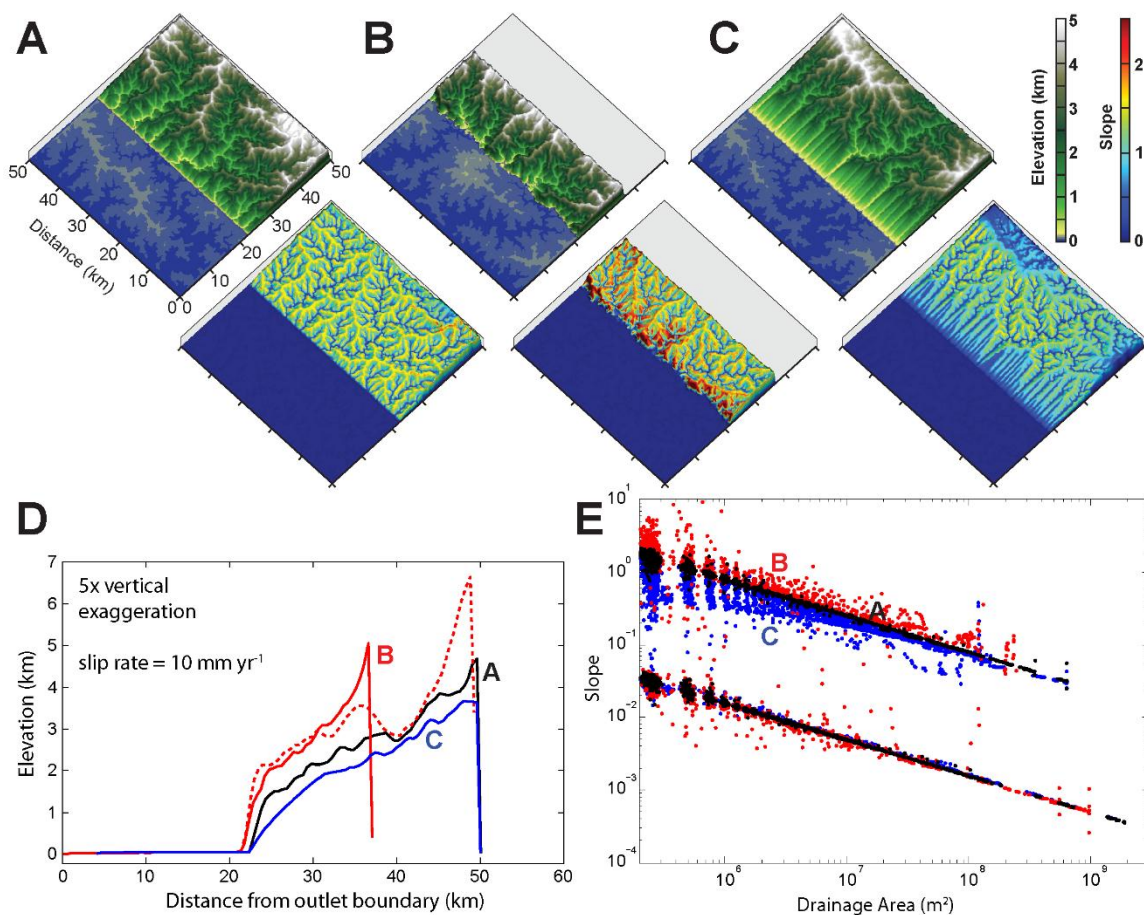
Figure 7.2. Elevation and slope data. (A) Block uplift, (B) reverse dip slip motion, and (C) normal dip slip motion. (D) Averaged topographic profiles for a, b, c. Dashed red line is a reverse dip slip example with material added to the hanging wall with continued reverse motion. (E) Slope versus area plot for a, b, c.

7.4.2. Model Set 2: Rock Displacement, Damage, and Topographic Shape

In this section I test the sensitivity of drainage network patterns and topography to

rock displacement and damage along a fault slip plane. Sensitivity analysis includes 5 mm

yr^{-1}, 10 mm yr^{-1}, and 20 mm yr^{-1} slip rates and no weakening, 10X weaker, and 1000X

weaker fault damage zones surrounding the slip surface. In addition, an ambient uplift rate

of 0.1 mm yr^{-1} is applied uniformly to the model surface. I am primarily interested in how

the drainage network patterns may respond to the different rates and degrees of damage associated with fault slip, so for visualization purposes I provide maps of elevation and drainage area for each experiment.

7.4.2.1. Reverse Dip-Slip Fault

Natural levels of fault rock damage attract more surface runoff and lead to the development of channels that are confined to the fault structure. Figure 7.3 shows results for the reverse dip slip fault experiments. The 1x (homogeneous strength) 5 mm yr^{-1} experiment displays a small preference for structurally confined tributaries, while a small decrease in fault rock strength in the 10x, 5 mm yr^{-1} experiment causes a small change in drainage network pattern attributed to slightly greater structural confinement along the fault plane. This effect increases significantly for the 1000x, 5 mm yr^{-1} experiment in which a structurally confined channel spans the entire width of the model domain.

Natural rates of reverse slip also encourage structural confinement, but to a lesser degree. All examples with reverse surface displacement show at least a small degree of structurally confined drainage even without rock damage (Figure 7.3: 1x, 5-20 mm yr^{-1}). The degree of structural confinement may increase with slip rate. However, this influence is limited to tributaries or short sections of larger channels. An increase in slip rate and rock damage leads to an even greater increase in structural confinement.

REVERSE DIP-SLIP

SLIP RATE

5 mm yr^{-1}

10 mm yr^{-1}

20 mm yr^{-1}

1X: NO WEAKENING

SHEAR DAMAGE

10X: MODERATE

1000X: SIGNIFICANT

A

B

C

D

E

F

G

H

I

100 km

ELEVATION (km)

0 1 2 3 4 5 6

DRAINAGE AREA (km²)

0   0.5   1
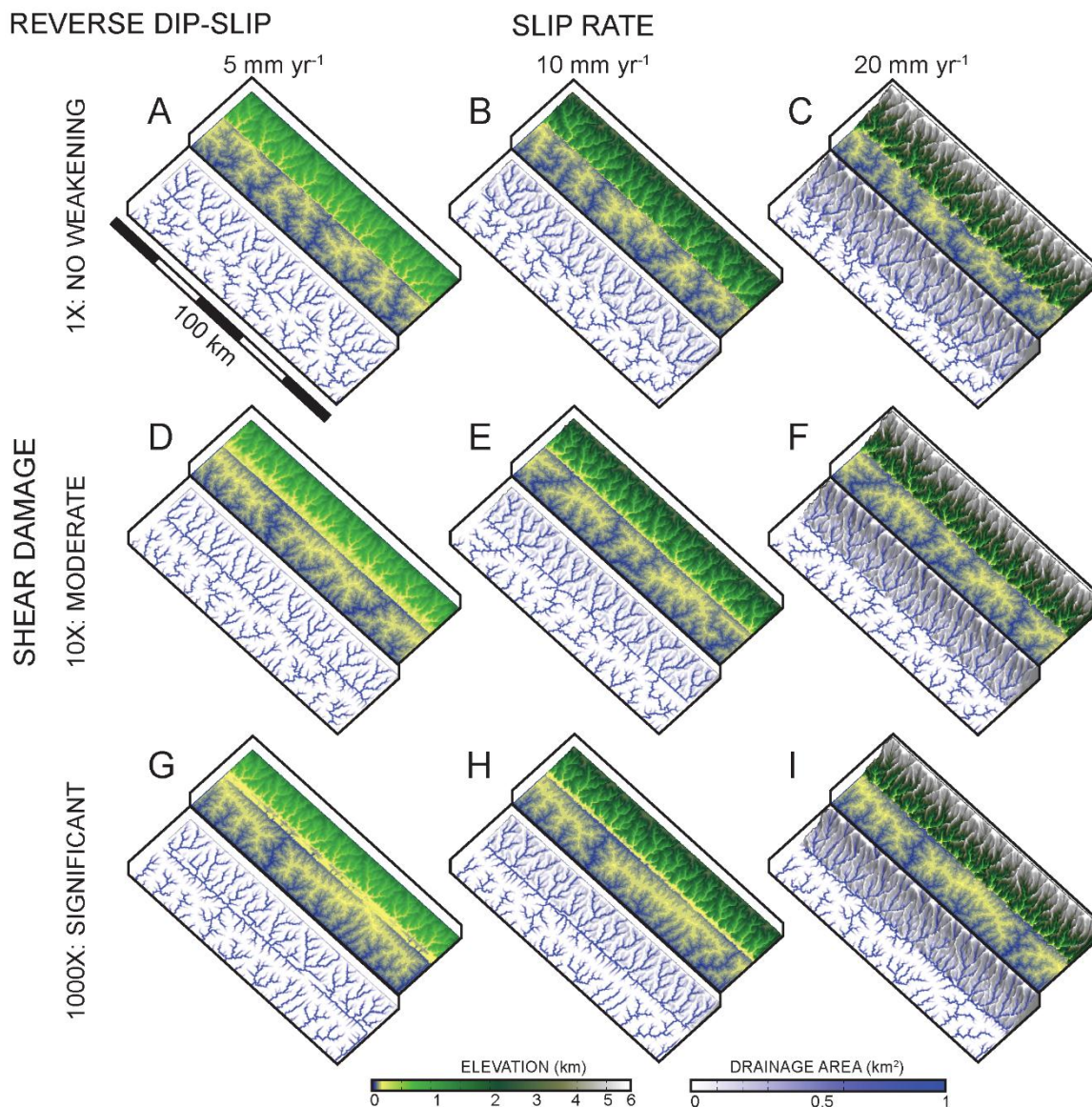
Figure 7.3. Reverse dip slip model results. For this and all following figures, images by row represent common degree of shear damage, images by column represent common slip rate. Topography and drainage area are displayed.

7.4.2.2. Normal Fault Slip

Natural rates of normal slip also encourage structural confinement, but to a lesser degree (Figure 7.4). Normal fault slip exposes new surface material at a slope of 60°. Channels that cross the fault are extended in the direction of surface displacement and there is a strong westward orientation in these channel sections, particularly in the 20 mm yr^{-1}

slip rate experiments. Slip along the fault plane introduces a greater drainage area adjacent to the fault, and as a consequence previously small tributaries become larger, anomalously straight channels that intersect the fault. These channels follow the fault structure until they intersect a large channel that traverses the fault and reaches the outlet boundary.
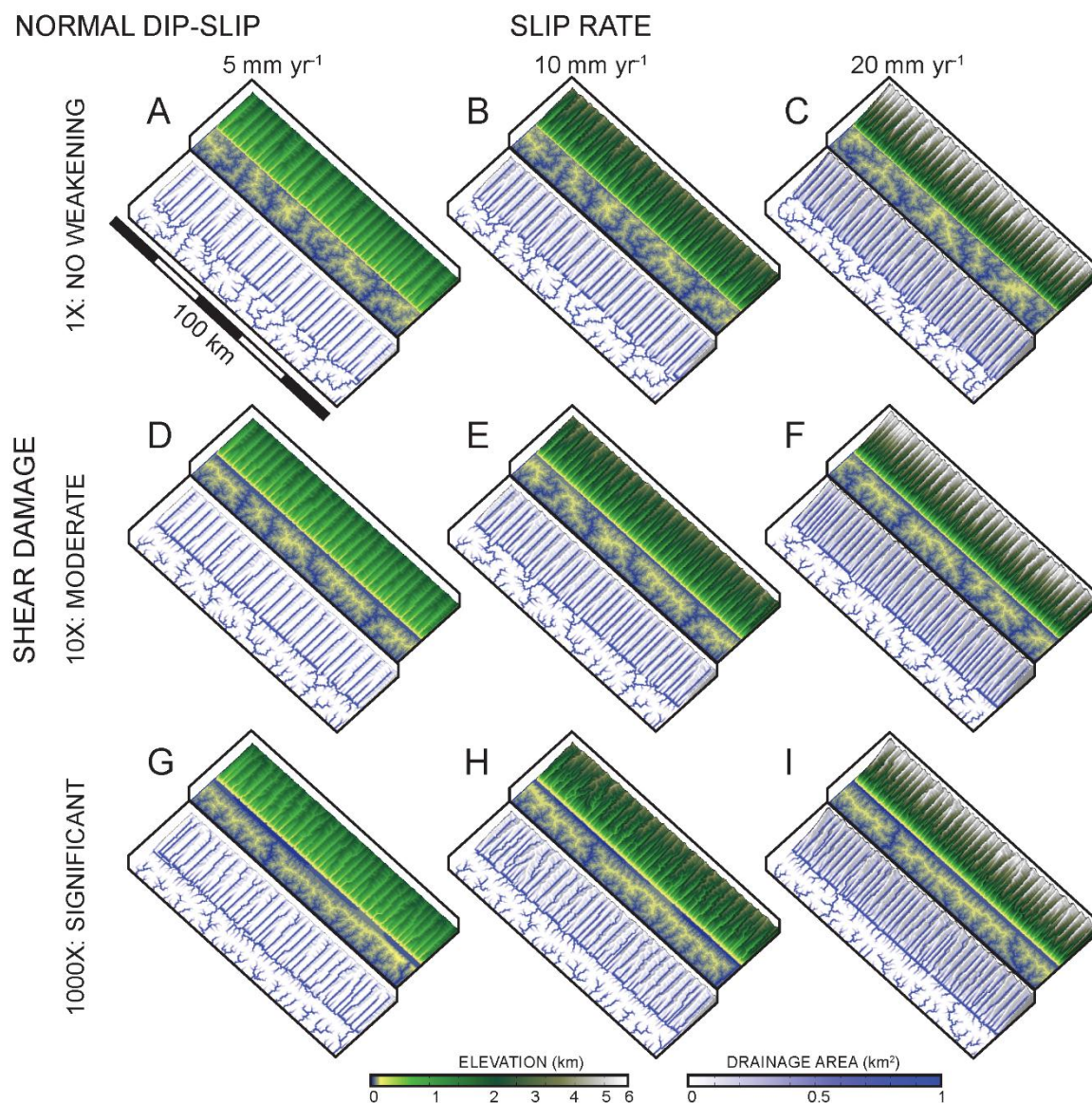
Figure 7.4. Normal dip slip model results.

7.4.2.3. Left Lateral Strike-Slip Fault

Strike-parallel fault motion encourages structural confinement of channels. Figure 7.5 shows experiment results for the left-lateral strike-slip fault experiments. As I discussed above, rock damage encourages a greater degree of structural confinement. However, even without damage along the slip plane, the drainage network pattern is influenced by slip and the influence increases with slip rate. The 1x, 20 mm yr^{-1} experiment displays a greater degree of structural confinement than 10x experiments at lower slip rates, and shows almost as much structural confinement as the 1000x experiments. For all experiments with 1000x rock damage or 20 mm yr^{-1} slip rate, a significant portion of the main channel is structurally confined. This forces many large channels to intersect and contribute to the structurally confined channel.

7.4.2.4. Reverse Oblique Fault

Reverse oblique fault slip encourages structural confinement of channels to a lesser degree than strike slip motion, but to a greater degree than dip slip motion. Figure 7.6 shows experiment results for the reverse oblique-slip fault experiments. This tectonic regime combines the mechanisms from dip slip motion and strike-slip motion that promote structural confinement of channels. As a result, there is a similar but less prominent fault-parallel drainage pattern that arises in the reverse oblique-slip regime even without fault damage. When fault damage is incorporated, there is a strong range-parallel pattern of drainage. Interestingly, the 1x 20 mm yr^{-1} experiment has the least amount of structural confinement of them all.
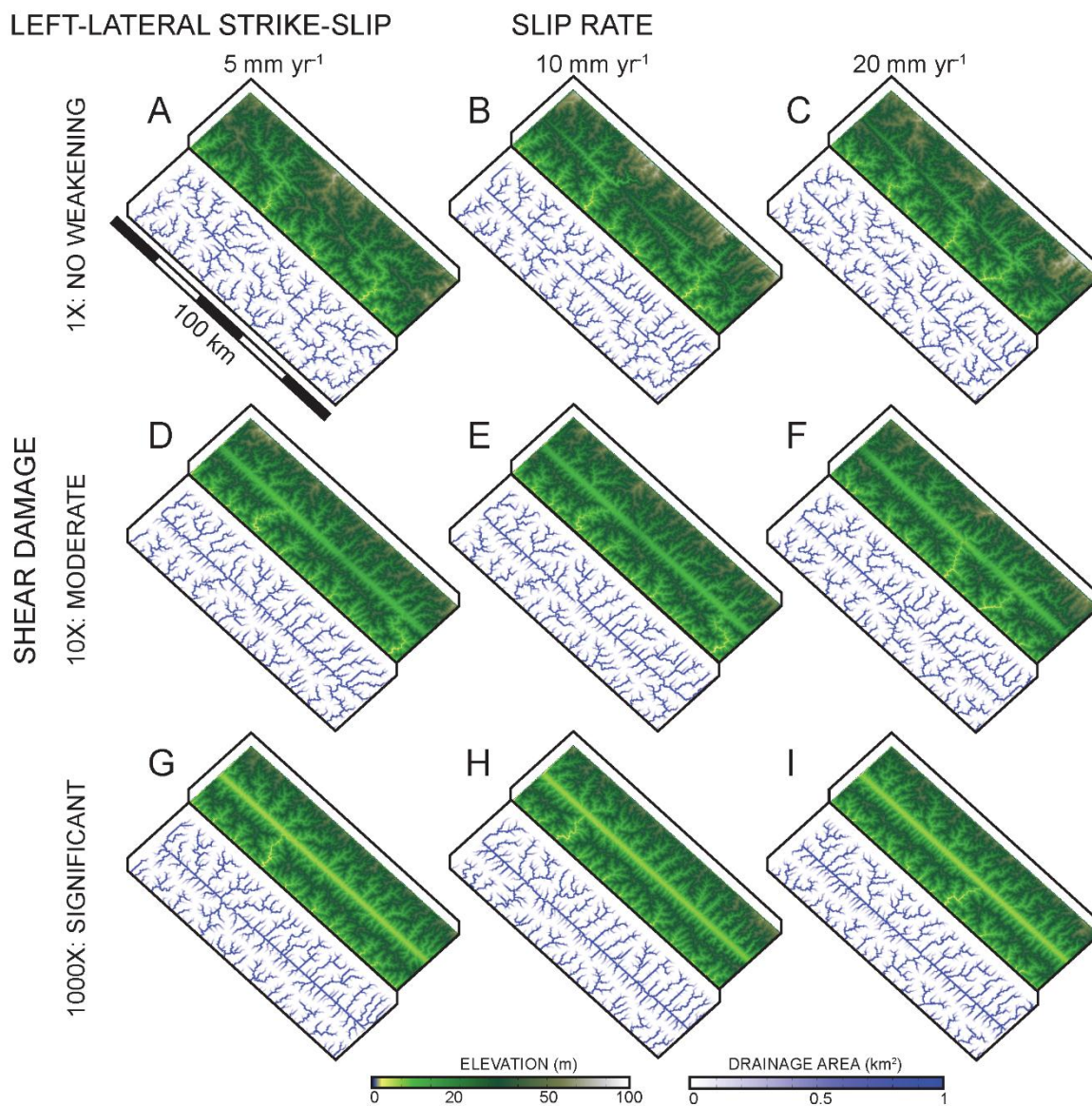
Figure 7.5. Left lateral strike slip model results.
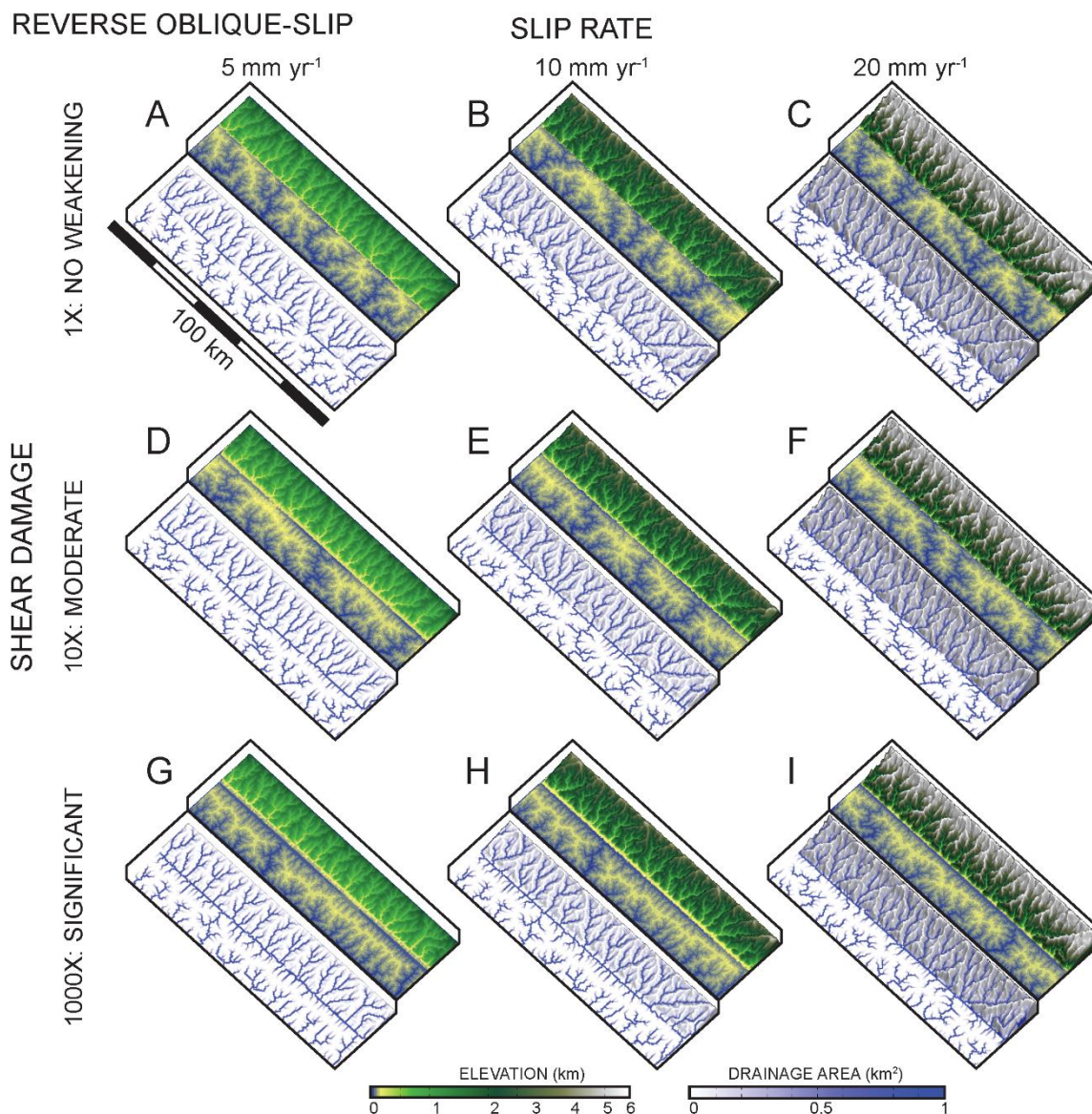
Figure 7.6. Reverse oblique slip model results.

7.4.3 Model Set 3: Lateral Channel Shifting Along a Gently Dipping Fault

In Chapter 3 I hypothesized that if a river becomes confined to a gently dipping, planar weak zone structure, the position of the river will shift laterally with the changing exposure of the weak zone as the surface continues to uplift and erode. This numerical experiment did not consider active motion, so I have chosen to revisit this problem and apply 1 mm yr^{-1} of slip along the fault plane. The channel continues to be confined to the

structure of the weak zone (Figure 7.7), however the rate of lateral migration is now not just a function of fault dip and ambient uplift rate relative to baselevel but also a function of slip rate along the fault. Greater fault slip will hinder lateral migration because the hanging wall continues to rebuild the downdip valley side, causing the channel to become perched and be less able to incise into the hanging wall.
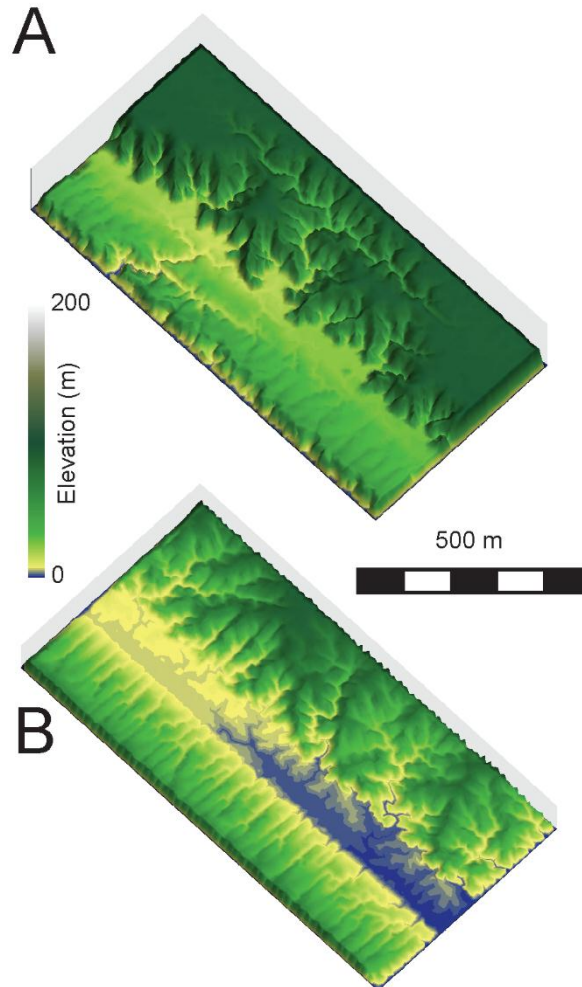
Figure 7.7. Comparison of lateral channel shifting pattern. (A) Kinematic and (B) static model from Chapter 3.

7.5. Discussion

7.5.1. Lateral Advection and Channel Slope

The lateral advection of topography can increase or reduce channel slope depending on fault dip angle, slip rate, and slip direction. Slope increases under reverse slip, where steep topography is advected laterally downstream faster than the erosion rate needed to equilibrate slope. Slope may decrease under normal slip if the slip plane dips at an angle that is shallower than what could be produced by river incision. For example, in Model Set 1 my normal dip slip experiment with a dip angle of 30° is significantly lower than the slope expected for the majority of channels incising into the mobile block. However, most normal faults dip at a greater angle than 30° and could potentially cause an increase in channel slope.

7.5.2. Structural Confinement

Surface displacement and rock damage both influence the drainage network pattern along faults. Based on my results, rock damage affects the drainage network pattern by creating a corridor of erodible material, while surface displacement collects drainage where the slip surface accommodates differential motion. First, erosion across rock erodibility gradients associated with fault damage leads to low relief corridors that attract more surface runoff (Roy et al., 2015). I have shown that natural levels of fault damage can strongly influence the drainage network pattern regardless of which tectonic regime caused the damage.

Second, under dip slip motion, channels in the mobile block are advected laterally toward the fault. As they reach the fault, on many occasions fault parallel channel sections

will remain along the fault because they continue to connect channels to the flow outlet boundary. Third, strike slip motion leads to shearing and extension of channels along fault strike.

7.5.3. Persistent Drainage Orientations in the Mobile Block

Channels oriented parallel to the plate vector will persist whereas channels oriented at an acute angle will be removed through lateral advection. For example, in Figure 7.6A-C, E, F, H, and I, the channel in the bottom right of model domain seems to persist because it has the same orientation as plate vector. However, the persistence of these channels also depends on a change in the divide position. For example, the divide may shift laterally, causing the channel orientation to change in time regardless of its previous orientation. The persistence of the channel in Figure 7.6 is partially due to its orientation but also due to the drainage divide being pinned to the corner of the domain.

7.6. Chapter Conclusions

Tectonics play a significant role in geomorphology by influencing the slope and drainage pattern of river channels. Accurate measurement of channel steepness requires a good sense of the full 3D kinematic field. Using only the vertical component of surface displacement does not adequately predict channel steepness near active tectonic boundaries. Surface displacement and rock damage play a significant role in topographic shape and drainage network patterns locally near the slip surface. Under conditions where a channel incises into a damage zone with a shallow dip angle, the channel will often shift

laterally in concert with the damage zone exposure. The rate of lateral migration is dependent on the ambient uplift rate, erosion rate, and the fault slip rate.

The application of simple block motion has been useful in determining the combined influence of rock damage and displacement on landscape evolution, however it is important to consider the stresses that drive the velocity conditions behind surface displacement. Models of block motion and erosion fall short of resolving the dynamic rheological responses of orogens to tectonic stresses and the more complex deformation patterns that arise from them. In the next chapter I explore a dynamic crustal model and couple it to landscape evolution and climate to determine its contribution to the landscape evolution cycle.

CHAPTER 8

DYNAMIC LINKS BETWEEN ROCK DAMAGE, EROSION, AND TECTONIC STRAIN IN ACTIVE OROGENS

8.1. Chapter Abstract

We provide model evidence for the amplification of tectonic strain within heavily eroded shear zones under the assumption that strain weakening increases the erodibility of rock. Plastic shear strain permanently damages the upper crust within planar shear zones and provides a greater ease for detachment and transport by fluvial processes. The subsequent rapid erosion of exposed shear zones reforms the topographic stress field in a way that encourages continued accommodation of strain. Greater shear damage leads to greater erosion and subsequently greater accommodation of strain localized within the eroded shear zone structure. Two experiments are used to study this occurrence, followed by a sensitivity analysis. For Experiment 1 we assume that strain weakening in the crust does not influence erodibility and therefore has no direct influence on the processes eroding the surface. For Experiment 2 we assume that erodibility is inversely proportional to the square root of rock cohesion. Experiment 1 produces an orogen in which strain is diffusely distributed and there is a dominant range-perpendicular drainage pattern. Conversely, Experiment 2 produces a strong range-parallel dominated drainage pattern and a greater partitioning of strain within eroded shear zones ~2 km wide. Further, these eroded shear zones remain active for a longer period of time. We then study the sensitivity of strain partitioning to a spectrum of shear weakening and determine that greater weakening leads to greater strain accommodation.

8.2. Chapter Introduction

The rheological properties of the lithosphere clearly dictate how the Earth's surface will deform with respect to tectonic stress, but there is also evidence that these same properties exert significant controls on the rates and patterns of surface processes as well. On the one hand, rheology controls the partitioning of tectonic strain and potentially initiates topographic relief through deformation, providing the gravitational potential for various hillslope, fluvial, and glacial transport processes (e.g. Penck and Penck, 1924). Relief can also partition climate and hence affect the distribution of surface runoff by vertical deflection of geostrophic winds (e.g. Smith, 1979; Roe, 2005). On the other hand, tectonic strain damages the brittle crust within meter- to kilometer-scale shear zones, which allows not only for a greater partitioning of strain but also facilitates rock disaggregation and removal by the same transport processes (e.g. Scheidegger, 1979; Molnar et al., 2007; Moore et al., 2009).

The connection between rock damage and erodibility is well recognized in the field and there are many studies that draw correlations between the mechanical strength of the substrate and rates of erosion (e.g. Mirtskhoulava, 1966; Hanson and Simon, 2001; Sklar and Dietrich, 2001; Sklar and Dietrich, 2004; Brideau et al., 2009; Moore et al., 2009). Still others have provided field evidence for tectonic responses to localized fluvial incision (e.g. Montgomery and Stolar, 2006). Despite these valuable efforts, there has been minimal progress in exploring the direct role of damage in the tectonic-surface processes link (e.g. Scheidegger, 1979; Molnar et al., 2007; Koons et al., 2012). For example, it is not clear how heterogeneous patterns of rock strength associated with the localized partitioning of

shear zones may influence the evolving drainage network patterns in an orogen, nor is it clear how sensitive strain partitioning will be to focused erosion in shear damaged rock.

In this paper, we explore orogenic-scale (>100 km) landscape evolution under the assumption that rheology is the link between tectonic activity and surface processes. More specifically, we make some theoretical predictions regarding the significance of damage in the tectonic-surface processes link by studying how patterns of shear damage can potentially 1) steer surface runoff and ultimately focus a greater amount of erosion in shear zones, and 2) encourage greater strain localization, partitioning more deformation within kilometer-scale shear zones relative to adjacent, intact crustal blocks, deep within active orogens.

Our method employs numerical models that use the rheological properties of the crust to couple tectonic strain, surface erosion, and orographic precipitation. In our first experiment, we combine a deforming mechanical model of the crust to deform the surface, a fluvial erosion model to erode the surface, and an orographic precipitation model to synthesize climate asymmetry across mountainous relief. In our second experiment, we use the first arrangement but introduce a link between rock cohesion and erodibility to relate fluvial erosion patterns and rates to the degree and orientation of mechanical shear weakening (e.g. Roy et al., 2015). For all experiments we track the time-dependent evolution of topography, strain, strain rate, and drainage network patterns. We find that shear weakening and the associated local increase in erodibility of rock causes shear zones to remain active for longer periods of time, leading to greater strain localization. Additionally, erosion in shear zones can help explain common range-parallel orogenic drainage network patterns.

8.3. Crustal Mechanics and Tectonic Conditions

In order to investigate the pattern of surface deformation during orogenesis, we model a 3D section of crust 200 km wide (= y), 400 km long (= x), and 20 km thick (=z) extending to the lower crust (Figure 8.1A). Orogenesis is the product of collision between two tectonic plates along a north-south trending plate boundary (Figure 8.1B). The western plate consists of an elastic block to simulate negligible deformation, while the eastern plate consists of a two-layered crust that is free to deform upon collision with the elastic block. The collision is driven by an imposed traction velocity at the base of the crust to approximate contributions from horizontal mantle advection. Lateral boundaries are sufficiently distant from the focus of deformation that they do not influence the solution.

We assume a vertical strength profile similar to that predicted by Brace and Kohlstedt (1980), with a rheological transition located at 14 km depth associated with the sharp reduction in flow stress at temperatures greater than 300-350° C for quartz/feldspar-dominated crust (Sibson, 1982; Handy et al., 2007; Bürgmann and Dresen, 2008). We describe the upper 14 km of crust as pressure-dependent with an elastic/strain softening plastic rheology. The strain softening rheological behavior imposes a permanent reduction in local cohesive strength and friction angle when plastic shear strain exceeds 20% (e.g. Buck, 1988). The lower crust is represented by a temperature dependent elastic/von Mises rheology with a post-yield non-associated flow rule based on published creep laws for quartzo-feldspathic crust at a reference strain rate of 10^{-14} s^{-1} and average geothermal gradient of 20° C km^{-1} (e.g. Upton and Koons, 2007; Upton et al., 2009). Model parameters are listed in Table 8.1.
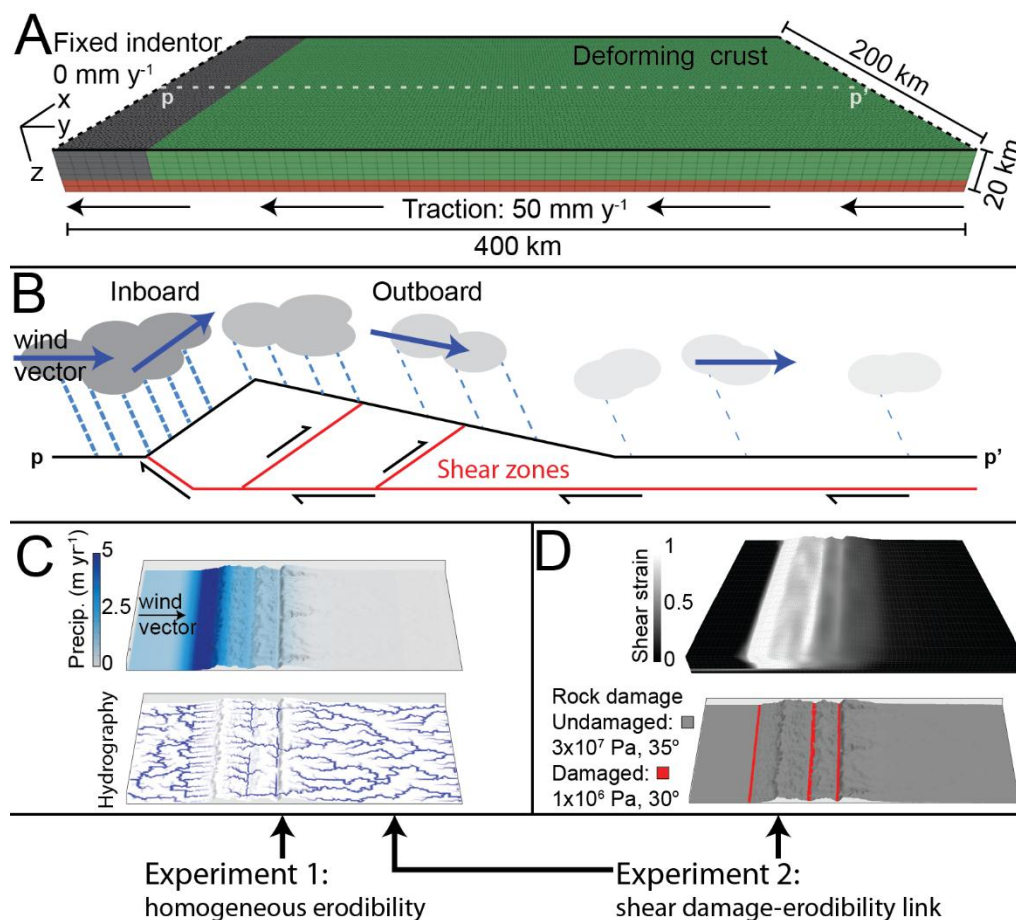
Figure 8.1. Model schematics. (A) Crustal geometry, grid resolution is 4 km on the horizontal plane and 3 km in the vertical. Grid resolution for the surface model is 2 km on average. Elastic plate is indicated in grey, strain softening crust is indicated in green, and the middle crust is indicated in red. Dashed and solid lines indicate open and closed flow boundaries for the surface model, respectively. Line P-P' is location of (B) a cartoonized topographic profile, indicating the general pattern of rainfall, wind motion, and the position and sense of nascent shear zones. (C) Example map of precipitation, the direction of the wind vector relative to the topography determines the rainfall distribution, rivers collect the surface runoff and erode (hydrography map). (D) Local peaks of plastic shear strain from the mechanical model translate to rock damage and a local increase in erodibility. In Experiment 1, erodibility is homogeneous, only the orographic precipitation and stream power models are used. In Experiment 2, erodibility is linked to the degree of rock damage caused by plastic shear strain, all model components are used.

Table 8.1. Mechanical model parameters. Strain softening values in parentheses active after 20% plastic shear strain

Bulk Modulus (Pa)	1×10^{10}
Shear modulus (Pa)	3×10^{9}
Density (kg m^{-3})	2700
Friction angle (deg)	35 (30)
Cohesion (Pa)	3×10^{7} (1×10^{6})
Plastic Yield stress (Pa)	5×10^{7}
Decollement slip rate (mm yr^{-1})	50

Solution of the mechanical equations is accomplished by using FLAC^{3D}, using a modified Lagrangian technique (Cundall and Board, 1988). We use modifications by Koons et al. (2002) and Upton et al. (2009) that allow for large strains and spatiotemporally variable erosion. The equations of motion are solved across a uniform, rectilinear grid of nodes, and velocity derivatives are discretized across a series of interconnected polyhedral 3D elements. The rheology of each element is mathematically approximated with a prescribed linear or nonlinear stress/strain or stress/strain rate relationship in response to applied forces or boundary restraints.

8.4. Surface Processes

We use a configuration of the Channel-Hillslope Integrated Landscape Developmental (CHILD) model (Tucker et al., 2001) to approximate the physics behind mechanical wear of the substrate under the assumption that rivers can erode bedrock and transport sediments at a rate roughly proportional to unit stream power, or the near-equivalent boundary shear stress (e.g. Bagnold, 1966; Howard and Kerby, 1983; Seidl and Dietrich, 1992; Howard et al., 1994; Stock and Montgomery, 1999; Kirby and Whipple, 2001; Hancock and Anderson, 2002; Whipple, 2004; Whittaker et al., 2007b; Yanites et al., 2010; Attal et al., 2011; Kirby and Whipple, 2012). CHILD has been used previously

to explore landscape sensitivity to tectonic forcing (Tucker and Slingerland, 1996; Miller et al., 2007; Whittaker et al., 2007a; Attal et al., 2008; Attal et al., 2011), sediment transport (Gasparini et al., 2004; Gasparini et al., 2007), storm events (Tucker and Bras, 2000; Sólyom and Tucker, 2004), and heterogeneous rock mass strength (Roy et al., 2015).

A steepest descent routing algorithm controls the spatial distribution of surface runoff in channels that are embedded as subgrid-scale features. Surface runoff leaves the domain through open flow boundaries. We assume a supply-limited condition in which all detached bedrock is immediately transported from the domain (e.g. Howard and Kerby, 1983; Stock et al., 2005; Whittaker et al., 2007b; Attal et al., 2008; Attal et al., 2011; Hobley et al., 2011). We model processes of landscape evolution using the following equation

$$\frac{\partial h}{\partial t} = -k_{b(x,y,z)}\omega + V_z + V_h \nabla h \qquad (8.1.)$$

where the rate of elevation change $\frac{\partial h}{\partial t}$ at any point on a surface depends on spatially variable erodibility $k_{b(x,y,z)}$, stream power ω per unit width, vertical rock motion relative to baselevel V_z, and lateral topographic advection $V_h \nabla h$. Our description of the heterogeneous 3D erodibility field is in Section 8.6 below. Rates of channel bed incision are assumed to be proportional to stream power per unit width

$$\omega = k_t \left(\frac{Q}{W}\right) S \qquad (8.2.)$$

where k_t is the unit weight of water (9800 kg m^{-2} s^{-2}), Q is fluid discharge, W is channel width, and S is channel slope. Upstream precipitation and drainage area values are integrated for every point in order to calculate fluid discharge. Channel width is calculated

using the empirical method (Leopold and Maddock, 1953) $W = k_w Q^{0.5}$, where k_w is the width-discharge coefficient, here given a value of $10 \text{ s}^{0.5} \text{ m}^{-0.5}$.

The stream power model shares the model free surface described in Section 8.3. However, we use a finer element resolution (2 km on average, Figure 8.1A) for the stream power model in order to better capture the scale at which fluvial processes influence topography. An irregular mesh discretization is used to seed the dendritic drainage patterns that tend to form in homogeneous landscapes (Roy et al., 2015). We use a linear interpolation to transfer changes in surface shape between the mechanical model and the surface dynamics model.

8.5. Orographic Precipitation

Atmospheric circulation is strongly sensitive to topography and can potentially lead to significant climate heterogeneity across mountainous relief (Smith, 1979; Tomlinson and Sansom, 1994; Roe, 2005; Galewsky et al., 2006; Gasparini and Whipple, 2014), with major implications for the distribution of runoff routing, stream power, and fluvial erosion rates. For our purposes we define an orographic model in which precipitation rate is a function of the vertical deflection of wind caused by surface slope and wind speed, the change in air temperature with elevation, and the loss of air moisture with distance traveled over the orogen.

$$P = S \, u \sin(\alpha) \, e^{-\frac{z}{H}} \qquad\qquad (8.3.)$$

where P is precipitation, S is precipitable water, u is lateral wind velocity, α is the angle of the surface topography, z is elevation, and H is the e-folding altitude representing the decrease in atmospheric moisture due to decreasing temperature. Equation 8.3 is meant to

reflect the typical heterogeneous pattern of orographic precipitation, producing a greater amount of precipitation on the inboard slopes facing the windward direction and low precipitation rates on the outboard slopes (Figure 8.1C). If the inboard slopes are large, more water is lost through precipitation sooner and there will be less precipitation across the outboard slopes. As a consequence, drainage density is higher and erosion rate tends to be greatest along the inboard side of the orogen.

8.6. Scaling Rule for Rock Strength-Erodibility Link

We choose to link processes of fluvial incision to rock mass strength through the erodibility parameter $k_{b(x,y,z)}$. The rock mass strength values we use are based on measurements and observations published in geotechnical and structural geology literature (Hoek and Brown, 1980; Thomson, 1993; Faulkner et al., 2003; Lockner et al., 2009; Tembe et al., 2009; Faulkner et al., 2010; Mitchell et al., 2011; Rempe et al., 2013). Assuming that bedrock anelastic strength is inversely proportional to erodibility (Sklar and Dietrich, 2001; Sklar and Dietrich, 2004), we apply the scaling rule used by Roy et al. (2015) and adapted from Hanson and Simon (2001)

$$k_{b(x,y,z)} = k_c C_{(x,y,z)}^{-1/2} \qquad (8.4.)$$

where C is cohesion and k_c is a coefficient equal to 0.2 with units $m^{1/2}$ s $kg^{-1/2}$. We elected to use cohesion as our gauge of anelastic strength because of its importance in the Mohr-Coulomb failure criterion and because of the greater accuracy of measurement over tensile strength in heavily damaged rock (Hoek and Brown, 1980; Hoek and Brown, 1997). We model rock damage as a function of plastic shear strain accommodation from deformation in the strain softening upper crust of the mechanical model. The mechanical weakening in

shear zones translates to a proportional increase in erodibility using Equation 8.4 (Figure 8.1D). Rock cohesion values are interpolated into the surface processes model along with the elevation data.

8.7. Model Results

In both experiments, the convergent plate shortens laterally upon collision with the elastic plate, leading to vertical displacement of the free surface (Figure 8.2A, 3A). A high strain decollement forms beneath the rheological boundary. Plastic shear strain is transferred to the stronger mid and upper crustal layers. The rheological response in the upper crust localizes strain in shear zones that grow toward the east with continued deformation. We allow for the mechanical model and the surface processes model to cooperatively influence topographic evolution (Figure 8.2A, 3A).

8.7.1. Experiment 1: Tectonics with Erosion

Assuming uniform erodibility and orographic precipitation, channels incise into the orogen following a general downslope direction, trending perpendicular to the collisional boundary. This dendritic drainage pattern persists despite channels crossing large strain gradients and sharp contrasts in strain rate associated with the outward growth of the orogen (Figure 8.2B, C). Conversely, channels on the inboard slope are more densely distributed and tend to be short, straight, and steep. The inboard network pattern correlates with maximum uplift and precipitation rates in addition to maximum strain along the collisional boundary, while the outboard pattern correlates with lower rates (Figure 8.2A, 8.5A).

Figure 8.2. Experiment 1. (A) Topography, (B) plastic strain, (C) strain rate. From left to right, surfaces from 50 km, 75 km, 100 km, and 125 km of crustal shortening. Arrowheads indicate the location of shear zones. Circle indicates a local topographic effect on plastic strain accommodation. Color scales located at lower left.

The overall width of the orogen grows to approximately 150 km (Figure 8.2A, 125 km shortening) and tends to widen in a slow, continuous pattern rather than with distinct thrusts (see Figure 8.4 in Section 8.7.3 for an example with no erosion displaying a wider orogen and distinct fold-thrusts). Plastic strain maps (Figure 8.2B) indicate significant localization of strain in eroded shear zones along the inboard side of the orogen and a gradual decrease in strain with distance from the drainage divide, a pattern that persists as deformation continues in time. This uniform pattern of diffuse strain in the outboard side of the orogen is perturbed slightly by the river network, which generates sharp relief at the sub-orogen scale (Figure 8.2B, 125 km shortening, dashed circle). As the orogen continues to build the strain field grows to the east. Strain rate maps (Figure 8.2C) indicate a relatively high strain rate along the indentor front and high strain rate along the growing eastern edge of the orogen. Within the orogen strain rate is relatively low and more diffuse, but does tend to concentrate approximately 40 km to the west of the growing edge of the orogen.

8.7.2. Experiment 2: Tectonics, Erosion, and the Strength-Erodibility Link

For Experiment 2 we use Equation 8.4 to link erodibility to rock cohesive strength values taken from the mechanical model. Results suggest that initially, the topographic pattern is nearly identical to that of Experiment 1 (Figure 8.3A, 50 km shortening). However, there is a noticeable increase in range-parallel channels in correlation with the strike of emerging shear zones, while range-perpendicular channels that correlate with the larger scale downslope gradient become less frequent (Figure 8.3A, 75 to 125 km shortening). The two or three major range-perpendicular channels must each accommodate a greater amount of surface runoff than each of the smaller, more frequent channels in
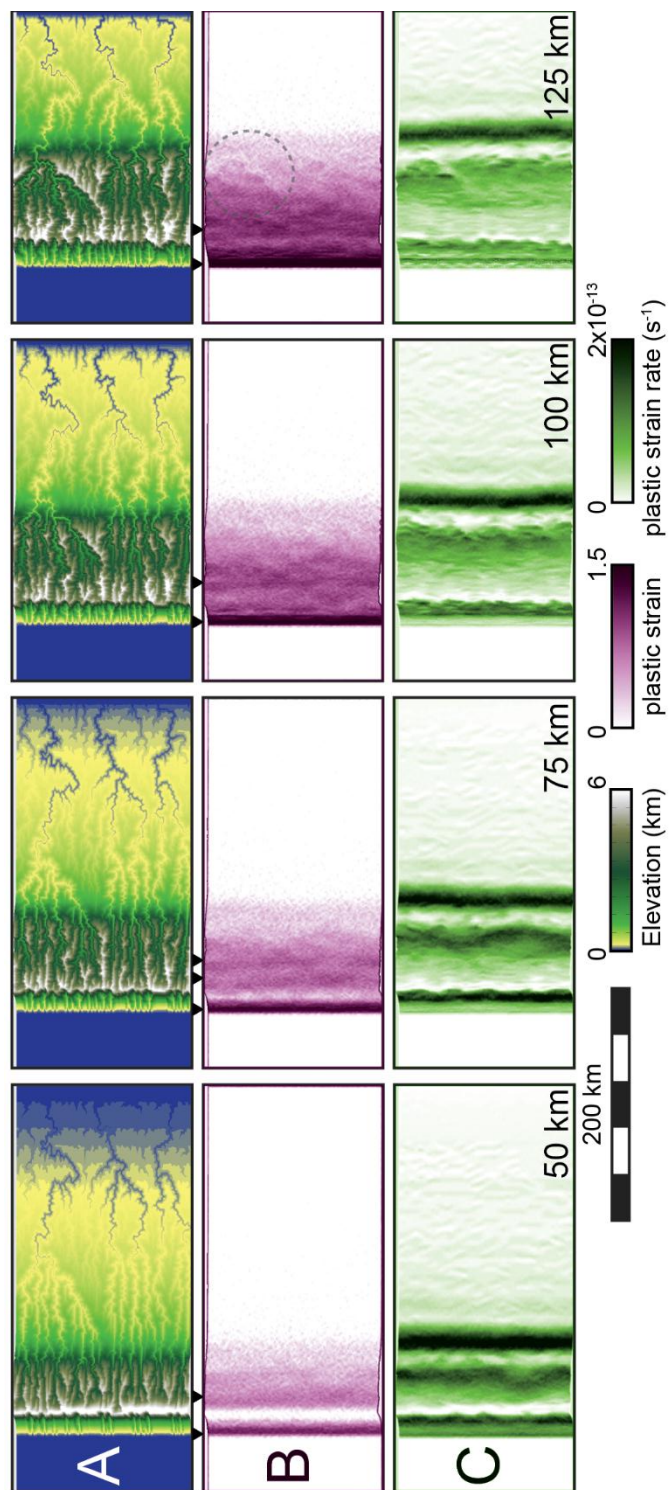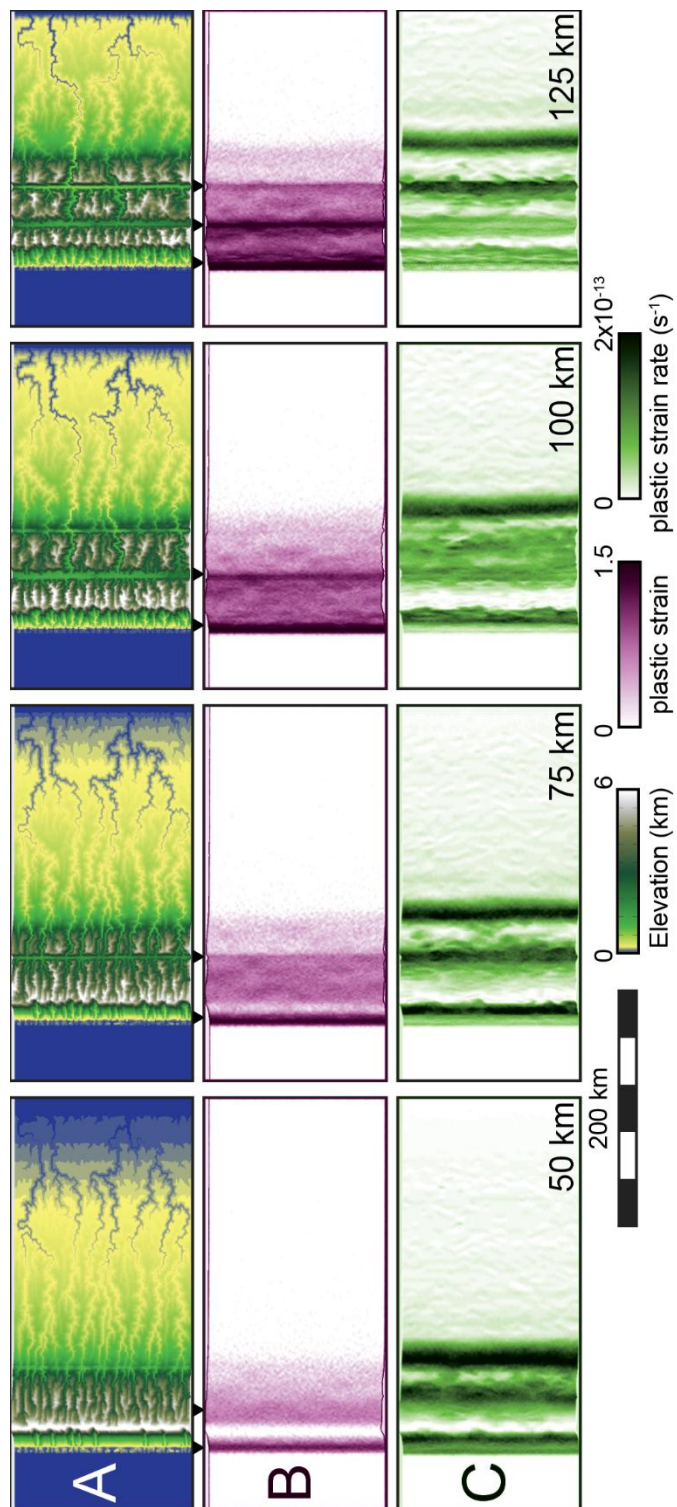
Figure 8.3. Experiment 2. (A) Topography, (B) plastic strain, (C) strain rate. From left to right, surfaces from 50 km, 75 km, 100 km, and 125 km of crustal shortening. Arrowheads indicate the location of shear zones. Color scales located at lower left.

Experiment 1. As a result there is significantly greater relief between the eroded shear zones and adjacent ridges when compared to Experiment 1 (Figure 8.5A versus Figure 8.5B). The inboard river network pattern is similar to Experiment 1 (Figure 8.3A versus Figure 8.2A).

The majority of strain in the orogen is concentrated along the eroding shear planes, but strain does also accumulate between the shear zones (Figure 8.3B). After 125 km of shortening in the orogen, eroded shear zones accommodate approximately 35% more strain than shear zones in Experiment 2, while crustal blocks between shear zones accommodate approximately 10% less strain. Again, strain rate tends to be greatest along the growing eastern edge of the orogen, but high strain rates do persist in the eroded shear zones even after they have migrated to the interior of the orogen (Figure 8.3C).

8.7.3 Supplemental Experiment 0: Tectonics with No Erosion

In supplemental Experiment 0, shear zones form iteratively with increasing distance from the plate boundary (Figure 8.4B). The shear zones host relatively large strain rates, but the greatest strain rate occurs along the growing outboard boundary of the orogen (Figure 8.4C). As a consequence, surface deformation takes the form of low amplitude fold-thrusts that grow outward from the indentor collectively in a wedge shape. This deformation pattern is similar to the fold-and-thrust belts and submarine accretionary complexes that generally follow critical wedge theory (Davis et al., 1983; Dahlen, 1984). Due to a lack of precipitation and erosion there is no river network pattern to compare for Experiment 0.
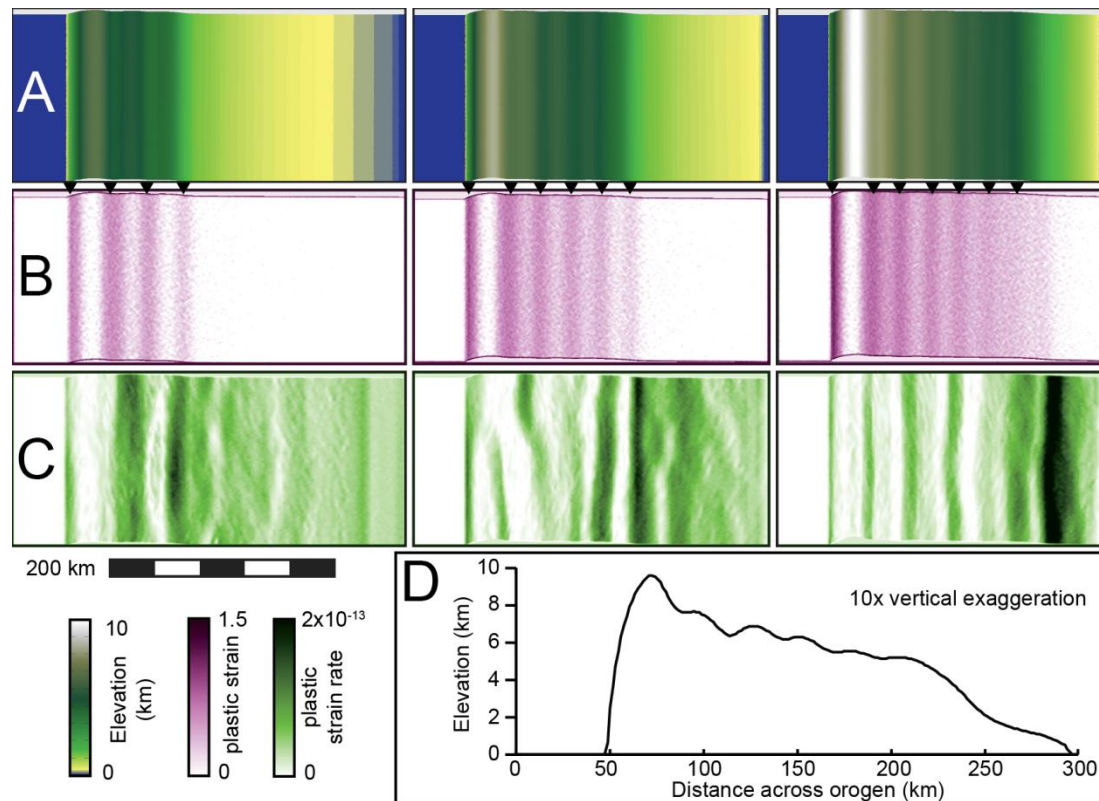
Figure 8.4. Experiment 0. (A) Topography, (B) plastic strain, (C) strain rate, and (D) Elevation profile. From left to right, surfaces from 50 km, 75 km, and 100 km of crustal shortening. Arrowheads indicate the location of shear zones. Color scales located at lower left.

8.8. Discussion

The noticeable difference in drainage network pattern between experiments coincides with a different pattern of tectonic strain partitioning in each orogen. The structurally confined drainage pattern of Experiment 2 indicates that strain weakening directly influences surface processes by locally increasing erosional efficiency and subsequently attracting a greater accumulation of surface runoff to power further erosion. Focused incision in shear zones leads to a subsequent increase in differential stress associated with range-parallel topographic relief. Consequently, as shear damage progresses with continued strain, greater erosion and greater strain is the expected result. The potential positive feedback attributed to rock damage can therefore play a significant

role in the evolution of strain within an orogen. For example, Norris and Toy (2014) hypothesize that the perseverance of oblique shear on the Alpine Fault of New Zealand may be partially attributed to heavy orographic precipitation and rapid exhumation of the shear zone.

In order to explore the potential sensitivity between erosion and strain, we measure strain localization, taken as the ratio of plastic shear strain inside the shear zone versus outside the shear zone over a distance spanning ~20 km (Figure 8.5C). Results from five experiments, each with a differing degree of strain-induced rock damage, indicate that strain localization is expected to increase with greater damage (Figure 8.5C). The most significant increase in strain localization occurs between 1x to 30x, when the pattern transitions from range-perpendicular (1x) to range-parallel (30x), indicating river channels that become confined to shear zone structures.

The damage scale in which the drainage pattern transition occurs is in agreement with Roy et al. (2015), who found that when using Equation 8.1, channels can become structurally confined when shear zones are more than 6 to 60 times weaker than intact rock. This degree of damage is well within the natural strength range of fault gouge and cataclasites (e.g. Ben-Zion and Sammis, 2003; Faulkner et al., 2010; Rempe et al., 2013) and many natural examples of structurally confined drainage exist (e.g. Ericson et al., 2005; Becker et al., 2014; Roy et al., 2015). The Three Rivers region along the eastern edge of the Himalayan Eastern Syntaxis is one such example where a strong correlation exists between the positioning of three larger rivers and three major shear zones (Hallet and Molnar, 2001; Liu et al., 2011). Similar correlations exist in New Zealand (Craw et al.,

2012), the Grand Canyon (Hodgson, 1961; Huntoon and Sears, 1975; Shoemaker et al., 1978), and the San Andreas Fault of California (Crowell, 1962), among other places.

Fluvial incision of outboard shear zones in Experiment 2 generates relief on the order of 2.5 km, generally over a distance of less than 20 km in an orientation conducive to local orographic effects (Figure 8.5B). The slight increase in rainfall associated with the erosional relief accounts for a small increase in fluid discharge and consequently an increase in erosional power in the structurally confined channel. Rainfall patterns in New Zealand are also sensitive to steep relief over similar length scales (Tomlinson and Sansom, 1994), but the magnitude is minimal compared to the large scale orographic pattern associated with the inboard side of the orogen in both the natural and model cases (Figure 8.5A, B).
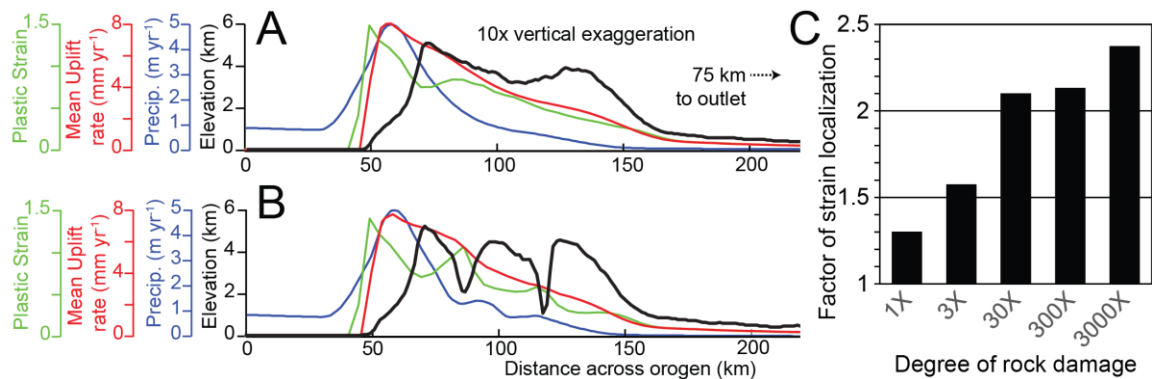
Figure 8.5. Cross-sectional profiles for Experiments 1 and 2 (A and B, respectively). Black: elevation, green: plastic strain, red: mean uplift rate, blue: precipitation rate. In all cases, peak values are located on the inboard side of the orogen, along the edge of the elastic plate. (C) Plot of strain localization factor versus degree of rock damage.

8.9. Conclusions

The strength-erodibility link explored in this work amplifies the cooperative responses between processes of erosion and tectonics. Crustal deformation facilitates the mechanical weakening of rock in distinct shear zones, establishing a network for

partitioning strain in permanently weakened rock. In addition, the efficient erosion of mechanically weakened rock amplifies the contrast of strain partitioning by unloading the topographic stresses that resist shear failure right above the shear zones. The geometry of shear zones is reflected by a shift in the drainage network pattern from range-perpendicular to range-parallel, matching the position and orientation of the eroding shear zones. Greater rock damage leads to a higher contrast of strain between shear damaged zones and the surrounding undamaged rock. Consequently, shear zones remain active for a longer period of time under these erosional conditions.

CHAPTER 9

CONCLUSIONS AND FUTURE WORK

9.1. Summary of Chapter Conclusions

Field evidence is suggestive of a fundamental link between the mechanical strength of rock and the rates and patterns of erosion by rivers. When this relation is applied in a numerical model of landscape evolution, results support the hypothesis that natural levels of rock damage, an order of magnitude weakening or more, positively influence the pattern of fluvial erosion and lead to structurally confined drainage network patterns. Erosion rates in weak zones can be an order of magnitude faster than in undamaged rock, due in part to the ease of greater erodibility but also to the greater attraction of runoff due to topographic steering by the eroded weak zone. The effect of runoff accumulation is great enough that rivers confined to weak zones with a shallow dip angle exhibit lateral shifting to coincide with the shifting exposure of the eroded weak zone.

Later exposure of weak zones, either by progressive erosion through a homogeneous medium or by some other mechanism of instantaneous emplacement on the surface, will still influence the drainage network pattern at the regional scale (100 km), and through it, topography. The introduction of multiple faults with nonparallel strike, for example produced by oblique collision or a combination of different tectonic events, may generate high tortuosity upon their intersection by a structurally confined river, the magnitude of which is equal to the difference in strike angle. The influence of late exposure weak zones is diminished with faster uplift rates. The eventual exposure of plutons will also alter the drainage network pattern.

The high rock erodibility and fracture density found in weak zones promotes rapid detachment and transport of fine grained materials after incision. Weak zones tend to erode far more quickly than surrounding intact rock and as a consequence, coarse grained sediments begin to accumulate in the low relief of the eroded damage zone. Field evidence also suggests that sediments armor the majority of weak zones except high up on valley walls or along channel heads. As a consequence, weak zones with structurally confined channels are armored for the majority of the time by sediments with coarser median grain size than expected from erosion of the weak zone itself. As a consequence, channel gradient in the weak zone is governed by alluvium rather than bedrock, while the opposite is true for the short, steep tributaries that incise into intact bedrock and deposit the coarse alluvium. Greater fault weakening leads to a greater reduction in relief and subsequently a greater residence time for sediments in or adjacent to the structurally confined channel.

The shape of topography holds valuable information about the scale dependency of tectonic and geomorphic forces. The signal of rivers is generally dominant at the 50 km wavelength or less, but this scale limit will vary by location. The tectonic signal dominates at the 100 km scale and greater, however features such as eroded faults, fault scarps, or heterogeneous lithology can influence topographic shape at any scale, including the scale traditionally dominated by fluvial processes. Different characteristic landforms exhibit signature multiscale patterns of anisotropy that can be used diagnostically to explore the geological history of a region. Our use of multiscale, every-directional variogram analysis has certain advantages over more traditional methods, including the ability to measure anisotropy for any spatially variable parameter, a strong sensitivity to spatial changes, a

fast calculation of directional-dependent elevation variance on a CUDA platform, and the ability to quantify variance at multiple scales.

Weak zone erosion is capable of perturbing the near surface stress field and may be capable of influencing the partitioning of tectonic strain in a tectonically active landscape. Coupled models used to explore this dynamic behavior suggest that localized erosion amplifies localized strain through an efficient unloading of normal topographic stress in a structural feature that is already accommodating a significant amount of shear strain. This response supports greater total accommodation of strain in shear zones, greater longevity for active shear zones, and a range-parallel drainage network pattern that is common in natural orogenic landscapes.

9.2. Future Work

9.2.1. A Failure-Based Model for Landscape Evolution

The future of tectonic-geomorphic-climate coupled modeling is in the creation of a failure-based landscape evolution model. My work uses traditional equations for stream power to parameterize the degree of work done on the bed of a river and a hypothetical scaling rule to relate rock mass strength to erodibility. My major conclusion from this thesis is that the mechanical properties of rock, largely controlled by tectonic strain, play a primary role in landscape evolution, and I reach this conclusion by using parametric models for river incision and a hypothetical scaling rule to relate cohesive strength to the nebulous parameter of erodibility. Ideally the determination of substrate detachment and transport should be based on the stress tensor at the surface, and recent improvements to computational fluid dynamics, combined with rapid advances in computational power,

mean that a physics-based model such as this may be well within reach. A lightweight engine for fluid dynamics is needed to generate the full stress tensor required to better understand the stress state along the wetted perimeter of a channel as well as the potential failure mechanisms that can occur along the base and sides of a channel. The strength of the bed would be derived from the mechanical strength of the rock and alluvium units it is composed of, which would account for anisotropies associated with mineralogy, stratigraphy, or structure. The flow dynamics of the river channel would impart stresses that are geometrically far more complex than assumed when using the scalar value of stream power or bed shear stress. An interesting experiment would be to see in what cases the solution diverges between a physics based and a parameterized model.

9.2.2. Landscapes with Greater Tectonic Complexity

Many of the tectonic regimes explored in this thesis are very simple and are not representative of the most interesting tectonic problems on Earth, namely collisional plate corners (Figure 9.1). For example, the Himalayan Eastern Syntaxis represents the tectonic edge of over 2000 km of crustal shortening between the Indian and Eurasian Plates (Hallet and Molnar, 2001). The resulting pattern of Tibetan uplift is a product of shallow slab subduction and thermal weakening north of the Himalayas. There is a significant degree of clockwise vorticity in the Eastern Syntaxis thought to be driven by a foundering Burma slab, which has widened the scale of deformation (Liu and Bird, 2008). Along the eastern edge in the Three Rivers region, active north striking strike-slip features host large rivers (Hallet and Molnar, 2001; Henck et al., 2011). The degree of tectonic strain, subsequent crustal weakening, and highly focused fluvial incision has led to extreme uplift/incision

rates and ~4 km of relief between Tsangpo Gorge and Gyala Peri-Namche Barwa Massif (Zeitler et al., 2001; Koons et al., 2002; Koons et al., 2013).

Patterns of deformation in these regions cannot be completely explained by fault block models or even the simple crust-scale dynamic models of Chapter 8, but require a numerical solution that takes into account spatially variable tectonic strain associated with spatiotemporal changes in mantle advection and lithospheric strength. In this section I provide preliminary results for a plate corner model that does not account for dynamic mantle advection or heterogeneous lithosphere strength at depth, but does provide some insight on the surface response to the intersection of horizontal and vertical coordinate shear strain.

My preliminary models of convergent plate corners (Figure 9.2.) are able to replicate some expected patterns of crustal deformation within the colliding plate corner. I implement the same tectonic, climatic, and surface processes conditions as in Chapter 8, except I limit the traction velocity on the middle crust to ¾ of the model base to enforce the creation of a corner. As a result, the colliding crust deforms in a pattern similar to a fold-thrust belt (Figure 9.2A, B). Shear strain localizes between thrusts, along the transverse fault, and along the decollement near the base (Figure 9.2C). Much like the experiments from Chapter 8, shear strain rate persists on the shear zones within the orogen but are greatest along the growing edge of the orogen (Figure 9.2D). There is a small amount of range-parallel displacement associated with the corner geometry (Figure 9.2E). The magnitude of vorticity is minimal, but I have indicated the basic trend with unscaled arrows in Figure 9.2E. This displacement and subsequent range-perpendicular shortening is enough to cause a small amount of uplift outside of the corner. Experiments with erosion

are shown in Figure 9.2F, G. Maximum elevation is approximately 6 km and vertical displacement is approximately double. Rivers tend to incise the orogen from the corner because of the relief pattern generated upon collision. In the experiment with the fault damage-erodibility link (Figure 9.2G), there is significant erosion along the transverse fault. This pattern of uplift leads to a strong range-parallel drainage pattern.

Time series data (Figure 9.3) reveal how the orogen builds through a series of outward stepping fold-thrusts. A distinct orogen forms by 800 ka and soon after, new thrusts initially form near the transverse fault, then propagate across the orogen. This pattern of uplift is probably due to the damage propagation along the decollement and the transverse fault: uplift initiates while the upper crust is still strong.

Despite these interesting results, the simple boundary conditions I use cannot replicate patterns of deformation associated with large corner vorticity, nor can I replicate plateau uplift associated with thermal weakening of the crust. However, model results act as a suitable first order attempt at corner collision because we can at least attribute these patterns of deformation to something beyond my simple constraints. An improved model would allow for thermal weakening of the crust and a larger model domain to account for wider deformation patterns and inclusion of the full lithosphere. In addition, models will need to be run to higher strains to better replicate the conditions of real plate corners. Such a model will require dedicated regridding algorithms to help stabilize the model solution. Such models do exist, and the incorporation of surface processes and a damage-erodibility link would be straightforward.

219

Figure 9.1. Himalayan Eastern Syntaxis. (A) Elevation map, colored lines represent channel tortuosity. River abbreviations: Y-T: Yarlung-Tsangpo, Br: Brahmaputra, S: Salween, M: Mekong, Y: Yangtze. Gyala Peri-Namche Barwa Massif is location of high relief where Y-T tortuosity is greatest. (B) Reference map. (C) Tectonic map with faults/suture zones in red, rivers in blue. MBT: Main Boundary Thrust; IYS: Indus-Yarlung Tsangpo Suture; S: Sagaing Fault; BS: Bangong-Nujiang suture; LS: Longmu Co-Shuang hu suture; JS: Jinsha suture.
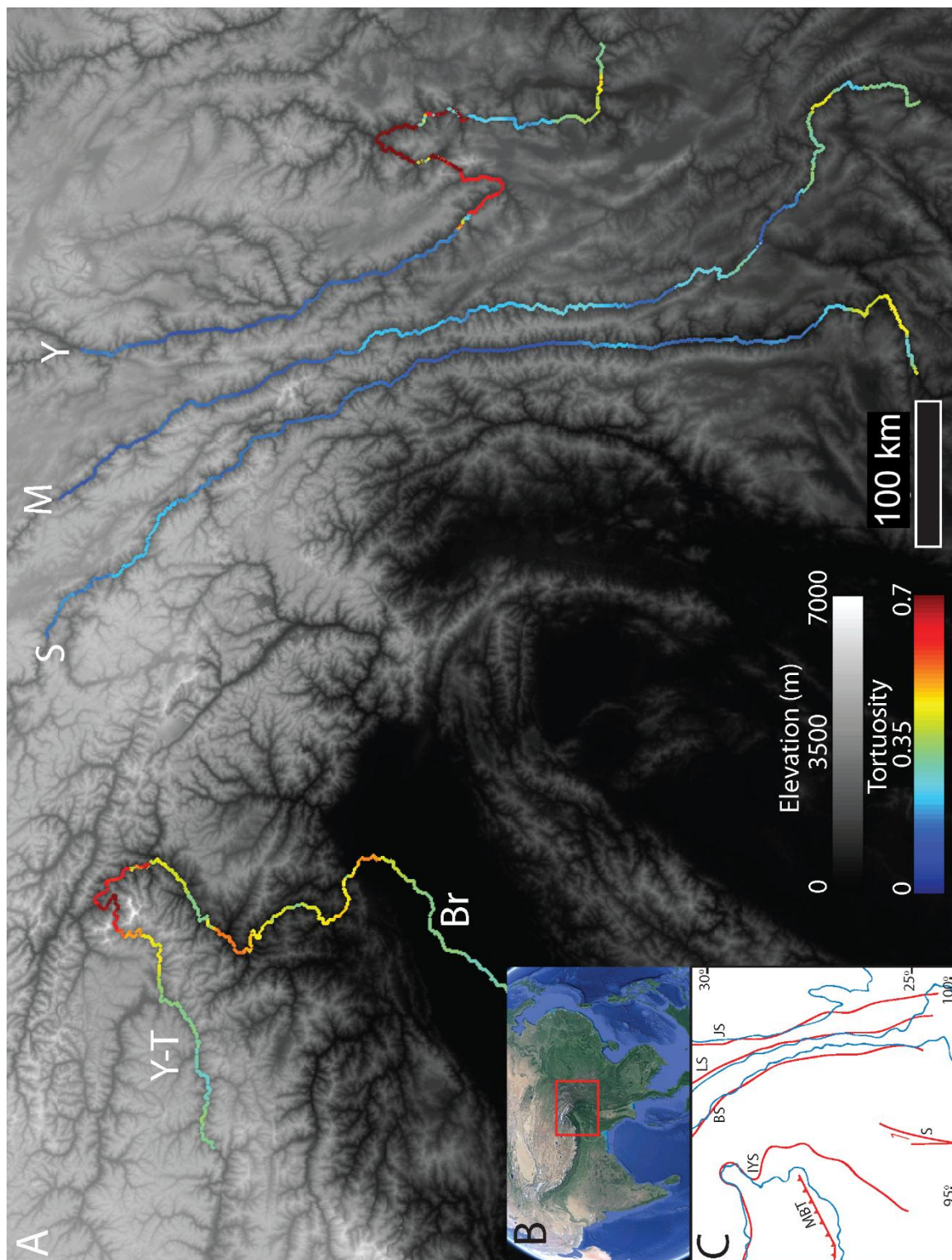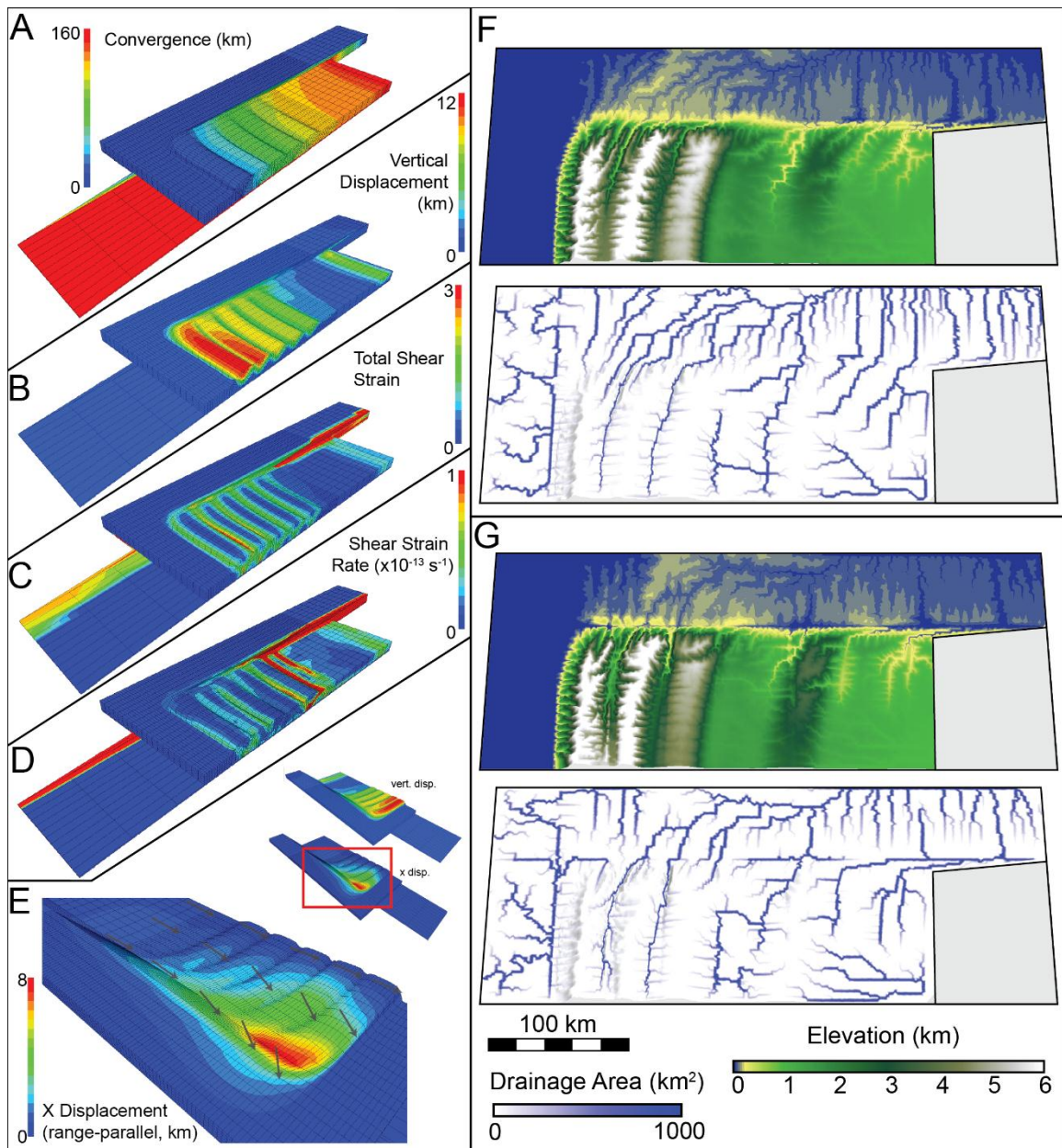
Figure 9.2. Example corner model. (A-E) Model with no erosion, (F) model with erosion but no damage-erodibility link, and (G) model with erosion and damage-erodibility link. (A) Total convergence, (B) vertical displacement, (C) total shear strain, (D) shear strain rate, (E) closeup of total displacement in x (range parallel) direction, small images on right indicate region of zoom. (F, G) surface elevation (top) and drainage area (bottom) maps.
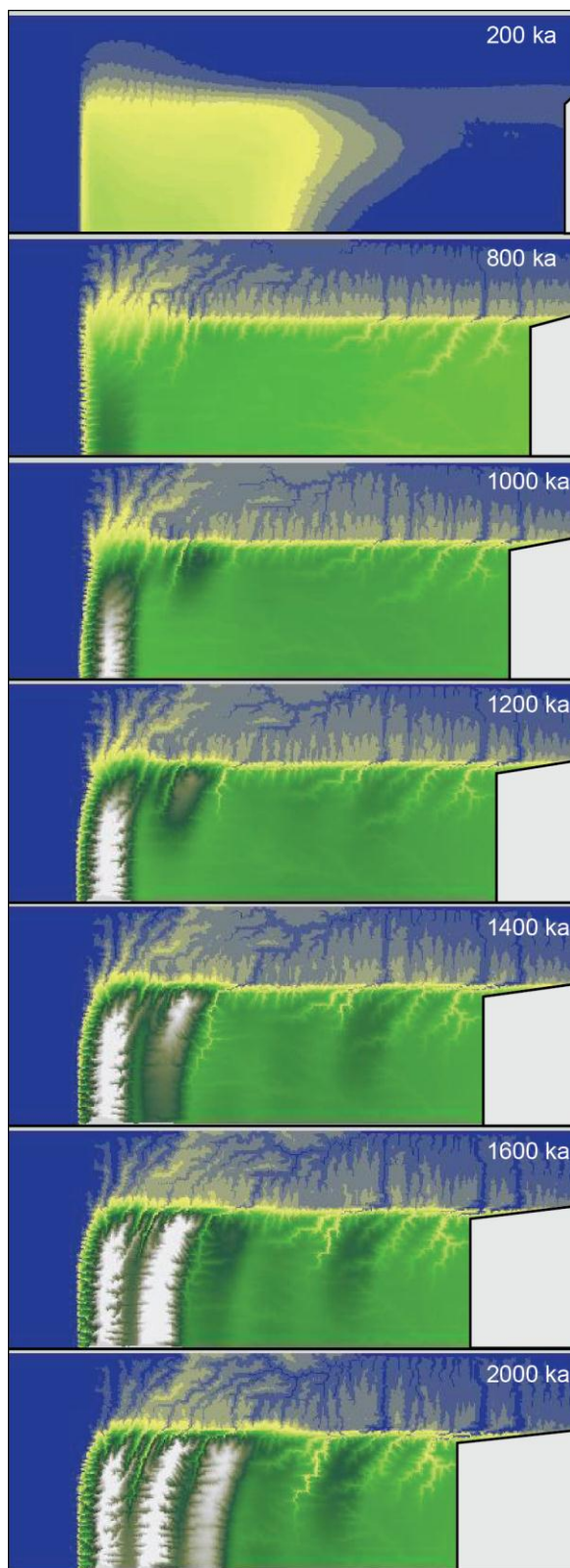
Figure 9.3. Time series of corner model elevation. Orogen grows by distinct fold-thrusts, which initiate near the transverse fault. A small amount of uplift occurs outside of the corner.

REFERENCES

Ambrosi, C., and Crosta, G.B., 2011, Valley shape influence on deformation mechanisms of rock slopes Valley shape influence on deformation mechanisms of rock slopes: Geological Society, London, Special Publications, v. 351, p. 215–233, doi: 10.1144/SP351.12.

Attal, M., Cowie, P.A., Whittaker, A.C., Hobley, D., Tucker, G.E., and Roberts, G.P., 2011, Testing fluvial erosion models using the transient response of bedrock rivers to tectonic forcing in the Apennines, Italy: Journal of Geophysical Research, v. 116, no. F2, p. F02005, doi: 10.1029/2010JF001875.

Attal, M., Tucker, G.E., Whittaker, A.C., Cowie, P.A., and Roberts, G.P., 2008, Modeling fluvial incision and transient landscape evolution: Influence of dynamic channel adjustment: Journal of Geophysical Research, v. 113, no. F3, p. 1–16, doi: 10.1029/2007JF000893.

Babenroth, D.L., and Strahler, A.N., 1945, Geomorphology and structure of the East Kaibab monocline, Arizona and Utah: Bulletin of the Geological Society of America, v. 56, p. 107–150.

Bagnold, R.A., 1966, An approach to the sediment transport problem from general physics: US Geol. Surv. Prof. Paper, v. 422-I.

Barnett, W., 2004, Subsidence breccias in kimberlite pipes—an application of fractal analysis: Lithos, v. 76, no. 1-4, p. 299–316, doi: 10.1016/j.lithos.2004.03.019.

Barnsley, M.F., Devaney, R.L., Mandelbrot, B.B., Peitgen, H.-O., Saupe, D., and Voss, R.F., 1988, The Science of Fractal Images (H.-O. Peitgen & D. Saupe, Eds.): Springer-Verlag, New York.

Beaumont, C., 2004, Crustal channel flows: 1. Numerical models with applications to the tectonics of the Himalayan-Tibetan orogen: Journal of Geophysical Research, v. 109, no. B6, p. B06406, doi: 10.1029/2003JB002809.

Becker, R.A., Tikoff, B., Riley, P.R., and Iverson, N.R., 2014, Preexisting fractures and the formation of an iconic American landscape: Tuolumne Meadows, Yosemite National Park, USA: GSA Today, v. 24, no. 11, p. 4–10, doi: 10.1130/GSATG203A.1.

Ben-Zion, Y., and Sammis, C., 2003a, Characterization of fault zones: Pure and Applied Geophysics, v. 160, p. 677–715.

Ben-Zion, Y., and Sammis, C.G., 2003b, Characterization of fault zones: Pure and Applied Geophysics, v. 160, p. 677–715.

Bercovici, D., and Ricard, Y., 2014, Plate tectonics, damage and inheritance: Nature, v. 508, p. 513–516, doi: 10.1038/nature13072.

Berlin, M.M., and Anderson, R.S., 2007, Modeling of knickpoint retreat on the Roan Plateau, western Colorado: Journal of Geophysical Research, v. 112, no. F3, p. F03S06, doi: 10.1029/2006JF000553.

Bieniawski, Z.T., 1974, Estimating the strength of rock materials: Journal of the South African Institute of Mining and Metallurgy, v. 74, p. 312–320.

Billen, M.I., 2008, Modeling the Dynamics of Subducting Slabs: Annual Review of Earth and Planetary Sciences, v. 36, no. 1, p. 325–356, doi: 10.1146/annurev.earth.36.031207.124129.

Blenkinsop, T.G., 1991, Cataclasis and processes of particle size reduction: Pure and Applied Geophysics, v. 136, no. 1, p. 60–86.

Bonnet, E., Bour, O., Odling, N.E., Davy, P., Main, I., Cowie, P., and Berkowitz, B., 2001, Scaling of fracture systems in geological media: Reviews of Geophysics, v. 39, no. 3, p. 347–383.

Brace, W., and Kohlstedt, D., 1980, Limits on lithospheric stress imposed by laboratory experiments: J. geophys. Res., v. 85, no. B11, p. 6248–6252.

Brideau, M.-A., Stead, D., and Couture, R., 2006, Structural and engineering geology of the East Gate Landslide, Purcell Mountains, British Columbia, Canada: Engineering Geology, v. 84, no. 3-4, p. 183–206, doi: 10.1016/j.enggeo.2006.01.004.

Brideau, M.-A., Yan, M., and Stead, D., 2009, The role of tectonic damage and brittle rock fracture in the development of large rock slope failures: Geomorphology, v. 103, no. 1, p. 30–49, doi: 10.1016/j.geomorph.2008.04.010.

Browne, G.H., 1992, The northeastern portion of the Clarence Fault: Tectonic implications for the late Neogene evolution of Marlborough, New Zealand: New Zealand Journal of Geology and Geophysics, v. 35, no. March 2015, p. 437–445, doi: 10.1080/00288306.1992.9514538.

Buck, W.R., 1988, flexural rotation of normal faults: Tectonics, v. 7, no. 5, p. 959–973, doi: 10.1029/TC007i005p00959.

Bulmer, M.G., 2012, Principles of Statistics: Courier Dover Publications.

Bürgmann, R., and Dresen, G., 2008, Rheology of the Lower Crust and Upper Mantle: Evidence from Rock Mechanics, Geodesy, and Field Observations: Annual Review of Earth and Planetary Sciences, v. 36, no. 1, p. 531–567, doi: 10.1146/annurev.earth.36.031207.124326.

Carpenter, B.M., Marone, C., and Saffer, D.M., 2011, Weakness of the San Andreas Fault revealed by samples from the active fault zone: Nature Geoscience, v. 4, no. 4, p. 251–254, doi: 10.1038/ngeo1089.

Chapple, W.M., 1978, Mechanics of thin-skinned fold-and-thrust belts: Geological Society of America Bulletin, v. 89, no. 8, p. 1189–1198.

Chase, C.G., 1992, Fluvial landsculpting and the fractal dimension of topography: v. 5, p. 39–57.

Chester, F.M., and Logan, J., 1987, Composite planar fabric of gouge from the Punchbowl fault, California: Journal of Structural Geology, v. 9, no. 5, p. 621–634.

Chester, F.M., and Logan, J.M., 1986, Implications for mechanical properties of brittle faults from observations of the Punchbowl fault zone, California: Pure and Applied Geophysics PAGEOPH, v. 124, no. 1-2, p. 79–106, doi: 10.1007/BF00875720.

Clarke, B.A., and Burbank, D.W., 2010, Bedrock fracturing, threshold hillslopes, and limits to the magnitude of bedrock landslides: Earth and Planetary Science Letters, v. 297, no. 3-4, p. 577–586, doi: 10.1016/j.epsl.2010.07.011.

Clarke, B.A., and Burbank, D.W., 2011, Quantifying bedrock-fracture patterns within the shallow subsurface: Implications for rock mass strength, bedrock landslides, and erodibility: Journal of Geophysical Research, v. 116, no. F4, p. F04009, doi: 10.1029/2011JF001987.

Clauset, A., and Shalizi, C.R., 2007, Power-Law Distributions in Empirical Data: Santa Fe Institute Working Paper.

Coulomb, C., 1773, Essai sur une application des règles de maximis & minimis à quelques problèmes de statique, relatifs à l'architecture: Mem. Acad. Roy. Div. Sav., v. 7, p. 343–387.

Craw, D., Burridge, C.P., Upton, P., Rowe, D.L., and Waters, J.M., 2008, Evolution of biological dispersal corridors through a tectonically active mountain range in New Zealand: Journal of Biogeography, v. 35, p. 1790–1802, doi: 10.1111/j.1365-2699.2008.01936.x.

Craw, D., Upton, P., Horton, T., and Williams, J., 2013, Migration of hydrothermal systems in an evolving collisional orogen, New Zealand: Mineralium Deposita, v. 48, p. 233–248, doi: 10.1007/s00126-012-0421-8.

Craw, D., Upton, P., Walcott, R., Burridge, C., and Waters, J., 2012, Tectonic controls on the evolution of the Clutha River catchment, New Zealand: New Zealand Journal of Geology and Geophysics, v. 55, no. 4, p. 345–359, doi: 10.1080/00288306.2012.709184.

Crosby, B.T., and Whipple, K.X., 2006, Knickpoint initiation and distribution within fluvial networks: 236 waterfalls in the Waipaoa River, North Island, New Zealand: Geomorphology, v. 82, no. 1-2, p. 16–38, doi: 10.1016/j.geomorph.2005.08.023.

Crowell, J.C., 1962, Displacement Along the San Andreas Fault, California: Geological Society of America Special Papers, v. 71, p. 1–58, doi: 10.1130/SPE71.

Cui, Y., 2003, Sediment pulses in mountain rivers: 2. Comparison between experiments and numerical predictions: Water Resources Research, v. 39, no. 9, p. 1–11, doi: 10.1029/2002WR001805.

Cundall, P., and Board, A., 1988, A microcomputer program for modelling large-strain plasticity problems, *in* Swoboda, G. and Balkema, A.A. eds., Proceedings, 6th International Conference on Numerical Methods in Geomechanics, Innsbruck, Austria, Rotterdam, p. 2101–2108.

Dahlen, F. a., 1984, Noncohesive critical Coulomb wedges: An exact solution: Journal of Geophysical Research, v. 89, no. B12, p. 10125–10133, doi: 10.1029/JB089iB12p10125.

Davis, W.M., 1899, The Geographical Cycle: The Geographical Journal, v. 14, no. 5, p. 481–504.

Davis, D., Suppe, J., and Dahlen, F.A., 1983, Mechanics of fold-and-thrust belts and accretionary wedges: Journal of Geophysical Research, v. 88, no. B2, p. 1153–1172, doi: 10.1029/JB089iB12p10087.

DeMets, C., Gordon, R.G., Argus, D.F., and Stein, S., 1994, Effect of recent revisions to the geomagnetic reversal timescale on estimates of current plate motions (Paper 94GL02118): Geophysical Research Letters, v. 21, no. 20, p. 2191–2194.

Demirel, N., 2011, Effects of the rock mass parameters on the dragline excavation performance: Journal of Mining Science, v. 47, no. 4, p. 441–449.

Densmore, L., Ellis, A., and Anderson, S., 1998, Landsliding and the evolution of normal-fault-bounded mountains incision: Journal of Geophysical Research, v. 103, no. B7, p. 15203–15219.

DiBiase, R.A., Whipple, K.X., Heimsath, A.M., and Ouimet, W.B., 2010, Landscape form and millennial erosion rates in the San Gabriel Mountains, CA: Earth and Planetary Science Letters, v. 289, no. 1-2, p. 134–144, doi: 10.1016/j.epsl.2009.10.036.

Dicken, C.L., Nicholson, S.W., Horton, J.D., Kinney, S.A., Gunther, G., Foose, M.P., and Mueller, J.A.L., 2005, U.S. Geological Survey Open-File Report: Integrated

Geologic Map Databases for the United States: Delaware, Maryland, New York, Pennsylvania, and Virginia:.

Dingley, D., 2004, Progressive steps in the development of electron backscatter diffraction and imaging microscopy: Journal of Microscopy, v. 213, no. 3, p. 214–224.

Van Dissen, R., and Yeats, R.S., 1991, Hope fault , Jordan thrust , and uplift of the Seaward Kaikoura Range, New Zealand: Geology, v. 19, p. 393–396.

Dodds, P.S., and Rothman, D.H., 2000, Scaling, universality, and geomorphology: Annual Review of Earth and Planetary Sciences, v. 28, p. 571–610.

Egholm, D., Knudsen, M., and Sandiford, M., 2013, Lifespan of mountain ranges scaled by feedbacks between landsliding and erosion by rivers: Nature, v. 498, p. 475–477, doi: 10.1038/nature12218.

England, P., and Searle, M., 1986, The Cretaceous-tertiary deformation of the Lhasa Block and its implications for crustal thickening in Tibet: Tectonics, v. 5, no. 1, p. 1–14, doi: 10.1029/TC005i001p00001.

Enlow, R., and Koons, P.O., 1998, Critical wedges in three dimensions: Analytical expressions from Mohr-Coulomb constrained perturbation analysis: JOURNAL OF GEOPHYSICAL RESEARCH, v. 103, p. 4897–4914.

Ericson, K., Migon, P., and Olvmo, M., 2005, Fractures and drainage in the granite mountainous area: a study from Sierra Nevada, USA: Geomorphology, v. 64, no. 1-2, p. 97–116, doi: 10.1016/j.geomorph.2004.06.003.

Faulkner, D.R., Jackson, C.A.L., Lunn, R.J., Schlische, R.W., Shipton, Z.K., Wibberley, C.A.J., and Withjack, M.O., 2010, A review of recent developments concerning the structure, mechanics and fluid flow properties of fault zones: Journal of Structural Geology, v. 32, no. 11, p. 1557–1575, doi: 10.1016/j.jsg.2010.06.009.

Faulkner, D.R., Lewis, A.C., and Rutter, E.H., 2003, On the internal structure and mechanics of large strike-slip fault zones: field observations of the Carboneras fault in southeastern Spain: Tectonophysics, v. 367, no. 3-4, p. 235–251, doi: 10.1016/S0040-1951(03)00134-3.

Finnegan, N.J., Roe, G., Montgomery, D.R., and Hallet, B., 2005, Controls on the channel width of rivers: Implications for modeling fluvial incision of bedrock: Geology, v. 33, no. 3, p. 229, doi: 10.1130/G21171.1.

Foster, M.A., and Kelsey, H.M., 2012, Knickpoint and knickzone formation and propagation, South Fork Eel River, northern California: Geosphere, v. 8, no. 2, p. 403–416, doi: 10.1130/GES00700.1.

Galewsky, J., Stark, C.P., Dadson, S., Wu, C.-C., Sobel, a. H., and Horng, M.-J., 2006, Tropical cyclone triggering of sediment discharge in Taiwan: Journal of Geophysical Research, v. 111, no. F3, p. F03014, doi: 10.1029/2005JF000428.

Gardner, T., 1983, Experimental study of knickpoint and longitudinal profile evolution in cohesive, homogeneous material: Geological Society of America Bulletin, v. 5, no. May, p. 664–672.

Gasparini, N.M., Tucker, G.E., and Bras, R.L., 1999, Downstream fining through selective particle sorting in an equilibrium drainage network: Geology, v. 27, no. 12, p. 1079–1082, doi: 10.1130/0091-7613(1999)027<1079:DFTSPS>2.3.CO;2.

Gasparini, N.M., Tucker, G.E., and Bras, R.L., 2004, Network-scale dynamics of grain-size sorting: implications for downstream fining, stream-profile concavity, and drainage basin morphology: Earth Surface Processes and Landforms, v. 29, no. 4, p. 401–421, doi: 10.1002/esp.1031.

Gasparini, N.M., and Whipple, K.X., 2014, Diagnosing climatic and tectonic controls on topography: Eastern flank of the northern Bolivian Andes: Lithosphere, , no. May, p. 230–250, doi: 10.1130/L322.1.

Gasparini, N.M., Whipple, K.X., and Bras, R.L., 2007, Predictions of steady state and transient landscape morphology using sediment-flux-dependent river incision models: Journal of Geophysical Research, v. 112, no. F3, p. F03S09, doi: 10.1029/2006JF000567.

Ghisetti, F.C., Gorman, A.R., and Sibson, R.H., 2007, Surface breakthrough of a basement fault by repeated seismic slip episodes: The Ostler Fault, South Island, New Zealand: Tectonics, v. 26, no. April, p. 1–15, doi: 10.1029/2007TC002146.

Gilbert, G., 1877, Report on the Geology of the Henry Mountains: US Geographical and Geological Survey of the Rocky Mountain Region, Region, Washington, DC.,.

Goode, J.R., and Wohl, E., 2010, Substrate controls on the longitudinal profile of bedrock channels: Implications for reach-scale roughness: Journal of Geophysical Research, v. 115, no. F3, p. F03018, doi: 10.1029/2008JF001188.

Goodfellow, B.W., Skelton, A., Martel, S.J., Stroeven, A.P., Jansson, K.N., and Hättestrand, C., 2014, Controls of tor formation, Cairngorm Mountains, Scotland: Journal of Geophysical Research: Earth Surface, v. 119, no. 2, p. 225-246, doi: 10.1002/2013JF002862.

Grant-Taylor, T.L., 1964, Volcanic history of Western Taranaki: New Zealand Journal of Geology and Geophysics, v. 7, no. 1, p. 78–86, doi: 10.1080/00288306.1964.10420158.

Hack, J.T., and Young, R.S., 1959, Intrenched meanders of the north fork of the Shenandoah River, Virginia: Geological Survey Professional Paper, v. 354-A.

Hallet, B., and Molnar, P., 2001a, Distorted drainage basins as markers of crustal strain east of the Himalaya: Journal of Geophysical Research, v. 106, no. B7, p. 13697–13709.

Hallet, B., and Molnar, P., 2001b, Distorted drainage basins as markers of crustal strain east of the Himalaya: Journal of Geophysical Research, v. 106, no. B7, p. 13697–13709.

Hancock, G.S., and Anderson, R.S., 2002, Numerical modeling of fluvial strath-terrace formation in response to oscillating climate: Geological Society of America Bulletin, v. 114, no. 9, p. 1131–1142.

Handy, M., Hirth, G., and Burgmann, R., 2007, Continental fault structure and rheology from the frictional-to-viscous transition downward, *in* Handy, M., Hirth, G., and Hovius, N. eds., Continental Fault Structure and Rheology from the Frictional-to-Viscous Transition Downward, MIT Press, p. 139–181.

Hanson, G., and Simon, A., 2001, Erodibility of cohesive streambeds in the loess area of the midwestern USA: Hydrological Processes, v. 38, p. 23–38.

Harrison, A.J., and White, R.S., 2004, Crustal structure of the Taupo Volcanic Zone, New Zealand: Stretching and igneous intrusion: Geophysical Research Letters, v. 31, no. L13615, doi: 10.1029/2004GL019885.

Henck, A.C., Huntington, K.W., Stone, J.O., Montgomery, D.R., and Hallet, B., 2011, Spatial controls on erosion in the Three Rivers Region, southeastern Tibet and southwestern China: Earth and Planetary Science Letters, v. 303, no. 1-2, p. 71–83, doi: 10.1016/j.epsl.2010.12.038.

Henne, a, Craw, D., and MacKenzie, D., 2011, Structure of the Blue Lake Fault Zone, Otago Schist, New Zealand: New Zealand Journal of Geology and Geophysics, v. 54, no. 3, p. 311–328, doi: 10.1080/00288306.2011.577080.

Hicks, D., Shankar, U., McKerchar, A., Basher, L., Jessen, M., Lynn, I., and Page, M., 2011, Suspended sediment yields from New Zealand rivers: Journal of Hydrology (New Zealand), v. 50, no. 1, p. 81–142.

Hobley, D.E.J., Sinclair, H.D., Mudd, S.M., and Cowie, P.A., 2011, Field calibration of sediment flux dependent river incision: Journal of Geophysical Research, v. 116, no. F4, p. F04017, doi: 10.1029/2010JF001935.

Hodgson, R.A., 1961, Reconnaisance of jointing in Bright Angel Area, Grand Canyon, Arizona: Bulletin of the American Asociation of Petroleum Geologists, v. 45, no. 1, p. 95–108.

Hoek, E., 1999, Putting numbers to geology—an engineer's viewpoint: Quarterly Journal of Engineering Geology and Hydrogeology, v. 32, no. 1, p. 1–19.

Hoek, E., 2001, Rock mass properties for underground mines: Underground Mining Methods: Engineering Fundamentals and International Case Studies, p. 467-474.

Hoek, E., and Brown, E.T., 1997, Practical estimates of rock mass strength: International Journal of Rock Mechanics and Mining Sciences, v. 34, no. 8, p. 1165–1186, doi: 10.1016/S0969-4765(04)00066-9.

Hoek, E., and Brown, E.T., 1980, Underground Excavations in Rock: Stephen Austin and Sons Ltd., London.

Howard, A., 1994, A detachment-limited model of drainage basin evolution: Water resources research, v. 30, no. 7, p. 2261–2285.

Howard, A.D., Dietrich, W.E., and Seidl, M.A., 1994, Modeling fluvial erosion on regional to continental scales: Journal of Geophysical Research, v. 99, no. B7, p. 13,971–13,986.

Howard, A.D., and Kerby, G., 1983, Channel changes in badlands: Geological Society of America Bulletin, v. 94, p. 739–752.

Hsu, H.-L., Yanites, B.J., Chen, C., and Chen, Y.-G., 2010, Bedrock detection using 2D electrical resistivity imaging along the Peikang River, central Taiwan: Geomorphology, v. 114, no. 3, p. 406–414, doi: 10.1016/j.geomorph.2009.08.004.

Huismans, R., and Beaumont, C., 2011, Depth-dependent extension, two-stage breakup and cratonic underplating at rifted margins: Nature, v. 473, p. 74–78, doi: 10.1038/nature09988.

Huismans, R.S., and Beaumont, C., 2014, Rifted continental margins: The case for depth-dependent extension: Earth and Planetary Science Letters, v. 407, p. 148–162, doi: 10.1016/j.epsl.2014.09.032.

Huntoon, P., and Sears, J., 1975, Bright angel and eminence faults, eastern Grand Canyon, Arizona: Geological Society of America Bulletin, v. 86, no. 4, p. 465–472, doi: 10.1130/0016-7606(1975)86<465.

Jébrak, M., 1997, Hydrothermal breccias in vein-type ore deposits: a review of mechanisms, morphology and size distribution: Ore geology reviews, v. 12, p. 111–134.

Judson, S., and Andrews, G., 1955, Pattern and form of some valleys in the Driftless Area, Wisconsin: The Journal of Geology, v. 63, no. 4, p. 328–336.

Julien, P.Y., 2010, Erosion and Sedimentation: Cambridge University Press.

Kirby, E., and Whipple, K.X., 2012, Expression of active tectonics in erosional landscapes: Journal of Structural Geology, v. 44, p. 54–75, doi: 10.1016/j.jsg.2012.07.009.

Kirby, E., and Whipple, K.X., 2001, Quantifying differential rock-uplift rates via stream profile analysis: Geology, v. 29, no. 5, p. 415–418.

Kirby, E., Whipple, K.X., Tang, W., and Chen, Z., 2003, Distribution of active rock uplift along the eastern margin of the Tibetan Plateau: Inferences from bedrock channel longitudinal profiles: Journal of Geophysical Research, v. 108, no. B4, p. 2217, doi: 10.1029/2001JB000861.

Kitanidis, P.K., 1997, Introduction to Geostatistics: Applications in Hydrogeology: Press Syndicate of the University of Cambridge, Cambridge, UK.

Kleffmann, S., Davey, F., Melhuish, A., Okaya, D., Stern, T., and SIGHT Team, 1998, Crustal structure in the central South Island, New Zealand, from the Lake Pukaki seismic experiment: New Zealand Journal of Geology and Geophysics, v. 41, no. 1, p. 39–49, doi: 10.1080/00288306.1998.9514789.

Klinkenberg, B., and Goodchild, M.F., 1992, The fractal properties of topography: a comparison of methods: Earth Surface Processes and Landforms, v. 17, p. 217–234.

Koons, P.O., 1995, Modeling the topographic evolution of collisional belts: Annual Review of Earth and Planetary Sciences, v. 23, p. 375–408.

Koons, P.O., 1989, The topographic evolution of collisional mountain belts; a numerical look at the Southern Alps, New Zealand: American Journal of Science, v. 289, no. 9, p. 1041–1069, doi: 10.2475/ajs.289.9.1041.

Koons, P.O., 1994, Three-dimensional critical wedges: tectonics and topography in oblique collisional orogens: Journal of Geophysical Research, v. 99, no. B6, p. 12,301–12,315.

Koons, P.O., 1990, Two-sided orogen: collision and erosion from the sandbox to the Southern Alps, New Zealand: Geology, v. 18, no. 8, p. 679–682.

Koons, P.O., Upton, P., and Barker, A.D., 2012, The influence of mechanical properties on the link between tectonic and topographic evolution: Geomorphology, v. 137, p. 168–180, doi: 10.1016/j.geomorph.2010.11.012.

Koons, P.O., Zeitler, P., Chamberlain, C., Craw, D., and Meltzer, A., 2002, Mechanical links between erosion and metamorphism in Nanga Parbat, Pakistan Himalaya: American Journal of Science, v. 302, no. 9, p. 749–773.

Koons, P.O., Zeitler, P.K., and Hallet, B., 2013, Tectonic aneurysms and mountain building, *in* Schroder, J.F. ed., Treatise on Geomorphology, Academic Press, San Diego, p. 318–349.

Lague, D., Hovius, N., and Davy, P., 2005, Discharge, discharge variability, and the bedrock channel profile: Journal of Geophysical Research: Earth Surface, v. 110, doi: 10.1029/2004JF000259.

Leckie, D.A., 1994, Canterbury Plains, New Zealand-implications for sequence stratigraphic models: AAPG Bulletin, v. 78, no. 8, p. 1240–1256.

Lee, D.T., and Schachter, B.J., 1980, Two algorithms for constructing a Delaunay triangulation: International Journal of Computer & Information Sciences, v. 9, no. 3, p. 219–242, doi: 10.1007/BF00977785.

Leopold, L., and Maddock, T., 1953, The hydraulic geometry of stream channels and some physiographic implications: geological survey professional paper, v. 252.

Lifton, N., and Chase, C., 1992, Tectonic, climatic and lithologic influences on landscape fractal dimension and hypsometry: implications for landscape evolution in the San Gabriel Mountains, California: Geomorphology, v. 5, p. 77–114.

Little, T.A., Cox, S., Vry, J.K., and Batt, G., 2005, Variations in exhumation level and uplift rate along the oblique-slip Alpine fault, central Southern Alps, New Zealand: Geological Society of America Bulletin, v. 117, no. 5, p. 707–723, doi: 10.1130/B25500.1.

Liu, Z., and Bird, P., 2008, Kinematic modelling of neotectonics in the Persia-Tibet-Burma orogen: Geophysical Journal International, v. 172, no. 2, p. 779–797, doi: 10.1111/j.1365-246X.2007.03640.x.

Liu, Y., Santosh, M., Zhao, Z.B., Niu, W.C., and Wang, G.H., 2011, Evidence for palaeo-Tethyan oceanic subduction within central Qiangtang, northern Tibet: Lithos, v. 127, no. 1-2, p. 39–53, doi: 10.1016/j.lithos.2011.07.023.

Lockner, D., Tanaka, H., Ito, H., Ikeda, R., Omura, K., and Naka, H., 2009, Geometry of the Nojima Fault at Nojima-Hirabayashi, Japan – I. A Simple Damage Structure Inferred from Borehole Core Permeability: Pure and Applied Geophysics, v. 166, no. 10-11, p. 1649–1667, doi: 10.1007/s00024-009-0515-0.

Loget, N., and Van Den Driessche, J., 2009, Wave train model for knickpoint migration: Geomorphology, v. 106, no. 3-4, p. 376–382, doi: 10.1016/j.geomorph.2008.10.017.

Lubowe, J.K., 1964, Stream junction angles in the dendritic drainage pattern: American Journal of Science, v. 262, p. 325–339.

Mandelbrot, B.B., 1967, How long is the coast of Britain? Statistical self-similarity and the fractal dimension: Science, v. 156, no. 3775, p. 636–638.

Mason, D.P.M., Little, T. a., and Van Dissen, R.J., 2006, Rates of active faulting during later Quaternary fluvial terrace formation at Saxton River, Awatere fault, New Zealand: Bulletin of the Geological Society of America, v. 118, no. 11, p. 1431–1446, doi: 10.1130/B25961.1.

Mirtskhoulava, T.E., 1966, Erosional Stability Of Cohesive Soils: Journal of Hydraulic Research, v. 4, no. 1, p. 37–50, doi: 10.1080/00221686609500091.

Mirtskhoulava, T.E., 1991, Scouring by flowing water of cohesive and noncohesive beds: Journal of Hydraulic Research, v. 29, no. 3, p. 341–354, doi: 10.1080/00221689109498438.

Mitchell, T.M., Ben-Zion, Y., and Shimamoto, T., 2011, Pulverized fault rocks and damage asymmetry along the Arima-Takatsuki Tectonic Line, Japan: Earth and Planetary Science Letters, v. 308, no. 3-4, p. 284–297, doi: 10.1016/j.epsl.2011.04.023.

Moglen, G., and Bras, R., 1995, The effect of spatial heterogeneities on geomorphic expression in a model of basin evolution: Water Resources Research, v. 31, no. 10, p. 2613–2623.

Molnar, P., Anderson, R.S., and Anderson, S.P., 2007, Tectonics, fracturing of rock, and erosion: Journal of Geophysical Research, v. 112, no. F3, p. F03014, doi: 10.1029/2005JF000433.

Montési, L.G.J., 2004, Controls of shear zone rheology and tectonic loading on postseismic creep: Journal of Geophysical Research, v. 109, no. B10, p. B10404, doi: 10.1029/2003JB002925.

Montési, L., and Zuber, M., 2002, A unified description of localization for application to large-scale tectonics: Journal of Geophysical Research: Solid Earth, v. 107, no. B3.

Montgomery, D.R., and Stolar, D.B., 2006, Reconsidering Himalayan river anticlines: Geomorphology, v. 82, no. 1-2, p. 4–15, doi: 10.1016/j.geomorph.2005.08.021.

Mooney, W., Beroza, G., and Kind, R., 2007, Fault Zones from Top to Bottom: A Geophysical Perspective, *in* Handy, M., Hirth, G., and Hovius, N. eds., Tectonic Faults Agents of Change on a Dynamic Earth, MIT Press, Cambridge, MA, USA, p. 24–61.

Moore, J.R., Sanders, J.W., Dietrich, W.E., and Glaser, S.D., 2009, Influence of rock mass strength on the erosion rate of alpine cliffs: Earth Surface Processes and Landforms, v. 34, no. June, p. 1339–1352, doi: 10.1002/esp.

Nash, D., 1980, Morphologic dating of degraded normal fault scarps: The Journal of Geology, v. 88, no. 3, p. 353–360.

Nicol, A., and Van Dissen, R., 2002, Up-dip partitioning of displacement components on the oblique-slip Clarence Fault, New Zealand: Journal of Structural Geology, v. 24, p. 1521–1535, doi: 10.1016/S0191-8141(01)00141-9.

Niemann, J.D., Gasparini, N.M., Tucker, G.E., and Bras, R.L., 2001, A quantitative evaluation of Playfair's law and its use in testing long-term stream erosion models: Earth Surface Processes and Landforms, v. 26, no. 12, p. 1317–1332, doi: 10.1002/esp.272.

Norris, R.J., and Cooper, A.F., 2001, Late Quaternary slip rates and slip partitioning on the Alpine Fault, New Zealand: Journal of Structural Geology, v. 23, no. 2-3, p. 507–520, doi: 10.1016/S0191-8141(00)00122-X.

Norris, R.J., and Cooper, A.F., 1995, Origin of small-scale segmentation and transpressional thrusting along the Alpine Fault, New Zealand: Geological Society of America Bulletin, v. 107, no. 2, p. 231–240, doi: 10.1130/0016-7606(1995)107<0231:OOSSSA>2.3.CO;2.

Norris, R.J., Koons, P.O., and Cooper, a. F., 1990, The obliquely-convergent plate boundary in the South Island of New Zealand: implications for ancient collision zones: Journal of Structural Geology, v. 12, no. 5-6, p. 715–725, doi: 10.1016/0191-8141(90)90084-C.

Norris, R.J., and Toy, V.G., 2014, Continental transforms: A view from the Alpine Fault: Journal of Structural Geology, v. 64, p. 3–31, doi: 10.1016/j.jsg.2014.03.003.

Ouimet, W.B., Whipple, K.X., Royden, L.H., Sun, Z., and Chen, Z., 2007, The influence of large landslides on river incision in a transient landscape: Eastern margin of the Tibetan Plateau (Sichuan, China): Bulletin of the Geological Society of America, v. 119, no. 11-12, p. 1462–1476, doi: 10.1130/B26136.1.

Penck, W., and Penck, A., 1924, Die morphologische Analyse: ein Kapitel der physikalischen Geologie: Engelhorn.

Price, N.A., Johnson, S.E., Gerbi, C.C., and West, D.P., 2012, Identifying deformed pseudotachylyte and its influence on the strength and evolution of a crustal shear zone at the base of the seismogenic zone: Tectonophysics, v. 518-521, p. 63–83, doi: 10.1016/j.tecto.2011.11.011.

Rabus, B., Eineder, M., Roth, A., and Bamler, R., 2003, The shuttle radar topography mission—a new class of digital elevation models acquired by spaceborne radar: ISPRS Journal of Photogrammetry and Remote Sensing, v. 57, no. 4, p. 241–262, doi: 10.1016/S0924-2716(02)00124-7.

Rattenbury, M.S., Townsend, D.B., and Johnston, M.R., 2006, Geology of the Kaikoura area. Institute of Geological and Nuclear Sciences 1:250000 geological map 13.1 sheet +70 p.:.

Read, S.A.L., Richards, L., and Perrin, N.D., 2000, Assessment of New Zealand Greywacke Rock Masses with the Hoek-Brown Failue Criterion: GeoEng2000, Melbourne,.

Rempe, M., Mitchell, T., Renner, J., Nippress, S., Ben-Zion, Y., and Rockwell, T., 2013, Damage and seismic velocity structure of pulverized rocks near the San Andreas Fault: Journal of Geophysical Research: Earth Surface, v. 118, p. 1–19, doi: 10.1002/jgrb.50184.

Richardson, G.K., 1982, Fowlers Fault site report: Earth Deformation Section, New Zealand Geological Survey.

Robl, J., Hergarten, S., and Stüwe, K., 2008, Morphological analysis of the drainage system in the Eastern Alps: Tectonophysics, v. 460, no. 1-4, p. 263–277, doi: 10.1016/j.tecto.2008.08.024.

Roe, G.H., 2005, Orographic Precipitation: Annual Review of Earth and Planetary Sciences, v. 33, no. 1, p. 645–671, doi: 10.1146/annurev.earth.33.092203.122541.

Roering, J.J., Kirchner, J.W., and Dietrich, W.E., 2001, Hillslope evolution by nonlinear, slope-dependent transport: Steady state morphology and equilibrium adjustment timescales: Journal of Geophysical Research, v. 106, no. B8, p. 16499, doi: 10.1029/2001JB000323.

Rosenbloom, N.A., and Anderson, R.S., 1994, Hillslope and channel evolution in a marine terraced landscape, Santa Cruz, California: Journal of Geophysical Research, v. 99, no. B7, p. 14013–14029.

Roy, S.G., Johnson, S.E., Koons, P.O., and Jin, Z., 2012, Fractal analysis and thermal-elastic modeling of a subvolcanic magmatic breccia: The role of post-fragmentation partial melting and thermal fracture in clast size distributions: Geochemistry Geophysics Geosystems, v. 13, no. 5, p. Q05009, doi: 10.1029/2011GC004018.

Roy, S.G., Koons, P.O., Upton, P., and Tucker, G.E., 2015, The influence of crustal strength fields on the patterns and rates of fluvial incision: Journal of Geophysical Research: Earth Surface, v. 120, p. 275–299, doi: 10.1002/2014JF003281.

Saether, E., and Ta'asan, S., 2004, A Hierarchical Approach to Fracture Mechanics: NASA STI Program Office Report.

Sammis, C.G., and Biegel, R.L., 1989, Fractals, fault-gouge, and friction: Pure and Applied Geophysics, v. 131, no. 1/2, p. 255–271.

Sammis, C.G., King, G., and Biegel, R., 1987, The kinematics of gouge deformation: Pure and Applied Geophysics, v. 125, no. 5, p. 777–812, doi: 10.1007/BF00878033.

Sammis, C.G., Osborne, R.H., Anderson, L., Banerdt, M., and White, P., 1986, Self-similar cataclasis in the formation of fault gouge: Pure and Applied Geophysics, v. 124, no. 1/2, p. 53–78.

Scheidegger, A.E., 2004, Morphotectonics: Springer Berlin Heidelberg, Berlin, Heidelberg.

Scheidegger, A.E., 2001, Surface joint systems, tectonic stresses and geomorphology: a reconciliation of conflicting observations: Geomorphology, v. 38, no. 3-4, p. 213–219, doi: 10.1016/S0169-555X(00)00091-X.

Scheidegger, A.E., 1998, Tectonic predesign of mass movements, with examples from the Chinese Himalaya: Geomorphology, v. 26, no. 1-3, p. 37–46, doi: 10.1016/S0169-555X(98)00050-6.

Scheidegger, A.E., 1979, The principle of antagonism in the Earth's evolution: Tectonophysics, v. 55, p. T7–T10.

Schellart, W.P., 2000, Shear test results for cohesion and friction coefficients for different granular materials: scaling implications for their usage in analogue modelling: Tectonophysics, v. 324, p. 1–16.

Schumacher, F.P., and Kim, E., 2014, Evaluation of directional drilling implication of double layered pipe umbrella system for the coal mine roof support with composite material and beam element methods using FLAC 3D: Journal of Mining Science, v. 50, no. 2, p. 335–348, doi: 10.1134/S1062739114020173.

Schwartz, A.J., Kumar, M., Adams, B.L., and Field, D.P. (Eds.), 2009, Electron Backscatter Diffraction in Materials Science: Springer, New York.

Seidl, M., and Dietrich, W., 1992, The problem of channel erosion into bedrock: Catena, v. Supplement, p. 101–124.

Shepard, M.K., Brackett, R.A., and Arvidson, R.E., 1995, Self-affine (fractal) topography: Surface parameterization and radar scattering: Journal of Geophysical …, v. 100, no. E6, p. 11709–11718.

Shimamoto, T., and Nagahama, H., 1992, An argument against the crush origin of pseudotachylytes based on the analysis of clast-size distribution: Journal of Structural Geology, v. 14, no. 8/9, p. 999–1006.

Shoemaker, E.M., Squires, R.L., and Abrams, J., 1978, Bright Angel and Mesa Butte fault systems of northern Arizona: Geological Society of Amrica Memoirs, v. 152, no. 15, p. 341–367, doi: 10.1130/MEM152.

Sibson, R.H., 1977, Fault rocks and fault mechanisms: Journal of the Geological Society, v. 133, p. 191–213.

Sibson, R.H., 1982, Fault zone model, heat flow, and the depth distribution of earthquakes in the continental crust of the United States: Bulletin of the Seismological Society of America, v. 72, no. 1, p. 151–163.

Simpson, G.D.H., Cooper, A.F., and Norris, R.J., 1994, Late Quaternary evolution of the Alpine Fault Zone at Paringa, South Westland, New Zealand: New Zealand Journal of Geology and Geophysics, v. 37, no. 1, p. 49–58, doi: 10.1080/00288306.1994.9514600.

Sklar, L.S., and Dietrich, W.E., 2004, A mechanistic model for river incision into bedrock by saltating bed load: Water Resources Research, v. 40, no. 6, p. 1–22, doi: 10.1029/2003WR002496.

Sklar, L., and Dietrich, E., 1994, River Longitudinal Profiles and Bedrock Incision Models : Stream Power and the Influence of Sediment Supply E = KyAr (•'•) S:.

Sklar, L.S., and Dietrich, W.E., 2001, Sediment and rock strength controls on river incision into bedrock: Geology, v. 29, no. 12, p. 1087–1090.

Smith, R.B., 1979, The influence of mountains on the atmosphere: Advances in Geophysics, v. 21, p. 87–217.

Smith, R., and Barstad, I., 2004, A linear theory of orographic precipitation: Journal of the Atmospheric Sciences, v. 61, p. 1377–1391.

Sol, S., Meltzer, A., Bürgmann, R., van der Hilst, R.D., King, R., Chen, Z., Koons, P.O., Lev, E., Liu, Y.P., Zeitler, P.K., Zhang, X., Zhang, J., and Zurek, B., 2007, Geodynamics of the southeastern Tibetan Plateau from seismic anisotropy and geodesy: Geology, v. 35, no. 6, p. 563–566, doi: 10.1130/G23408A.1.

Sólyom, P.B., and Tucker, G.E., 2004, Effect of limited storm duration on landscape evolution, drainage basin geometry, and hydrograph shapes: Journal of Geophysical Research, v. 109, no. F3, p. F03012, doi: 10.1029/2003JF000032.

Sornette, D., and Davy, P., 1991, Fault growth model and the universal fault length distribution: Geophysical Research Letters, v. 18, p. 1079–1081.

Stock, J., and Montgomery, D.R., 1999, Geologic constraints on bedrock river incision using the stream power law: Journal of Geophysical Research, v. 104, no. B3, p. 4983–4993.

Stock, J.D., Montgomery, D.R., Collins, B.D., Dietrich, W.E., and Sklar, L., 2005, Field measurements of incision rates following bedrock exposure: Implications for process controls on the long profiles of valleys cut by rivers and debris flows: Geological Society of America Bulletin, v. 117, no. 11/12, p. 174–194, doi: 10.1130/B25560.1.

Stüwe, K., Robl, J., Hergarten, S., and Evans, L., 2008, Modeling the influence of horizontal advection, deformation, and late uplift on the drainage development in the India-Asia collision zone: Tectonics, v. 27, no. 6, doi: 10.1029/2007TC002186.

Sung, Q.-C., and Chen, Y.-C., 2004, Self-affinity dimensions of topography and its implications in morphotectonics: an example from Taiwan: Geomorphology, v. 62, no. 3-4, p. 181–198, doi: 10.1016/j.geomorph.2004.02.012.

Sutherland, R., 1999, Cenozoic bending of New Zealand basement terranes and Alpine Fault displacement: A brief review: New Zealand Journal of Geology and Geophysics, v. 42, no. 2, p. 295–301, doi: 10.1080/00288306.1999.9514846.

Sutherland, D.G., Ball, M.H., Hilton, S.J., and Lisle, T.E., 2002, Evolution of a landslide-induced sediment wave in the Navarro River, California: Bulletin of the Geological Society of America, v. 114, no. 8, p. 1036–1048, doi: 10.1130/0016-7606(2002)114<1036:EOALIS>2.0.CO;2.

Tembe, S., Lockner, D., and Wong, T., 2009, Constraints on the stress state of the San Andreas Fault with analysis based on core and cuttings from San Andreas Fault Observatory at Depth (SAFOD) drilling phases 1 and 2: Journal of Geophysical Research, v. 114, no. B11, p. B11401, doi: 10.1029/2008JB005883.

Terzaghi, K. von, 1944, Theoretical Soil Mechanics.

Thomson, R., 1993, Clyde Dam engineering geological completion report volume 1: text and appendices.

Tomlinson, A.I., and Sansom, J., 1994, Rainfall normals for New Zealand for the period 1961 to 1990: NIWA Science and Technology Series Number 3.

Trevisani, S., Cavalli, M., and Marchi, L., 2009, Variogram maps from LiDAR data as fingerprints of surface morphology on scree slopes: Natural Hazards and Earth System Science, v. 9, no. 1, p. 129–133, doi: 10.5194/nhess-9-129-2009.

Tucker, G., 2004, Drainage basin sensitivity to tectonic and climatic forcing: Implications of a stochastic model for the role of entrainment and erosion thresholds: Earth Surface Processes and Landforms, v. 29, p. 185–205, doi: 10.1002/esp.1020.

Tucker, G., and Bras, R., 2000, A stochastic approach to modeling the role of rainfall variability in drainage basin evolution: Water Resources Research, v. 36, no. 7, p. 1953–1964.

Tucker, G.E., and Hancock, G.R., 2010, Modelling landscape evolution: Earth Surface Processes and Landforms, v. 35, no. 1, p. 28–50, doi: 10.1002/esp.

Tucker, G., Lancaster, S., and Gasparini, N., 2001, The channel-hillslope integrated landscape development model (CHILD), *in* Harmon, R.S. and Doe, W.W. eds., Landscape erosion and Evolution Modeling, Kluwer Academic/Plenum Publishers, New York.

Tucker, G.E., and Slingerland, R., 1996, Predicting sediment flux from fold and thrust belts: Basin Research, v. 8, p. 329–349.

Twiss, R.J., and Moores, E.M., 1992, Structural Geology: Macmillan.

Upton, P., and Craw, D., 2014, Extension and gold mineralisation in the hanging walls of active convergent continental shear zones: Journal of Structural Geology, v. 64, p. 135–148, doi: 10.1016/j.jsg.2013.08.004.

Upton, P., and Koons, P.O., 2007, Three-Dimensional Geodynamic Framework for the Central Southern Alps, New Zealand: Integrating Geology, Geophysics and Mechanical Observations, *in* A Continental Plate Boundary: Tectonics at South Island, New Zealand, p. 253–270.

Upton, P., Koons, P.O., Craw, D., Henderson, C.M., and Enlow, R., 2009, Along-strike differences in the Southern Alps of New Zealand: Consequences of inherited variation in rheology: Tectonics, v. 28, no. 2, p. 1–15, doi: 10.1029/2008TC002353.

Wagner, T., Fabel, D., Fiebig, M., Häuselmann, P., Sahy, D., Xu, S., and Stüwe, K., 2010, Young uplift in the non-glaciated parts of the Eastern Alps: Earth and Planetary Science Letters, v. 295, no. 1-2, p. 159–169, doi: 10.1016/j.epsl.2010.03.034.

Wagner, T., Fritz, H., Stüwe, K., Nestroy, O., Rodnight, H., Hellstrom, J., and Benischke, R., 2011, Correlations of cave levels, stream terraces and planation surfaces along

the River Mur-Timing of landscape evolution along the eastern margin of the Alps.: Geomorphology, v. 134, no. 1-2, p. 62–78, doi: 10.1016/j.geomorph.2011.04.024.

Walcott, R.C., and Summerfield, M. a., 2008, Scale dependence of hypsometric integrals: An analysis of southeast African basins: Geomorphology, v. 96, no. 1-2, p. 174–186, doi: 10.1016/j.geomorph.2007.08.001.

Webb, R.H., Melis, T.S., Griffiths, J.G., Elliot, T.E., Cerling, R.J., Wise, R.H., and Pizzuto, J., 1999, Lava Falls Rapid in Grand Canyon : effects of late Holocene debris flows on the Colorado River: U.S. Geological Survey.

Wellman, H.W., 1979, An uplift map for the South Island of New Zealand, and a model for uplift of the Southern Alps: Royal Society of New Zealand Bulletin, v. 18, p. 13–20.

Whipple, K.X., 2004, Bedrock Rivers and the Geomorphology of Active Orogens: Annual Review of Earth and Planetary Sciences, v. 32, no. 1, p. 151–185, doi: 10.1146/annurev.earth.32.101802.120356.

Whipple, K.X., 2002, Implications of sediment-flux-dependent river incision models for landscape evolution: Journal of Geophysical Research, v. 107, no. B2, p. 2039, doi: 10.1029/2000JB000044.

Whipple, K.X., DiBiase, R.A., and Crosby, B.T., 2013, Bedrock Rivers, *in* Shroder, J.F. ed., Treatise on Geomorphology, Academic Press, San Diego, p. 550–573.

Whipple, K.X., and Tucker, G.E., 1999, Dynamics of the stream-power river incision model: Implications for height limits of mountain ranges, landscape response timescales, and research needs: Journal of Geophysical Research, v. 104, no. B8, p. 17661–17674.

Whittaker, A.C., Cowie, P.A., Attal, M., Tucker, G.E., and Roberts, G.P., 2007a, Bedrock channel adjustment to tectonic forcing: Implications for predicting river incision rates: Geology, v. 35, no. 2, p. 103, doi: 10.1130/G23106A.1.

Whittaker, A.C., Cowie, P.A., Attal, M., Tucker, G.E., and Roberts, G.P., 2007b, Contrasting transient and steady-state rivers crossing active normal faults: new field observations from the Central Apennines, Italy: Basin Research, v. 19, no. 4, p. 529–556, doi: 10.1111/j.1365-2117.2007.00337.x.

Wibberley, C. a. ., and Shimamoto, T., 2003, Internal structure and permeability of major strike-slip fault zones: the Median Tectonic Line in Mie Prefecture, Southwest Japan: Journal of Structural Geology, v. 25, no. 1, p. 59–78, doi: 10.1016/S0191-8141(02)00014-7.

Wilcock, P.R., 2005, Persistence of armor layers in gravel-bed streams: Geophysical Research Letters, v. 32, no. 8, p. L08402, doi: 10.1029/2004GL021772.

Wilcock, P.R., 2001, Toward a practical method for estimating sediment-transport rates in gravel-bed rivers: Earth Surface Processes and Landforms, v. 26, no. 13, p. 1395–1408, doi: 10.1002/esp.301.

Wilcock, P.R., 1998, Two-Fraction Model of Initial Sediment Motion in Gravel-Bed Rivers: Science, v. 280, no. 5362, p. 410–412, doi: 10.1126/science.280.5362.410.

Wilcock, P., Pitlick, J., and Cui, Y., 2009, Estimating Bed-Material Transport in Gravel-bed Rivers: , no. May.

Williams, H., and Hatcher, R., 1982, Suspect terranes and accretionary history of the Appalachian orogen: Geology, v. 10, p. 530–536, doi: 10.1130/0091-7613(1982)10<530.

Wilson, T.H., and Dominic, J., 1998, Fractal interrelationships between topography and structure: Earth Surface Processes and Landforms, v. 23, no. 6, p. 509–525, doi: 10.1002/(SICI)1096-9837(199806)23:6<509::AID-ESP864>3.0.CO;2-D.

Wilson, C.K., Jones, C.H., Molnar, P., Sheehan, A.F., and Boyd, O.S., 2004, Distributed deformation in the lower crust and upper mantle beneath a continental strike-slip fault zone: Marlborough fault system, South Island, New Zealand: Geology, v. 32, no. 10, p. 837, doi: 10.1130/G20657.1.

Wilt, N., 2013, The cuda handbook: A comprehensive guide to gpu programming: Pearson Education, Crawfordsville, Indiana.

Wobus, C.W., Tucker, G.E., and Anderson, R.S., 2006, Self-formed bedrock channels: Geophysical Research Letters, v. 33, no. 18, p. 0–5, doi: 10.1029/2006GL027182.

Wolman, M.G., 1954, A method of sampling coarse river-bed material: Transactions, American Geophysical Union, v. 35, no. 6, p. 951–956.

Xu, T., Moore, I.D., and Gallant, J.C., 1993, Fractals, fractal dimensions and landscapes — a review: Geomorphology, v. 8, no. 4, p. 245–262, doi: 10.1016/0169-555X(93)90022-T.

Yanites, B.J., Tucker, G.E., Hsu, H.-L., Chen, C., Chen, Y.-G., and Mueller, K.J., 2011, The influence of sediment cover variability on long-term river incision rates: An example from the Peikang River, central Taiwan: Journal of Geophysical Research, v. 116, no. F3, p. F03016, doi: 10.1029/2010JF001933.

Yanites, B.J., Tucker, G.E., Mueller, K.J., Chen, Y.G., Wilcox, T., Huang, S.Y., and Shi, K.W., 2010, Incision and channel morphology across active structures along the

Peikang River, central Taiwan: Implications for the importance of channel width: Geological Society of America Bulletin, v. 122, no. 7-8, p. 1192–1208, doi: 10.1130/B30035.1.

Zeitler, P.K., Meltzer, A.S., Koons, P.O., Craw, D., Hallet, B., Chamberlain, C.P., Kidd, W.S.F., Park, S.K., Seeber, L., Bishop, M., and others, 2001, Erosion, Himalayan geodynamics, and the geomorphology of metamorphism: GSA Today, v. 11, no. 1, p. 4–9, doi: 10.1109/IEMBS.2009.5332464.

Zernitz, E., 1932, Drainage patterns and their significance: The Journal of Geology, v. 40, no. 6, p. 498–521.

APPENDIX A

NUMERICAL MODELING IN THE CLASSROOM

Models are simplified or idealized concepts used to determine how different phenomena, agents, or conditions are related within a system. Regardless of what form they take, models allow the curious mind to make connections between seemingly unrelated observations of instances and by doing so expand our understanding of how systems operate. They are therefore an integral component of the scientific method because they allow us to build, test, and revise hypotheses. Their ability to expand and give meaning to observations and measurements make models an invaluable tool in research and education.

In this appendix I explore the educational capabilities of a numerical model of landscape evolution, known as the channel-hillslope integrated landscape dynamics (CHILD) model. CHILD uses formulae that produce patterns resembling natural patterns of river and hillslope erosion, and can therefore be used not only to estimate short and long term changes in landscape form, but also can be compared directly to natural landscape patterns and rates of erosion. I first describe the organization of a graphical user interface used to prepare, run, and visualize simulations, then I provide some example modules that can be used in the undergraduate classroom.

A.1. Approach: Graphical User Interface

There are many examples of robust numerical models that can be used to predict the sensitivity of processes that drive landscape evolution. However, their design is for

advanced users who need flexibility and a wide control of parameterized processes. In its current state, students and other beginners may feel too intimidated to use such code. For this reason I have designed a graphical user interface (GUI) for the CHILD code to allow for greater ease of use. The CHILDGUI simplifies the method for choosing parametric values used to drive the simulation and it provides clear options for visualization and the import of data.

A.2. GUI framework

A.2.1. Preprocessing simple parametric controls and running the simulation

The CHILDGUI (Figure A.1) consists of a series of menu windows that list the model parameters. Each parameter has a dropdown menu that provides a natural range of parametric values. In the main window, three panels allow the user to control rock type, environment, and uplift rate. Rock type represents the cohesive strength of the surface that is eroded, and this value is used to calculate the erodibility. Environmental conditions are represented by the mean annual precipitation rate and the frequency of rainstorms per year. Uplift rates reflect typical low, medium and high rates seen in natural tectonic settings. Other model parameters include the amount of simulated time and the size of the model in meters (the model is assumed to be square, so all dimensions are of the same length). Experiments are executed by pressing the red button, and model progress can be tracked from the Matlab terminal. When complete, the experiment is listed in the model listbox in the lower right corner of the main window.
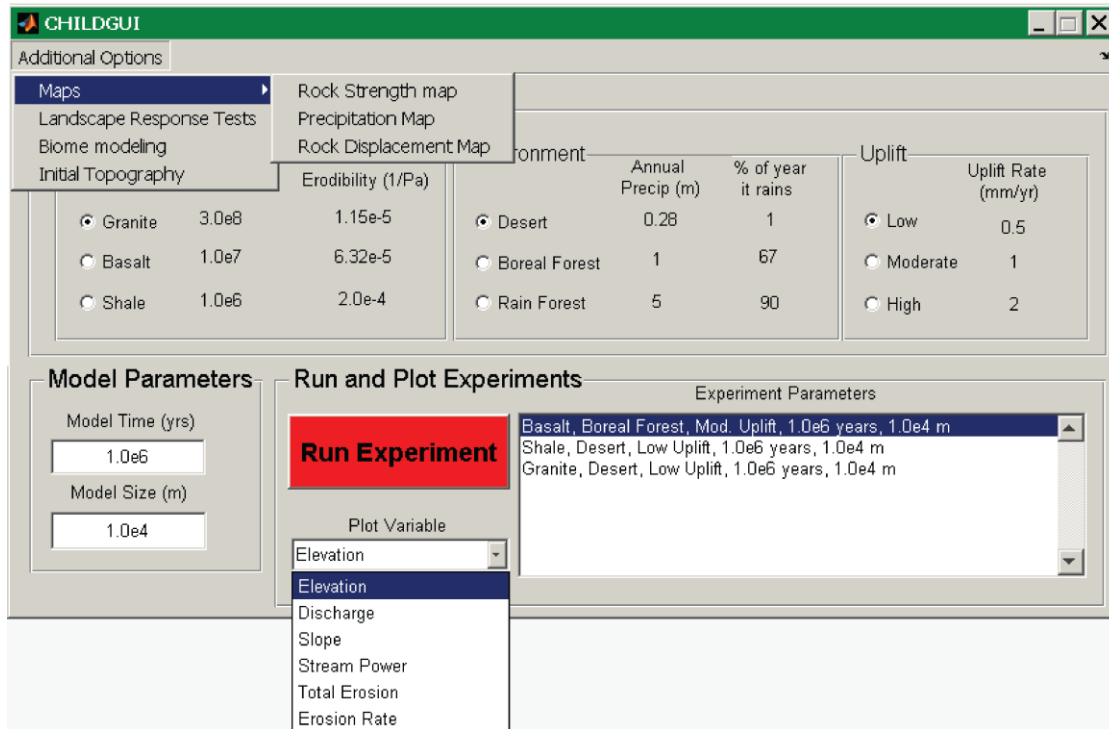
Figure A.1. Main menu of CHILDGUI. Additional options are accessed from dropdown menu, plot options are accessed from popup menu, model parameter values are accessed through radio buttons. Big red button runs experiment.

A.2.2. Visualize the model results

You can choose any simulation to visualize by clicking on the simulation name in the model listbox. Plot the results by clicking the plot variable dropdown box. Options include: elevation, discharge, slope, stream power, total erosion, and erosion rate (Figure A.2). These options give the user simple controls to track the evolution of topography and the drainage network pattern in time, as well as locations of high stream power and the progression of erosion rate as rivers cut into the landscape.
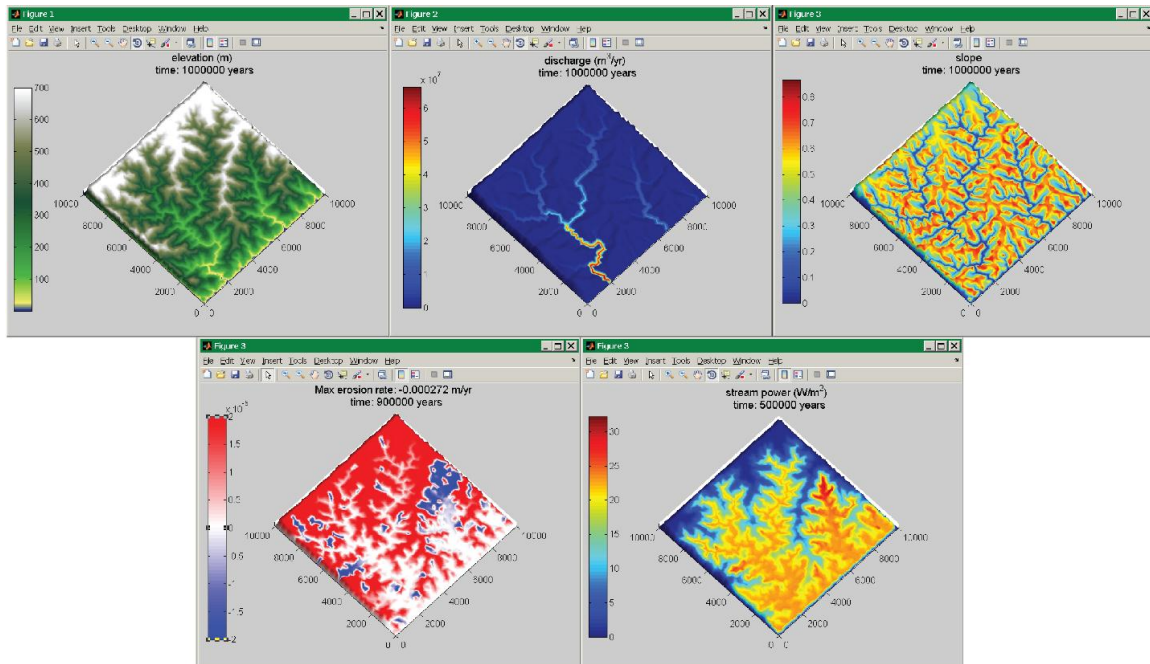
Figure A.2. Examples of plot options. Clockwise from top left: elevation, discharge, slope, erosion rate, and total erosion.

A.2.3. Advanced Options

A.2.3.1. Heterogeneity

In many natural landscapes, heterogeneous conditions of climate, tectonics, or lithology play a primary role in landscape evolution. It is therefore useful to include these heterogeneities in a model if we want to make connections between the shape of the landscape and the initial conditions. Under the advanced options / maps menu, there are options to incorporate maps of rock strength and displacement and climate. Checking Rock strength variability under the rock strength map option (Figure A.3A, B) initiates either a fault zone or a pluton geometry in your model. General options include strength versus host, strength difference factor, size, and depth to exposure. Fault specific options include one or multiple faults, position, and geometric data to position the planar fault zone in the landscape. When switched to pluton, the options are to have a square or circular pluton,

and to allow the presence of weak joints. To turn off all of these options you must click the check box before closing the window.
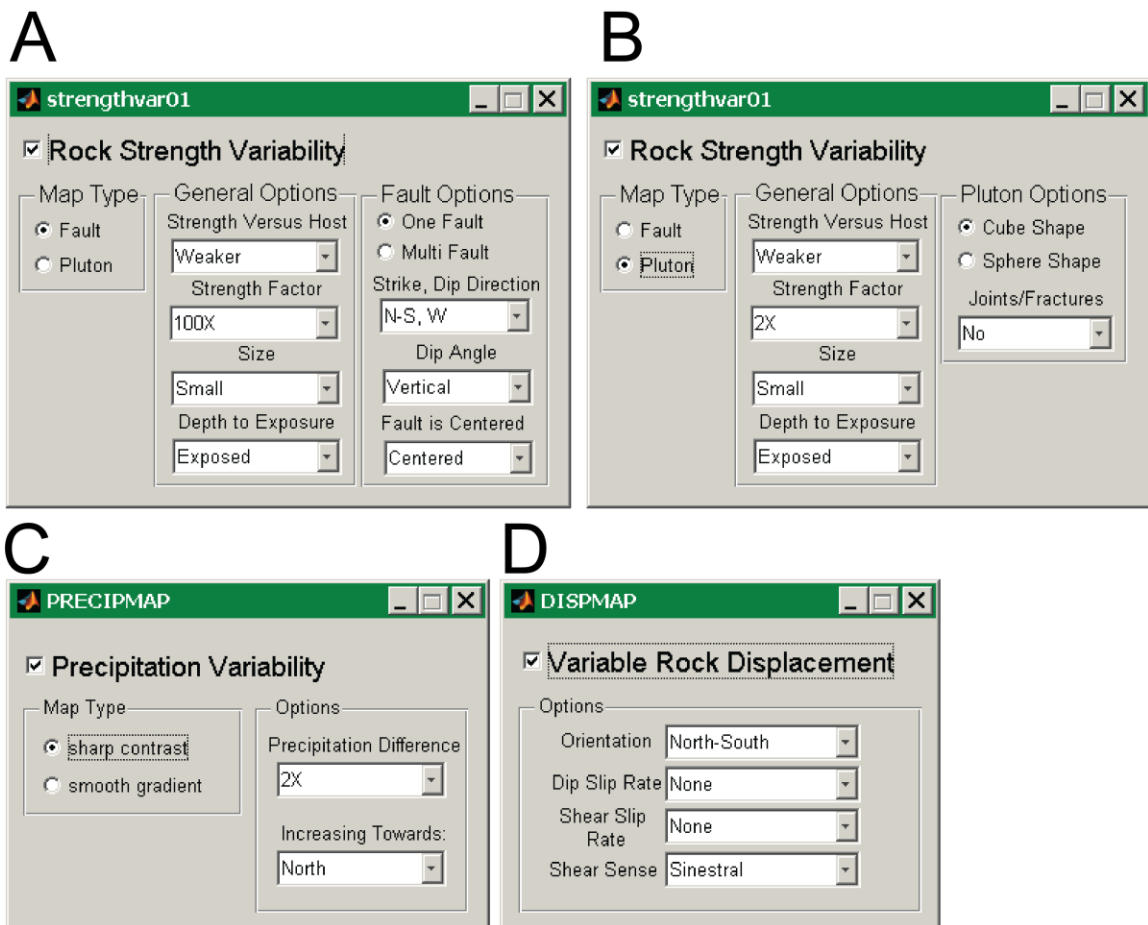

Figure A.3. Additional map options. (A) Fault zone, (B) pluton, (C) precipitation, (D) surface displacement map options.

Precipitation variability is turned on by clicking the check box under precipitation map (Figure A.3C). There are two options: one divides precipitation in the landscape with a sharp transition, and another applies a smooth precipitation gradient. There are additional controls for the magnitude difference between high and low precipitation and the direction in which precipitation increases.

Rock displacement maps are activated by checkbox next to variable rock displacement (Figure A.3D). Here there are options to displace the surface according to

simple fault block motions. CHILDGUI assigns simple kinematic velocity conditions to both fault blocks. Options include the strike direction of the slip plane, the rate of dip-slip, the rate of strike-slip, and the shear sense.

A.2.3.2. Landscape Response Tests

In addition to spatial variability, landscape and environmental conditions can change in time as well. Geomorphologists are interested in studying how landscapes are able to respond to changes in these conditions, and one way to do this is by using a landscape evolution model. In the CHILDGUI advanced options menu, choose landscape response tests (Figure A.4A). The response test is activated by clicking the checkbox next to run a landscape response test. The type of responses include knickpoint, change in uplift rate, change in environment, and change in rock type. Adding a knickpoint is meant to replicate a sudden and sharp change in baselevel, which could be caused by a sudden change in sea level or a sudden seismic event. A change in uplift rate could represent a sudden change in tectonic activity, while environmental changes represent a shift in atmospheric circulation that forces climate change. A change in rock type may occur due to the exposure of a new rock unit with different rock strength. The options for each example generally represent the magnitude of change; for example, you can indicate how large the initial knickpoint is. These tests double the simulation time so you have plenty of time to reach steady surface conditions, then see how the surface changes shape under the new conditions.
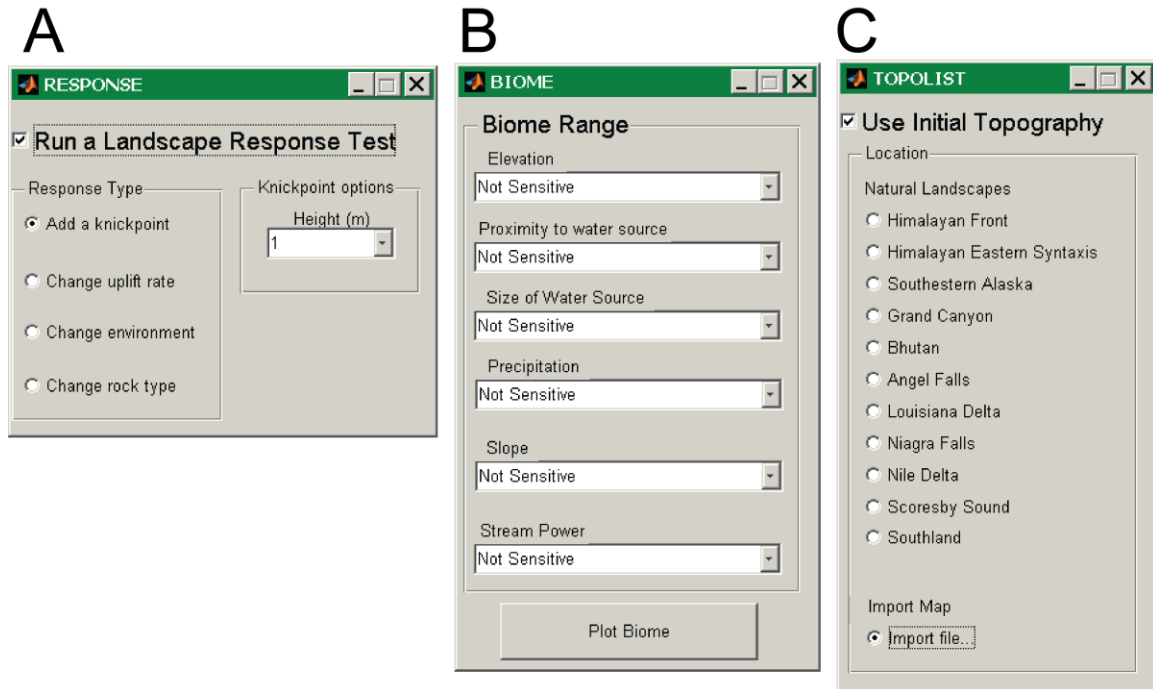
Figure A.4. More options. (A) Response test, (B) Plotting biome range, (C) Using initial topography.

A.2.3.3. Biome Proxy Modeling

Landscapes can host a diverse distribution of organisms depending on gradients of tectonics, climate, and even lithology. Spatial information about topography, rivers, and climate can be used to determine the probability field for the existence of various organisms within the landscape (Figure A.4B). I have written code that allows a user to visualize a probability field for specific organisms based on topography and precipitation rate. The probability field is a function of comfort range of proximity to fluid discharge threshold, precipitation, elevation, and slope, an attempt to quantitatively plot the major factors that would allow for the existence of an organism. The code is only a way of visualizing the probability of organism accommodation, it is not a dynamic contributor to the landscape model. It does not track the progress of an organism using an agent-based or cellular autonomy method, but it is possible to include such methods.

A.2.3.4. Importing Maps, Using Preloaded Surfaces

All of the examples I have given so far are for idealized landscapes that start off with a flat surface. If you are interested in discovering landscape evolution in a real location on Earth, it is possible to run experiments on a number of preloaded surfaces or import an elevation map of your own (Figure A.4C). CHILDGUI accepts geotiff format as well as any ASCII- or column vector-based data formats.

A.3. Hypothetical Course Modules

CHILDGUI has applications for any course involving earth surface dynamics. It has been used in combination with dynamic models of mantle and lithospheric advection to study how erosional processes will respond to real tectonic activity. It has also been used to determine the potential capacity for various locations on Earth to sequester atmospheric CO_2 by silicate weathering in physically disaggregated rock. It has also been used to compare general rates of river incision and glacial incision in landscapes from Southeast Alaska. Apart from these more sophisticated applications, it is a useful tool for predicting simple landscape sensitivity to various internal and external drivers. Below I have provided a few thought questions and modules that can be incorporated in any geoscience classroom.

A.3.1. Basic modules: Sensitivity of landscape to tectonic, climate, and lithological perturbations

1) How does lithology affect relief? Run three simulations with uniform uplift and environment conditions, each with a unique lithology (Figure A.5). How different is the relief between each example and why?
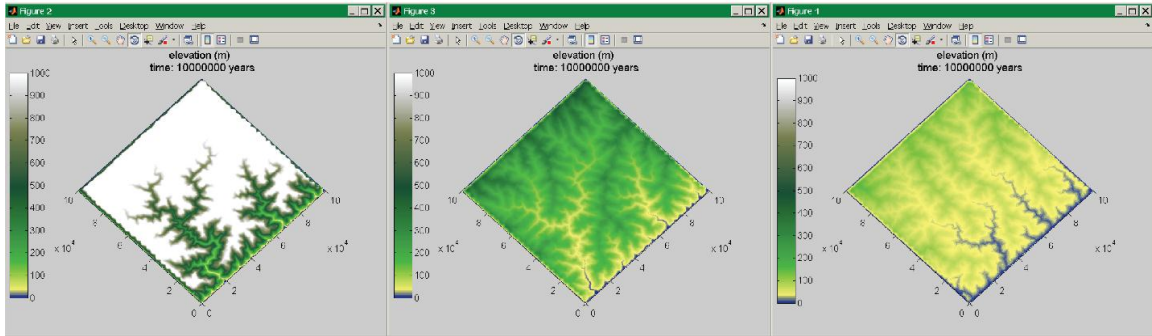
Figure A.5. Lithology experiment. From left to right: Granite (strong), basalt, and shale (weak).

2) Can heterogeneous lithology affect the shape of topography? Using the rock strength map option it is possible to see how a landscape will evolve under conditions of heterogeneous lithology. For example: fault damage zones versus homogeneous rock (Figure A.6) or the exposure of resistant plutons (Figure A.7).

3) How does the landscape respond to an aseismic drop in base-level? Using the Landscape Response Tests option, it is possible to observe the pattern of landscape response to a sudden seismic shift and to track the total amount of time it takes the landscape to respond to the shift.

4) How is sediment yield linked to tectonic uplift rate? Using the total erosion plot option provides the total volume of sediment produced by erosion and uplift, making it simple to compare between uplift rates, climate, and rock type.

5) Do landscapes keep a record of past tectonic activity? The landscape response tests option allows the user to track the change in landscape shape based on a shift in tectonic activity.

6) How can climate change reshape a landscape? Do landscapes keep a record of past climate? Similarly, the landscape respone tests option can be used for climate change.
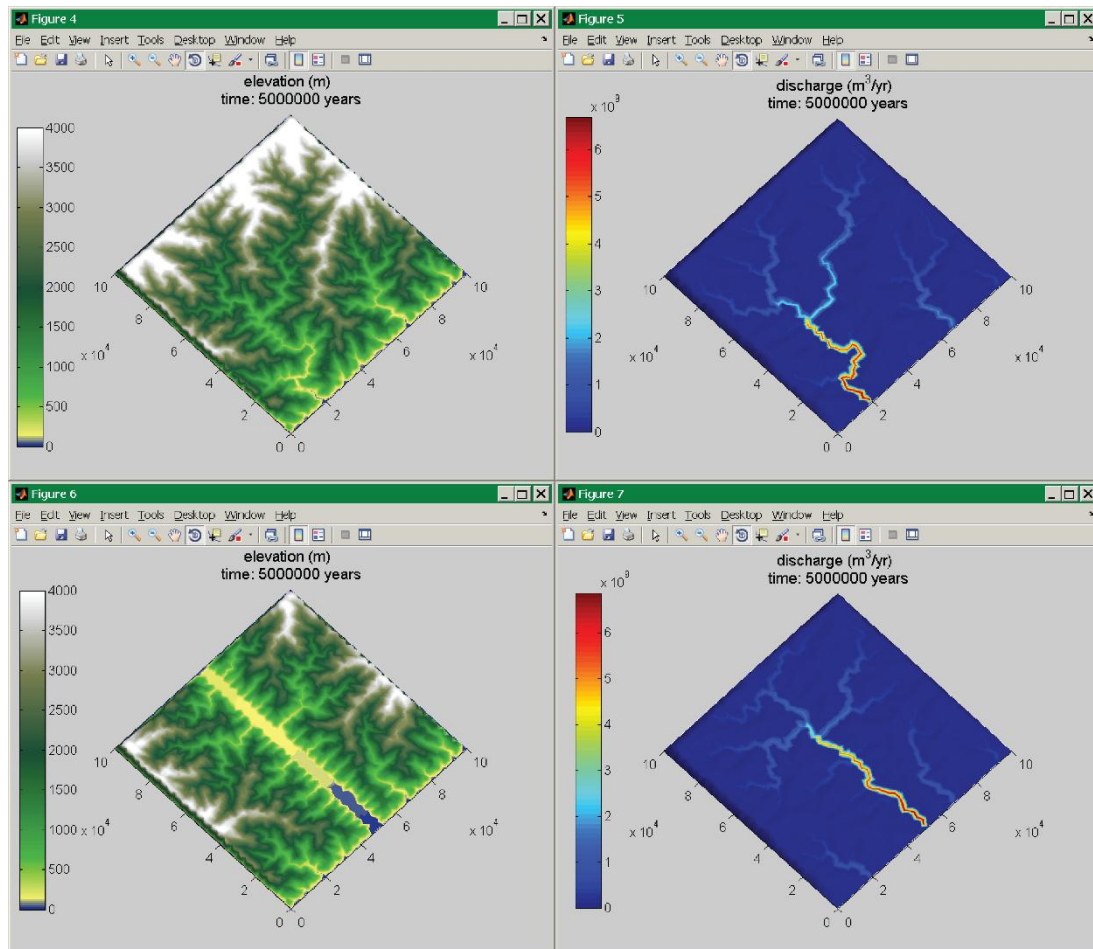
Figure A.6. Fault erosion experiment. Counter-clockwise from top left: Elevation for homogeneous experiment, faulted experiment, discharge for faulted experiment, homogeneous experiment.
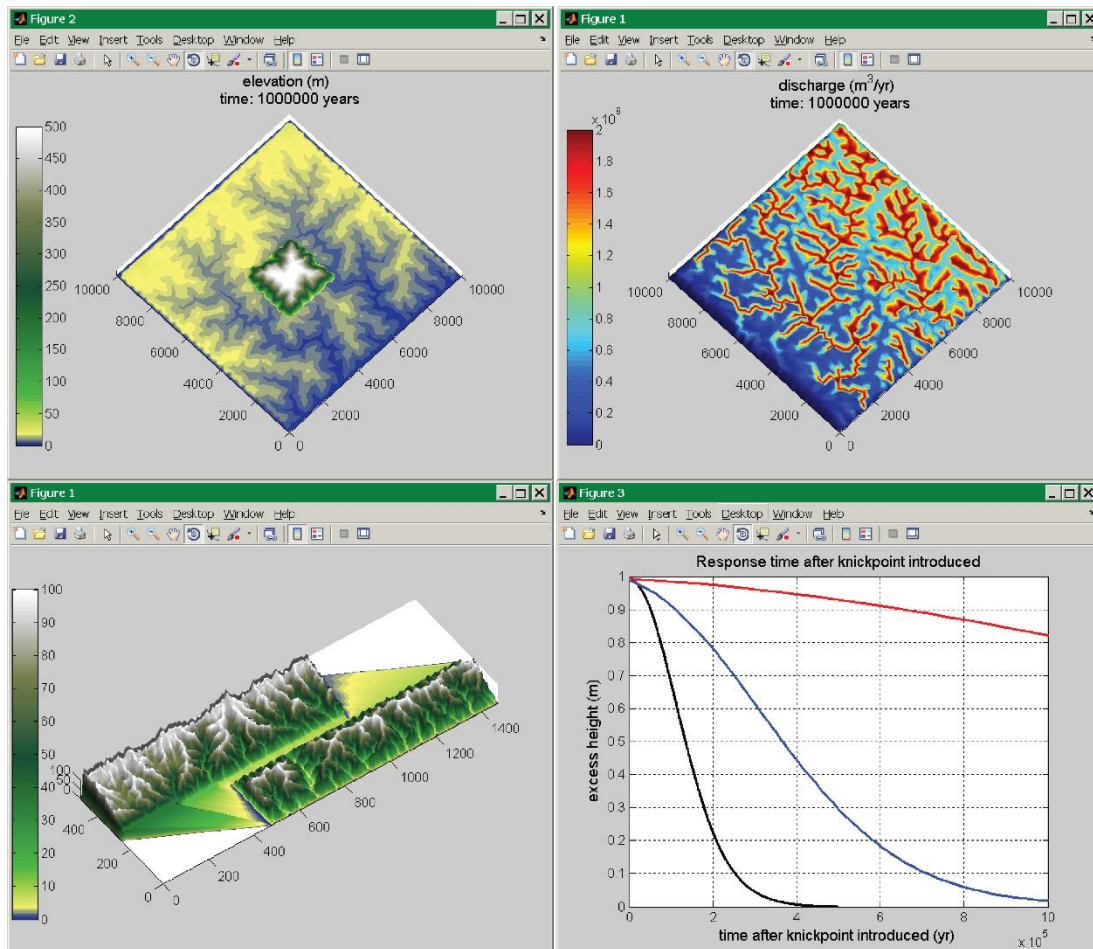
Figure A.7. Pluton, rainfall gradient, and strike-slip fault experiments. Clockwise from top left: erosion of resistant pluton, discharge map for landscape with precipitation gradient increasing to the east, erosion of left-lateral strike slip fault, plot of response rate for the three separate experiments from Figure A.5.

A.3.2. Outlined Theme Modules

A.3.2.1. Exploring the Role of Physical Weathering in Carbon Sequestration: Geomorphology, Tectonics, and Geochemistry

Upon completion of this module students will be able to model the physical erosion of bedrock using CHILDGUI and make estimates for the volume of atmospheric CO2 sequestered under different tectonic, lithological, or climatic conditions, and in doing so be able to provide an educated prediction for the efficiency of carbon sequestration for

different locations on Earth. The students are given a location to study, with information on lithology, tectonics, and climate. They will feed these values into CHILDGUI to get a measure of mean erosion rate and total eroded bedrock in the landscape. These numbers provide the volume of sediment that could sequester CO_2 upon chemical weathering. Based on the mineralogy of their rocks, they can then calculate the volume of sequestered CO_2, understanding that this is probably a maximum estimate. This method can be replicated for any location on Earth, and the students can get an estimate for a global potential. The estimate can then be refined by determining how the sediments will be exposed to chemical weathering in the atmosphere, how much sediments will be shunted into the ocean without chemical weathering, and how much will be buried without undergoing the necessary reactions.

A.3.2.2. Biome Mapping: Geology, Ecology

Upon completion of this module, students will understand the importance of landscape and climate in ecology, and will be able to model the probability field for certain organisms within varying landscapes and under changing tectonic and environmental conditions. This module utilizes the basic sensitivity analysis described above with the biome modeling option (Figure A.8).

1) What tectonic and climatic conditions would be ideal for an organism? Come up with an example organism whose preferred living conditions are well understood, and try replicating those conditions with the CHILDGUI. Using the biome proxy tool, track the probability field for that the organism's existence. Can that organism

survive in this landscape? why or why not? Run a few sensitivity tests to find the right match. What tectonic and climate conditions are ideal for the organism?

2) How sensitive would the organism be to perturbations in climate or tectonics? Try a model in which climate or uplift rate changes suddenly. Could it possibly become endangered, extinct, separated into isolated groups, or required to move a significant distance across the landscape? What is the change is only temporary? Will the organism be able to survive a short-term change in its environment?
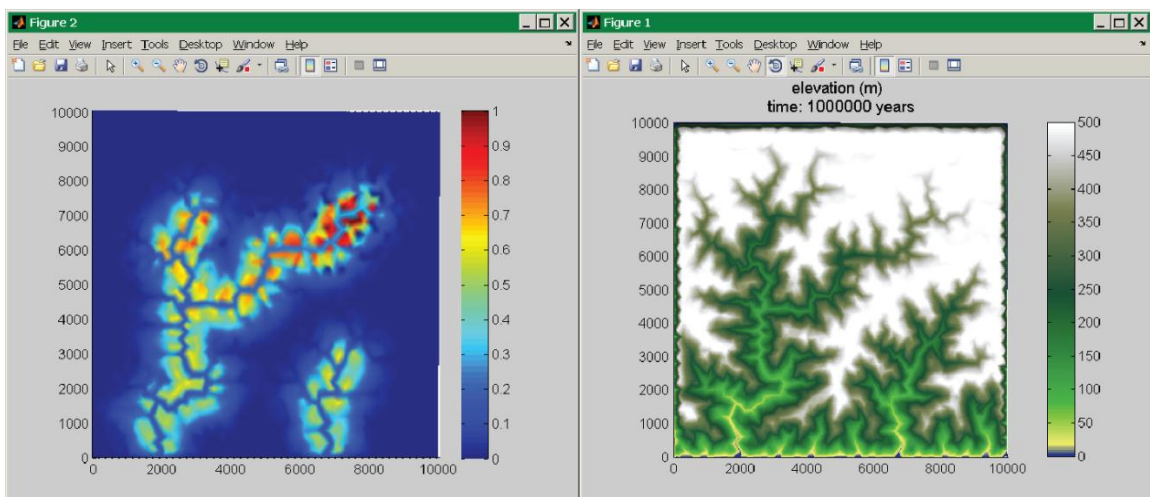

Figure A.8. Example of topography-dependent ecology. From left to right: probability field for an organism comfortable at a moderate elevation with close proximity to large rivers, elevation map used to create the biome proxy map.

A.3.2.3. Dynamics of Natural Resources; Geology, Ecology, and Economics

Upon completion of this module students will be able to understand the importance of tectonics, climate, and surface processes in how natural resources are distributed across the Earth. Additionally, students will learn the economic significance of tectonic and environmental factors using simple board games. Tectonics plays a critical role in shaping the earth's surface and influencing climate. As a result, landscapes reflect tectonic processes through topographic shape and the distribution of surface water, both of which

play a fundamental role in ecology and the distribution of natural resources on Earth. In this module, tectonic models are used to shape the surface of the Earth and arrange the distribution of biomes and natural resources. To make this connection, the board game Settlers of Catan (http://www.catan.com/) is used to play a game of resource collection across the landscape created by the tectonic model. Students should then be able to see the primary role tectonics plays in global ecology and the economy.

1) Students choose a geologic setting and see how the landscape evolves. Which setting was chosen and why? What biomes do you predict will arise from the patterns of topography and climate? Run the biome proxy model over this landscape and replicate the results with the Settlers of Catan board.

2) What does the surface look like? How do different settings influence the spatial distribution of natural resources? Do some conditions lead to greater diversity than others? Greater concentration of resources? Isolation? Difficulty in building trade networks? Port access?

3) How does the rain shadow effect alter the productivity of some natural resources (ample wood and stone on windward side, ample sheep, wheat, brick on lee side)?

4) How does geology play into bargaining, trade agreements, conflict, and strategy?

5) Are there societal timescale transient effects of geology and climate? How would these dynamic changes affect your model economy?

A.3.2.4. Stream power and the inland expansion of Maine settlements: geomorphology, American history, and microeconomics.

Maine has a robust history of watermill-based industries starting as early as the 18th century. New settlers were able to take advantage of the vast array of natural resources inland Maine has to offer by building communities near reliable sources of stream power. Watermills became an essential part of the burgeoning Maine economy, producing goods used locally and abroad from grist mills, sawmills, carding mills, tanneries, shingle mills, woolen mills, and edge tool mills. Stream power played a singular role in Maine settlement throughout the 18th to 20th centuries and its mark is left on the many old mill towns that remain today. But, where does the power come from? This module focuses on what contributes to stream power, how we can predict the distribution of stream power using models, and why some locations were chosen for settling over others (access to stream power, resources, transportation).

1) Contributions to stream power: taking a close look at water flowing down a stream: driving and resisting components (simple navier-stokes), what optimizes stream power?

2) Models for stream power in Maine using elevation and climate data.

3) Historical locations and why they were settled: Rumford, Freedom, Oakland. Have students do some internet searches and see what they can find. Use the biome proxy code combined with Maine elevation and stream data to determine optimal locations for stream power. Do these locations correlate to actual towns? Do they correlate to regions with other natural resources (woods, arable land, ore) were they

accessible to early pioneers? Is there a common trend? Are resources, stream power, and transportation factors all supportive of a settlement? Why or why not?

4) Why is stream power no longer used no longer heavily relied on? Use this opportunity to shift into another module about energy resources and a discussion about relative cost effectiveness of hydro power, oil, wind, solar, nuclear, etc.

APPENDIX B

BEDROCK INCISION, SEDIMENT STORAGE, AND SENSITIVITY TO

STORMS

Here we explore the predicted influence of storm frequency, duration, and magnitude on the mean elevation (Figure B.1A-D) and sediment thicknesses (Figure B.1E-G) in a landscape using three experiments with variable mean rainfall intensity and storm frequency. In all experiments, the drainage network pattern reflects the fault weak zone. Infrequent, high intensity storms lead to less aggradation of sediments in the weak zone (Figure B.1B, E). By increasing the storm/interstorm ratio and reducing the mean rainfall intensity proportionately to preserve a common 1 m a^{-1} rainfall occurrence, alluvium thickness increases in the weak zone and there is some aggradation in larger tributaries (Figure B.1C, D, F, G). Frequent, low intensity storms reduce bedrock slopes (Figure B.1B, C, D) and cause an overall reduction in mean elevation (Figure B.1A). It might seem surprising that bedrock erosion is more efficient when flow is less variable. This reflects the particular formulation we have used, in which bedrock detachment rate is proportional to discharge per unit channel width, and width is proportional to the square root of discharge. This combination of assumptions means that incision rate scales with the square root of discharge. The less-than-linear dependence on discharge means that incision rate decreases when discharge becomes more variable. This would not necessarily be the case if we had included a threshold for detachment (for more on this issue, see (Tucker and Bras, 2000; Molnar, 2001; Snyder, 2003; Tucker, 2004; Lague et al., 2005; Molnar and Burlando, 2005)).

The frequency and amplitude of storm events can influence the supply and residence time of gravel-dominant alluvium. Model watersheds with large, infrequent storms host steep bedrock relief and relatively thin alluvium in the banks of the structurally confined channel. Conversely, watersheds with small, frequent storms host shallow bedrock relief and relatively thick alluvium. Alluvium thickness depends on the frequency of large storm events that are more likely to mobilize sediment.
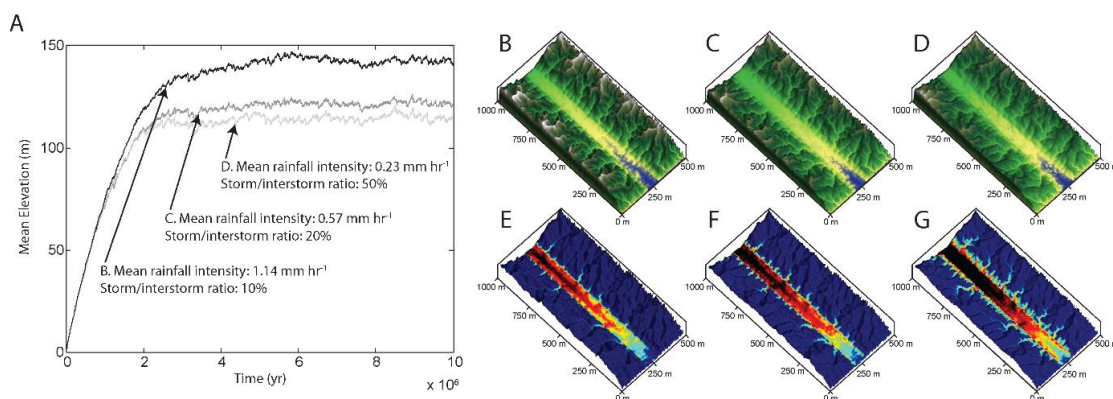

Figure B.1. Storm sensitivity experiment. (A) Plot of mean elevation over time for three different storm arrangements. (B-D) Elevation of the three experiments, (E-G) mean alluvium thickness for the three experiments.

APPENDIX C

GRID MAINTENANCE FOR KINEMATIC-TECTONIC LANDSCAPE

EVOLUTION MODELS

Surface regridding is necessary to maintain a consistent grid resolution and domain size and to ensure that the 3D kinematic solution is applied to the correct surface points. The need to continually regrid the surface stems from the differential lateral motion along the fault. The regrid algorithm fits within the full algorithm for KCHILD, a series of MatLab scripts I have written to control the input, output, and execution of CHILD (Figure C.1).
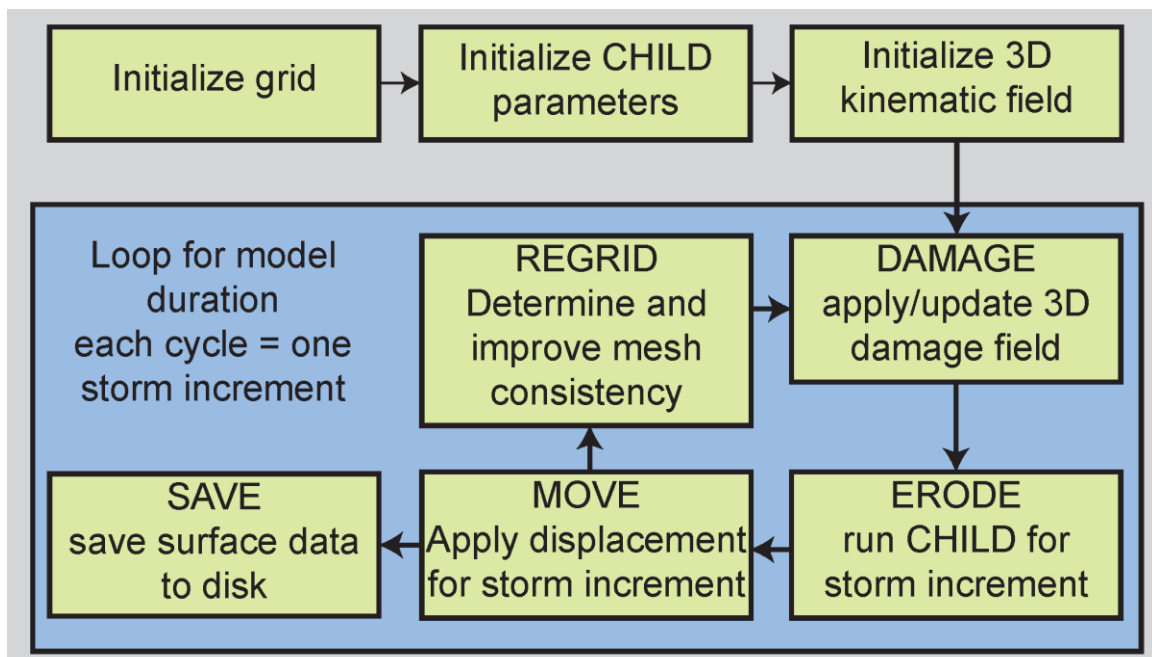

Figure C.1. Algorithm for KCHILD. Grid is initialized, parameters are applied to the model, and the kinematic field is assigned to the model surface before simulation begins. Within the simulation cycle, check and update the condition of the rock damage field in 3D, erode the surface using CHILD, apply the displacement based on the kinematic field, and if mesh quality is reduced, regrid. With every cycle data are saved to disk.

There are three different cases where regridding is necessary: reverse motion leads to the convergence of surface points, normal motion leads to the divergence of surface points, and any lateral motion leads to points departing from or crossing through the model domain boundaries.

A.1. Case 1

For reverse motion models, surface points representing the mobile block (MB) converge on and rise above points representing the fixed block (FB). Two situations may arise. First, points representing the MB may thrust over points representing the FB (Figure C.2). In this case, the FB points are buried by the overlying points and they are removed from the grid. However, the elevation of the overlying points is corrected to equal the elevation of the now buried FB points and the thickness of the MB at each point. Alternatively, erosion at MB points may exceed the thickness of the MB before they thrust over the FB (Figure C.2). In this case the points become fixed with the FB and their position is either reinterpolated or they are removed in order to maintain a consistent point grid resolution.

A.2. Case 2

For normal motion models, the MB diverges from the FB and this leads to a local decrease in grid resolution (Figure C.2). New points are added to the domain in regions where spacing between points exceeds twice the average spacing length. New nodes are added with a small randomized irregularity in order to match the initially irregularly discretized grid.
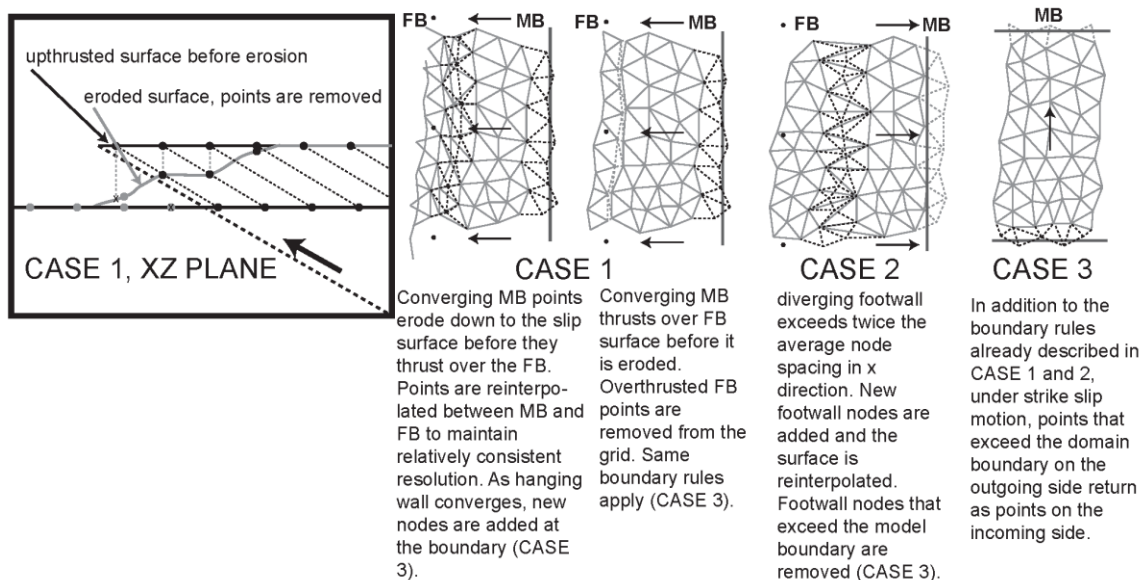
Figure C.2. Cartoon scenarios for the three different cases for grid reinterpolation. MB: mobile block. FB: fixed block.

A.3. Case 3

This case of grid maintenance is used for Model Set 2 only. In all cases with lateral motion the shape and size of the model domain will change with continued surface displacement unless points are added or removed along boundaries. I apply periodic tectonic boundary conditions on the north and south borders to conserve the shape and size of the model domain (Figure C.2). Under strike slip motion, points that approach the northern or southern boundaries are relocated to the opposing boundary.

Under reverse dip slip motion, points are added on the eastern boundary to account for area lost through convergence (Figure C.2). When the easternmost located points exceed twice the average point spacing distance from the boundary, new points are added at the boundary. The elevations of these new points are equal to their nearest neighbors with an additional amount of random noise applied. This is a simple boundary condition that assumes the MB is semi-infinite and experiences a uniform degree of erosion.

Conversely, points are removed on the eastern boundary to account for area gained by divergence (Figure C.2). When points exceed the boundary position, they are removed from the model domain. The western boundary is adjacent to the fixed block and is therefore a passive margin; it only experiences the small ambient uplift rate relative to baselevel.

BIOGRAPHY OF THE AUTHOR

Samuel Geoffrey Roy was born in Waterville, Maine on September 9, 1985. He was raised in Oakland, Maine and graduated from Messalonskee High School in 2004. He attended the University of Maine and graduated with a Bachelor's degree in Earth Sciences. After an internship at the Stillwater Mining Company in Nye, Montana and a semester of graduate courses at Southern Illinois University, Carbondale, Samuel returned to the University of Maine in 2009 where he earned a Master of Science degree in Earth Sciences in 2011.

Samuel Geoffrey Roy is a candidate for the Doctor of Philosophy degree in Earth and Climate Sciences from the University of Maine in August 2015.